



HAL
open science

Parametrized growth and procedural noise for mechanical metamaterial design

Semyon Efremov

► **To cite this version:**

Semyon Efremov. Parametrized growth and procedural noise for mechanical metamaterial design. Computational Geometry [cs.CG]. Université de Lorraine, 2022. English. NNT : 2022LORR0046 . tel-03704004

HAL Id: tel-03704004

<https://hal.univ-lorraine.fr/tel-03704004v1>

Submitted on 24 Jun 2022

HAL is a multi-disciplinary open access archive for the deposit and dissemination of scientific research documents, whether they are published or not. The documents may come from teaching and research institutions in France or abroad, or from public or private research centers.

L'archive ouverte pluridisciplinaire **HAL**, est destinée au dépôt et à la diffusion de documents scientifiques de niveau recherche, publiés ou non, émanant des établissements d'enseignement et de recherche français ou étrangers, des laboratoires publics ou privés.



**UNIVERSITÉ
DE LORRAINE**

**BIBLIOTHÈQUES
UNIVERSITAIRES**

AVERTISSEMENT

Ce document est le fruit d'un long travail approuvé par le jury de soutenance et mis à disposition de l'ensemble de la communauté universitaire élargie.

Il est soumis à la propriété intellectuelle de l'auteur. Ceci implique une obligation de citation et de référencement lors de l'utilisation de ce document.

D'autre part, toute contrefaçon, plagiat, reproduction illicite encourt une poursuite pénale.

Contact bibliothèque : ddoc-theses-contact@univ-lorraine.fr
(Cette adresse ne permet pas de contacter les auteurs)

LIENS

Code de la Propriété Intellectuelle. articles L 122. 4

Code de la Propriété Intellectuelle. articles L 335.2- L 335.10

http://www.cfcopies.com/V2/leg/leg_droi.php

<http://www.culture.gouv.fr/culture/infos-pratiques/droits/protection.htm>



UNIVERSITÉ
DE LORRAINE



Loria
Laboratoire lorrain de recherche
en informatique et ses applications

Inria
INVENTEURS DU MONDE NUMÉRIQUE

Université de Lorraine
ECOLE DOCTORALE IAEM-LORRAINE
MFX Team LORIA, Inria Nancy-Grand Est

Thèse présentée pour obtenir le grade universitaire de
Docteur

Discipline: Informatique

Semen Efremov

Croissance paramétrée et bruit procédural
pour la conception de métamatériaux
mécaniques

Parametrized growth and procedural noise for mechanical metamaterial
design

Sous la direction de Sylvain Lefebvre et Jonàs Martínez

Soutenance le 03/05/2022 devant le jury composé de:

Stefanie Hahmann	Rapporteur
Jean-Michel Dischler	Rapporteur
Kostas Danas	Examineur
Alexandra Ion	Examineur
Marie-Odile Berger	Président du jury
Jonàs Martínez	Codirecteur de thèse
Sylvain Lefebvre	Codirecteur de thèse

Résumé

Le défi de la conception de structures au comportement physique sur mesure est essentiellement géométrique par nature : diverses propriétés sont obtenues en modifiant l'architecture interne d'un volume de pièce. Ce phénomène a suscité l'intérêt des chercheurs il y a plus d'un siècle, car il offre un large éventail de matériaux dont les propriétés conviennent à différentes applications industrielles, où il est crucial d'obtenir des propriétés extrêmes. Cela peut conduire à des améliorations significatives des propriétés du produit et se traduire par un bénéfice économique et une réduction de la consommation de matériaux. De plus, il y a quelques dizaines d'années, avec les améliorations significatives de l'électronique, ce défi a été suivi par le développement de méthodes de calcul efficaces à haute résolution permettant l'exploration des propriétés physiques des matériaux conçus.

Le terme "métamatériau" a été utilisé pour la première fois par Walser [223] en 2001, mais à ce jour, il n'existe aucun accord sur une définition commune. Nous considérerons la définition la plus générale proposée par [99] : les métamatériaux sont à la fois des composites conçus à l'aide de méthodes ciblées (conception rationnelle), constitués d'un ou de plusieurs matériaux de base et composés de blocs avec la topologie de la microstructure adaptée. Les propriétés de ces matériaux peuvent aller bien au-delà de celles de leurs constituants et atteindre finalement des propriétés physiques exotiques non observées dans la nature. La variété des propriétés effectives des métamatériaux étudiés de nos jours est impressionnante, concernant divers domaines tels que l'acoustique, la mécanique, l'optique et l'électromagnétisme, entre autres.

Motivation

Comme il a été mentionné plus haut, le thème de la création de matériaux aux propriétés physiques prescrites a commencé à évoluer rapidement au cours des deux dernières décennies. Plusieurs raisons peuvent expliquer ce regain d'intérêt, mais la plupart sont liées au développement récent de la production et des systèmes informatiques. La croissance explosive de la puissance de calcul et de l'accessibilité des ordinateurs personnels ainsi que le développement rapide des méthodes numériques (optimisation de la topologie) et des modèles mathématiques (problèmes directs et inverses) dans la conception assistée par ordinateur des structures ont permis une validation relativement rapide des propriétés physiques. En plus, cela a permis de modéliser des structures au comportement physique adapté. Les récentes améliorations dans le domaine de la fabrication additive (AM) ont considérablement accru la pertinence de la recherche en conception assistée par ordinateur. Les raisons en sont les améliorations constantes de la qualité de production et de la variété des matériaux, ainsi que la possibilité de reproduire des géométries complexes.

En outre, le développement constant de nouvelles technologies dans différentes applications crée une forte demande de nouveaux matériaux

aux propriétés mécaniques adaptées : l'industrie aérospatiale, l'automobile, l'architecture et la conception d'implants. Des recherches récentes ont montré le fort potentiel des métamatériaux comme solution adéquate et plus écologique à ces problèmes. Le développement de matériaux optimisés peut contribuer à l'amélioration de l'environnement. Par exemple, l'utilisation de matériaux poreux à haute résistance au lieu de pièces solides réduit les déchets de matériaux pendant la production et la consommation de carburant en réduisant le poids, ce qui diminue les émissions de CO₂.

Il existe un grand nombre d'approches pour générer des matériaux aux propriétés physiques adaptées : de l'optimisation de la topologie aux modèles analytiques pour explorer des familles spécifiques de structures. Mais même jusqu'à présent, l'espace complet des matériaux 3D n'a pas été entièrement exploré en raison de sa taille énorme. La raison peut également en être que la majorité des méthodes et études existantes sont basées sur la recherche d'une seule solution optimale. Cette solution est optimale dans le sens où elle possède les valeurs prescrites exactes des paramètres effectifs conçus pour une classe géométrique spécifique. Par conséquent, cela conduit à une classe de solutions relativement restreinte. Il existe un besoin de méthodes de calcul rapides qui pourraient générer des métamatériaux basés sur des propriétés moins restrictives (telles que la symétrie ou la direction de l'anisotropie) et qui soient flexibles en termes de fourniture d'une large gamme d'interfaces différentes dans ces conditions (sans considérer une seule géométrie). Dans certaines applications de la conception de matériaux (par exemple, l'architecture, la conception de voitures, de vêtements et de meubles), il peut être important de pouvoir choisir l'apparence du matériau, la topologie de sa microstructure dans une classe de matériaux donnée et, éventuellement, de trouver dans cette classe ceux qui ont des propriétés physiques spécifiques. Par ailleurs, la génération de matériaux périodiques arbitraires avec une gradation spatiale régulière reste un problème ouvert : avoir plusieurs tuiles périodiques et interpoler de manière régulière entre elles n'est pas un problème trivial. Cette caractéristique permettrait de modéliser des matériaux périodiques, ayant des propriétés différentes à diverses échelles ou des propriétés locales variables, appelés matériaux à gradation fonctionnelle (FGM).

Contributions principales

Cette thèse a été consacrée au développement et à l'analyse de méthodes pour la conception assistée par ordinateur de matériaux aux propriétés mécaniques adaptées. J'ai considéré l'approche de conception avancée, lorsque le point de départ du processus de calcul sont les conditions sur les propriétés géométriques de la structure, car il y avait une intuition que ces dernières peuvent être associées aux propriétés mécaniques. J'ai divisé la description de mes recherches (correspondant à deux chapitres de ce manuscrit) en deux sujets principaux différents : la conception de matériaux périodiques 3D basés sur des distances étoilées et l'analyse théorique des propriétés du bruit de phase,

un bon candidat pour les matériaux de modélisation à haute performance avec une bonne isotropie et anisotropie contrôlable.

Je présente un algorithme de croissance cellulaire 3D pour générer des matériaux périodiques à cellules fermées et une méthode pour extraire une structure à cellules ouvertes (figure 1.1). J'ai conçu deux méthodes différentes pour paramétrer une partie étoilée 3D : explicite et implicite. Une famille de distances étoilées, associée à un large éventail de treillis périodiques possibles, donne naissance à un espace de métamatériaux extrêmement vaste. Pour faciliter l'exploration de cet espace, j'ai utilisé la symétrie, qui est un outil très important dans la conception des matériaux, et je l'ai appliquée à la méthode de croissance. De plus, la principale contribution de la méthode est qu'elle est capable de générer de manière transparente et efficace des matériaux à gradient fonctionnel (voir figure 1.2). La paramétrisation de la distance permet l'interpolation spatiale entre différents matériaux, ce qui permet de générer des matériaux cellulaires gradués avec des transitions spatiales dures ou douces. Tous les résultats obtenus ici ne présentent qu'une seule composante connectée, ce qui montre implicitement que cette approche fournit une connectivité structurelle complète de la conception. J'ai étudié et mis en œuvre deux algorithmes d'homogénéisation itérative pour calculer les propriétés mécaniques effectives des matériaux conçus. De plus, j'ai imprimé certains des matériaux architecturés à l'aide de la technologie d'impression 3D et j'ai effectué des tests de compression. En conséquence, l'approche présentée ici est devenue un outil complet et efficace pour l'exploration de l'espace des matériaux.

Un élément clé de ma recherche est de réaliser une homogénéisation numérique des microstructures que j'étudie. Pour y parvenir, je propose dans un chapitre séparé une revue des implémentations et des comparaisons des méthodes que j'ai utilisées à cette fin.

La deuxième contribution de cette thèse est l'étude d'un nouveau type de bruit : le bruit de phasor procédural. En particulier, j'ai effectué une analyse théorique de ce bruit dans l'espace de Fourier et j'ai obtenu des expressions analytiques pour extraire les hautes ou basses fréquences pour les deux cas de superposition de noyaux de directions uniques et multiples.

Les résultats ont été publiés dans les revues CAD et TOG et présentés à la société de recherche lors des conférences SIGGRAPH 2019 et SPM 2021 ([64], [214]). Le bruit de phasor est actuellement utilisé dans l'industrie de l'infographie : il a été employé dans le logiciel RenderMan de PIXAR et utilisé pour la production de certaines scènes du film "*Star Wars : The Rise of Skywalker*". L'auteur espère que les résultats de ses travaux susciteront de futures études sur les matériaux cellulaires et le développement de nouvelles méthodes de conception.

Description du contenu

Le chapitre 2 présente les travaux liés à la recherche actuelle. Je commence par un aperçu des métamatériaux en fonction de leurs propriétés physiques et de leurs applications. Ensuite, je discute d'une approche robuste pour la conception des matériaux - l'optimisation topologique (TO) - et des techniques d'homogénéisation pour l'étude de leurs propriétés mécaniques. En outre, j'aborde la cristallographie à travers les travaux qui ont déjà employé la symétrie au problème de la conception de matériaux périodiques. Je discute également des articles consacrés aux types de matériaux les plus connus : les treillis périodiques et les surfaces minimales triplement périodiques (TPMS). Je passe ensuite aux études connexes des matériaux à gradient fonctionnel (FDM) et aux approches de la conception de métamatériaux basées sur des techniques issues de l'infographie. Enfin, je donne un bref aperçu des principales méthodes de fabrication existantes.

Dans le chapitre 3 Je présente la méthode de croissance discrète 3D basée sur la distance étoilée et les réseaux cristallins [64]. Au lieu de résoudre le problème inverse (en essayant de calculer une interface résultante à partir de paramètres effectifs donnés), je choisis comme base l'idée d'une connexion entre la géométrie microscopique de la structure et ses propriétés mécaniques macroscopiques. Sur la base de recherches antérieures en 2D [138], je construis une méthode de croissance en 3D et je l'analyse du point de vue de la cristallographie. Cette approche permet à un concepteur d'imposer la symétrie cristalline souhaitée et donne ainsi accès à un grand nombre de matériaux dans une classe correspondante de comportement élastique.

Dans le chapitre 4 je présente deux schémas itératifs pour résoudre le problème d'homogénéisation pour les déformations élastiques linéaires. Tout d'abord, je commence par introduire le problème de la déformation d'un matériau élastique périodique. Ensuite, je passe à la description des méthodes, puis aux détails d'implémentation. Enfin, je termine par une brève comparaison des méthodes.

Le chapitre 5 est dédié au bruit phasor [214]. Il est fortement lié au bruit de Gabor qui est largement utilisé dans le domaine de l'infographie. Il est apparu qu'une onde sinusoïdale phasor est adaptée à la génération de matériaux composites en raison de sa représentation d'amplitude discrète, d'un bon contrôle de sa distribution spatiale et de son spectre, mais aussi de ses performances de calcul élevées. En effet, cette caractéristique permet d'employer l'onde sinusoïdale phasor pour la conception efficace de matériaux biphasés avec des microstructures complexes [215]. La possibilité de définir une direction spatiale arbitraire du champ résultant conduit à un grand contrôle des propriétés mécaniques du matériau en changeant la direction de l'anisotropie ou même en créant un matériau isotrope [47]. Je divise le travail en plusieurs étapes. Tout d'abord, en considérant le cas d'un stratifié (champ unidirectionnel), et en obtenant une dérivation analytique de son spectre et de son spectre de variance. Ensuite, en passant au cas de deux directions, en obtenant et en analysant également les expressions analytiques du spectre du bruit et de sa variance.

Enfin, j'étudie le cas des directions multiples.

Liste des publications

- Tricard, T., Efremov, S., Zanni, C., Neyret, F., Martínez, J., and Lefebvre, S. (2019). Procedural phasor noise. *ACM Transactions on Graphics (TOG)*, 38(4), 1-13.
- Efremov, S., Martínez, J., and Lefebvre, S. (2021). 3D periodic cellular materials with tailored symmetry and implicit grading. *Computer-Aided Design*, 140, 103086.

Liste des référentiels

- Méthode de croissance paramétrée en 3D: https://github.com/SemyonEfremov/3D_star_shaped_growth_method
- Méthodes d'homogénéisation itératives 3D basées sur la FFT: https://github.com/SemyonEfremov/iterative_FFT_homogenization_scheme

Abstract

With constant development of technologies, computational and manufacturing capabilities increase, production methods evolve, and new techniques appear. As a result, the need for new materials with tailored, optimized properties for different applications arises. Periodic composites with tailored microstructure topology, called cellular metamaterials are extensively studied in this context. These structures are known for their remarkable mechanical properties, including high strength, lower weight, and increased energy absorption. The use of these materials allows to achieve improved physical properties or specific functional features and provides economical gain and ecological benefit.

This thesis is dedicated to the development and analysis of methods for computer-aided design of materials with tailored mechanical properties. The mechanical metamaterials were studied through two different approaches: modelling periodic structures through a parameterized growth model and procedural noise functions. To tackle the challenge of obtaining near-regular microstructures with progressively varying properties, I proposed and studied a cellular material spawned by a growth process. The growth is parameterized by a 3D star-shaped set at each lattice point, defining the geometry that will appear around it. Individual tiles may be computed and used in a periodic lattice, or a global structure may be produced under spatial gradations, changing the parametric star-shaped set at each lattice location. Beyond free spatial gradation, an important advantage of this approach is that elastic symmetries can be intrinsically enforced. It is shown in this work how shared symmetries between the lattice and the star-shaped set directly translate into symmetries of the periodic structures' elastic response. Thus, the approach enables restricting the symmetry of the elastic responses – monoclinic, orthorhombic, trigonal, and so on – while freely exploring a wide space of possible geometries and topologies. I provide a comprehensive study of the space of symmetries and broad combinations of growth process parameters. Furthermore, I demonstrate through numerical and experimental results the expected responses triggered by the obtained structures.

The second contribution of this thesis is a novel procedural pattern synthesis technique. This approach exhibits desirable properties for modeling highly contrasted patterns, that are well suited to produce surface and microstructure details. This approach defines a stochastic smooth phase field — a phasor noise — that is then fed into a periodic function (e.g. a sine wave), producing an oscillating field with prescribed main frequencies and preserved contrast oscillations. I present in this thesis a mathematical model, that builds upon a reformulation of Gabor noise in terms of a phasor field that affords for a clear separation between local intensity and phase. In particular, I study the behavior of phasor noise in terms of its power spectrum. Hence, a comparative theoretical study of phasor noise was performed in order to gain understanding of links between its properties and parameters.

Aknowledgements

I would like to express my deepest gratitude to my co-advisors Sylvain Lefebvre and Jonàs Martínez for their highly qualified scientific guidance and immediate help and support in solving problems that arose during my experience as a PhD student.

I also thank Pierre Bedell and Pierre-Alexandre Hugron for their assistance and mentoring in 3D printing and creating photos of the obtained results, Thibault Tricard and Cédric Zanni for great experience of joint research on phasor noise, and the entire MFX team for their exceptional responsiveness and pleasant working atmosphere.

The current PhD program was financially supported by the ANR MuFFin (ANR-17-CE10-0002) and "Région Lorraine and FEDER" projects.

Contents

1	Introduction	18
1.1	Motivation	18
1.2	Main contributions	19
1.3	Description of the content	21
1.4	List of publications	23
1.5	List of repositories	23
2	Related work	24
2.1	Metamaterials	25
2.1.1	Mechanical metamaterials	25
2.1.2	Electromagnetic and optical metamaterials	27
2.1.3	Acoustic and transport metamaterials	29
2.1.4	Stimuli-responsive metamaterials	30
2.2	Numerical design approaches	30
2.2.1	Topology optimization	30
2.3	Computation of the elastic behavior	35
2.4	Crystallography in metamaterials design	37
2.5	Design of cellular materials: periodic trusses	42
2.6	Minimal surface materials	46
2.7	Functionally graded materials	50
2.8	Noise-based design of materials	55
2.9	Fabrication methods	57
3	3D periodic cellular materials with tailored symmetry and implicit grading	65
3.1	Notations	65
3.2	Introduction	66
3.3	Growth method	68
3.4	Symmetry and point group	71
3.5	Crystal lattice	74
3.6	Star-shaped distance	77
3.7	Materials with prescribed elastic tensor	84
3.7.1	Symmetry: distance, lattice, and resulting structure	86
3.7.2	Growth instabilities	89
3.8	Materials with spatial grading	92
3.8.1	Interpolation between star-shaped distances	92

3.8.2	Interpolation between lattices	96
3.9	Results	97
3.9.1	Numerical results	97
3.9.2	Experimental results	99
3.10	Conclusion	101
3.11	Future work	102
4	Computation of the elastic behavior of 3D periodic materials	104
4.1	Notations	104
4.2	Introduction	104
4.3	Investigation and validation of mechanical properties	105
4.3.1	Homogenization of periodic material	107
4.3.2	Numerical methods	108
4.3.3	Methods validation and comparison	111
4.4	Implementation	115
4.5	Conclusion and future work	115
5	Procedural phasor noise	117
5.1	Notations	117
5.2	Introduction	118
5.3	Notations and formulation of the problem	119
5.3.1	Gabor noise	119
5.3.2	Phasor noise	119
5.3.3	Complex Gabor noise	120
5.3.4	Noise variance	120
5.3.5	Fourier transform	121
5.4	Bi-lobe case	121
5.4.1	Spectrum of the intensity	122
5.4.2	Spectrum of Gabor noise	123
5.4.3	Variance spectrum of Gabor noise	123
5.4.4	Spectrum of phasor sinewave	125
5.4.5	Variance spectrum of phasor sinewave	127
5.5	Two-directional case	128
5.5.1	Spectrum of the intensity	129
5.5.2	Spectrum of Gabor noise	129
5.5.3	Variance spectrum of Gabor noise	130
5.5.4	Spectrum of phasor sinewave	131
5.5.5	Variance spectrum of phasor sinewave	133
5.6	General case	134
5.6.1	Spectrum of the intensity	135
5.6.2	Spectrum of Gabor noise	136
5.6.3	Variance spectrum of Gabor noise	137
5.6.4	Spectrum of phasor sinewave	138
5.6.5	Variance spectrum of phasor sinewave	139
5.7	A note on indeterminate points	140
5.8	Conclusion	143
5.9	Future work	143

6 Conclusion	145
6.1 General discussion	145
Appendices	168
A Symmetry notation	169
B Structures gallery	171

List of Figures

1.1	Visualization of the growth method.	20
1.2	Example of 3D closed and open cell FGMs obtained with our method.	20
1.3	Examples of Phasor sine wave for the cases of a single direction (a), two directions (b) and a two-phase material (c) corresponding to (a).	22
2.1	Examples of cellular materials seen in nature [23].	24
2.2	Examples of mechanical metamaterials.	25
2.3	Examples of electromagnetic metamaterials [99].	28
2.4	Photos of an acoustic metamaterial [233].	29
2.5	Design of an anti-tetrachiral anisotropic honeycomb unit cell presented in [42].	38
2.6	Examples of 3D printed samples containing $6 \times 3 \times 3$ unit cells for designed and optimized materials with prescribed symmetry [250].	39
2.7	Example of mechanical metamaterial with chiral geometry [74].	40
2.8	Effective mechanical properties of 17087 structures designed in [131].	40
2.9	A unit cell of an auxetic composite with prescribed symmetry [179].	41
2.10	Cellular material with optimized for maximum energy absorption topology [39].	43
2.11	Examples of anisotropic lattices designed in [209].	43
2.12	Examples of single unit cells of compound cubic supertrusses [249].	45
2.13	Experimental deformation data of different octet-trusses [198].	45
2.14	Example of a shell-core lattice design [155].	46
2.15	Examples of TPMS-based materials considered in [140]: unit cells (top) and $4 \times 4 \times 4$ arrangements (bottom).	48
2.16	Von Mises stress computed for a gyroid structure under 3.5% compressive strain [2].	48
2.17	CAD models and 3D printed specimen of interpenetrating phase composites based on different types of TPMSs (Neovius, Gyroid, Fischer) [50].	49
2.18	Optimized ETPMS-based structures presented in [118] before (top) and after (bottom) smoothing.	51

2.19	Examples of structures representing different FDM design strategies [169]: topology optimization with SIMP penalization (a), inserted lattices of double primitive (b) and body-centered cubic (c) cells, graded double primitive lattice (d), scaled double primitive lattice (e) and original double primitive lattice (f).	52
2.20	An example of a 3D FGM with spatial variation of the shear modulus (top) and its cross section (bottom) [176].	52
2.21	An example of real (left) and replicated (right) with a 3D printer objects [24]. The internal structure of the replicated design (bottom) consists of two different materials (black and blue).	53
2.22	Examples of FDM materials composed of primitive and gyroid lattices with poor mechanical properties in the transition area (left) and after correction with increased strength (right) [139].	54
2.23	Example of texture synthesis-based reproduction of a 3D material (Berea sandstone) [127].	55
2.24	Examples fiber-shaped (left) and disc-shaped (right) anisotropic microstructures [47].	56
2.25	An example of FDM architecture with horizontal spatial variation between columnar (orange) and lamellar (orange) materials presented in [106].	57
2.26	Examples of metallic foams corresponding to different manufacturing process and the degree of control over their microscopic structure [114].	59
2.27	AM manufacturing techniques [81].	62
3.1	Some classic examples of periodic trusses.	66
3.2	Overview of our method.	69
3.3	Visualization of the growth process.	70
3.4	Three types of a cubic Bravais unit cell.	74
3.5	Examples of crystal lattices with more complex structure: orthorhombic.	75
3.6	Examples of crystal lattices with more complex structure: monoclinic.	75
3.7	Examples of crystal lattices with more complex structure: trigonal.	76
3.8	Illustration of 3D star-shaped distance.	78
3.9	Examples of star-shaped sets obtained with the explicit parametrization.	80
3.10	Parameterization with spherical polyhedra.	81
3.11	An example of the implicit parametrization.	82
3.12	Two star-shaped sets obtained with the same implicit parametrization but different scaling parameters.	83
3.13	Some star-shaped sets are centered in a lattice, both sharing a hexagonal symmetry.	86
3.14	Example of closed and open cell structures corresponding to BCC crystal lattice in Figure 3.4b with a different type of a central nucleus with $\bar{4}$ symmetry.	87

3.15 Example of closed and open cell structures corresponding to the complex crystal lattice in Figure 3.5 with 222 symmetry. 88

3.16 Example of closed and open cell structures corresponding to the complex crystal lattice in Figure 3.6 with $\frac{2}{m}$ symmetry. 89

3.17 A simple example of growth instabilities. 90

3.18 An example of slight rotational symmetry-breaking event. 91

3.19 Illustrative coincident case in two-dimensions. 91

3.20 Linear interpolation between S_1 and S_2 93

3.21 Closed-cell geometry gradation: central part with S_2 and the rest with S_1 94

3.22 Example of a closed cell FDM with internal radial inclusion of Kelvin cells. 95

3.23 Example of an open cell FDM with internal radial inclusion of Kelvin cells. 96

3.24 Cellular geometry gradation between two lattices (a) and (b). 97

3.25 Different surface frame structures, geometrically smoothed. 98

3.26 3D printed elongated with spatially varying structures. 99

3.27 3D printed periodic cellular materials. 100

3.28 3D printed, progressive gradation between two closed-cell materials. 101

3.29 3D printed concentric grading, with a sharp transition. 101

4.1 Given a periodic structure (a) we compute its homogenized elasticity tensor (b) from the prescribed strain and stress fields over G 106

4.2 Von Mises stress distribution computed with both implementations. 111

4.3 The first test tile of periodic material and corresponding effective elastic tensors. 113

4.4 The second test tile of periodic material and corresponding effective elastic tensors. 114

5.1 Bi-lobe Gabor noise (a) and its spectrum (b). 123

5.2 Bi-lobe Gabor noise (a) and its variance spectrum (b). 124

5.3 When the intensity field of Gabor noise fades. 126

5.4 Bi-lobe phasor sinewave (a) and its spectrum (b). 126

5.5 Bi-lobe phasor sinewave (a) and its variance spectrum (b). 127

5.6 Two-directional Gabor noise (a) and its normalized version without low-frequencies components in its variance spectrum. 130

5.7 Phasor sinewave instances for different angles between the directions \vec{F}_1 and \vec{F}_2 of constituent bi-lobes. 132

5.8 Phasor sinewaves Ψ_{Δ^-} (a) and Ψ_{Δ^+} (b) and corresponding Gabor noise $\mathcal{G}(\vec{x})$ (c). 134

5.9 Four instances of Gabor noise (background), its spectrum (left bottom) and its variance spectrum (right bottom). 137

5.10 Four instances of phasor sinewave (background), its spectrum (left bottom) and its variance spectrum (right bottom). 139

List of Tables

3.1	Notations for Chapter 3.	65
3.2	Crystal systems, crystal classes and corresponding Schoenflies and Hermann-Mauguin notations.	73
3.3	Basic Bravais lattices.	77
3.4	Computational timings for the closed-cell structures in Figure B.1.	97
3.5	Computational timings for the open-cell structures in Figure B.2.	99
3.6	Comparison of the experimental and numerical relative Young's moduli of three different specimens.	100
4.1	Notations for Chapter 4.	104
5.1	Notations for Chapter 5.	117
A.1	Crystal systems, associated point groups, and its the corresponding definition of the star-shaped set \mathcal{S} (either using spherical harmonics or spherical polyhedra).	170
B.1	Gallery closed-cell	172
B.2	Gallery open-cell	173

List of abbreviations

3DP	Three-Dimensional Printing
AM	Additive Manufacturing
APM	Advanced Pore Morphology
BESO	Bi-Directional Evolutionary Structural Optimization
CAD	Computer-Aided Design
CAL	Computed Axial Lithography
CJP	ColorJet Printing
CNC	Computer Numerical Control
CT	Computer Tomography
DED	Direct Energy Deposition
DLM	Direct Laser Microfusion
DLP	Digital Light Processing
DMLS	Direct Metal Laser Sintering
DMP	Direct Metal Printing
EBM	Electron-Beam Melting
ETPMS	Extended Triply Periodic Minimal Surface
FDM	Filament Deposition Molding
FEF	Freeze-Form Extrusion Fabrication
FEM	Finite Element Method
FFF	Fused Filament Fabrication
FGM	Functionally Graded Material
FFT	Fast Fourier Transform
GAN	Generative Adversarial Network
GBS	Graded Base Cell
IPC	Interpretating Phase Composite
LCM	Lithography-based Ceramics Manufacturing
LENS	Lase Engineered Net Shaping
LOM	Laminated Object Manufacturing
MJM	Multi-Jet Modelling
MJP	MultiJet Printing
MRI	Magnetic Resonance Imaging
PBF	Powder Bed Fusion
PBS	Primitive Base Cell

PDE	Partial Differential Equation
RP	Rapid Prototyping technologies
RVE	Representative Volume Element
SIMP	Simplified Isotropic Material with Penalization
SLA	Stereolithography (3D printing approach)
SLM	Selected Laser Melting
SLS	Selected Laser Sintering
STL	Stereolithography (Standart Triangle Language)
TO	Topology Optimization
TPMS	Triply Periodic Minimal Surface
UAM	Ultrasonic Additive Manufacturing
UV	Ultraviolet

Chapter 1

Introduction

The challenge of designing structures with tailored physical behavior is essentially geometric in nature: various properties are achieved by changing the internal architecture of a part volume. This raised the interest of researchers over a century ago as it brings a vast span of materials with properties suitable for different industrial applications, where achieving extreme properties is crucial. This can lead to significant improvements of the properties of the product and turn into economic profit and reduced material consumption. Moreover, a couple decades ago, with significant improvements in electronics, this challenge was followed by the development of efficient high-resolution computational methods enabling the exploration of physical properties of designed materials.

The term "metamaterial" was first used by Walser [223] in 2001, but up to date there is no agreement on a common definition. We will consider the most general definition proposed by [99]: metamaterials are composites designed using targeted methods (rational design) and composed of blocks with tailored microstructure topology that consist of one or more base materials. The properties of these materials can go far beyond the ones of their constituents and ultimately reach exotic physical properties not seen in nature. The variety of metamaterials' effective properties studied nowadays is impressive and involves various fields such as acoustics, mechanics, optics, and electromagnetism, among others.

1.1 Motivation

As it was mentioned above, the topic of creating materials with prescribed physical properties started rapidly evolving during the last two decades. There are several possible reasons for such gain of attention, but most are connected to the recent development of production and computer systems. The explosive growth of computational power and accessibility of personal computers along with the rapid development of numerical methods (topology optimization) and mathematical models (forward and inverse problems) in computer-aided design of structures enabled a relatively fast validation of the physical properties and allowed to model structures with tailored physical behavior. Recent improvements in the field of Additive Manufacturing (AM) significantly gained

the relevance of the research in computer-aided design. The reasons for that are constant improvements of production quality and variety of the materials, as well as the possibility to reproduce complex geometries.

In addition, the constant development of new technologies in different applications create high demand on new materials with tailored mechanical properties: the aerospace industry, automotive, architecture, and the design of implants. Recent research showed high potential of metamaterials to be a suitable and more ecological solution for these problems. Development of optimized materials can contribute to ecological improvement. For example, the use of high strength porous materials instead of solid parts lowers the material waste during production and fuel consumption by weight reduction, which in turn decreases the CO₂ emissions.

There exists a vast amount of approaches to generate materials with tailored physical properties: from topology optimization to analytical models for exploring specific families of structures. But even up to now the 3D full materials' space has not been fully explored due to its enormous size. The reason can be also that the majority of the existing methods and studies are based on finding a single optimal solution. This solution is optimal in the sense of having the exact prescribed values of the effective parameters devised for a specific geometry class. As a result, this leads to a relatively restricted class of solutions. There is a need in fast computational methods, which could generate metamaterials based on less restricting properties (such as symmetry or direction of anisotropy) and is flexible in terms of providing a wide range of different interfaces under these conditions (not considering only one geometry). In some applications of material design (e.g., architecture, car, clothes, and furniture design) it can be important to have a choice in appearance of the material, topology of its microstructure within a considered class of materials and possibly to find within this class the ones with specific physical properties. In addition, it is still an open problem the generation of arbitrary periodic materials with smooth spatial gradation: having several periodic tiles and smoothly interpolate between them is not a trivial problem. This feature would enable the modelling of periodic materials with different properties on different scales or varying local properties known as functionally graded materials (FGM).

1.2 Main contributions

This thesis was dedicated to the development and analysis of methods for the computer-aided design of materials with tailored mechanical properties. I considered the forward design approach, when the starting point in the computational process are conditions on the structure's geometrical properties, as there was an intuition that the latter can be associated with the mechanical properties. I divide the description of my research (corresponding to two chapters of this manuscript) into two different main topics: design of 3D periodic materials based on star-shaped distances and theoretical analysis of phasor noise properties, a good candidate for high-performance modelling materials with

good controllable isotropy and anisotropy.

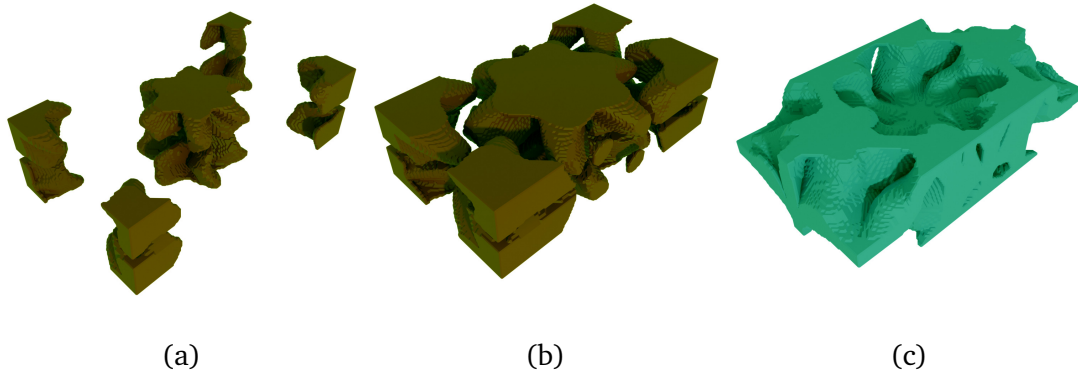


Figure 1.1: Visualization of the growth method: cells start expanding from prescribed points according to a given star-shaped set (a), they expand until their boundaries reach a certain distance between each other (b), then a corresponding closed-cell structure is extracted (c).

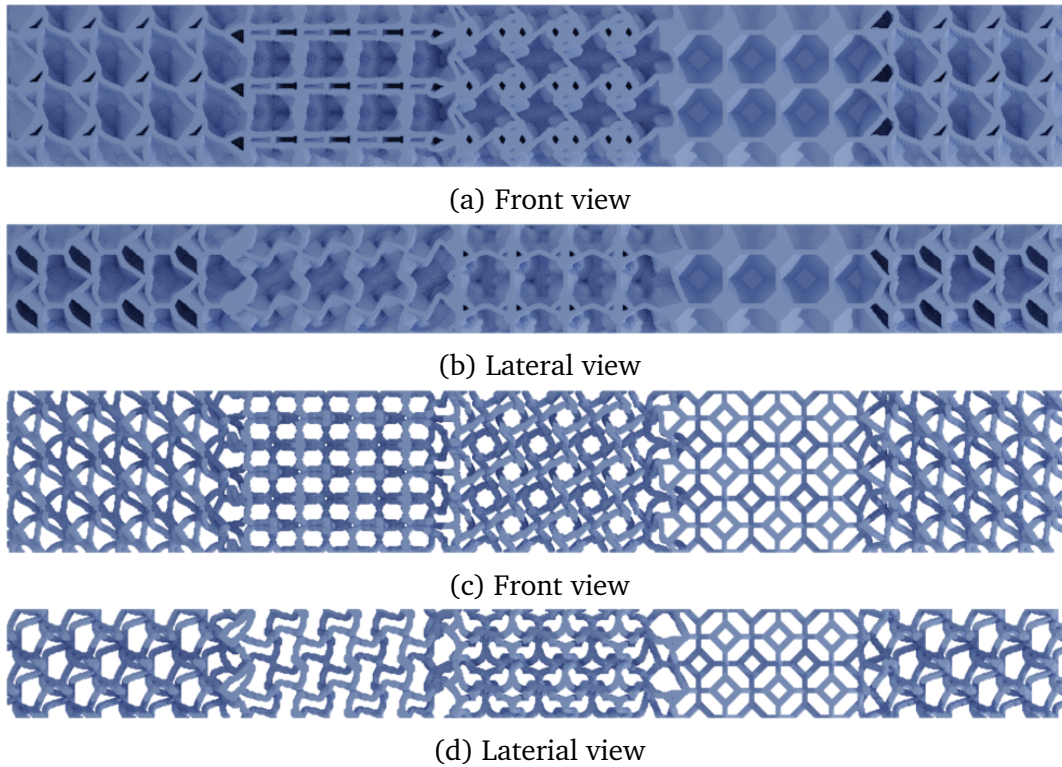


Figure 1.2: Example of 3D closed and open cell FGMs obtained with our method. The sample consists of spatial transition (from left to right) between triclinic, monoclinic, orthorhombic, cubic and, again, triclinic materials. Looking at the material samples from different angles reveals how significant is the difference in the microstructure of some cells depending on a viewpoint.

I introduce a 3D cell-growth algorithm to generate periodic closed-cell materials and a method to extract an open-cell structure (Figure 1.1). I devised

two different methods to parametrize a 3D star-shaped set: explicit and implicit. A family of star-shaped distances together with a wide range of possible periodic lattices spawns a dramatically large space of metamaterials. To ease the exploration through this space, I used symmetry, which is a very important tool in material design, and applied it to the growth method. Moreover, the main contribution of the method is that it is capable of a seamless, efficient generation of functionally graded materials (see Figure 1.2). The distance parametrization enables spatial interpolation between different materials yielding graded cellular materials with hard or smooth spatial transitions. All the results obtained here only exhibit a single connected component, which implicitly shows that this approach provides full structural connectivity of the design. I studied and implemented two iterative homogenization algorithms to compute the effective mechanical properties of the designed materials. Moreover, I printed some of the architected materials using 3D printing technology and carried out compression tests. As a result, the approach introduced here became an efficient comprehensive tool for the exploration of the material space.

A key element of my research is to perform numerical homogenization of the microstructures I study. To achieve this I propose in a separate chapter a review, implementations and comparisons of methods that I used for this purpose.

The second contribution of this thesis is the study of a novel noise type – procedural phasor noise. In particular, I carried out theoretical analysis of this noise in the Fourier space and obtained analytical expressions for extracting either high or low frequencies for both cases of superposition of kernels of single and multiple directions.

The results were published in CAD and TOG journals and presented in SIGGRAPH 2019 and SPM 2021 conferences to the research society ([64], [214]). Phasor noise is currently used in the computer graphics industry: it was employed in PIXAR’s RenderMan software and used for production of some scenes in *"Star Wars: The Rise of Skywalker"* movie. The author hopes that the results of his work will spark future study of cellular materials and development of novel design methods.

1.3 Description of the content

Chapter 2 presents the work related to the current research. I start with an overview of metamaterials based on their physical properties and applications. Then, I discuss a robust approach for the materials design – topology optimization (TO) – and the homogenization techniques for the investigation of their mechanical properties. In addition, I touch on crystallography through the works that have already employed symmetry to the problem of periodic materials design. Further, I discuss papers dedicated to the most well-known types of materials: periodic trusses and triply periodic minimal surfaces (TPMSs). I move to related studies of functionally graded materials (FGMs) and approaches for metamaterial design based on techniques originating from com-

puter graphics. Finally, I provide a brief overview of the main existing fabrication methods.

In Chapter 3 I present the 3D discrete growth method based on star-shaped distance and crystal lattices [64]. Instead of solving the inverse problem (trying to compute a resulting interface based on given effective parameters), I choose as a basis the idea of a connection between the structure's microscopic geometry and its macroscopic mechanical properties. Based on previous 2D research [138] I build a 3D growth method and analyze it through the point of crystallography. This approach allows a designer to impose the desired crystal symmetry and thus provides access to a large number of materials within a corresponding class of elastic behavior.

In Chapter 4 I present two iterative schemes for solving homogenization problem for linear elastic deformations. First, I start by introducing the problem of the deformation of a periodic elastic material. Then, I move to the description of the methods followed by the implementation details. Finally, I finish with a short comparison of the methods.

Chapter 5 is dedicated to phasor noise [214]. It is strongly connected to Gabor noise which is widely used in the field of Computer Graphics. It appeared that a phasor sinewave is suitable for generating composite materials due to its discrete amplitude representation, good control over its spatial distribution and spectrum, and also high computational performance. Indeed, this feature allows employing phasor sinewave for efficient design of two-phase materials with complex microstructures [215]. The ability to set an arbitrary spatial direction of the resulting field leads to great control over the mechanical properties of the material by changing the direction of anisotropy or even creating an isotropic material [47]. I divided the work into several stages. First, considering a laminate case (one-directional field), and obtaining an analytical derivation of its spectrum and spectrum of variance. Then, moving to the case of two directions, also obtaining and analyzing the analytical expressions for the noise spectrum and its variance. Finally, I studied the case of multiple directions.

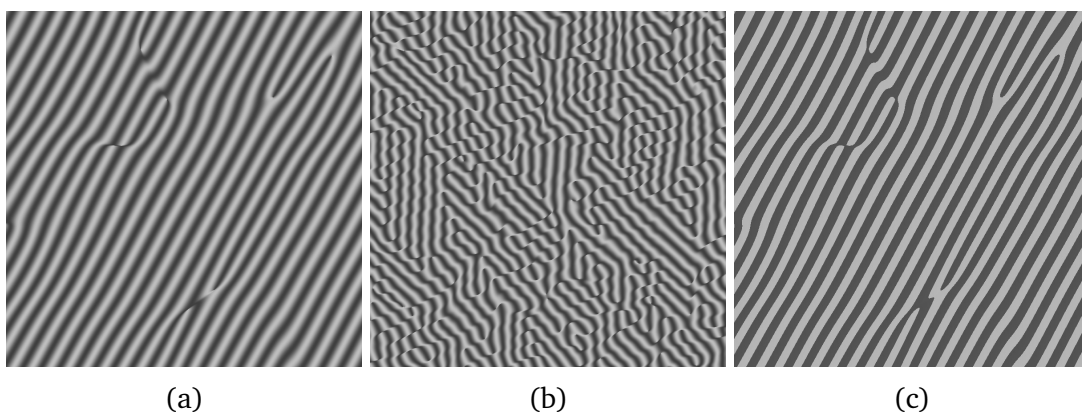


Figure 1.3: Examples of Phasor sinewave for the cases of a single direction (a), two directions (b) and a two-phase material (c) corresponding to (a).

1.4 List of publications

- Tricard, T., Efremov, S., Zanni, C., Neyret, F., Martínez, J., and Lefebvre, S. (2019). Procedural phasor noise. *ACM Transactions on Graphics (TOG)*, 38(4), 1-13.
- Efremov, S., Martínez, J., and Lefebvre, S. (2021). 3D periodic cellular materials with tailored symmetry and implicit grading. *Computer-Aided Design*, 140, 103086.

1.5 List of repositories

- 3D parametrized growth method: https://github.com/SemyonEfremov/3D_star_shaped_growth_method
- 3D iterative FFT-based homogenization methods: https://github.com/SemyonEfremov/iterative_FFT_homogenization_scheme

Chapter 2

Related work

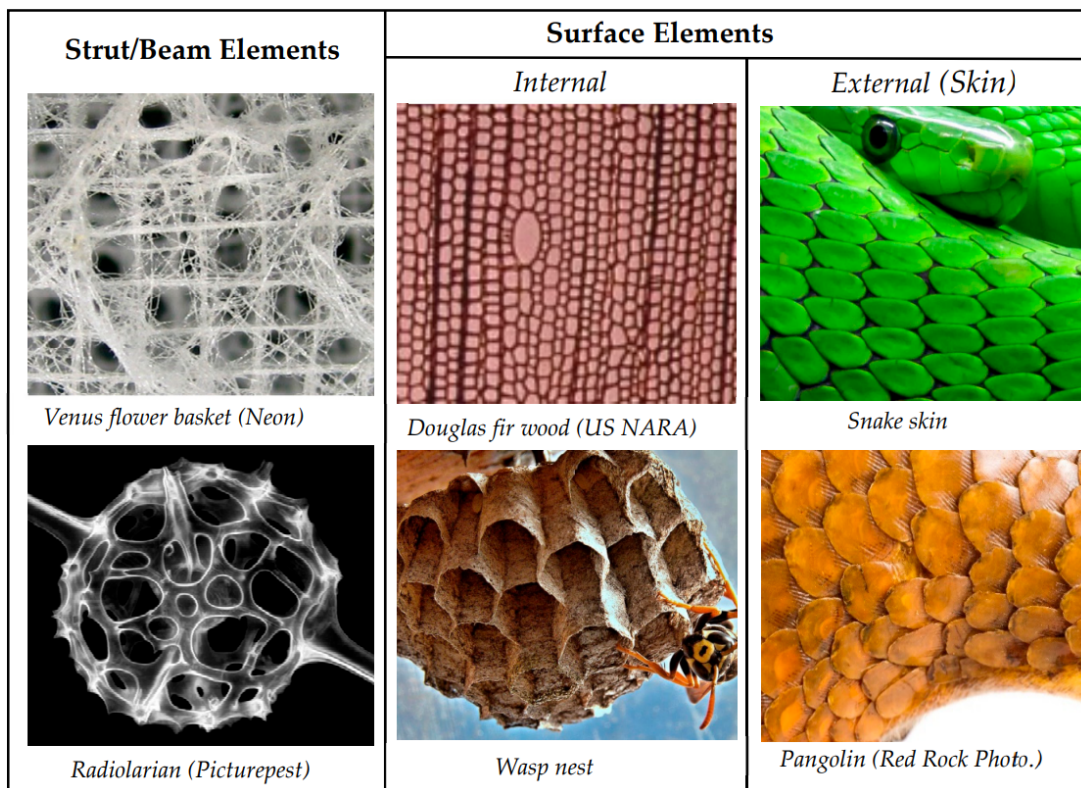


Figure 2.1: Examples of cellular materials seen in nature [23].

For the last two decades the topic of periodic metamaterials was under active investigations held by scientists involved in various research fields. There is a numerous amount of papers dedicated to material design opening access to very specific properties.

Even though the number of metamaterials and their possible applications is countless, there are two main approaches for modeling them: forward solutions and inverse design.

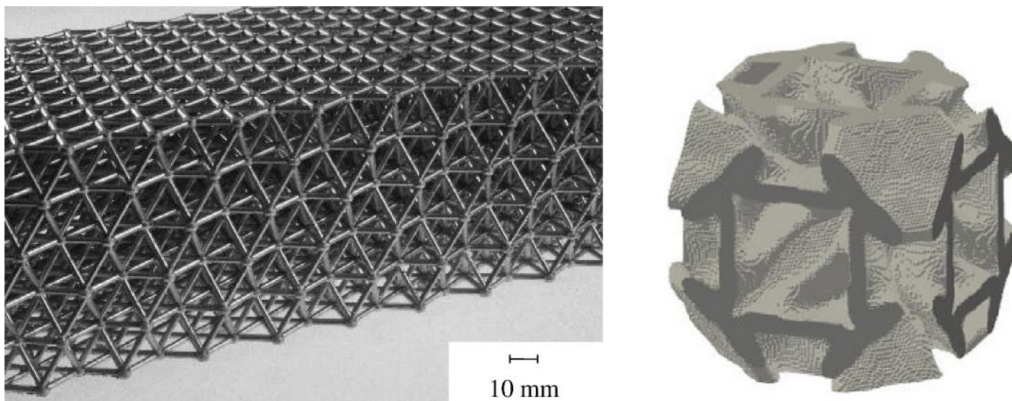
It can happen that a family of structures was discovered based on some topological properties. It could be inspired by observing some natural specific structures (e.g., animal bones, tree trunk, bee honeycomb). Indeed, a large

number of artificial metamaterials were inspired by the examples of cellular materials arising from nature. The study of the naturally occurring structures with specific properties and reproducing them gave understanding of underlying physics and thus ideas for generating and producing metamaterials.

As most metamaterials are considered being periodic microscopic (or relatively small) structures the way to study them is to analyze their effective macroscopic properties if it is possible to map continuum descriptions on the latter. This method is known as homogenization [87]. The set of these effective properties may vary due to possible applications. This approach allows to significantly reduce the problem's complexity and thus simplify a considered model.

2.1 Metamaterials

2.1.1 Mechanical metamaterials



(a) An octet-truss lattice fabricated from a cast-aluminium alloy [55].

(b) A primitive cell of periodic material with negative Poisson ratio [243].

Figure 2.2: Examples of mechanical metamaterials.

There are two widely discussed types of mechanical behavior of cellular materials: bending-dominated and stretching-dominated [201]. While bending-dominated structures (such as conventional foams), being deformed, perform strong bending of their structural components (struts, plates) stretching-dominated materials deform through uniaxial compression/tension of their elements. It has been found that their topology defines their behavior type. Gibson and Ashby proposed a scaling law for describing mechanical behavior of generic cellular materials ([72], [43]). It states that for 3D materials during linear deformation regime (the strain does not exceed elastic limit of the base material) the effective Young's modulus of strut-based lattices can be described through the following expression:

$$\frac{E}{E_S} \propto \left(\frac{\rho}{\rho_S} \right)^2, \quad (2.1)$$

where E , ρ and E_S , ρ_S are the Young's modulus and density of the base material and the designed structure respectively. It has been observed that the relations between the scaling ratios for two different types of mechanical behavior obeys different laws [210]. For bending-dominated behavior the effective Young's modulus $\frac{E}{E_S}$ and strength $\frac{\sigma}{\sigma_Y}$ can be described through the relative density $\frac{\rho}{\rho_S}$ by a power law:

$$\frac{E}{E_S} \propto \left(\frac{\rho}{\rho_S} \right)^2, \quad \frac{\sigma}{\sigma_Y} \propto \left(\frac{\rho}{\rho_S} \right)^{\frac{3}{2}} \quad (2.2)$$

and for the stretching-dominated materials this relation is linear:

$$\frac{E}{E_S} \propto \left(\frac{\rho}{\rho_S} \right), \quad \frac{\sigma}{\sigma_Y} \propto \left(\frac{\rho}{\rho_S} \right). \quad (2.3)$$

In addition, the topological criteria proposed by Maxwell for predicting material being bending- or stretching-dominated has been evolved into a connectivity criteria stating that for 3D case when all nodes are placed in similar manner the minimal connectivity of the nodes N should be equal to 12 (for 2D case $N = 6$) to reach stretching-dominated behavior [122]. Well known octet-truss lattice has shown almost linear scaling in stiffness with relative density of the structure [235].

However, a different situation is observed for linear deformations of closed-cell and plate-like structures. Here the effective Young's modulus is derived by cell-wall bending, cell-face stretching, and cell-face bending [164]:

$$\frac{E}{E_S} = C_1 (1 - \phi) \frac{\rho}{\rho_S} + C_2 \phi^2 \left(\frac{\rho}{\rho_S} \right)^2 + C_3 (1 - \phi)^3 \left(\frac{\rho}{\rho_S} \right)^2. \quad (2.4)$$

In this expression C_1 , C_2 , C_3 are some constant values and ϕ is the material fraction distributed within cell edges as opposed to cell faces.

Contrary to optics, where nonlinear effects are mostly treated as slight corrections to the main linear fields, in mechanics these effects can play a crucial role in an overall response of a metamaterial [206]. For example, using structures formed by various combinations of beams can help to achieve multistable behavior, that could be useful in shock absorbing applications. For these materials the pass in strain-stress space is not the same through a series of equivalent loads.

The Poisson ratio ν of a structure is derived as a proportion between the strain in direction of applied loading ϵ_L and its orthogonal direction ϵ_T :

$$\nu = \frac{\epsilon_T}{\epsilon_L}. \quad (2.5)$$

For auxetic materials the shear modulus G is greater than the bulk modulus B , therefore, the Poisson ratio of such materials is negative. This means that the material contracts laterally when pushed and expands while being stretched [22]. This results in good energy (shock) absorption leading to a wide range of applications ([68], [22], [182], [177], [12], [97], [21]). The opposite case when the shear modulus is much smaller than the bulk modulus is represented by the class of pentamode materials ([210], [22], [98], [37]), which behavior in the limit case $G = 0$, $\nu = 0.5$ is close to liquids (hard to compress but easy to deform). The ratio $\frac{B}{G}$ for these materials overcomes rubbers with a maximum value of 10^3 . Moreover, pentamode materials cover all possible 3D Cauchy elasticity tensors [146].

Although this thesis is dedicated to the design of mechanical metamaterials, it is important to point out other fields of applications [99].

2.1.2 Electromagnetic and optical metamaterials

This wide class of materials is represented by structures with topology that induces very specific electromagnetic and optical properties.

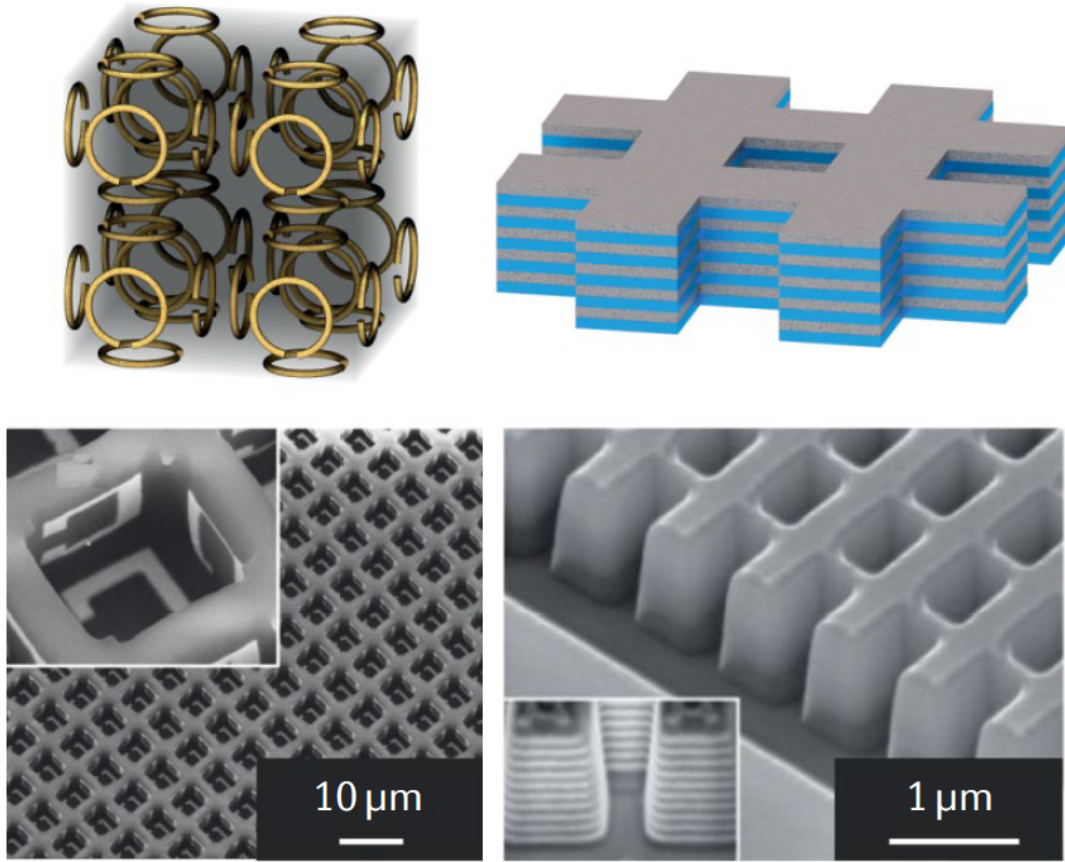
A very well-known example is a split-ring resonator (SRR) ([183], [171]) that achieves high capacitance, which results in lower resonant frequencies (big positive permeability) followed by low radiative losses and high Q-factor. SRR is represented by a series of gapped enclosed rings made of nonmagnetic material (for example, copper). Also this design allows to achieve an effect of negative permeability, which means that being excited by a time varying magnetic field it behaves as a media with a negative refractive index.

Another way to achieve negative refraction values is to refer to anisotropic materials ([229]). There is a special class of anisotropic materials (hyperbolic metamaterials) with nonuniform permittivity ([241], [48], [105], [80], [70]). The latter is represented by positive values along one direction and negative ones along a perpendicular one. This allows the light to gain large momenta and thus reach extremely small effective wavelength and super-resolution at optical frequencies.

Moreover, it is possible to achieve values of impedance Z through manipulation over the effective magnetic permeability μ_r^* and the electric permittivity ϵ_r^* of a metamaterial and the permeability μ_0 and the permittivity ϵ_0 of a constituent material:

$$Z = \sqrt{\frac{\mu_0 \mu_r^*}{\epsilon_0 \epsilon_r^*}}, \quad (2.6)$$

which can be made to equal to the impedance of the vacuum. Then, matching the impedance of two neighboring media allows creation of such metamaterials as perfect absorbers (with high loss rates) ([109], [125], [228], [113]), 2D Huygen metasurfaces [173] or magnetic mirrors (with a different phase shift compared to ordinary ones) [126].



(a) A metamaterial with artificial negative uniaxial magnetism composed of metallic split-ring resonators. (b) A metamaterial with negative uniaxial refractive indices made of different constituent materials stacked as thin layers in a fishnet arrangement.

Figure 2.3: Examples of electromagnetic metamaterials [99].

In addition, an important property to work with is chirality ([123], [213]). All the chiral effects on a macroscopic level can be described by the chirality parameter $\xi(\omega)$, here ω denotes the angular frequency of the light. Using the following relation:

$$n_{\pm}^* = \sqrt{\epsilon_r^* \mu_r^*} \pm \xi, \quad (2.7)$$

it is possible to obtain negative refractive index n_{\pm}^* values by manipulating over the chirality parameter. Moreover, taking into account that the wave impedance and absorption of the media depend on the direction of the polarized light eigenstates, one can design a circular polarizer [79], where only one direction of circular polarization is transmitted and the other one is completely absorbed. 3D helical materials show high efficiency applied to this problem ([78], [102], [103]).

2.1.3 Acoustic and transport metamaterials

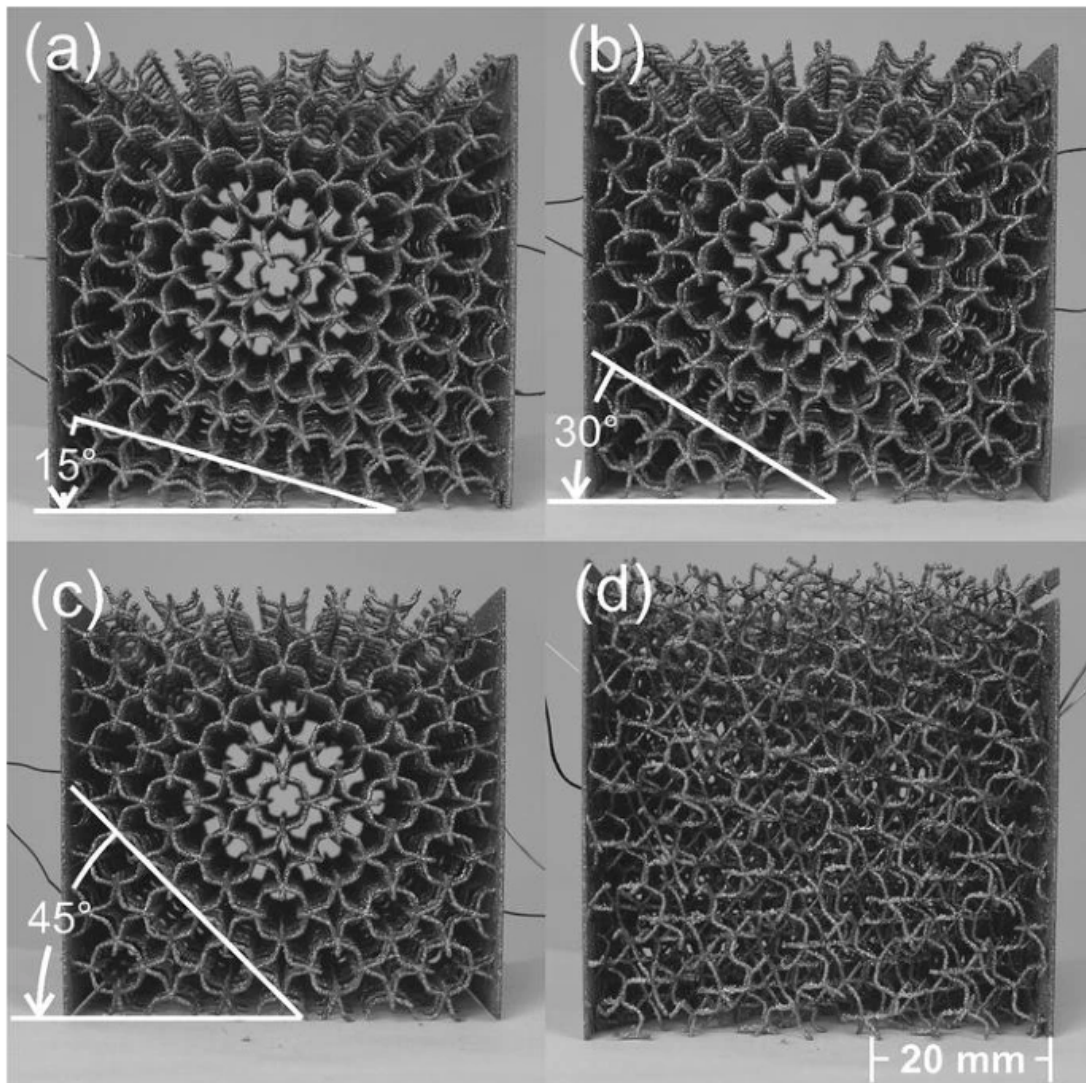


Figure 2.4: Photos of an acoustic metamaterial [233].

As two acoustic effective isotropic media parameters: compressibility k and mass density ρ are described by the same mathematical model as electric permittivity ϵ_r and magnetic permeability μ_r , respectively, it is possible to design systems with negative acoustic refractive index or almost complete absorption [49]. Indeed, a certain configuration of Fabry-Perot resonators with different resonance frequencies enables almost 100 % energy absorption within the 500 Hz to 3000 Hz frequency range [238]. Later this metamaterial has been even commercialized in noise reduction applications. The problem is that the acoustic impedance of most of interfaces is much greater than the air impedance, therefore, almost entire wave gets reflected from the material surface. Labyrinth-like structures can be a solution as their construction reduces overall impedance closer to the values of the air allowing the wave field pass inside the material ([121], [73]).

Although the transport coefficients, such as the electrical σ and thermal κ conductivity or the diffusivity D cannot get values below 0 for passive materials in a stationary state, as it is restricted by the second law of thermodynamics and energy conservation principle, active metamaterials open an opportunity to physically reach negative values of some parameters related to heat or electricity transport ([174], [34], [33], [211], [100]). For example, the effective isotropic Hall mobility μ_H^* of a composite made of nonmagnetic materials can be twice as big as the maximal Hall coefficient of the constituent materials and can be even increased using specific spatial organization of materials with static paramagnetic or diamagnetic properties. Also presence of a strong magnetic field acting on a metamaterial that consists of one thermoelectrically active constituent and the other one with a significant Hall effect can allow the effective parameter ZT^* be greater than the maximum ZT value of its constituents ([20], [199]). The ZT parameter can be expressed as follows:

$$ZT = \frac{\sigma S^2 T}{\kappa}. \quad (2.8)$$

2.1.4 Stimuli-responsive metamaterials

Finally, design of stimuli-responsive metamaterials with spatially or temporarily varying properties is a highly important topic ([54], [200], [186], [207], [208], [245], [136], [150], [160], [170]). A material is created in the way to achieve specific behavior ([52],[51], [94], [95], [96]) under an external stimulus such as light intensity, temperature, pressure, electric or magnetic field, e.t.c. These materials can be even programmable obtaining and keeping new properties after the stimulation (for some time or forever). A representative example are the liquid crystals which change their direction according to an applied electric field. Another example are metallic interfaces that can be programmed by an applied force triggering prescribed deformations and causing specific mechanical properties.

2.2 Numerical design approaches

It appears that the topic of metamaterials and mechanical design is connected to optimization methods. Indeed, as there is a goal to achieve certain (prescribed) physical properties (features provided by the designed material), it is possible to represent it as an optimization problem.

2.2.1 Topology optimization

A family of optimization methods representing the inverse design is based on topology optimization method [194], which was first introduced by Bendsoe and Kikuchi in 1988 to the field of structural mechanics [17]. Since then, the method was being under constant investigations and improvements made by

numerous specialists. Nowadays three classical approaches exist: density, level set and phase field approaches.

Density approach. The topology optimization problem of the discrete material can be derived in term of density as follows [18]

$$\min_{\rho} : F(u(\rho), \rho) = \sum_i \int_{\Omega_i} f(u(\rho_i), \rho_i) dV, \quad (2.9)$$

$$s.t. : G_0(\rho) = \sum_i u_i \rho_i - V_0 \leq 0, \quad (2.10)$$

$$: G_j(u(\rho), \rho) \leq 0, j = 1, \dots, M, \quad (2.11)$$

$$: \rho_i = 0 \text{ or } 1, i = 1, \dots, M. \quad (2.12)$$

Here the density $\rho(\mathbf{x})$ is assumed to be a discrete value function, it means that the material is represented only by "solid-void" state. As it was shown in [195], this problem does have a solution (or only one - empty domain), because the goal function value always can be reduced by removing some solid material from the computational domain. Therefore, a continuous problem was formulated to provide the method's convergence.

$$\min_{\rho} : F(u(\rho), \rho) = \sum_i \int_{\Omega_i} f(u(\rho_i), \rho_i) dV, \quad (2.13)$$

$$s.t. : G_0(\rho) = \sum_i u_i \rho_i - V_0 \leq 0, \quad (2.14)$$

$$: G_j(u(\rho), \rho) \leq 0, j = 1, \dots, M, \quad (2.15)$$

$$: 0 \leq \rho_i \leq 1, i = 1, \dots, M. \quad (2.16)$$

The problem's formulation in terms of continuous density may provide better convergence to a good quality solution which is closer to a discrete material, but some more constraints - so called penalization laws - have to be imposed. The most famous is Simplified Isotropic Material with Penalization (SIMP) model, where the material's Young's modulus is connected to the density through a power law

$$E(\rho_i) = g(\rho_i) E_0 = \rho_i^p E_0. \quad (2.17)$$

The case of $p = 1$ is called "variable-thickness-sheet" problem, which is a convex problem with an unique solution ([172], [18]). However, the final solution obtained with this penalization method often does not correspond to the expectations: it is far from the discrete form, which is mostly the final goal of the material design. The values $p > 1$ penalize intermediate thickness and, therefore, provides better match with a 0-1 solution. In the other hand too high values of p result in too fast convergence. In some papers [16] it was observed that the choice $p = 3$ provides a better optimized design with a good contrast.

Besides the power law there are explicit penalizations, which require sensitivity filtering, perimeter and gradient control [6].

One-field SIMP can be implemented through sensitivity filtering when an element's sensitivity value is formed by a weighted sum of its neighbors within a mesh-independent radius R [192]. Unfortunately, this approach results in low contrast with "grey-zones" with a size of R . The other way is use of different penalizations in a form of gradient perimeter constraints, such as a following penalization scheme [30]

$$\alpha \int_{\Omega} \|\nabla \rho\|_q dV, \quad (2.18)$$

where α is a weight coefficient and q is a norm type which crucially affects the solution's quality and its value depends on the particular problem being under investigation.

Also a regularized explicit penalization scheme can be referred to the one-field SIMP approaches [30]. Here an average density $\bar{\rho}$ is obtained in a neighborhood of a fixed radius R and the scheme then can be written as follows

$$\alpha \int_{\Omega} \bar{\rho}(1 - \bar{\rho}) dV. \quad (2.19)$$

Two-field SIMP is called so as two fields are used: the design variable ρ and the physical density $\bar{\rho}$ ([36], [31]). This filter bonds two variables ρ and $\bar{\rho}$ through Helmholtz equation

$$-r^2 \Delta \bar{\rho} + \bar{\rho} = \rho, \quad (2.20)$$

where a parameter r depends on neighborhood radius R . Here also there is a problem with the intermediate "grey" zone, which can be solved by a right choice of R or reducing the density gradient constraints.

Three-field SIMP is based on working with the design variable ρ , filtered field $\bar{\rho}$ and projected field $\hat{\rho}$ obtained by a smoothed Heaviside projection ([85], [193], [236]). It is important to mention that these schemes allow to obtain solutions with better contrast in cases where the grey zones may occur due to filtering, but this fact, however, does not guarantee convergence to solid-void designs in general.

The level set approach ([167], [188], [7], [8], [225]) is an alternative to the density approach, it is based on a level set function $\phi(\mathbf{x})$, which is, on its side, connected with the design variable field in a following way

$$\rho = \begin{cases} 0 & \forall \mathbf{x} \in \Omega : \phi < 0 \\ 1 & \forall \mathbf{x} \in \Omega : \phi \geq 0. \end{cases} \quad (2.21)$$

In this terms the topology optimization problem can be derived through a Hamilton-Jacobi equation

$$\frac{\partial \phi}{\partial t} = -V|\nabla \phi|. \quad (2.22)$$

Here a velocity function $V(\mathbf{x})$ at each point of the isosurface $\phi(\mathbf{x}) = 0$ represents an interface propagation sensitivity along its vector of normal. To meet the design constraints the velocity function needs to be derived through some specific formulations which usually are penalty or augmented Lagrange multiplier approaches (often through solving and additional PDE) [132]. For a stable evolution of the interface it is vital that the gradient of the level set function along the former is uniform, therefore, taking into account that the Hamilton-Jacobi equation does not provide this feature, in order to avoid too much or too low steepness of the gradient some re-initialization schemes are used [166]. Also some additional method needs to be used to derive the speed function in all the computational domain (either solid or void). In this formulation the algorithm does not introduce new holes in the base material, this may significantly decrease efficiency of the method as some more optimal configurations in this case are not achievable. Therefore, some additional modifications are required. Often a modified form of the Hamilton-Jacobi equation with diffusive \mathcal{D} and reactive \mathcal{R} terms is used ([8], [41]):

$$\frac{\partial \phi}{\partial t} + V|\nabla \phi| - \mathcal{D}(\phi) - \mathcal{R}(\phi) = 0. \quad (2.23)$$

Here different diffusion type operators can be used for smoothening the level set field. For instance, linear diffusion:

$$\mathcal{D}(\phi) = \nabla \cdot \nabla \phi \quad (2.24)$$

or a nonlinear operator with isotropic diffusion:

$$\mathcal{D}(\phi) = \gamma \nabla \cdot \left(\epsilon \nabla \phi - \frac{1}{\epsilon} (1 - \phi)(1 + \phi) \frac{\nabla \phi}{\|\nabla \phi\|} \right), \quad (2.25)$$

The reactive operator \mathcal{R} can be used for introducing new holes in a material (for example, using topological derivatives) and, thus, changing topology of the interface.

Like SIMP methods, the level set approach requires some sort of heuristic filtering of the velocity field [194]. It is important, that in general the filtering process does not ensure the mesh-independence of the solution. In addition, as initially the method evolves only from a given shape and does not provide holes nucleation, the latter needs to be introduced as a separate step though heuristic approaches or topological sensitivity, which can affect convergence of the algorithm. Moreover, the velocity function mentioned above needs to be designed under multiple constraints through an additional model, as a result, increasing total computational complexity. However, as the level set approach defines the structure's geometry though the "solid-void" concept (in contrast to the density approach), it is possible to impose some geometrical constraints into the optimization process explicitly.

In [237], a relaxed level set approach was presented that allows creation of new holes in a structure:

$$\frac{\partial \phi}{\partial t} = -\alpha \frac{\partial \bar{F}}{\partial \phi}, \quad (2.26)$$

where the functional \bar{F} is defined as a sum of the elastic energy and a diffusion operator:

$$\bar{F} = \int_{\Omega} fH(\phi) dV - \frac{1}{2} \int_{\Omega} \tau \|\nabla \phi\|^2 dV. \quad (2.27)$$

The Phase field formulation is the third separate approach, besides the density and the level set methods [222]. It is based on optimization of the functional:

$$\bar{F}(u(\rho), \rho) = \int_{\Omega} \left(\frac{1}{\epsilon} w(\rho) + \epsilon \|\nabla \rho\|^2 \right) dV + \eta F \quad (2.28)$$

through the density ρ . Here $w(\rho)$ is a double well function that penalizes intermediate density values, ϵ is a parameter representing thickness of the intermediate layer between the solid and void phases and η is a weight coefficient. The functional is minimized based on the Cahn-Hilliard equation:

$$\frac{\partial \rho}{\partial t} = \nabla \cdot \left(M \nabla \frac{\partial \bar{F}}{\partial \rho} \right), \quad (2.29)$$

$$\frac{\partial \bar{F}}{\partial \rho} = \frac{1}{\epsilon} \frac{\partial w}{\partial \rho}(\rho) + \epsilon \Delta \rho + \eta \frac{\partial F}{\partial \rho}, \quad (2.30)$$

where M is a diffusion coefficient.

Also discrete topology optimization methods exist such as: ESO/BESO [91], multiple step shape optimization (for instance, the bubble method), DSC scheme, various Lagrangian methods, e.t.c.

Finally, it is important to mention that topology optimization problem covers a vast space of important challenges and applications, it provides a great instrument for search and study of very specific and efficient materials. On the other hand the current topology optimization methods have several drawbacks, that could someone not to favor them in some applications if there are alternatives. Dependence on an initial guess of a starting interface, mesh-dependent convergence, a big number of tunable parameters which can also affect the method's convergence, frequent association with FEM algorithms, possible difficulty of imposing some geometrical or physical constraints - all of this significantly increases overall complexity of the method and make the design process quite laborious. These methods are successful in computation of structures with very specific properties which are hard to find, such as a negative Poisson's ratio or isotropy. Indeed, unlike 2D case, in three dimensions this problem still remains to be challenging as the necessary and sufficient criteria

for periodic structures for being isotropic has not been found yet – a sufficient criteria in fact has been formulated, but as it states that the object should have 3 axes of 5-fold rotational symmetry it is not applicable to periodic materials, because this type of symmetry is not compatible with periodicity. However for fast material prototyping, discovering the material space, where structure's "optimality" is no longer the main goal, nowadays TO methods do not seem a reasonable choice.

2.3 Computation of the elastic behavior

In any material design, regardless of a computational method chosen for this purpose, it is likely important to validate mechanical properties of a resulting interface. As long as periodic materials are under consideration, homogenization model may be a good choice.

The study of microheterogenous materials goes back to J.C. Maxwell, Lord Rayleigh (theoretical investigation of electric conductivity of a heterogenous material) and A. Einstein (study of viscosity of a fluid with suspended solid particles) and extends over 150 years of development and improvements. The last 50 years became the most productive and intensive in terms of solving already existing problems, complexifying analytics and, of course, evolving numerical methods.

The basis idea of homogenization is to find a material's macroscopic response – or its "structural property" – by means of averaging response of a microstructure (concluded in a Representative Volume Element – RVE). Initially these methods were mostly analytical and required extensive amount of experimental data that would allow to tune well parameters of the model, but through the last two decades, as the computational capability of computers enormously increased and continues improving, numerical approaches started dominating in the field of mechanics.

There is a range of different homogenization methods based on different approaches to solve a classical problem (of evaluation of considered physical properties: deformation, thermal or electrical conductivity, e.t.c.), that can be classified based on an approach used [165]: mean-field homogenization schemes, finite element methods, asymptotic homogenization algorithms, generalized method of cells, embedded cell or embedding approach, windowing method and Fast Fouries Transform schemes.

Mean-field homogenization appeared when relatively high computational complexity was a serious adversity. This class of methods is based on computing macroscopic behavior of a material in terms of averages with low computational costs. Initially only a linear regime was considered, but later the model was extended to nonlinear deformations linearizing the local constitutive laws for nonlinear materials.

Regardless its high performance the method has drawbacks such as inability to obtain local distributions of strain and stress in a microstructure, which does not allow to describe some local effects (clustering, perlocation, size effects,

e.t.c.).

Finite element methods are if not the most frequently used, then at least ones of the most popular approaches applied to the homogenization problem. The reason is that they represent full field models (including nonlinear range), provide great precision and high flexibility, in addition periodic boundary conditions lead to a reduction of computational time.

On the other hand this approach requires computation of a finite element mesh, which is not straightforward and can lead to a significantly high computational costs.

Asymptotic homogenization algorithms introduced by ([19], [124]) is based on a representation the variables in both fine ($\frac{\bar{x}}{\epsilon}$) and coarse (\bar{x}) scales and their asymptotic expansion with respect to ϵ leading to a set of PDEs with periodic boundary conditions [46]. The latter can be solved via any suitable numerical solver.

Generalized method of cells allows computation of macroscopic material properties in both linear and nonlinear formulations ([1], [168], [61]). It is based on representing a computational domain by an arbitrary number of generic elements, which are in its turn divided into several (4 or 8) subcells of a rectangular or parallelepipedal shape. Each of these subcells is assumed representing a homogenous material which differs from one cell to another. All the macroscopic properties are obtained through averaging and a displacement field is imposed being a linear function. This formulation is computationally effective and quite accurate in providing the global material characteristics, but quite not precise in predicting the local fields.

Embedded cell or embedding approach lies on replacing some particular region of interest (heterogeneous region) by a heterogeneous material with corresponding detailed mathematical model while the rest of the computation domain (effective region) of the considered object is described through a suitable simplified method [27]. These algorithms are widely used to describe some local effects that occur in inhomogeneous materials. These methods allow to obtain local stress-strain fields in the heterogeneous region with high precision and do not require strict periodicity of the microgeometry or microfields. However, this family of algorithms is computationally expensive and there is a risk that some "parasitic" effects will appear (spurious boundary layers around the inclusion). There are three main approaches in the literature. The first method is based on using discretization within both subdomains but the embedding material is represented by a much coarser mesh [181]. For example, this approach was used in [205] with FEM method embedding a finer mesh in some regions. This strategy in case of well-defined and well-compliant meshes allows to avoid or reduce undesired artifacts on the boundaries of the heterogeneous region. The second approach is based on defining in an embedding subdomain a suitable semiempirical or micromechanical model to be in agreement with overall mechanical behavior in a heterogeneous region. Finally, the third strategy implies defining effective response of the embedding region through computed homogenized behavior of the heterogeneous subdomain.

Windowing methods are formulated through introducing space windows (usually of a rectangular or a hexagonal shape) with a size smaller than RVE and placed in a random position with special boundary conditions providing the energy balance between both scales [27]. A set of such windows of comparable size can provide lower and upper bounds of the macroscopic material properties. This method also may result in appearance of some spurious layers that likely will affect computation of the macroscopic parameters. On the other hand this approach can be applied for non-periodic materials.

Fast Fouries Transform schemes form a class of iterative schemes based on FFT introduced by ([153], [152]). The RVE is discretized into a set of voxels, which represent corresponding mechanical properties. All the equations are written in an integral form through a Green function (Lippmann-Schwinger equation). This equation is being solved then through multiple iterations until convergence of strain/stress is reached. Since first introduced this method has been improved multiple times. There are several formulations of this method: original iterative scheme, polarization scheme proposed by [154], discrete Green function based iterative algorithm introduced by [232] and iterative method on a staggered grid presented in [142].

The initial system of equations is written as follows:

$$\begin{aligned}\sigma(\vec{x}) &= C(\vec{x}) : \epsilon(\vec{x}), \\ \operatorname{div}\sigma(\vec{x}) &= 0, \\ \epsilon(\vec{x}) &= \frac{1}{2}(\nabla u(\vec{x}) + \nabla^T u(\vec{x})).\end{aligned}$$

The corresponding Lippmann-Schwinger equation is then:

$$\epsilon(\vec{x}) + \Gamma^0(\vec{x}) \star (\delta C(\vec{x}) : \epsilon(\vec{x})) = 0.$$

This family of methods is well known for its memory and computational efficiency, ability to predict a nonlinear behavior and implementation simplicity. On the other hand convergence of the method crucially depends on parameters values, Young modulus contrast between the phases and, as it seems, even topology of a structure. Nevertheless, the method of Willot et al. [232] shows a good convergence even for an infinite contrast, but is less precise for low resolutions. In general iterative FFT-based schemes provide less precision than, for example, FEM methods and poorer quality strain/stress local distributions.

In this work FFT based iterative schemes were favored due to significantly lower computational costs and simplicity for solving homogenization problem in 3D space.

2.4 Crystallography in metamaterials design

One can bond each cell of a cellular structure to a point in the space (usually an origin or a center point of the cell or struts' knots for the open cell structures).

Thus periodic cellular materials can be associated with periodic lattices (point distributions). This fact describes a fundamental aspect of the connection between the design of cellular structures and crystallography. Crystallography has become popular in the design of periodic solids a long time ago ([220], [161], [197], [88], [69]) and now is strongly associated with this domain.

It is well known how strong is the connection between the geometrical symmetry of a material and its mechanical properties. Indeed, there are multiple works dedicated to the investigation of the effect of the material's symmetry on the symmetry of its elasticity tensor. In [40] the effective elasticity tensor of the periodic materials based on their geometrical symmetry was analyzed. This work aimed to connect the terms of the symmetry planes with the symmetry groups, discussed in the literature before as different viewpoints on the same problem. The authors showed that using a simple approach presented in this paper leads to the same results as more complex classifications. However, this is not true in more general cases, where fewer elasticity classes can be obtained with the symmetry plane approach than with the symmetry group classification. Moreover, it was shown that there are only eight classes of the elasticity tensors corresponding to 7 crystallographic point groups: triclinic, monoclinic, orthorhombic, tetragonal, trigonal, transversely isotropic, orthotropic, and isotropic (orthotropic and isotropic materials both correspond to cubic symmetry).

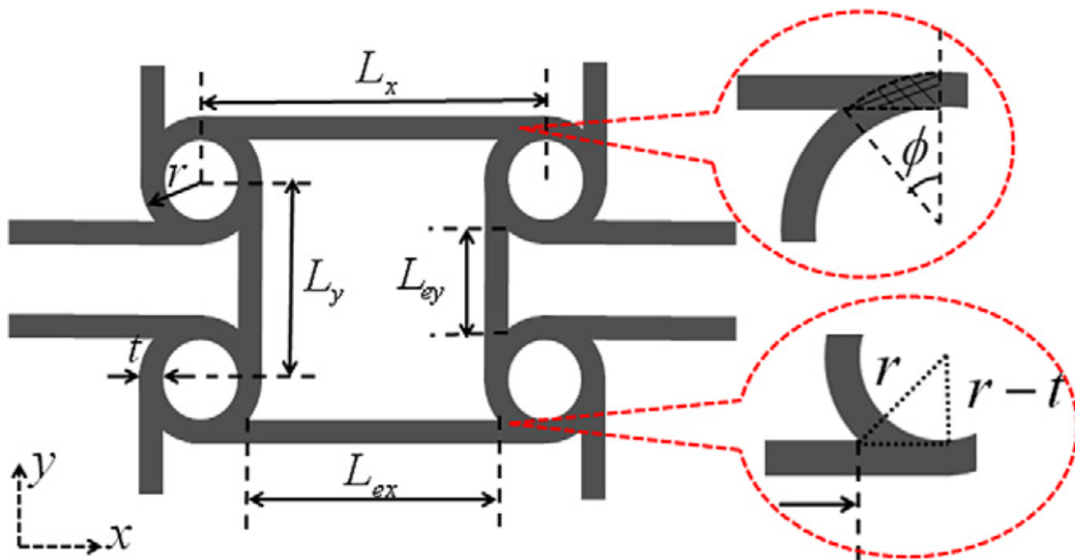


Figure 2.5: Design of an anti-tetrachiral anisotropic honeycomb unit cell presented in [42].

In the design of metamaterials, symmetry is often used for achieving some specific properties. For instance, chirality (when an object cannot be brought into coincidence with its reflection) is a geometric property that can result in negative Poisson's ratio, specific polarization, vibration or sound attenuation, energy absorption or negative thermal expansion.

In [42], the theoretical, numerical, and experimental descriptions of the

elastic behavior of the class of 2D anti-tetrachiral anisotropic periodic lattices (that were expanded into 3D structures by introducing a thickness along the third axis) was presented. In addition, the authors presented analytical expressions for computation of the effective Poisson's ratio, the elastic modulus, and the transverse shear modulus that showed good agreement with the FEM simulations and experimental data. The results presented in this paper show the high potential of these structures towards reaching low negative values of Poisson's ratio and generating materials with low density and high in-plane elastic modulus.

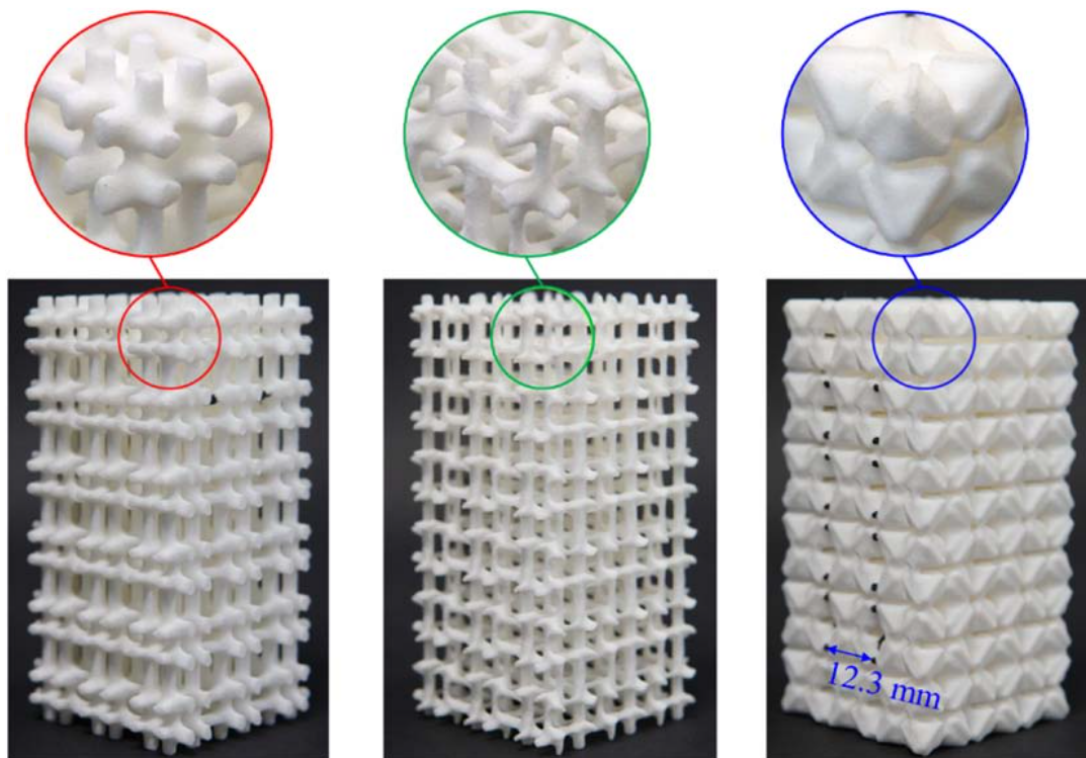
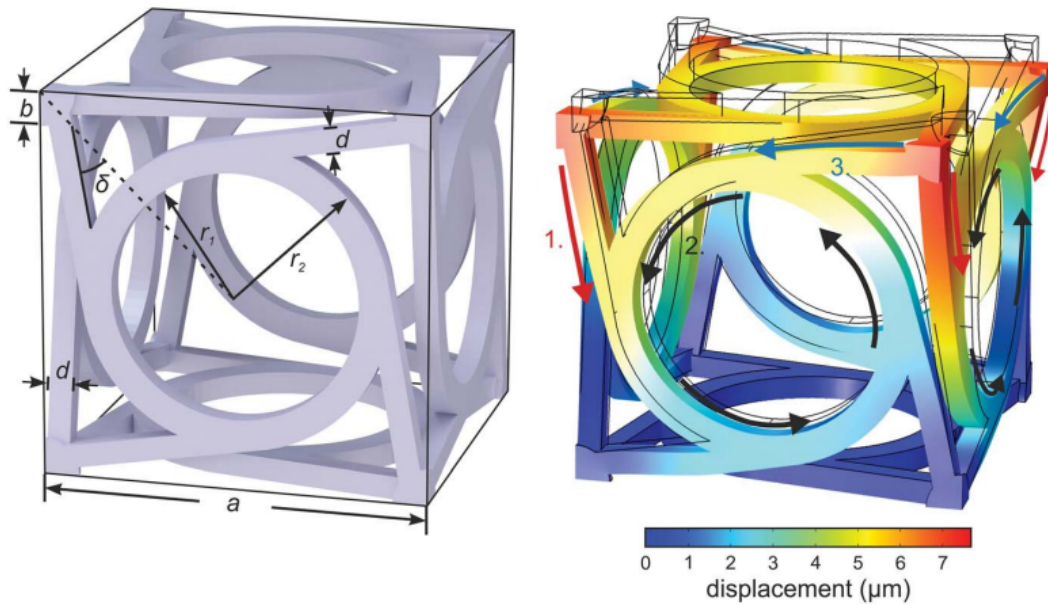


Figure 2.6: Examples of 3D printed samples containing $6 \times 3 \times 3$ unit cells for designed and optimized materials with prescribed symmetry [250].

In [250], dedicated to the design of periodic closed- and open-cell microstructures with a given Poisson's ratio, symmetry is used as a constraint for achieving chirality and thus negative values of Poisson's ratio. The approach is represented by a two-step computational optimization method. The first step contains a grid-based optimization process, where the structure's design is formed by following a projection-based interpolation method of the elasticity tensor and homogenization approach. In the second step, the grid-based design is transformed into its mesh-based analog for better printing performance and subsequently optimized using a level-set approach.

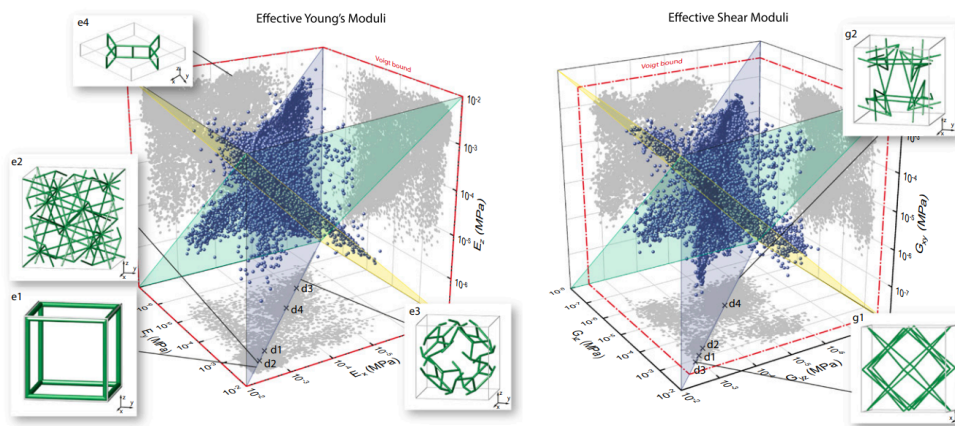
[74] presents a class of chiral periodic materials that perform significant twisting in a plane perpendicular to an applied force. A maximal twist value achieved with these structures is $2^\circ/\%$ of axial strain.

It is crucial to point out the paper [131] as it is very close to our research.



(a) A unit cell of a chiral metamaterial (b) A deformed unit cell of a chiral meta-
with significant twisting mechanical be- material with significant twisting me-
havior chanical behavior

Figure 2.7: Example of mechanical metamaterial with chiral geometry [74].



(a) A constellation of the effective Young (b) A constellation of the effective shear
moduli moduli

Figure 2.8: Effective mechanical properties of 17087 structures designed in [131].

In this work, the authors explore the material space using crystal networks as a base for the design of microstructures and a homogenization method for calculating the effective macroscopic parameters. As usual, a periodic crystal network is represented by a unit cell (the smallest periodic arrangement of the lattice elements) with periodic boundary conditions. The corresponding structure is computed by connecting different nuclei of the crystal lattice with

respect to given connectivity in the Euclidean space (when the connections are represented by straight bars – struts). This approach enables fast computation of a structure with given parameters, which makes possible massive exploration of the material parameters' space. All the networks were taken from [163] and [178], and the resulting gallery contains more than 17000 structures with computed macroscopic elastic properties. The results show that even within periodic trusses, there are many materials with extremal properties.

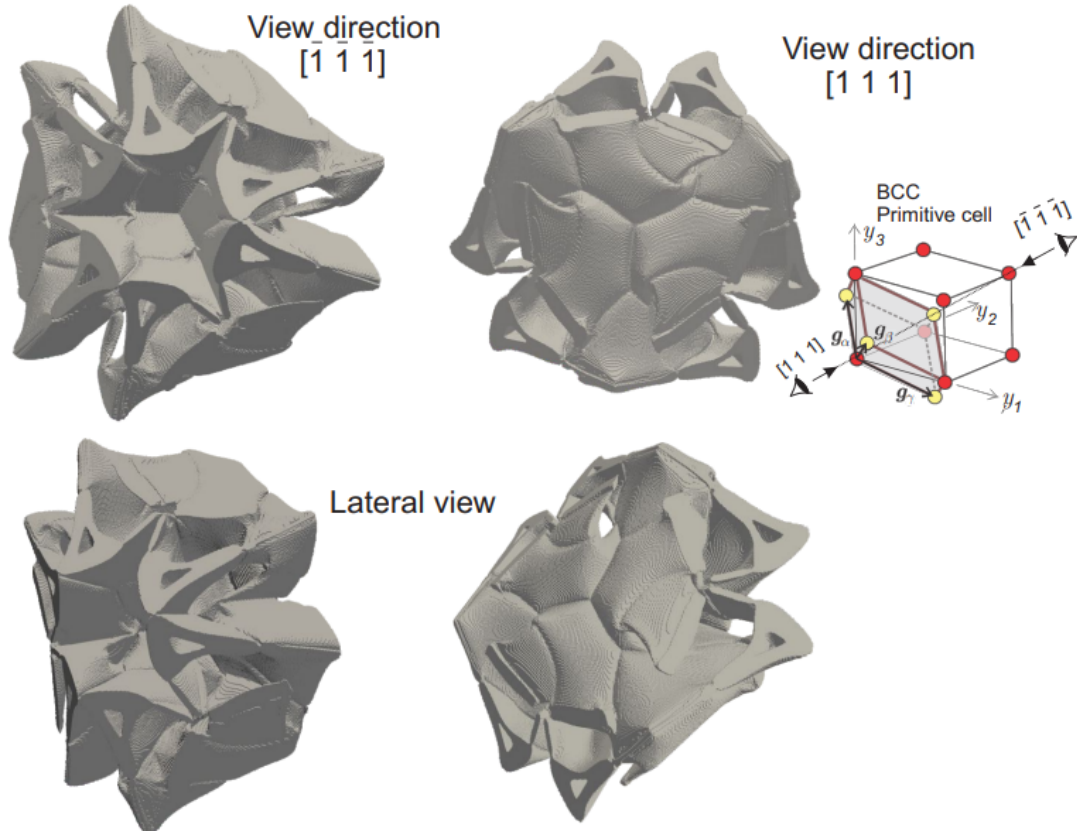


Figure 2.9: A unit cell of an auxetic composite with prescribed symmetry [179].

Finally, the paper [179] is an excellent example of employing crystallography concepts in the topology optimization approach. The numerical method presented in this paper is aimed at the design of 3D two-phase periodic microstructures with extremal isotropic effective macroscopic parameters that are close to the theoretical bounds. The topology optimization problem is solved using a combination of a level-set approach and topological derivatives. The method is based on the assumption that cubic symmetry is the necessary condition for the isotropy of a material. Therefore, a given symmetry is imposed to the topology by introducing cavities based on a chosen Bravais lattice into the computational domain that corresponds to the unit cell of the lattice (need to recheck). As the computational domain, in this case, conforms to the primitive cell of the lattice that is derived on a nonorthogonal basis, the homogenization problem was solved with a modified FFT method. The FFT algorithm was derived in an arbitrary vector basis corresponding to a chosen Bravais lattice

(this provides the flexibility of the choice of the crystal network). After the cubic symmetry is imposed directly through the initialization of the method, a constraint of the isotropic behavior of the material can be represented just by a scalar expression.

2.5 Design of cellular materials: periodic trusses

Periodic cellular materials are structures composed of a combination of primitive elements called cells [84]. The latter is formed by a combination of interconnected solid struts or plates. In the presence of both the struts and the faces completely separating the pores from each other the material is called closed-cell, but if there are only the struts it is called open-cell. In addition, there are partially (closed-) open-cell structures.

Cellular materials represent a big class of interfaces (periodic microstructures) widely used in various industrial and research fields due to their porous nature, providing extremely lightweight, great strength, outstanding compressibility, and even more very specific mechanical, acoustical, electrical, and optical properties [246]. The cellular solids are very often seen in nature and were used already in Roman Empire [10]. For instance, the Romans used cork to stop wine bottles – thanks to the transverse isotropy, it provided uniform pressure along the bottleneck. Despite this fact, the active study of the cellular structures started not so long time ago. However, there is great progress made in this field, including various analytical and numerical methods for the design of such materials, investigating their properties, and their fabrication.

Nowadays, there are many works dedicated to the study of periodic cellular materials involving various techniques. However, in this work, we will discuss only papers that are the most relevant to our methods and results.

The idea of the design of a cellular material through computation of its unit cell is widely used nowadays in research as it derives macroscopic and microscopic behavior of the periodic structure.

So, in [39] a topology optimization method for the design of cellular materials with maximized energy absorption was built. In this work, instead of the widely used topology optimization problem for cellular materials corresponding to linear deformations, the authors took a topology optimization problem describing through the sensitivity analysis two nonlinear mechanisms: geometrical and materials nonlinearities. As a penalization criterion, the SIMP model along with the Heaviside projection method was taken. The latter provides control over a minimal scale length of the design and thus helps to avoid well-known checkerboard and mesh-dependency problems. Also, the Heaviside function can yield discrete 0-1 solutions. The geometrical nonlinearities are characterized by finite deformations followed by significant shape and location changes in a deformed configuration corresponding to the initial configuration. This fact breaks the assumption of small deformations and results in the fact that the equilibrium condition can no longer be described in terms of Cauchy stress and infinitesimal strain. To describe the material nonlinearities,

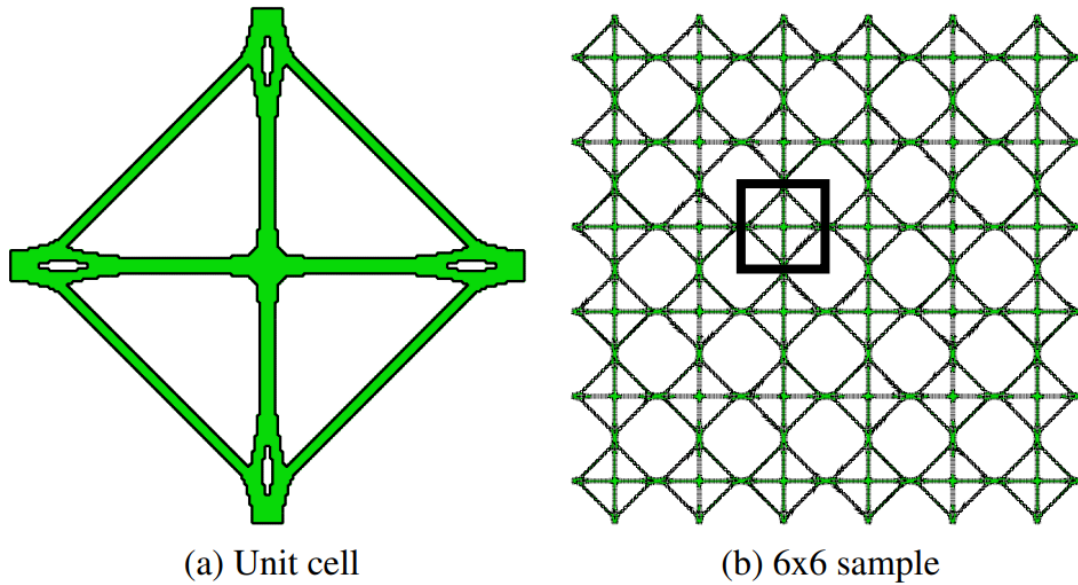


Figure 2.10: Cellular material with optimized for maximum energy absorption topology [39].

the Von Mises yield function with isotropic hardening was chosen. Indeed, as overall absorbed energy is subject to maximization here, the resulting designs provide higher absorption rates for the same volume fraction.

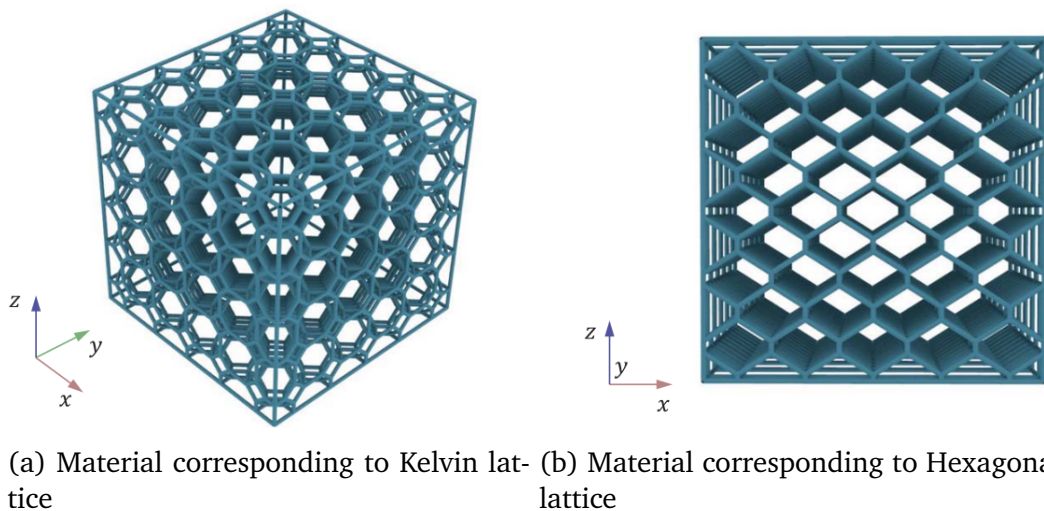


Figure 2.11: Examples of anisotropic lattices designed in [209].

A closely related to our approach is [209], where the authors considered the design of lattice structures based on Voronoi diagram representation. They also consider computation of an open-cell interface unit cell, corresponding to an element of the periodic body-centered cubic Bravais lattice. The periodic lattice layout is introduced for defining centers of the resulting Voronoi tessellation. Thus, this approach allows a compact mathematical formulation with scaling (of the lattice) along one of the principal axes, which results in

Voronoi cells altered in the corresponding direction. The smooth mapping of the lattice is represented by defining stretching/compressing coefficients for each of two axes corresponding to the third one. For this transformation of the Bravais lattice, the resulting RVE tile will have the same size proportions corresponding to the lattice scaling parameters. Therefore, the resulting structures are scaled to conform to the initial size of the cubic body-centered cell. The overall computation process is represented by an optimization process of the structure's volume, where at each iteration, the model parameters are being modified in order to reach given target properties. Each step involves the lattice element generation according to the directional scaling factors, computation of corresponding Voronoi tessellation, its rescaling, extraction of the open-cell structure, and validation of mechanical behavior. At the end of the iteration, corrected values of the parameters are computed if convergence is not reached.

One of the most well-known and widely used materials are periodic trusses. These structures are known for their mechanical strength and, therefore, are widely used in applications where good energy absorption or high Young modulus values in combination with low weight are needed. In addition, spatial organization of the trusses results in relatively low computational costs (possible to derive an analytical model) and a simple manufacturing process (as it can be assembled from struts attaching them in the nodes by any suitable technique).

Following [249], there is a large number of different periodic truss structures, which can be organized in a hierarchical system. The core class is represented by elementary cubic trusses: simple cubic, body-centered cubic, and face-centered cubic. Then compound cubic trusses can be obtained by combining unit truss elements of different types by scaling them and merging the nodes. Finally, a class of super trusses is represented by various spatial arrangements of primitive trusses. Also, there are two separate classes of non-cubic trusses with tetrahedral and octahedral symmetry. For these types of structures, the concept of compound trusses and super trusses is defined the same way. One of the most important features of periodic trusses are the compactness of their derivation: they can be defined only through their nodes' position in the space and their connectivity. In this sense, periodic trusses are periodic 3D graphs.

In [198] design of the octet-truss structures (as it is possible to achieve elastic behavior which is close to the isotropic) with extremal Young modulus-to-weight ratio was considered. The studied structure was represented by 3x3x3 unit octet-truss cells. To obtain an optimal interface, Multi-objective Genetic Algorithm with Krigin surrogate model were employed. For the optimization process, a series of sampling points for different values (according to the 3D printer's capability) of the struts' diameter and the cell's length (these parameters are considered further as design variables) was created using the Central Composite Design approach. The function of a ratio of the Young modulus and the mass of the structure is subject to minimization on the design variables. In each iteration, all population of the design points is divided into two sub-

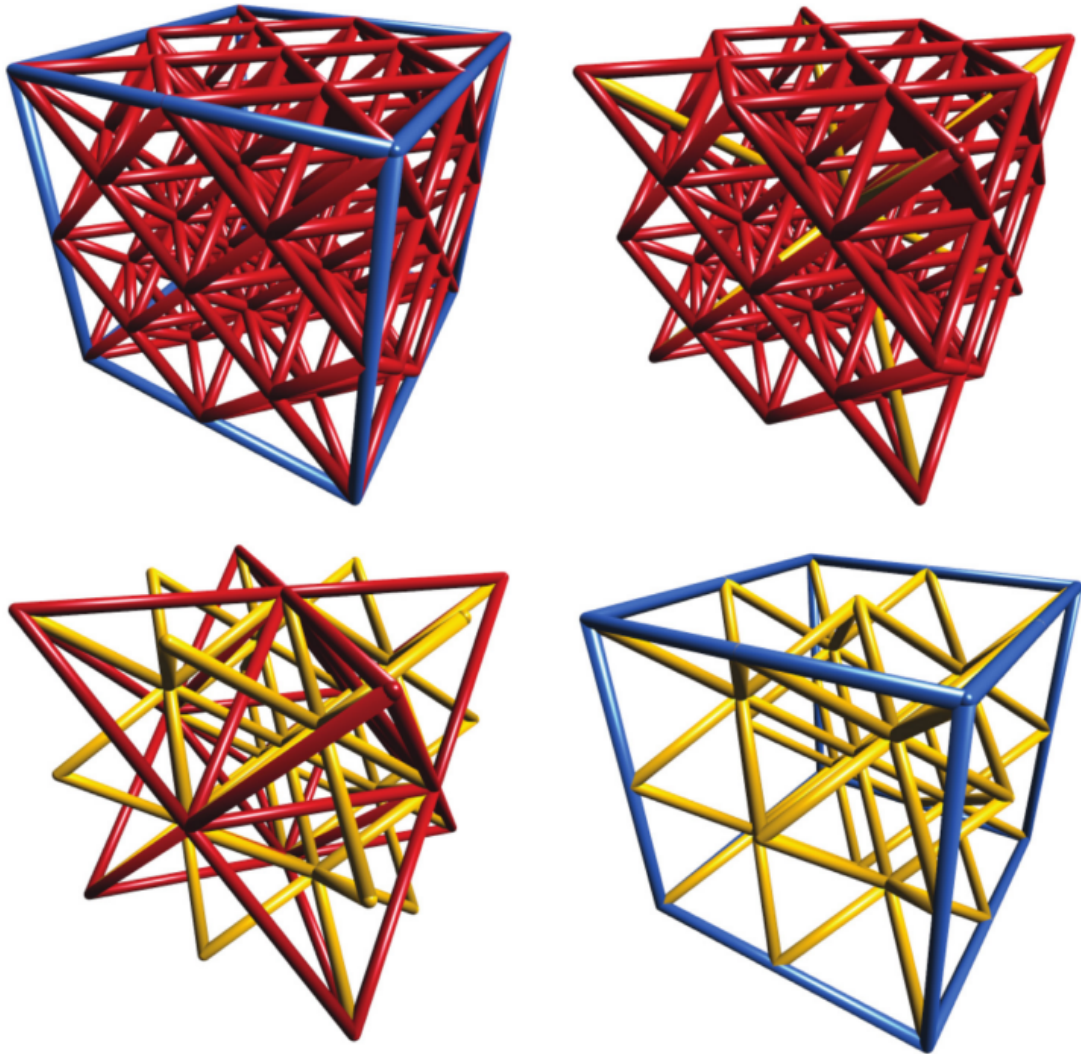


Figure 2.12: Examples of single unit cells of compound cubic supertrusses [249].

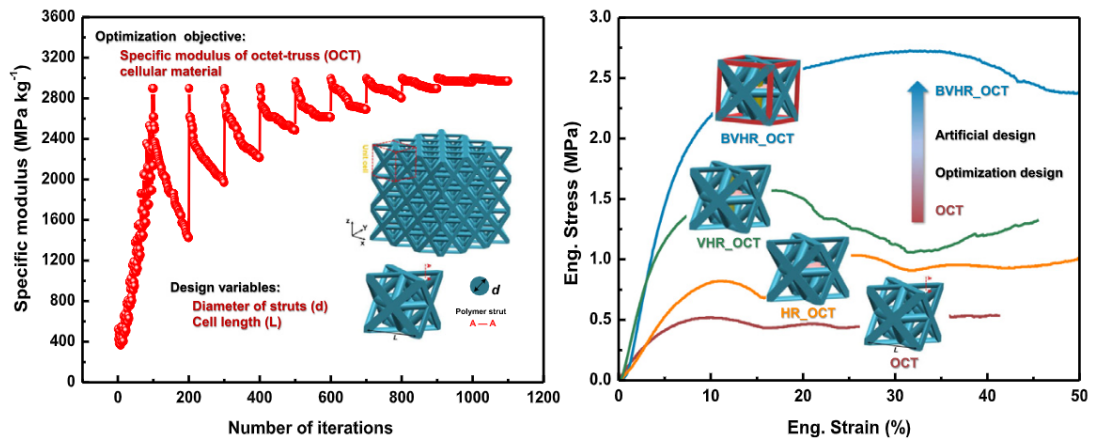


Figure 2.13: Experimental deformation data of different octet-trusses [198].

categories: non-dominated points, that are less than 30% of all the population and are directly inherited from the previous generation, and offspring points, that undergo crossover or mutation. Corresponding response values (of objective functions) are carried out through numerical simulation. The iteration process continues until a prescribed number of iterations is reached. To find non-dominated designs Krigin Surrogate Model was used.

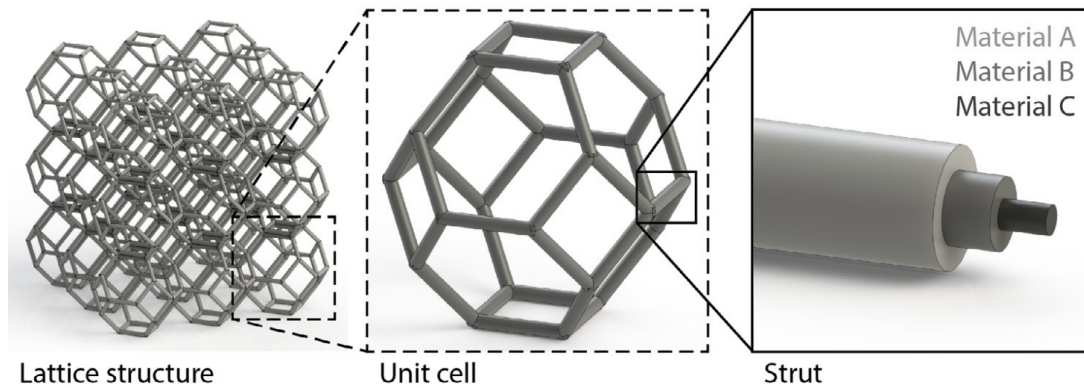


Figure 2.14: Example of a shell-core lattice design [155].

Moreover, a shell-core model for increasing the energy absorption with minimal losses of the strength and stiffness of bending dominated lattices was presented in [155]. This approach is based on removing an internal part of the struts' material and replacing it with one or a few coaxial layers of other tougher materials. This results in significantly increased toughness and small sacrifice in stiffness and strength.

2.6 Minimal surface materials

Another approach for modeling periodic materials widely used in different applications is the triply periodic minimal surfaces (TPMSs). TPMSs are the surfaces with locally a minimized area for a given boundary such that the mean curvature is equal to zero. This fact results in some interesting properties. For instance, they are smooth and divide the space into separate, non-intersecting, and interweaved components that can be periodically extended along all principal axes. Furthermore, one says that a TPMS is balanced (primitive, gyroid minimal surfaces) if it spawns only subdomains that are congruent and interchangeable. Otherwise, it is called unbalanced (I-WP, F-RD). Examples of TPMS structures can be observed in nature: a soap film [184], block copolymers [141], butterfly wings [175], e.t.c. As it was the case with most composite materials, TPMSs were introduced a long time ago [187], and during the last couple of decades, these periodic materials gained their popularity.

Recently, TPMS based materials have found much interest in multiple applications thanks to their multifunctionality. In tissue engineering, there are multiple works dedicated to modeling scaffolds with TPMS structures. For example, the work [26] dedicated to manufacturing titanium TPMS sheet-networks

with the AM techniques revealed a great mixture of relatively low elastic properties corresponding to the range observed for the trabecular bone and high yield strengths which are greater than limit values for the cortical bone. Also, they discovered that the permeability values for the designed biomaterials corresponded to the range of values known for the trabecular bone. Moreover, TPMS-based structures are widely used in the application for modeling interpreting phase composites (IPCs) - materials that have all the constituent phases being interconnected. A novel type of cellular IPCs was presented in [4]. These structures consist of a hard shell and soft core components. The mechanical properties of these materials were investigated. Results revealed that overall toughness values resulted from the shell-core combination and that these composites are suitable for applications where energy absorption is required.

There are various approaches for computing TPMS: using the evaluation of the corresponding Weierstrass function [129], through the FEM simulation [32], topology optimization through minimizing principal curvatures of the fundamental unit [29] and the level-set approach [77]. The latter is represented by the level-set approximation equations derived from a Fourier-series representation. There are multiple (more than one hundred) TPMS analytical expressions that are found and presented in [130]. A typical equation for the TPMS is

$$\phi(\vec{x}) = C, \quad (2.31)$$

where C is a constant, that directly affects the surface area of the solution ($C = 0$ value corresponds to the maximal area).

There are two main techniques for the transformation of TPMS into corresponding cellular solids. The first is to consider one of the subdomains (separated from each other by a minimal surface) being solid, and the other one is assumed to be void. The other approach is to generate TPMSs for two different values of the constant C , overlap them and solidify the volume enclosed between them. The second approach seems to help avoiding connectivity problems (for so-called sheet-networks or $|\phi(\vec{x})| \leq C$) for low volume fraction ratios.

In the paper [140], three types of TPMS based materials were studied: primitive, gyroid, and diamond. These networks were computed with corresponding level-set equations for different material volume fractions. For numerical validation of mechanical properties, FEM approach was chosen. Also, tensile-compressive experimental tests were carried out. The results revealed that primitive and diamond with gyroid networks are suitable for different loading scenarios. Also, the measurements showed high anisotropy of the considered structures.

In a similar work [2], mechanical properties of 3D-printed gyroid cellular materials were investigated. The gyroid sheet network type material samples represented by 4x4x4 periodic unit cells were printed out of polymeric base materials with different mechanical properties and tested on a compression machine. Also, computational tests were carried out with FEM analysis

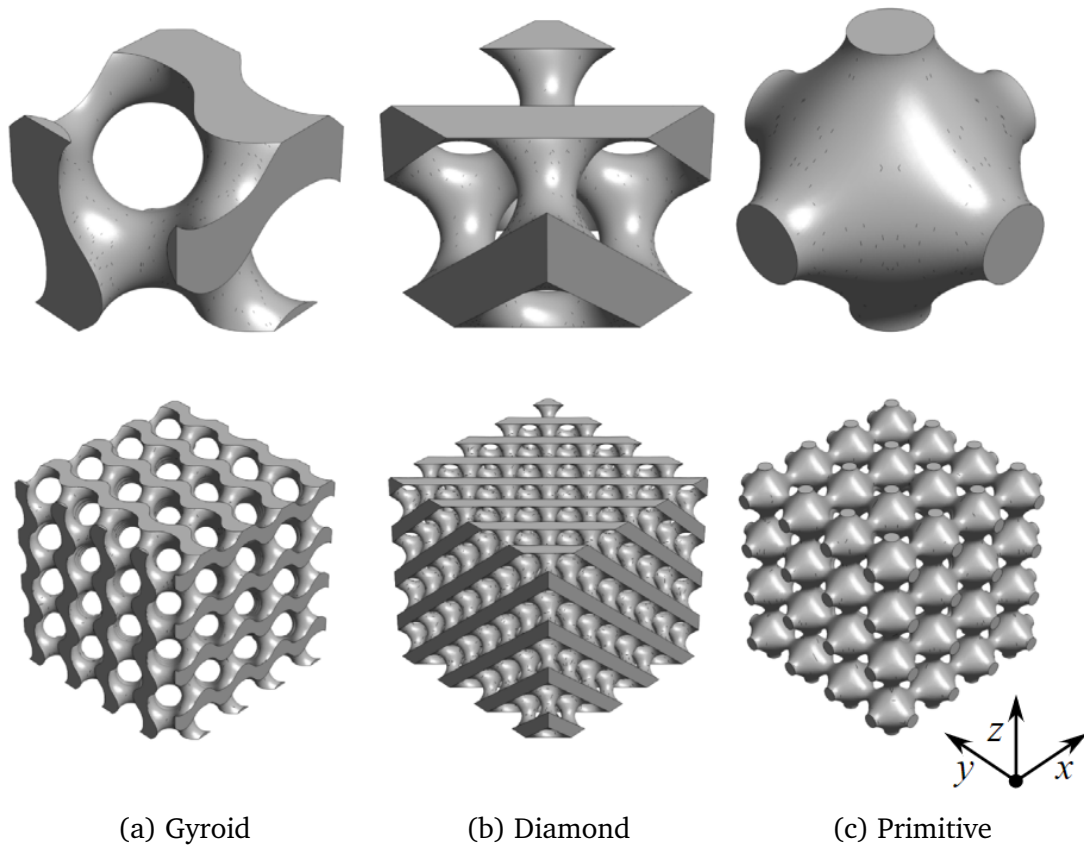


Figure 2.15: Examples of TPMS-based materials considered in [140]: unit cells (top) and 4x4x4 arrangements (bottom).

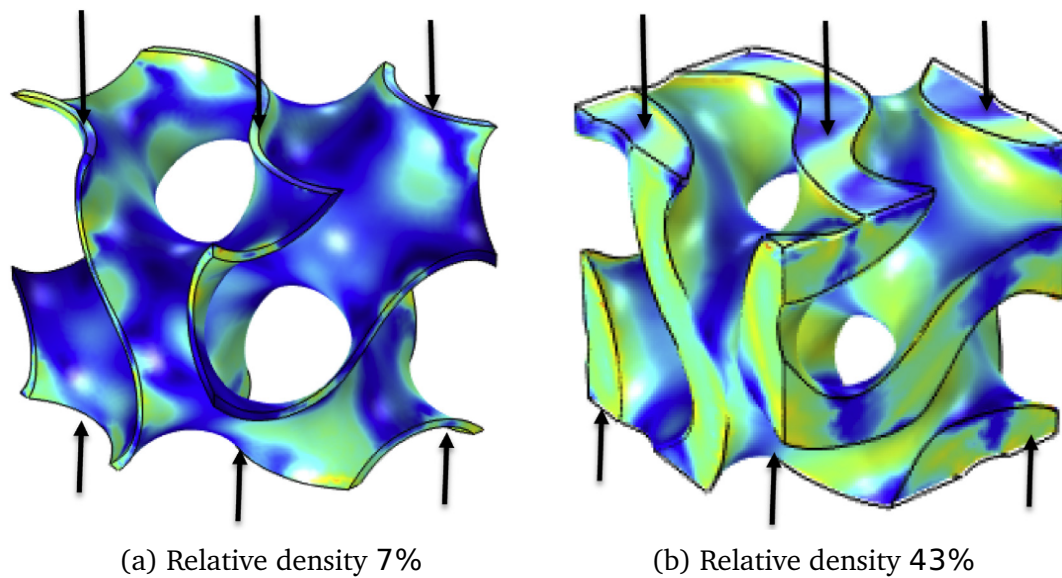


Figure 2.16: Von Mises stress computed for a gyroid structure under 3.5% compressive strain [2].

method. Printed with SLS 3D printer, samples passed through a series of compressive and tensile test loads. The authors showed a good agreement between

numerical and experimental results with great strength and energy absorption properties.

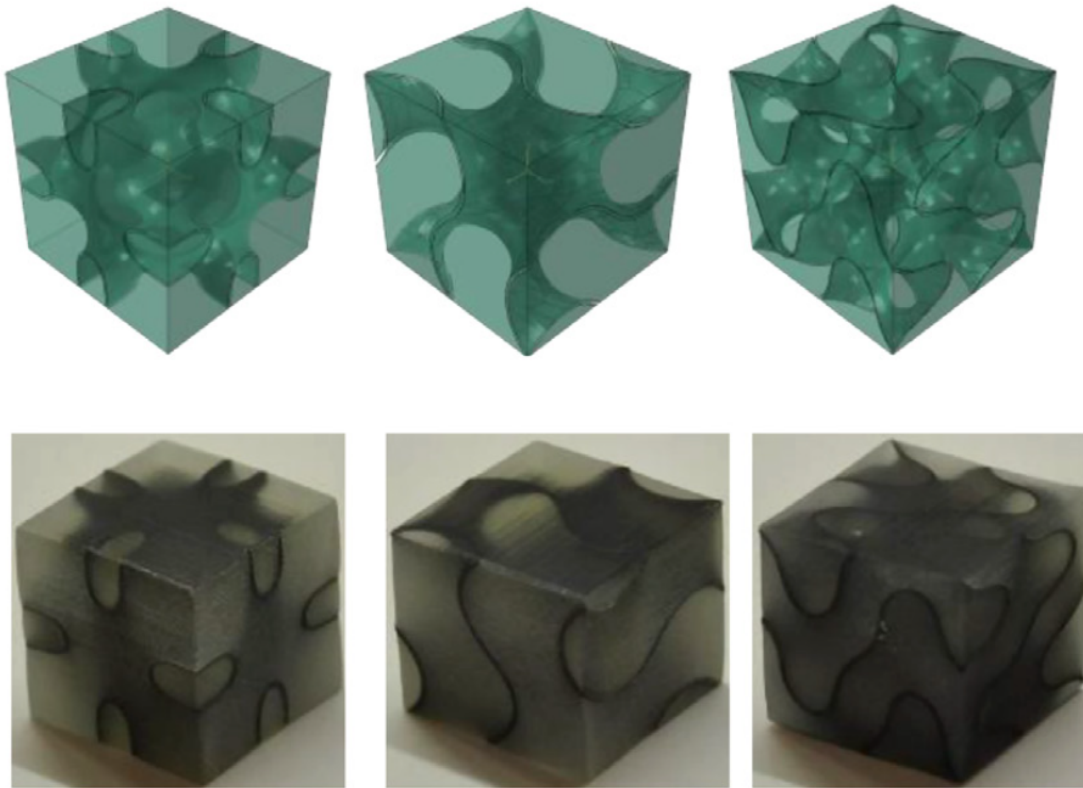


Figure 2.17: CAD models and 3D printed specimen of interpenetrating phase composites based on different types of TPMSs (Neovius, Gyroid, Fischer) [50].

One more particular approach was shown in [50] dedicated to studying composite materials reinforced with several types of TPMS sheet networks. The structures considered in the paper are assumed to consist of two parts: the soft matrix and the reinforcement made of a stiffer material, which is embedded into the matrix material. The TPMS structures were compared to the "classical" reinforcements such as fibers or spheres widely used in applications and well studied in the literature. The effective mechanical properties were calculated with FEM homogenization method for linear elasticity. As the two-phase composites were considered, the volume fraction of the reinforcement has been chosen very small, 1%-6% of all unit cell's volume. Thus the effect of the integrated TPMS structures was studied through two parameters described by the ratios of the uniaxial Young's moduli and the bulk moduli of two solid phases. It was shown that although the fiber-reinforced composites show a high uniaxial effective modulus corresponding to maximal theoretical bounds in one direction, it shows a weak response in the other directions (because it is transversely isotropic). In contrast, TPMS structures provide the tetragonal or cubic symmetry and thus same or relatively close effective moduli in different directions. Therefore, they can be considered less directional than the materials with fiber reinforcement. The study of the dependence of the effective

uniaxial and bulk moduli on the volume fraction of the reinforcement material (for values below 10%) showed a linear correlation between them.

2.7 Functionally graded materials

The other very important type of materials are functionally graded materials (FGM). FGM are materials with spatial variations of a composition or a structure according to a given law and hence locally tailored properties ([240], [128]). This spatial gradation gives serious advantages such as, for example, conforming to a prescribed geometry, effective load distribution through their volume, efficient shock absorption in wide range of the energy spectrum (for instance, absorbing weak and strong impulses equally well), control over a direction of thermal expansion, e.t.c. One more feature provided by functionally graded materials is an ability to avoid delamination process that can often occur in composites under specific heating or loading conditions.

There are multiple examples of FGMs coming from nature ([134], [247], [120]) observed in trees, bamboo, turtle shell, human skin, teeth, bones, e.t.c. As one of the application examples, recently the design of orthopedic implants started attracting more interest in the research society thanks to significant developments in computer aided design and additive manufacturing. The precision of modern computer tomography (CT) or magnetic resonance imaging (MRI) equipments provides the possibility for creation of high resolution 3D CAD models of any part of a human body from a set of 2D scan images and then transformed into a stereolithography (STL) file suitable for additive manufacturing [134]. The CAD model can be computed through multiple numerical methods based on given functional constraints which depend on a tissue/bone being under consideration. The high quality imaging also can enable a good identification of gradations between different tissues. Therefore, having methods that provide materials closely approximating these functional gradations will bring us to closer the possibility for manufacturing of implants perfectly conforming to the properties of the original tissue.

There are several approaches for the design of functionally graded materials and they can be classified almost the same way the design methods for cellular materials without spatial gradation (homogeneous cellular materials). According to the current flow of research there are three most popular approaches: be means of direct or inverse methods based on truss-like structures or regular periodic lattices, through the implicit surfaces, and using the topology optimization methods (during the last years this approach became more used).

The paper [118] proposes an optimization method for design of interconnected FGM materials based on extended triply periodic minimal surfaces (ETPMS). The difference between ETPMS and TPMS is that the former is defined not only through an implicit expression but with additional control parameters (nonconstant) consistently defining the structure's anisotropy and heterogeneity. The ETPMS cell is defined through a corresponding TPMS im-

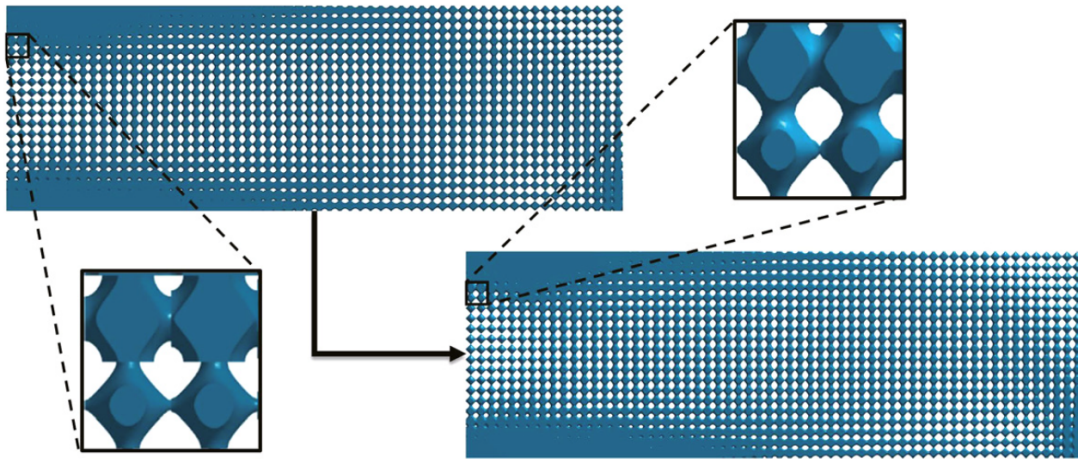


Figure 2.18: Optimized ETPMS-based structures presented in [118] before (top) and after (bottom) smoothing.

explicit expression where each directional component is scaled with the control parameter thus defining anisotropy of the material. These parameters are also used to control the structural connectivity of the design by defining a connectivity criteria at control points of the unit cell that helps to identify if the corresponding (according to periodic boundary conditions) points belong to the same (interior/exterior) side of the ETPMS. Finally, the design problem is defined as a problem of compliance tensor minimization in the space of control parameters with the equilibrium equation volume fraction limitation and interconnection criteria as additional constraints. To ensure smooth connectivity between different cells filtering through averaging the control parameters was applied.

An approach in topology optimization applied to the design of FGM materials was presented in [169]. The SIMP topology optimization model was chosen for finding an optimal gray-scale design. Based on obtained density distribution, a lattice with spatial gradation of the volume fraction is computed. Finally, three different ways to map the computed lattice on the TO solution were presented. It was shown that the lattices designed with the embedded TO method show up to 40%-50% higher stiffness than their uniform analogs.

One more TO approach presented in [176] is based on solving TO problem for a given spatial variation of the bulk or shear moduli by means of bi-directional evolutionary structural optimization (BESO) ([92], [11]) in the form of the inverse homogenization problem. The graded base cell (GBS) representing a periodic in directions perpendicular to the spatial gradation computational domain is divided into multiple primitive cells (PBS). For each PBS a separate TO problem with a given bulk or shear moduli value is defined. To ensure connectivity of the designed PBSs all the local TO problems are solved in parallel by SIMP method in combination with nonlinear diffusion technique ([226], [11]). The results show good structural connectivity and agreement of the mechanical properties with target values of the obtained designs.

Nevertheless, besides the features provided by the existing methods there

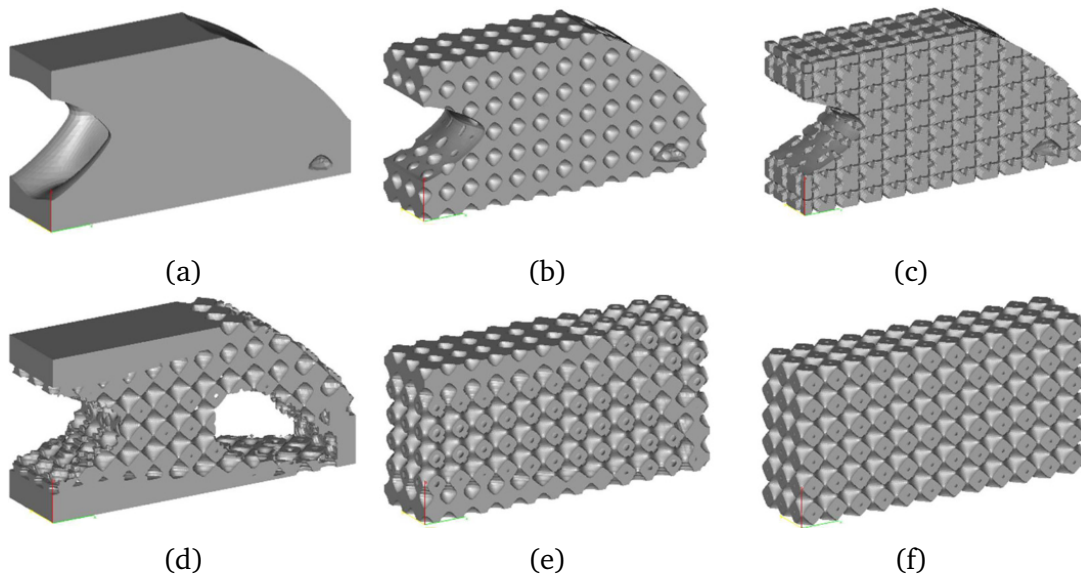


Figure 2.19: Examples of structures representing different FDM design strategies [169]: topology optimization with SIMP penalization (a), inserted lattices of double primitive (b) and body-centered cubic (c) cells, graded double primitive lattice (d), scaled double primitive lattice (e) and original double primitive lattice (f).

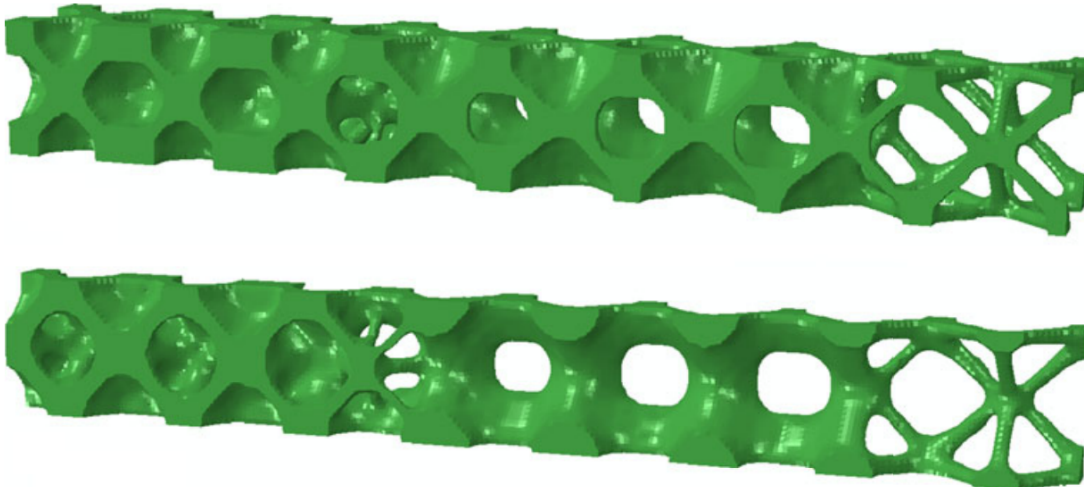


Figure 2.20: An example of a 3D FGM with spatial variation of the shear modulus (top) and its cross section (bottom) [176].

are still open challenges remaining to be solved. One of the main problems (still is not solved in the general case to the best of our knowledge) in the design of FGM structures is to preserve connectivity of all structural elements in transition areas as the lack of connectivity or sharp connectivity can result in weak spots accumulating redundant stress or performing undesired nonlinear behavior.

For example, [24] presents a data-driven approach for modeling objects which consists of FGM materials. The method is based on several steps includ-



Figure 2.21: An example of real (left) and replicated (right) with a 3D printer objects [24]. The internal structure of the replicated design (bottom) consists of two different materials (black and blue).

ing deformation data measurement of base (continuous and cellular) materials, composition of an optimal stacked-layer combination of the materials and a fabrication process of the resulting object. The deformation properties of the base materials from a chosen materials gallery was computed through quasi-static FEM approach [25] with an employed model for capturing nonlinear material properties represented by a radial basis function (RBF) interpolation and validated with experimental tests. As the target object is defined through a set of experimentally measured strain values, a suitable base material is found through minimization of the discrepancy between the target strain values and the strain computed based on the radial basis function decomposition. The core optimization problem for finding an optimal configuration of base materials' layers in a given object's shape is represented by an original branch-and-bound method with clustering. The domain is divided into a number of cells (each cell can only correspond to one out of a chosen set of the base materials). The further optimization process is organized with the use of a decision tree. The authors of the paper provide the sufficient approach from a target object to a fabricated optimal design. However, it seems that the different material layers are simply attached to each other through a continuous horizontal plane and there is no additional method (analytics- or optimization-based) employed to the model to ensure smooth connectivity of all structural components.

In addition, the paper [139] dedicated to the design of TPMS-based lattices with control over the volume fraction grading and spatial transition between different cell types. The structure design was modeled through TPMS model (of six different minimal surface types) represented by transcendental equations with a parameter controlling the structure's volume fraction. The obtained lattices were discretized in a finite element mesh. A finite element method was used to analyze the structure's mechanical response and investigate the connection between the effective elastic modulus and the volume

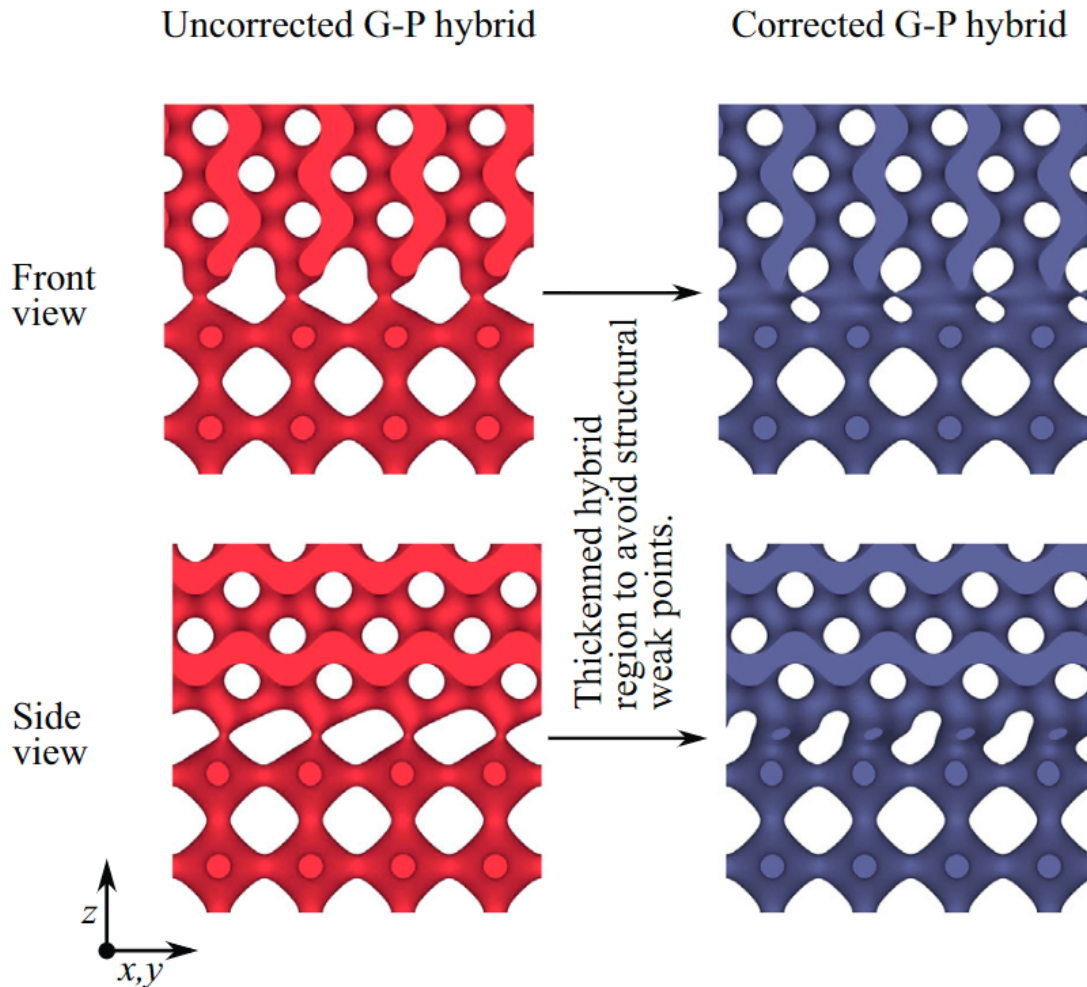


Figure 2.22: Examples of FDM materials composed of primitive and gyroid lattices with poor mechanical properties in the transition area (left) and after correction with increased strength (right) [139].

fraction along with the orientation of the cells. Then, the functional relation between the effective elastic modulus and the volume fraction was interpolated taking into account the loss of structural connectivity (in this case the elastic modulus should be equal to zero) and compared for all considered lattice types. The overall elastic modulus explicit prediction mechanism through a set of local elastic moduli was presented. Moreover, the authors acknowledge that in case of spatial transition between different cells can cause serious structural connectivity problems or weakening of the lattice in the transition area. This problem was demonstrated on the example of linear interpolation between two cell types with a parameter defined by the inverse exponential law with the sigmoid function as a factor [239]. In this approach as a possible solution of insufficient connectivity a method of the material volume fraction local correction was proposed.

2.8 Noise-based design of materials

Besides the approaches for architecting materials through TO-based algorithms or direct implicit methods using trusses or TPMS lattices, there are multiple works dedicated to modeling of materials through explicit mathematical formulations. Some of these methods come from the field of texture synthesis (procedural or reproductive) ([127], [47], [44]) and some are originated from corresponding mathematical models describing physical processes in nature [106]. This functional representation usually provides a significant boost of the performance which can be useful in the materials' space exploration or in creation of the inverse design algorithms. In addition, some of the methods exploiting this approach allow to impose complex directions of anisotropy that (as it was shown in [215]) enable very specific and complex nonlinear mechanical behavior. Moreover, using procedural random functions (like noise functions) enable generation of stochastic microstructures with highly controllable anisotropic properties.

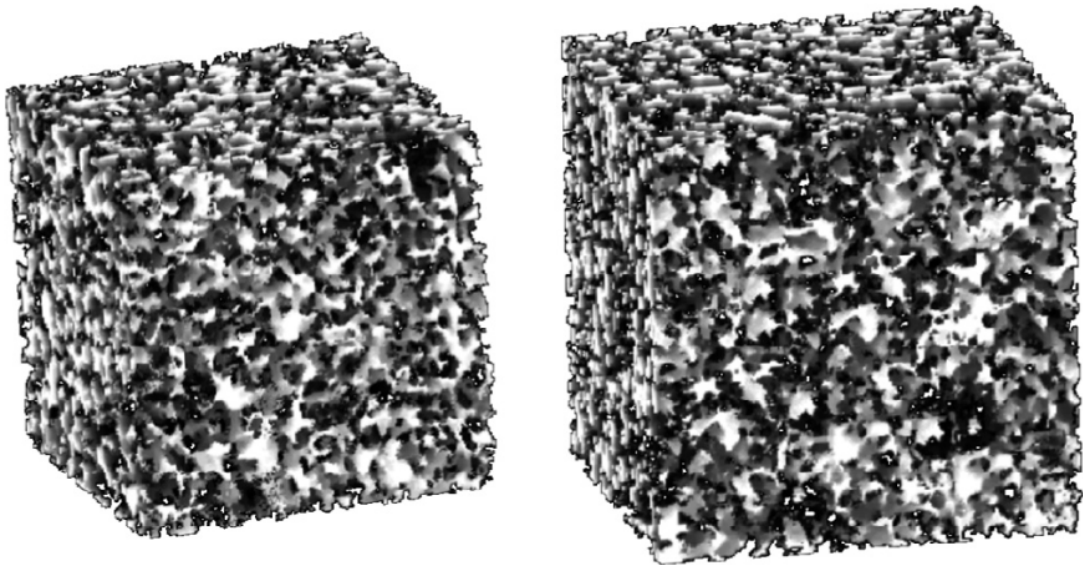


Figure 2.23: Example of texture synthesis-based reproduction of a 3D material (Berea sandstone) [127].

A very representative work for employing a widely used in texture synthesis spatial stochastic process in the design of stochastic materials is shown in [127]. The Markov process was taken as a basis for creating a data-driven model for reproducing 2D and 3D random materials based not only on its constituents' volume fractions but more specific descriptors. As descriptors here n -point correlation functions and Minkovski functionals were chosen as they contain more information about the material's structure and hence are more descriptive about its properties. Based on the input structure and a given window size an analogous material with corresponding correlation functions and Minkowski functional can be reproduced with good precision. It was shown that the right choice the window size is crucial for reducing the approxima-

tion error. Moreover, analytical expressions for the size of the window were presented. The method shows good performance without any additional calculations and optimization process required.

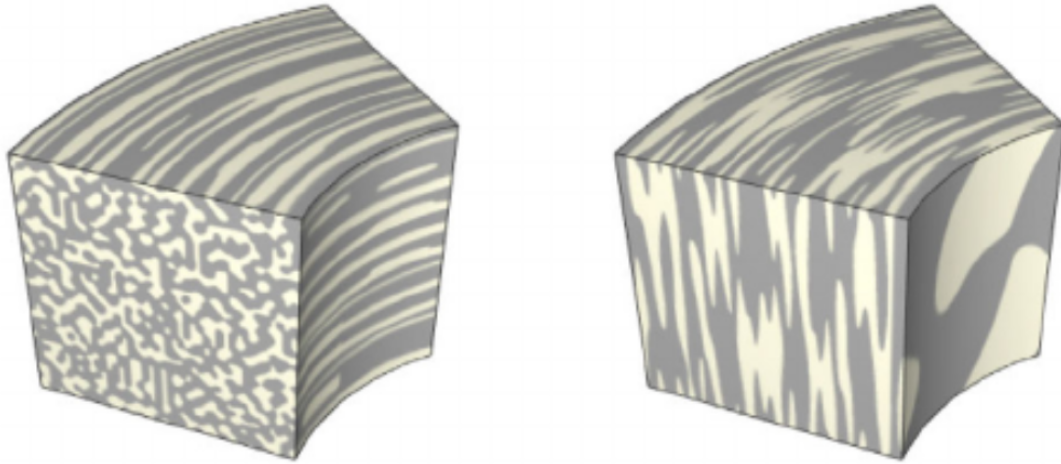


Figure 2.24: Examples fiber-shaped (left) and disc-shaped (right) anisotropic microstructures [47].

On the other hand, in [47] presented a model for procedural generation of anisotropic functionally graded materials based on the Perlin noise function. The heterogeneous material was represented by a mapping from a parametric domain into the real space with Bezier hyperpatches which are computed as sums of Bezier functions with two different coefficient types. One set of coefficients represents spatial coordinates of a given point and the other defines the proportion of base materials at this point. There, the Bezier hyperpatch represents a pair of position/material. It was also shown that the proposed method provides good control over continuity of a shape and material distribution (up to C_1). For modeling the base material distribution in the composite a modified version of Perlin noise was chosen. The original noise was normalized to vary in $[0, 1]$ and the original distribution was changed in order to achieve a uniform distribution of the stochastic process. Some of the presented results show that through the frequencies of the noise function it is possible to define a direction of anisotropy, change the shapes of the constituent materials' phases and the microstructures' scale. The approach appears to be an efficient method for modeling complex solid composite objects.

An other important work that strongly correlates to our work is presented in [106]. This paper provides a data-driven approach for the inverse design of mechanical metamaterials with prescribed effective properties. As spinodoid materials, minimal surface-based lattices, are known to have mean curvature close to zero, when the stress distributes more uniformly through their structure. This fact results in potentially higher strength (points with higher rate of stress accumulation are usually the weakest spots). Although spinodoidal topologies come from solution of time-dependent Cahn-Hilliard problem of a phase separation process it is possible to use a linearized model for the early stage phase separation. In this case, the spinodoidal structure can be expressed

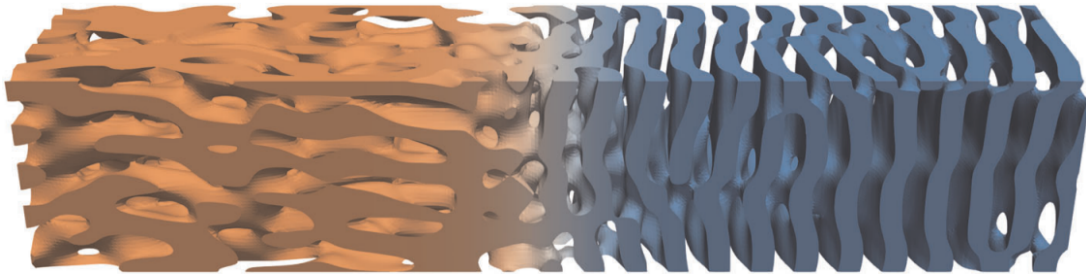


Figure 2.25: An example of FDM architecture with horizontal spatial variation between columnar (orange) and lamellar (orange) materials presented in [106].

through a superposition of gaussian waves with random phase and direction angles. Then, the anisotropy direction, microstructure's shape and scale can be controlled directly through the parameters of this model. To implement the data-driven material design approach the generative adversarial network (GAN) method was used [56]. The first deep neural network (generator) was trained on a large dataset of generated spinodoid materials and effective mechanical parameters computed with a FEM method. In addition the second neural network (discriminator) was used to validate the design proposed by the first network. The method shows high design quality and computational performance along with very good accuracy of prediction of material's effective properties.

2.9 Fabrication methods

Besides the problem of the design of cellular metamaterials there are multiple challenges connected with their fabrication. As the spatial organization of such materials initially could not be reproduced by traditional industrial techniques for a long period of time, the need of finding new possible production methods has appeared. Indeed, regardless of the fact that the first results in study of composite materials appeared long time ago (for example, the first commercialized cellular material, sponge rubber, was presented in 1914 [38]), the latter came into industrial production reaching significant commercial importance years after (for polymer foams it was in 1935 with Talalay process and in 1991 for metallic foams with patents of Baumeister) [101]. Moreover, random cellular materials were introduced significantly earlier than lattices with regular spatial organization. In their turn, polymer foams were introduced significantly earlier than the ones of metal. The first polystyrene foam sample was obtained in 1931, then flexible polyurethane foams were introduced several years after the Second World War and during the next couple decades found their use in global market for multiple applications including production of furniture and vehicules. This significant growth of popularity also stimulated development of these materials and their manufacturing techniques. Commercial production of phenolic foams started in 1945 with subse-

quent development of syntactic foams manufactured with tiny hollow phenolic microscopic spheres (microballoons) filled with an inert gas in 1953. For solving a problem of light weight encapsulation of electronic components epoxy foams were employed in 1949. In addition, silicone foams started being developed since 1950 as the need of light-weight materials with good long-term heat resistance arised. Recently, multiple cellular materials were presented to face high-temperature regimes (fluorocarbon and syntactic polybenzimidazole foams, cellular aromatic polyamides) [101]. Nowadays, foams can be made from almost any type of polymer material (butadiene-styrene, neoprene, acrylics, cellulose acetate, e.t.c.) using one or several existing fabrication techniques.

The history of metallic foams started with the first French patent on cellular materials in 1920 [53], but this topic did not cause any particular interest [114]. Although several results in this field along with multiple patents presented by Elliott ([67], [66], [65]) in 60s attracted attention of the scientific community, the massive investigation in the field of manufacturing of metallic cellular materials and their commercialization started in 90s. At this time patents of Baumeister ([13], [14]) were met with enthusiasm as there was high need in innovative light-weight and high-strength materials for transport [115] and aerospace applications [Lufthansa Fuel Efficiency im Lufthansa Konzern—Kosten Sparen und die Umwelt Schonen. 2017]. Since then, numerous research works have been carried out to increase the quality of the manufactured materials, reduce high fabrication costs, and diminish ecological impact (emission of some blowing agents affects the ozone layer). Nowadays, were have large number of different metallic foams made from different types of metal and alloys with wide spectrum of effective properties including very high porosity and thus extremely light weight. Moreover, there are multiple fabrication techniques including use of different precursor type (a melt or a powder), source of porosity (hollow particles, blowing agents, external gas source, dissolved gas), and presence stabilization method (ceramical addition, on-situ oxidation, natural viscosity).

In the literature cellular materials with random position of pores of uncontrolled shape and size are usually called "foams". This term denotes a mixture of a base material (precursor) and a gas which under a chain of physical processes and chemical reactions form a resulting structure. In order to induce the foaming process the gas needs to be released into the precursor. For that, the gas is introduced in the liquid matrix directly by an external source or using a chemical or physical blowing agent.

Polymeric foams are generally manufactured through the process of nucleation and growth of pores (not for syntactic foams) requiring several subsequent stages: bubble formations, buble growth and bubble stabilization [101]. The process of foaming a polymeric material is usually conducted by mechanical, chemical, or physical techniques:

- Thermal decomposition of a chemical blowig agent (by direct heating or as a consequence of an exothermic polymerization reaction)



Figure 2.26: Examples of metallic foams corresponding to different manufacturing process and the degree of control over their microscopic structure [114].

- Mechanical injection (whipping) of gas into a fluid polymer.
- Inclusion of low-boiling liquids with subsequent evaporation in the matrix material induced by exothermic polymerization reaction or heating.

- Chemical foamization by in-situ reaction during material polymerization.
- Injection of dissolved gas into a polymer mass with following expansion due to pressure reduction.
- Incorporation of microscopic beads or spheres [3].

Although manufacturing methods of metallic and polymeric foams have a lot in common as they often share similar underlying principles, it is important to discuss the variety of materials and their manufacturing methods available and commercially used nowadays. Metallic foams can be classified based on their ability to control porosity properties during the manufacturing process (spatial organization of cells, their shape and size): stochastic, partially ordered, ordered metallic foams and designed structures with tailored properties.

Metallic stochastic foams are manufactured with methods where there is no (or almost no) individual control over a shape, size or spatial distribution of cells within a material. The most well-known production methods used here are melt foaming with blowing agents or uncontrolled gas introduction and powder metallurgy with blowing agents. The melt foaming can be carried out by introducing a blowing agent into a molten matrix (Alporas technology) ([148], [147]) or by incorporating the blowing agent with powder metallurgical production of the base material (Foaminal method) ([13], [14], [15], [15]). An alternative technique is the Hydro or Arcan process which is based on gas injection into an aluminium melt stabilized by 10%-20% with ceramic particles.

Partially ordered metallic foams are the foams with some (not full) control over the shape, size or distribution of pores in space in a sense that their manufacturing process allows one to control these parameters in a limited degree. Many types of syntactic foams and APM foams are typical representatives of this type of materials. Templating technique, used for production of these foams, is based on using placeholders to introduce pores at exact places or a nonmetallic materials to make the metallic precursor to follow their shape thus forming the pores with exact characteristics. Another approach is to control the pore generation directly: solidification-controlled GASAR foams ([190], [189]) or a similar method introduced by Nakajima et al ([156], [157]). Moreover, there is a replication-based technique (M-Pore process) based on creating a polymer foam, during a heat treatment obtaining an open cell structure, creating a mold by covering the open cell foam by a heat resistant material with further thermal removal of the polymer material. The resulting metallic foam is obtained by injecting a matrix phase into the mold (melt infiltration-based synthesis). Perlite-based metal matrix syntactic foams are produced by infiltrating melt of precursor metal into packs of porous particles ([234], [224], [28]). The use of these particles for the pores formation provides control over their size and geometry ([202], [204], [203], [35]), but not precise prediction of their space distribution. Metal powder injection molding is also widely used for production of the partially ordered metal foams: the metal powder is mixed in relatively high fractions with a polymeric binder, then mixed and kneaded into a "green

part", which is treated chemically and thermally to remove the organic part. To finish the manufacturing process the obtained structure undergoes sintering. Hollow sphere structures are represented by hollow metallic spheres, that are joined via metallic matrix. These materials are typically produced through direct sintering their surfaces or a subsequent step requiring some bonding agent [71]. APM foams are close to the concept of the hollow sphere materials, except that the spheres are joined to each other through their surface and there is no rigid matrix between them. The production method consists of several stages: first a mixture of metallic precursor and a blowing agent is prepared and compacted to wire shape, then from cut-off pieces of the resulting (Foaminal) foamable material foam spheres are obtained, on the final stage these spheres are covered with a bonding agent, shaped into a mold and undergo a process of re-melting of the thermoplastic coating.

Ordered metallic foams have perfectly controlled spatial organization and, as a consequence, more predictable properties. Usually they are represented by regular periodic cellular structures, such as: Kagome-type [216] or corrugated sheet metal structures and, therefore, their manufacturing does not require any foaming step. In production of open cell ordered foams so-called weaving techniques are used, which provide good control of the truss geometry [112]. The wires of varying thickness [111] are given a helical shape and arranged into a periodic 3D structure. All the wires in their cross-couplings are joined using any of suitable techniques: soldering, brazing, sintering, e.t.c. Also it is possible to combine these helical wires with metallic hollow spheres [119].

Designed cellular structures with tailored properties often cannot be produced by traditional industrial methods as in most cases complex geometry of such materials goes beyond the capability of the conventional fabrication techniques. Moreover, applying these massive and poorly adaptive methods to the problems of prototyping or producing low quantities of objects with different tailored properties (customization) can become expensive and challenging. One of the possible partial solutions for these problems is the concept of additive manufacturing (AM). This fabrication approach comes from rapid prototyping (RP) which was introduced several decades ago and with development of technologies led to AM [81]. All additive manufacturing methods contain two common points: layer-by-layer material deposition (an exception is the CAL method) and specific preparation of the manufacturing process containing several steps (preparation of the base material and preparation of the production space – heating, calibrating, e.t.c.). Some AM methods also require post-processing to upgrade mechanical performance and/or structural quality.

3D printing is an AM approach which recently gained high popularity and these trends seem to stay in the future. Due to significant growth of the interest for this domain, there are multiple studies (done and ongoing) dedicated to development of new 3D printing methods and improving the performance of the existing ones. Let us briefly describe the main methods in 3D printing [159].

Fused deposition method (FDM) is based on building an object by deposition of a thermoplastic polymer. The filament is pushed through the heated

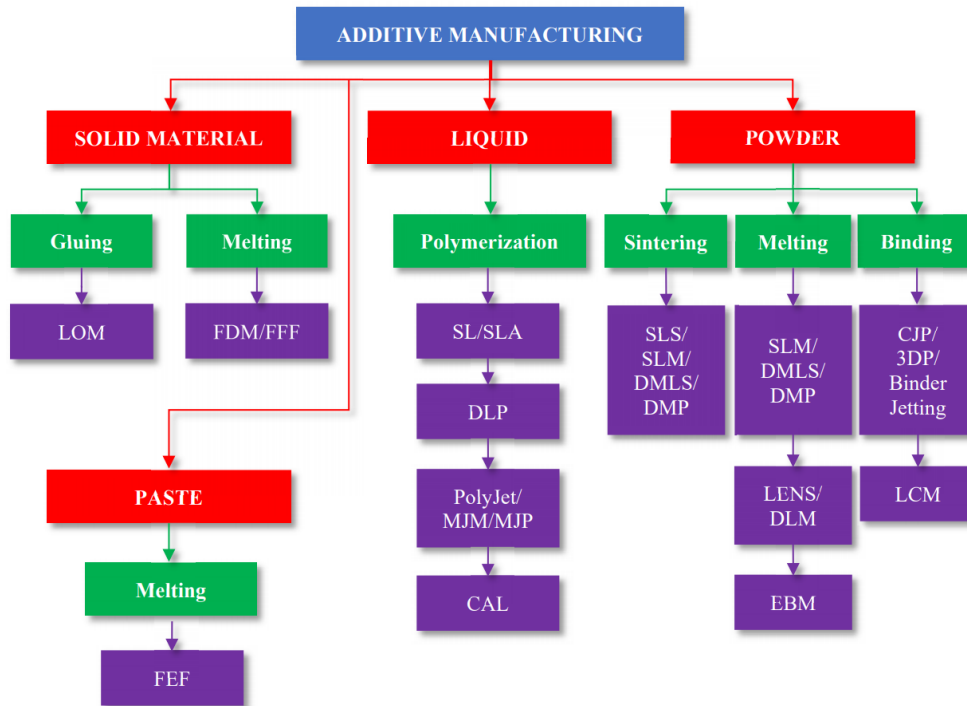


Figure 2.27: AM manufacturing techniques [81].

nozzle where it reaches semi-liquid state and thus is placed in a building platform (either the nozzle or the platform move). It is crucial for the polymer to be thermoplastic as this property allows neighboring layers to fuse together and provide mechanical strength for the entire object. In FDM printing the main parameters affecting the mechanical properties of the manufactured object are the layer height (thickness) direction of the filament trajectories and gap between them [149]. Unfortunately, due to high heterogeneity along the printing axis this method provides poor mechanical performance, laminate (layer-stacked) appearance, low surface quality and small range of base materials (because of thermoplasticity) [45]. However, FDM printers are widely used regarding their low cost and simple construction and high fabrication speed.

Powder bed fusion method requires processing thin powder layers subsequently rolled on top of each other. The powder particles are fused together by means of a laser beam radiation or a liquid binder. After printing, some additional manipulation over an object (such as coating, sintering infiltration) are required. Laser radiation is used for material powders with low sintering (or melting) temperature. Selective laser sintering (SLS) method is applied for various polymers, metal and alloy powders, but selective laser melting can only be used for several metals such as steel and aluminium [242]. As during SLM printing material particles are fused together by melting while in SLS they are heated to temperature near but less than the melting point, the SLM method shows higher mechanical performance [110]. When a liquid binder is used the method is called three-dimensional printing (3DP). This technique provides higher porosity than the mentioned above laser-based methods [217].

SLS, SLM and 3DP methods provide high resolution with high printing quality with the price of high costs and slow fabrication speed. In addition, the powder bed provides natural support for the printed structure that makes possible printing complex shapes. However, these manufacturing methods do not allow fabrication of structures with closed hollow elements. All advantages of powder bed fusion approach made it widely used in multiple domains including tissue engineering, aerospace and electronics.

Inkjet printing and contour crafting is widely applied for building complex ceramic structures (for example, in tissue engineering). The printing process includes deposition of material droplets via a nozzle onto a substrate. The material is represented by a stable suspension of ceramics [57]. This technique provides fast and efficient fabrication of even complex geometry. There are two main types of ceramic inks: wax-based inks and ceramic suspensions. Wax-based inks require heating in order to melt the wax with subsequent cooling for solidification. Ceramic suspensions solidify through evaporation process. On the other hand, inkjet printers need complex workability maintenance but provide coarse resolution and weak adhesion between the material layers. Contour crafting is a method similar to the inkjet approach but is aimed on building large objects out of concrete or soil (extruding it from a large nozzle under high pressure). Contour crafting prototypes are considered as an option for building constructions on the moon [104].

Stereolithography (SLA), being introduced in 1986, is one of the oldest additive manufacturing methods [144]. In this approach as a material for printing a liquid UV-active monomer (usually acrylic or epoxy-based) is used. The UV radiation locally induces (radicalization) polymerization process with further solidification for maintaining subsequent layers. In addition, it is possible to use dispersion of ceramics particles in a monomer to build ceramic-polymer composites [212] or polymer-derived ceramifiable monomers [63]. Often post-processing is required to remove the liquid monomer from the object's surface and to achieve desired mechanical performance (heating or photo-curing). As a radiation source either an electron-beam UV light devices can be used to initiate the chemical reaction. SLA provides high quality printing with high resolution up to $10 \mu m$ [227]. However, the process is relatively expensive, slow and accepts limited range of materials. Moreover, SLA has been observed to be an effective solution for fabrication of complex nanocomposites [135].

Direct energy deposition (DED) (laser engineered net shaping, or laser solid forming, or directed light fabrication, or direct metal deposition, or electron beam/wire + Arc additive manufacturing) is used to fabricate high-performance super-alloys [93]. This method requires a powerful laser or electron beam energy source which is used to melt instantly a small area of the substrate and a feedstock material. Melted materials in the substrate and the feedstock further are fused together and solidify after the radiation beam location is changed [93]. Moreover, it is possible to employ multiple-axis deposition and usage of several materials at the same time (LASERTEC 65 3D: Additive Manufacturing in Milling Quality). In addition, DED can be used in combination with conventional subtractive techniques in order to complete fabrication. Ti-

tanium, aluminium, stainless steel, inconel and related aerospace alloys are widely used with this AM approach. High fabrication speed (Optomec LENS 850-R,[231]), very large fabrication volume (size of the resulting structures, for more details see Largest Metal 3D Printer Available | Industrial 3D Printing | Sciaky), excellent mechanical properties of the printed objects along with low precision, surface quality and reproducible geometry constraints [93] made DED often used for repairing and building large metallic components with low geometrical complexity.

Laminated object manufacturing (LOM) is one of the first commercialized additive manufacturing techniques which is used for multiple materials such as polymer composites, ceramics, metals, paper. It is based on cutting with subsequent layer-by-layer stacking (lamination) of different material sheets/rolls. The manufacturing depending on the material types used can be required. Ultrasonic additive manufacturing (UAM) combines ultrasonic metal seam welding and CNC milling for building laminated structures [117]. It is the only AM method working with metal which does not require high temperatures ([86], [89]). LOM provides reduced tooling costs and manufacturing time and is an effective method for building large objects. However, it provides poor accuracy and is not suitable for printing complex shapes as a time-consuming post-processing procedure is needed.

Chapter 3

3D periodic cellular materials with tailored symmetry and implicit grading

3.1 Notations

Notation	Definition	First introduced
G	computational grid	Algorithm 1
L	crystal lattice	Algorithm 1
\mathcal{R}	radius of a checked neighborhood	Algorithm 1
\mathcal{M}_c	closed-cell structure	Algorithm 2
\mathcal{M}_o	open-cell structure	Algorithm 3
$\mathcal{S}, \partial\mathcal{S}$	star-shaped set and its boundary	Figure 3.8
O	origin of a star-shaped set	Figure 3.8
(r, φ, θ)	spherical coordinate system	Equation 3.2
$f_{\mathcal{S}}$	parametrized star-shaped boundary	Equation 3.2
$d_{\mathcal{S}}$	parametrized star-shaped distance	Equation 3.3
\mathcal{Y}	spherical harmonic	Equation 3.13
(ϱ, ω)	polar coordinate system	Figure 3.11
\mathcal{T}	point group	Equation 3.16
σ	stress field	Equation 3.14
ϵ	strain field	Equation 3.14
C	elasticity tensor	Equation 3.14

Table 3.1: Notations for Chapter 3.

3.2 Introduction

3D periodic cellular materials are an essential ingredient in the manufacture of advanced functional parts. They allow triggering various elastic responses within a part by structuring its internal volume at a small scale. Ideally, a method to model cellular materials would allow for a wide gamut of elastic responses and geometries that could be freely chosen within the part volume.

A central line of research presented in this chapter is the design of *periodic* cellular materials, defined from a representative volume element (or *tile*) repeated in space. The periodicity simplifies the design and analysis while limiting computational and storage requirements.

Two types of cellular materials are considered here [84]: *closed-cell* structures which are formed by isolated void cavities (cells), and *open-cell* structures, formed by connected solid beams (possibly curved).

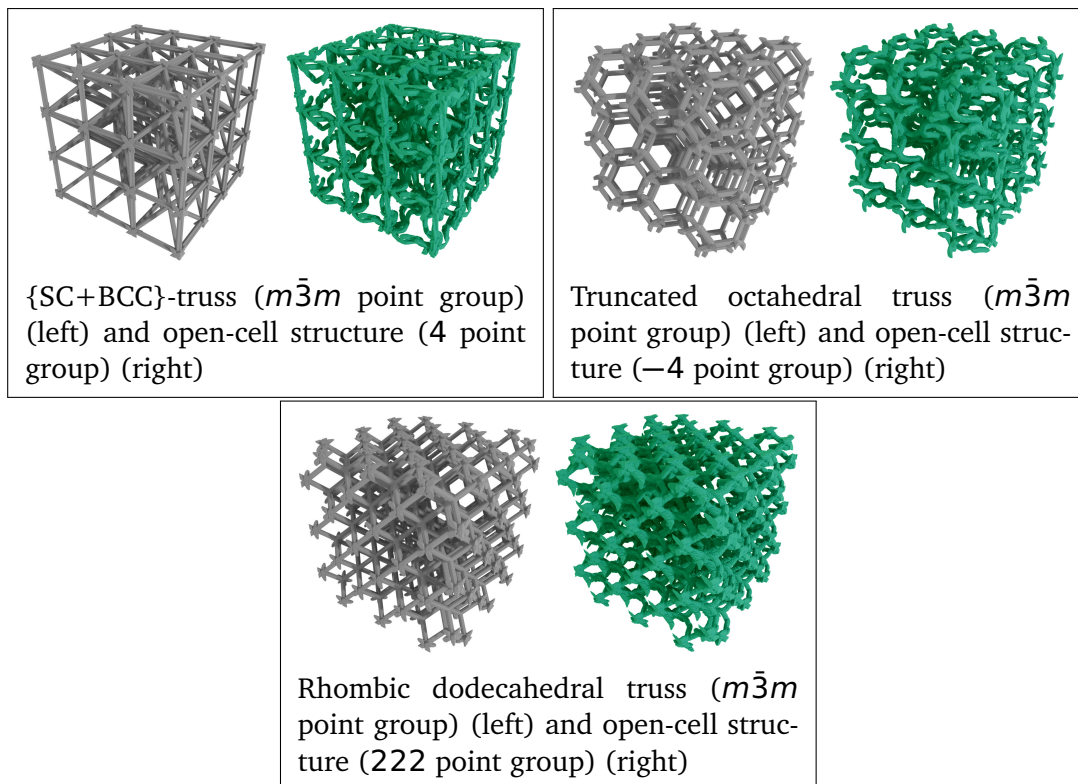


Figure 3.1: Our approach is able to compute some well-known periodic trusses and a vast space of open-cell structures with enhanced geometrical and mechanical diversity. Here we show some classic examples of periodic open-cell structures computed with our growth method using the Euclidean distance (in gray color) and other open-cell structures using the same underlying lattice with tailored symmetries (in green color).

A key to achieving complex, dynamic behaviors [22] is to allow for free spatial gradation of the structures within the part volume. Most techniques employ a catalog of tiles, pre-determined or optimized, placing different tiles

with different elastic responses in different locations. Adjacent tiles will generally not connect properly, requiring applying constraints on the sets of tiles or optimizing after placement (see Chapter 2).

In this work, we take a distinct view on this problem. Rather than reasoning in terms of a fixed number of tiles, we start from a periodic lattice of nuclei (points) and associate each a parametric description of the local structure being produced – a 3D star-shaped set. Each star-shaped set implicitly defines a distance function. Since the star-shaped set is possibly non-convex, we span a wide range of possible distance functions and a more diverse space of cellular solids compared to existing techniques.

An efficient computational process grows the structures around each nucleus. Intuitively speaking, the cells centered around the lattice nuclei grow, obeying a law of growth governed by the star-shaped distance while being forbidden to overlap. Once the growth process is complete, we obtain a cellular structure, which can be extracted as either closed or open-cell. If the same star-shaped distance is used at every nucleus, we obtain a periodic structure, from which a single period can act as a traditional periodic tile. If different star-shaped distances or lattices are used, we obtain spatial gradations.

Resorting to a classical Voronoi diagram under the star-shaped distance may lead to Voronoi cells with more than one connected component. Instead, the growth process ensures that each cell is connected by construction. More precisely, we consider a discrete growth process since it is challenging to formulate a continuous one: our growth process is atypical, guided by the growth of a non-convex set. To the best of our knowledge, continuous growth processes have been studied for convex distances (e.g. [5]) but not for star-shaped ones.

Our structures can be prescribed to enforce certain crystallographic geometric symmetries – and hence a given type of elastic response: monoclinic, orthorhombic, trigonal, and so on. The parametric star-shaped distances can also be easily interpolated, making it possible to transition from one geometry to another smoothly. Thus, our approach supports interpolation across different symmetries and topologies without any special treatment. It spans a broad space of possible geometries with controlled symmetries that can be freely combined and spatially graded. Finally, the compact parameterization of the distance and the lattice facilitates exploring the wide variety of possible cellular materials.

Definitions For more clarity the terminology used throughout the chapter should be defined. A *tile*, or representative volume element of a structure, is a periodic computational domain. The domain is covered by a *regular grid*, a set of discrete points each representing the center of a *voxel* (a cubic cell of the grid centered on the point). We define a *nucleus* as the starting point of growth of *cavities* or *cells* on the grid. We call a *lattice* the discrete set of nuclei distributed within the tile. The lattice has translational symmetries; therefore, it can be represented by *periodic crystals* [219]. Finally, a compact set $S \subset \mathbb{R}^3$ is *star-shaped* with respect to the origin O if for all $x \in S$, the segment $[O, x]$ is contained in S .

3.3 Growth method

Growth-based model. In this work the method for generation periodic cellular structures is based on a discrete growth process. The growth process is represented by Q – a queue of voxels ordered by distance to a corresponding nuclei (the closest is the first). Intuitively, this results in that the shape of the growing cells closely corresponds to the shape of the distance. Computations start only with the ordered set of voxels, which contain the nuclei and their 6-voxel neighborhood and then on each iteration when the next empty closest voxel is marked as occupied by a corresponding cell its 6 neighboring voxels are added to this set. The process stops when all the voxels are occupied, this corresponds to Q being empty. The output of this procedure is a 3D voxel grid, where each voxel is labeled with respect to its associated nuclei (a periodic tiling). To obtain a closed cell structure from this tiling one needs to extract the faces between the cells (Algorithm 2). The voxels corresponding to those faces are not occupied by cells and therefore are identified with a specific value. In case of d_S being the Euclidean distance the resulting tiling corresponds approximately to the Voronoi faces [162].

Algorithm 1 Growth(L, S, \mathcal{R})

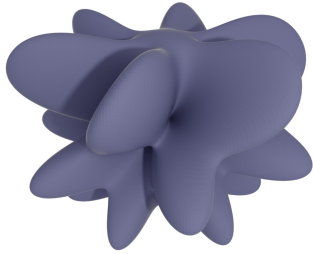
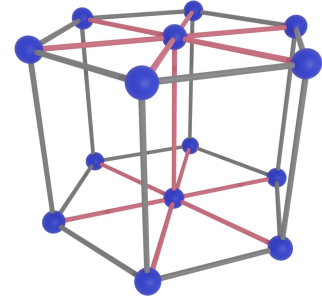
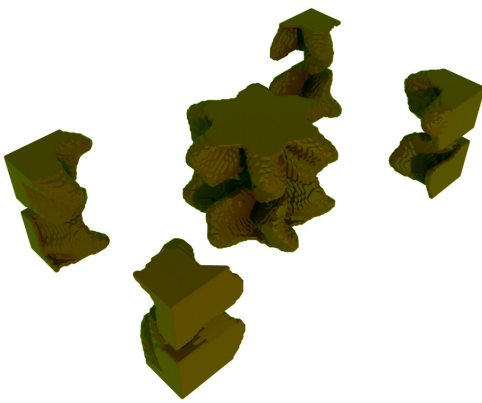
```

1:  $G = 0$  ▶ Initialization
2: for  $l \in L$  do
3:   Let  $v$  be the voxel containing the lattice point  $l$ 
4:   Insert  $(l, v)$  in  $Q$ 
5: while  $Q$  is not empty do ▶ Growth
6:   Let  $(l, v) \in Q$  with smallest distance  $d_S(l, \text{center}(v))$ 
7:   Remove  $(l, v)$  from  $Q$ 
8:   Let  $i$  be the index of  $v$  in  $G$ 
9:   Let  $k > 0$  be the identifier of  $l$ 
10:  if  $G[i] = 0$  then
11:    Let  $v_{\mathcal{R}}$  be the voxels at distance at least  $\mathcal{R}$  from  $v$ 
12:    if  $v_{\mathcal{R}}$  only contains the labels 0 or  $k$  then
13:       $G[i] = k$ 
14:      for  $v_n$  in 6-voxel neighbourhood of  $v$  do
15:        Insert  $(l, v_n)$  in  $Q$ 
return  $G$ 

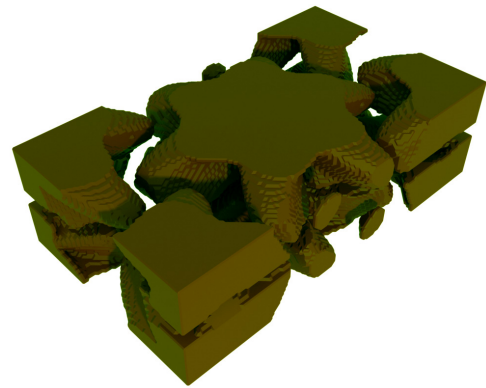
```

Distance-based model. In the case of a distance d_S of a convex shape S this would be sufficient to provide good solutions without exceptions. In more general approach when one uses star-shaped sets to compute the distance this can lead to undesired effects, such as isolated cell components. These defects are described in the section below. In this case using a "spacing" radius \mathcal{R} between the cells appeared to be a good solution. In each iteration before labeling an empty voxel the algorithm checks its neighborhood within this fixed

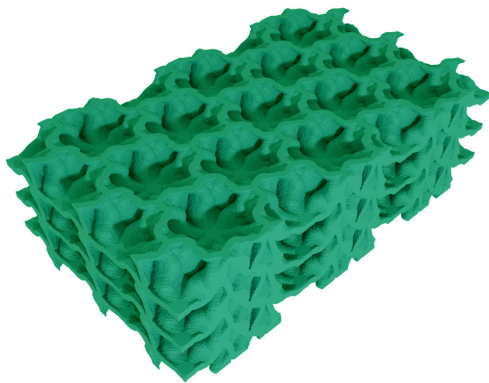
radius and if there is at least one voxel belonging to another cell it is labeled as belonging to an edge.

(a) Star-shaped set \mathcal{S} (b) Lattice L 

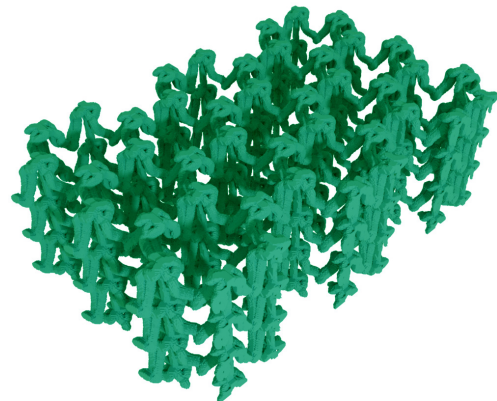
(c) Growth process



(d) Growth process



(e) Closed 3x3 cell



(f) Open 3x3 cell

Figure 3.2: Overview of our method. Given a starshaped set (a) and a periodic lattice (b) we compute a growth process (d) that leads to a periodic closed-cell structure (e). Afterward, if required, a periodic open-cell structure can be extracted (f).

Here the resulting tiling will contain cells with gaps of radius between them. The structure is obtained again by extracting the edge voxels. It would be easier to think about this method as when one starts with a continuous bulk material and then the pores (cells) are grown at the given point of the computational domain. The algorithm is shown on a scheme 1.

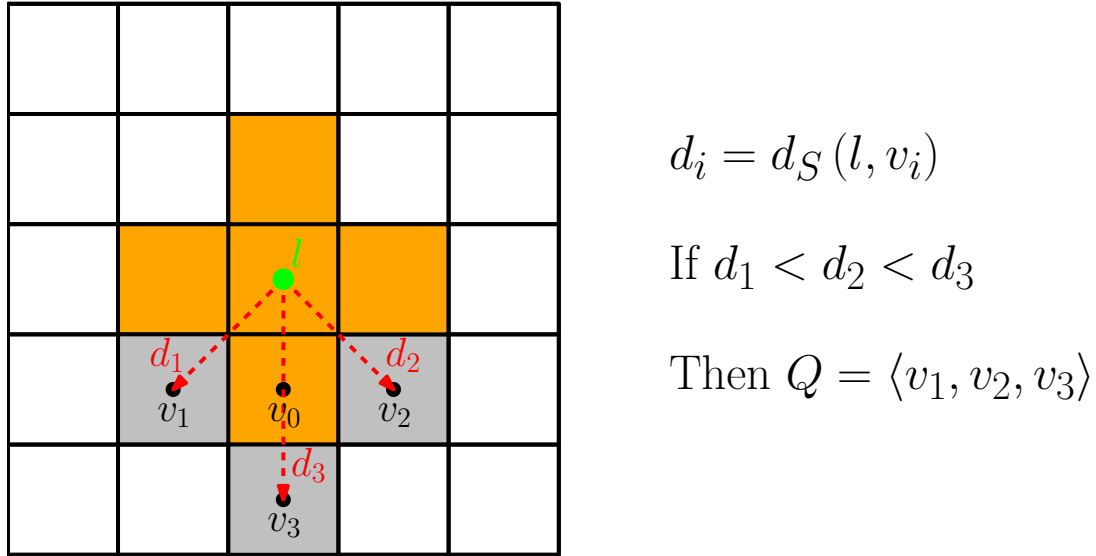


Figure 3.3: Visualization of the growth process presented in Algorithm 1. Voxels marked with orange color are already occupied by a cell corresponding to a lattice point l . After a voxel v_0 has been already occupied, one needs to append all its unlabeled neighbors (marked with grey) v_1 , v_2 , and v_3 to the ordered set Q . To do so, one needs to compute the corresponding distance d_1 , d_2 , and d_3 from centers of these voxels to l . The elements in Q are ordered corresponding to the values of d_1 , d_2 , and d_3 . Therefore, if $d_1 < d_2 < d_3$ then $Q = \langle v_1, v_2, v_3 \rangle$.

The problem of obtaining an open cell interface also is not trivial as it may seem. The first question that can arise is how to define computation of the open cell structure as a separate algorithm or as a part of post processing extracting it from the closed cell tile. As it occurred the implementation of it as a separate process does not give satisfactory results for nonconvex distances due to the fact that the edges are generated only at places where three and more cells meet, it brings us to the same problem which was described above: some cells can penetrate their neighbors and thus produce undesired degenerative effects. These occurrences more likely result in isolated (or connected but breaking overall symmetry) components of the computed structure.

Algorithm 2 ClosedCellStructureExtraction(G, L)

```

1:  $\mathcal{M}_c = 0$  the closed cell structure ▶ Initialization
2: for  $v \in L$  do
3:   if  $G[v] == 0$  (if a voxel does not belong to any cell) then
4:      $\mathcal{M}_c[v] = 1$ 
5:   return  $\mathcal{M}_c$ 

```

Taking into account issues mentioned above in this work we decided to obtain open cell structures by extracting them from a corresponding closed cell material sample. This method ensures that the resulting structure will not contain disconnected components or/and have different symmetry properties (Algorithm 3). For each voxel labeled as a part of the structure its neighborhood is being checked for presence of other cells. If there are three or more different cells within a given radius (therefore, line 4 in Algorithm 3 contains $\sum \text{sign}^2(k_i) \geq 3$ as three different cells represent a minimal criteria) the voxel is labeled as a part of an open cell structure.

Algorithm 3 OpenCellStructureExtraction($\mathcal{M}_c, L, \mathcal{R}$)

```

1:  $\mathcal{M}_o = 0$  the open cell structure ▶ Initialization
2: for  $v \in L$  do
3:   Let  $v_{\mathcal{R}}$  be the voxels at distance at least  $\mathcal{R}$  from  $v$ 
4:   if  $v_{\mathcal{R}}$  contains the labels  $k_i \neq k_j \neq 0, \sum \text{sign}^2(k_i) \geq 3$  then
5:      $\mathcal{M}_o[v] = 1$ 
6:   return  $\mathcal{M}_o$ 

```

3.4 Symmetry and point groups

As it was outlined in Chapter 2, the topic of symmetry in periodic material design plays a significant role as it is connected with a number of effective properties of the interface and helps predicting some material's properties in advance. Periodic materials can be associated with periodic crystals which have been studied for a long time by a discipline called crystallography and symmetry is a strong tool for analyzing properties of crystals. As a result, it is possible to use results of crystallography to analyze physical properties of periodic materials.

An object is symmetrical with respect to an isometric mapping if it is mapped onto itself without changing the structure. There are three basic Euclidean symmetry operators: rotation, reflection and translation. Also the other symmetries exist, but they are formed by combinations of the former ones. For example, inversion is a combination of rotation over 180 degrees and subsequent reflection with respect to a plane of rotation. The periodic nature of crystals imposes some limitations on possible symmetries occurring in these interfaces. So, for example, only 2-, 3-, 4- and 6-fold rotational symmetry can occur in periodic lattices.

As there is a big amount of possible combinations of symmetric operators these combinations have been well studied and classified. A set of symmetry operators form a point group – a groups of mappings which leave at least one point of a lattice still, thus a point group never contain translation. There are 32 point groups in 3D space that cover all possible symmetries of periodic lattices. There is a number of notation systems dedicated to specifying the point groups, but the most widely used in crystallography seem to be Schoenflies and Hermann-Mauguin notations. But the latter usually is more preferred as translational symmetry elements also can be included in this notation.

Schoenflies notation consists of the following symmetry elements: centers of inversion i , mirror planes σ , proper rotation C (from "cyclic") and improper rotation S (from "spiegel" – mirror) axes (which are usually accompanied by a subscript number denoting an order of rotation). Dihedral point groups with n -fold rotational axis and n 2-fold rotational axes perpendicular to the former are denoted by D_n . Tetrahedral point group is T with rotation symmetry of tetrahedron, which are three 2-fold and four 3-fold rotation axes. Octahedral point group O has the same rotation axes as cube (three 4-fold, four 3-fold and six 2-fold axes). Finally, icosahedral point group is I and has symmetry of icosahedron with six 5-fold, ten 3-fold and fifteen 2-fold rotational axes. Additional subscript letters h and d denote a perpendicular mirror plane and mirror plain containig the principal rotation axis, respectively.

Hermann-Mauguin notation is more specific about connection of the underlying symmetry elements. Axes with rotation symmetry are denoted by n – a number of maximum symmetric rotation allowed. Rotoinversion axes are indicated by \bar{n} . A plane of reflectional symmetry is represented by m . If one has a mirror plane perpendicular to n -fold rotational axis, it is denoted as $\frac{n}{m}$.

On table 3.2 all crystal families and corresponding Shoenflies and Hermann-Mauguin notations are presented.

Crystal system	Crystal class	Shoenflies	Hermann-Mauguin
Triclinic	Pedial	C_1	1
	Pinacoidal	C_i	$\bar{1}$
Monoclinic	Sphenoidal	C_2	2
	Domatic	C_s	m
	Prismatic	C_{2h}	$\frac{2}{m}$
Orthorhombic	Rhombic-disphenoidal	D_2	222
	Rhombic-pyramidal	C_{2v}	$mm2$
	Rhombic-dipyramidal	D_{2h}	mmm
Tetragonal	Tetragonal-pyramidal	C_4	4
	Tetragonal-disphenoidal	S_4	$\bar{4}$
	Tetragonal-dipyramidal	C_{4h}	$\frac{4}{m}$
	Tetragonal-trapezohedral	D_4	422
	Ditetragonal-pyramidal	C_{4v}	$4mm$
	Tetragonal-scalenohedral	D_{2d}	$\bar{4}2m$
	Ditetragonal-dipyramidal	D_{4h}	$\frac{4}{m}mm$
Trigonal	Trigonal-pyramidal	C_3	3
	Rhombohedral	C_{3i}	$\bar{3}$
	Trigonal-trapezohedral	D_3	32
	Ditrigonal-pyramidal	C_{3v}	$3m$
	Ditrigonal-scalenohedral	D_{3d}	$\bar{3}m$
Hexagonal	Hexagonal-pyramidal	C_6	6
	Trigonal-dipyramidal	C_{3h}	$\bar{6}$
	Hexagonal-dipyramidal	C_{6h}	$\frac{6}{m}$
	Hexagonal-trapezohedral	D_6	622
	Dihexagonal-pyramidal	C_{6v}	$6mm$
	Ditrigonal-dipyramidal	D_{3h}	$\bar{6}m2$
	Dihexagonal-dipyramidal	D_{6h}	$\frac{6}{m}mm$
Cubic	Tetartoidal	T	23
	Diploidal	T_h	$m\bar{3}$
	Gyroidal	O	432
	Hextetrahedral	T_d	$\bar{4}3m$
	Hexoctahedral	O_h	$m\bar{3}m$

Table 3.2: Crystal systems, crystal classes and corresponding Shoenflies and Hermann-Mauguin notations.

A space group is a group of isometric symmetry operators which do not need to keep a lattice point at its place and, therefore, different types of translations or combinations translations with the other operators are possible. As there is a significantly big number of space groups (248 space groups in 3D space), this research is conducted in terms of point groups, but all the results can

be translated into space groups without loss of generality. Moreover, as we work here with periodic lattices, the symmetry of a lattice yields the exact symmetry of the material (even translational); for more details, see Section 3.7. Therefore, the space group of a crystal lattice and a star-shaped set leads to the corresponding space group of the material.

In addition, in terms of the growth method this approach is convenient also because symmetry allows to classify distances by their shape. This leads to the question of how does combination of symmetries of the lattice and the distance result in symmetry of an obtained structure. We give further insights into that in Section 3.7.

3.5 Crystal lattice

Due to periodicity and porosity cellular structures can be associated with periodic lattices (nonperiodic cellular materials also can be associated with non-periodic stochastic lattices) denoting centers of the pores. There are several models for replicating periodic lattices, but here Bravais lattices were chosen. This approach is quite simple, flexible and covers all 32 crystal classes. Crystal classes are 32 possible types of periodic crystals corresponding to 32 point groups in 3D space (see Table 3.2). The periodic lattice is represented by an infinite combination of unit cells

$$L = \{i\vec{a} + j\vec{b} + k\vec{c}\} \quad (3.1)$$

formed by a basis of three vectors a , b , c , which do not have to be orthogonal or orthonormal.

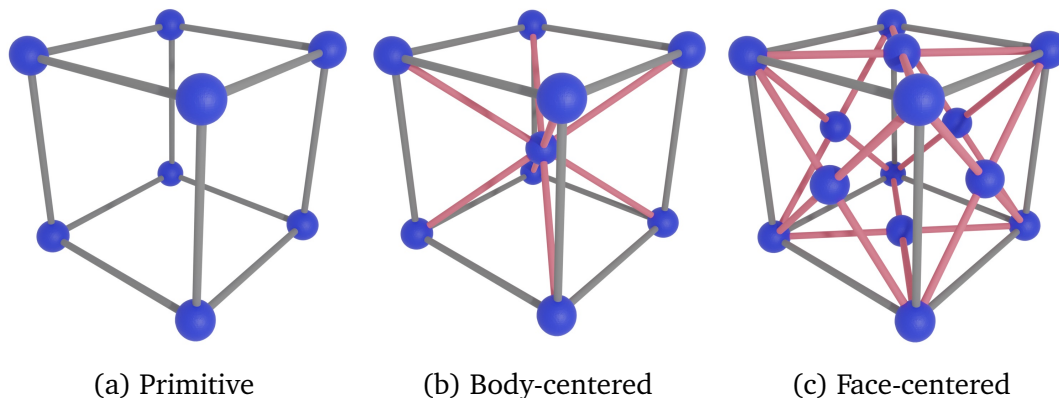


Figure 3.4: Three types of a cubic Bravais unit cell.

For i , j , k being integers a cell is called primitive. In general, these indices can be represented by real numbers. In this case the cell of a Bravais lattice will contain one or more additional points, that can give it more specific symmetry properties. In other words, a unit cell is a smallest repeating element of a crystal lattice that has the symmetry of the entire crystal structure.

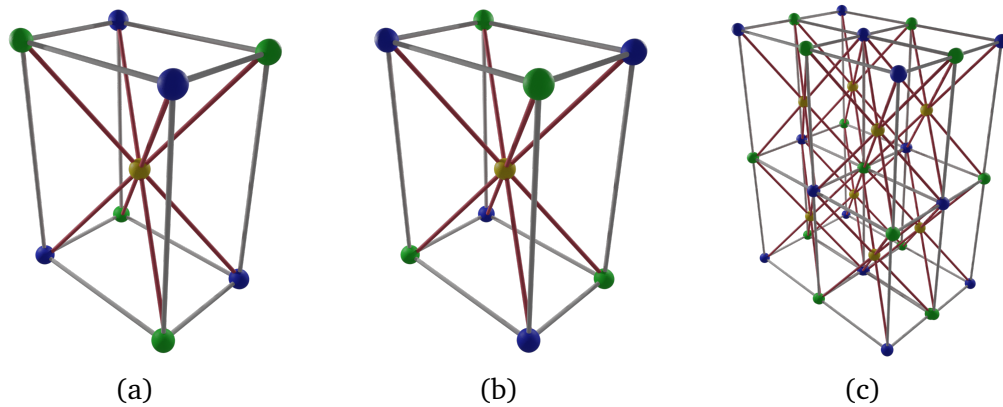


Figure 3.5: Examples of crystal lattices with more complex structure: a unit cell with orthorhombic symmetry (Figure 3.5c) is composed of two orthorhombic unit cells (Figures 3.5a and 3.5b) containing nodes of three types (yellow, blue, and green).

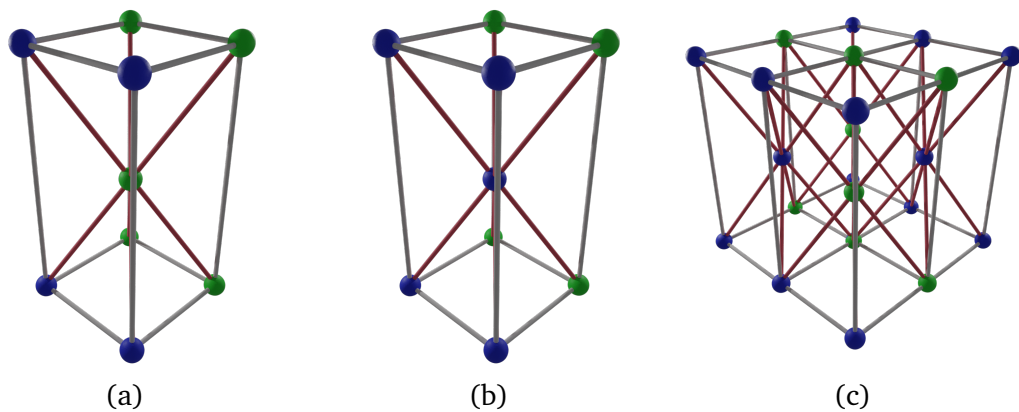


Figure 3.6: Examples of crystal lattices with more complex structure: a unit cell with monoclinic symmetry (Figure 3.6c) is composed of two tetragonal unit cells (Figures 3.6a and 3.6b) containing nodes of two types (blue and green).

There are three main types of nonprimitive Bravais cells: base-centered with two additional point at the center of two opposite faces, body-centered with a point in the center of the cell and face-centered where there is an additional point on each face. In Figure 3.4 all these cell types are demonstrated by the example of the cubic lattice.

Even though there is a big freedom in choice of the basis vectors a , b , c , the number of completely independent lattices is limited after all. The first limitation is symmetry: as it was said before, there are 7 crystal systems. Second, within a given crystal symmetry a nonprimitive cell can be represented through a primitive cell by changing a choice of a , b , c . As a result, it has been shown that there are 14 basic Bravais lattices, that correspond to 7 crystal systems, they are shown in Table 3.3.

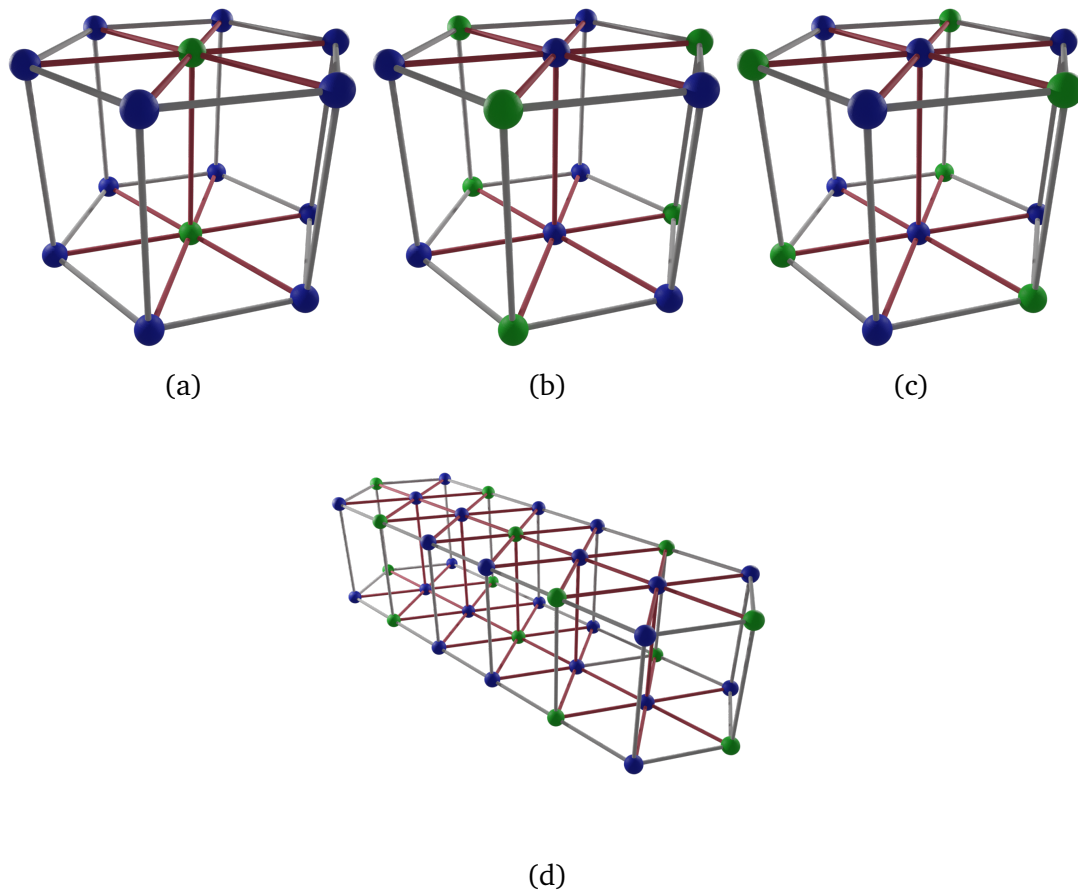


Figure 3.7: Examples of crystal lattices with more complex structure: a unit cell with trigonal symmetry (Figure 3.7d) is composed of three orthorhombic unit cells (Figures 3.7a, 3.7b, and 3.7c) containing nodes of two types (blue and green).

As one can see, although presented Bravais lattices cover all 7 crystal systems, all of them have maximal symmetry of a corresponding system. Therefore, only 7 point groups can be reproduced with them. The solution here is to choose more complex crystal structures, that can be associated with Bravais lattices and, therefore, can be analogously periodically parametrized. For, example, diamond cubic has the symmetry corresponding to $d3m$ point group. Moreover, it is possible to assign nodes of a considered lattice to different types. Similarly to real crystals where the lattice can be composed of molecules of multiple types, here each node type (or each node color) corresponds to different parameters (in this case different star-shaped sets). Thus, assembling the same unit cells but with different nodes type distribution together can yield complex unit cells with internal anisotropy and belonging to various point groups (see Figures 3.5, 3.6, and 3.7).

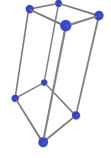
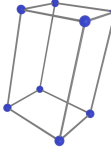
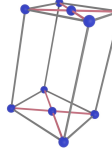
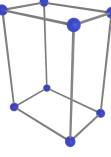
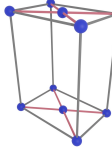
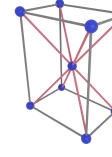
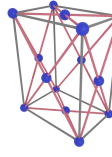
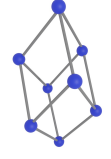
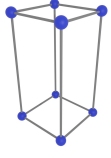
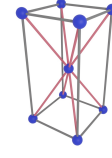
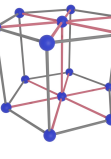
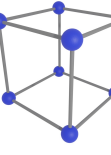
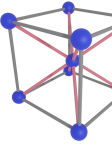
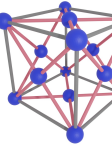
Bravais lattice	Lattice symmetry	Primitive	Base-centered	Body-centered	Face-Centered
Triclinic	$1, \bar{1}$				
Monoclinic	$2m$				
Orthorhombic	mmm				
Trigonal	$\bar{3}m$				
Tetragonal	$4/mmm$				
Hexagonal	$6/mmm$				
Cubic	$m\bar{3}m$				

Table 3.3: Basic Bravais lattices.

3.6 Star-shaped distance

In this work, the growth process leads to the topic of star-shaped distance which plays a crucial role in cells' growth deriving a shape of the pores in the resulting cellular material. As it was mentioned, using growth algorithm with Euclidean distance results in a Voronoi diagram. These materials are well-known and widely used as cellular structures. On the other hand, the resulting structure is defined only through the lattice and the cells are always convex sets. This fact leads to some possible limitations on the achievable material properties.

Distance is a mapping $d : \mathbb{R}^3 \times \mathbb{R}^3 \rightarrow \mathbb{R}^+$ that represents distance from one

point to another in \mathbb{R}^3 and satisfies the identity axiom:

$$\forall p, q \in \mathbb{R}^3 : d_S(p, q) = 0 \Leftrightarrow p = q.$$

Metric is a mapping $d : \mathbb{R}^3 \times \mathbb{R}^3 \rightarrow \mathbb{R}^+$ that satisfies the following axioms of identity, symmetry, and triangle inequality:

$$\begin{aligned} \forall p, q \in \mathbb{R}^3 : d_S(p, q) &= 0 \Leftrightarrow p = q, \\ d_S(p, q) &\geq 0, \\ \forall p, q, n \in \mathbb{R}^3 : d_S(p, q) &\leq d_S(p, n) + d_S(n, q). \end{aligned}$$

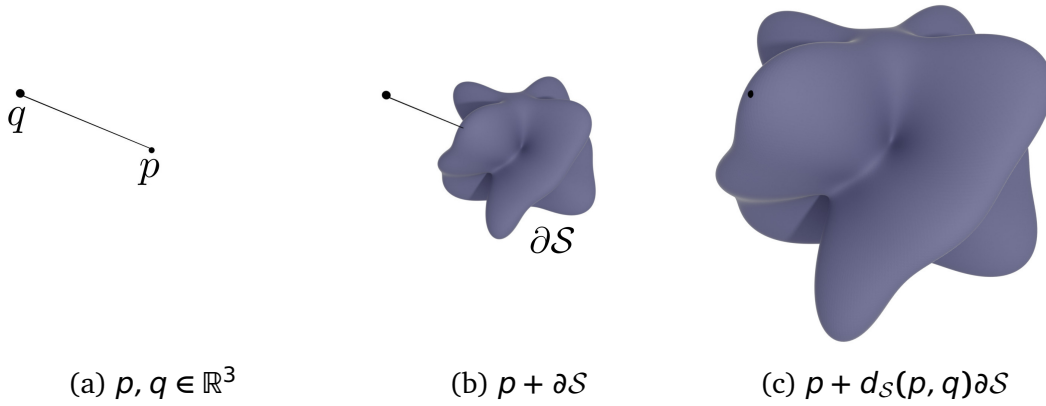


Figure 3.8: Illustration of 3D star-shaped distance. (a) Two points p and q are linked by a line segment. (b) Boundary set ∂S with origin at p . (c) Scaling of ∂S by a factor of $d_S(p, q)$ such that it touches q . In that particular case $d_S(p, q) = 2$.

To start the topic of the distance parametrization it is necessary to associate it with with a corresponding compact set in 3D space. To do so one can take a ball $B(x_0, 1)$ of unit radius centered at a given point x_0 and consider a mapping:

$$\zeta : B \rightarrow \mathcal{B}$$

of this ball into a compact set \mathcal{B} . The mapping ζ is derived in a form of a vector function:

$$\zeta(x_0, x) = \frac{d(x - x_0)}{\|x - x_0\|} x, \quad x \in B.$$

For Euclidean distance this mapping is the same ball, in other words it is the identity transform. We say, that a distance is convex/nonconvex if the corresponding resulting object \mathcal{B} is convex/nonconvex. Thus if \mathcal{B} for a distance d is star-shaped, then d is also called star-shaped.

A compact set S is called star-shaped with a point of origin O if for any point x of this set S also contains the cut Ox . Thus, a ray starting from the

origin intersects with the boundary ∂S only once. This allows one to consider a local spherical coordinate system centered at O and parametrize the boundary ∂S of the star-shaped set S as a radius star-shaped function $f_S(\varphi, \theta)$ of the polar φ and azimuthal θ angles:

$$0 < r_{min} \leq (f_S(\varphi, \theta) = r) \leq r_{max} < \infty. \quad (3.2)$$

Finally, the star-shaped distance $d_S(p, q)$ can be derived as a fraction of Euclidean distance and the star-shaped function:

$$d_S(p, q) = \frac{\|\vec{pq}\|}{f_S(\varphi_{pq}, \theta_{pq})}. \quad (3.3)$$

As $f_S(\varphi, \theta)$ is bounded and always positive (does not reach a zero value), the distance $d_S(p, q)$ is always bounded and single-valued. The star-shaped distance satisfies the following axioms:

$$\forall p, q \in \mathbb{R}^3 : d_S(p, q) = 0 \Leftrightarrow p = q, \quad (3.4)$$

$$d_S(p, q) \geq 0, \quad (3.5)$$

$$d_S(\alpha p, \alpha q) = \alpha d_S(p, q) \quad \alpha \geq 0. \quad (3.6)$$

In contrary to Euclidean distance or any other metric the star-shaped distance do not follow the triangle inequality, but it satisfies a weaker form.

Lemma. Let $d_S(p, q)$ be a parametrized star-shaped distance. Then for $\forall p, q, n \in \mathbb{R}^3$ the following (q_1, q_2) -triangle inequality holds:

$$d_S(p, q) \leq q_1 d_S(p, n) + q_2 d_S(n, q) \quad (3.7)$$

Proof. Using the definition of star-shaped distance in eq. 3.3 the given inequality can be written as follows:

$$\frac{\|q - p\|}{f_S(\varphi_{pq}, \theta_{pq})} \leq q_1 \frac{\|n - p\|}{f_S(\varphi_{pn}, \theta_{pn})} + q_2 \frac{\|q - n\|}{f_S(\varphi_{nq}, \theta_{nq})}. \quad (3.8)$$

Therefore, the coefficients q_1, q_2 are bounded by the values:

$$q_1 = \max_{p, n, q \in X} \frac{f_S(\varphi_{pn}, \theta_{pn})}{f_S(\varphi_{pq}, \theta_{pq})} = \max_{p, n, q \in X} \frac{f_S(\varphi_{nq}, \theta_{nq})}{f_S(\varphi_{pq}, \theta_{pq})} = q_2. \quad (3.9)$$

Taking into account the bounds imposed on the star-shaped function the coefficients will be defined as

$$q_1 = q_2 = \frac{r_{max}}{r_{min}}. \quad (3.10)$$

This implies that the inequality 3.7 is true for the values from the the Equation 3.10:

$$d_S(p, q) \leq \frac{r_{max}}{r_{min}} (d_S(p, n) + d_S(n, q)) \quad (3.11)$$

End of proof.

In summary the star-shaped distance is a (q_1, q_2) -quasimetric. It is also important to point out that in general it is not symmetric. That is, the distance $d_S(p, q)$ is not necessarily equal to $d_S(q, p)$.

Distance parametrization. Now the question of defining the parametrized star-shaped function $f_S(\varphi, \theta)$ will be discussed. In this work two ways of parametrization of a star-shaped set have been chosen: explicit and implicit. The explicit parametrization means defining $f_S(\varphi, \theta)$ directly through an analytical expression. The implicit approach costs the parametrization of the star-shaped function through implicit surfaces.

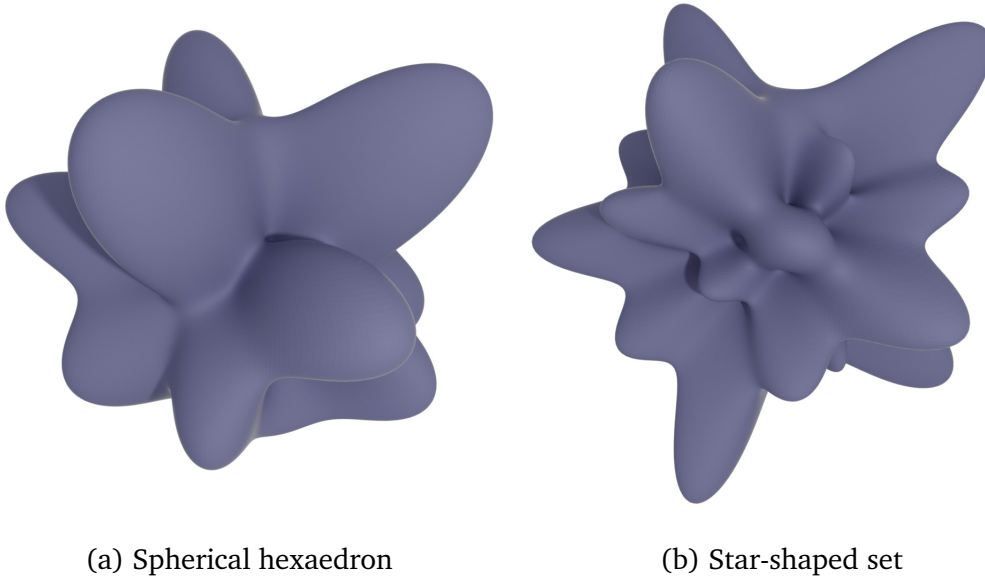


Figure 3.9: Examples of star-shaped sets obtained with the explicit parametrization.

The explicit parametrization in our work was implemented through spherical harmonics as functions to model the star-shaped boundary since they represent a full infinite orthonormal basis, are defined in spherical coordinates as radius functions of angles, and can be easily associated with rotational symmetry. There is a number of works showing a high potential and efficiency in reproducing any closed shape with a linear combination of spherical harmonics ([191], [244], [196]).

We define the parametrized star-shaped function as

$$f_S(\varphi, \theta) = \sum_i y_{li}^{m_i}(\varphi, \theta), \quad (3.12)$$

where

$$\mathcal{Y}_l^{m_i}(\varphi, \theta) = (-1)^{m_i} \sqrt{\frac{(2l_i + 1)! (l_i - m_i)!}{4\pi (l_i + m_i)!}} P_{l_i, m_i}(\cos \theta) \exp^{im_i\varphi} \quad (3.13)$$

is the spherical harmonics of given degree l_i and order m_i with $P_{l_i, m_i}(\cos \theta)$ as an associated Legendre polynomial. Note that it is always true that $|m_i| \leq l_i$.

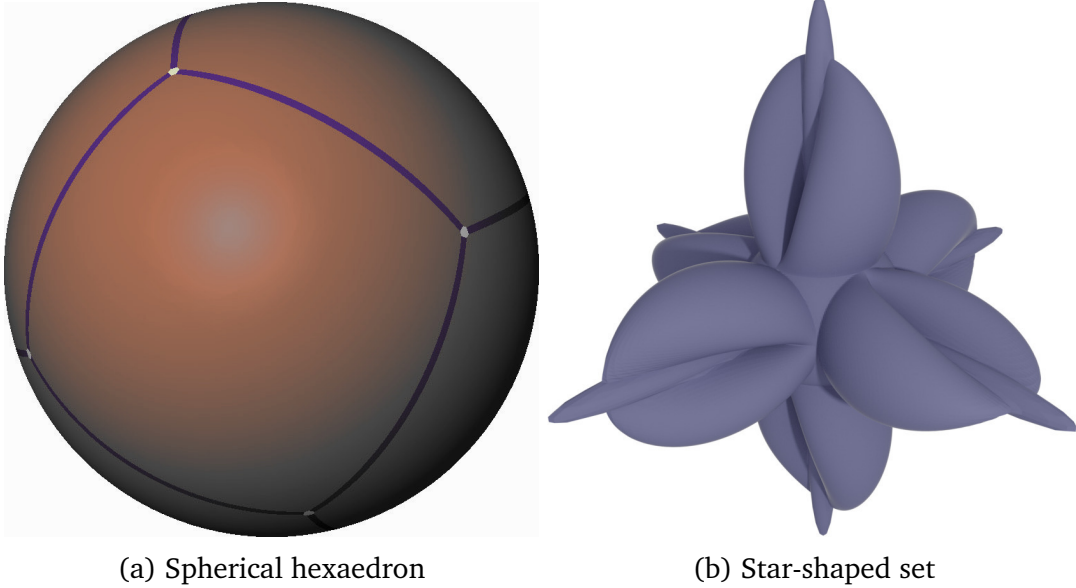


Figure 3.10: Parameterization with spherical polyhedra. (a) is regular spherical polyhedron, that has six identical faces and (b) is the corresponding star-shaped set with six identical spikes, each corresponding to a face of the spherical polyhedron.

The implicit parametrization was derived through polyhedral shapes as they are highly symmetric and consist of one or several types of identical faces of polygonal shape. Here we chose regular and quasiregular polyhedra as they are the most known and representative examples. Regular polyhedra consist of all identical regular polygonal faces and quasiregular polyhedra are represented by two types of faces which have also regular polygonal shapes. The difference between the identical faces is their position in the space.

If one projects a polyhedron on a sphere centered at the same point \vec{O} the resulting object is called a spherical polyhedron (Figure 3.11). In this case, in a spherical system of coordinates which is also centered at \vec{O} each face can be defined through its center point \vec{O}_F . Thus, for a given point \vec{x} on the spherical polyhedron one can identify a face which contains \vec{x} by finding the closest \vec{O}_F to this point. Then, the corresponding face can be parametrized in a local curvilinear coordinate system (ϱ, ω) centered at \vec{O}_F . Here, $\varrho(\varphi, \theta)$ represents a radius vector $\vec{x} - \vec{O}_F$ and $\omega(\varphi, \theta)$ is an angle corresponding to a chosen

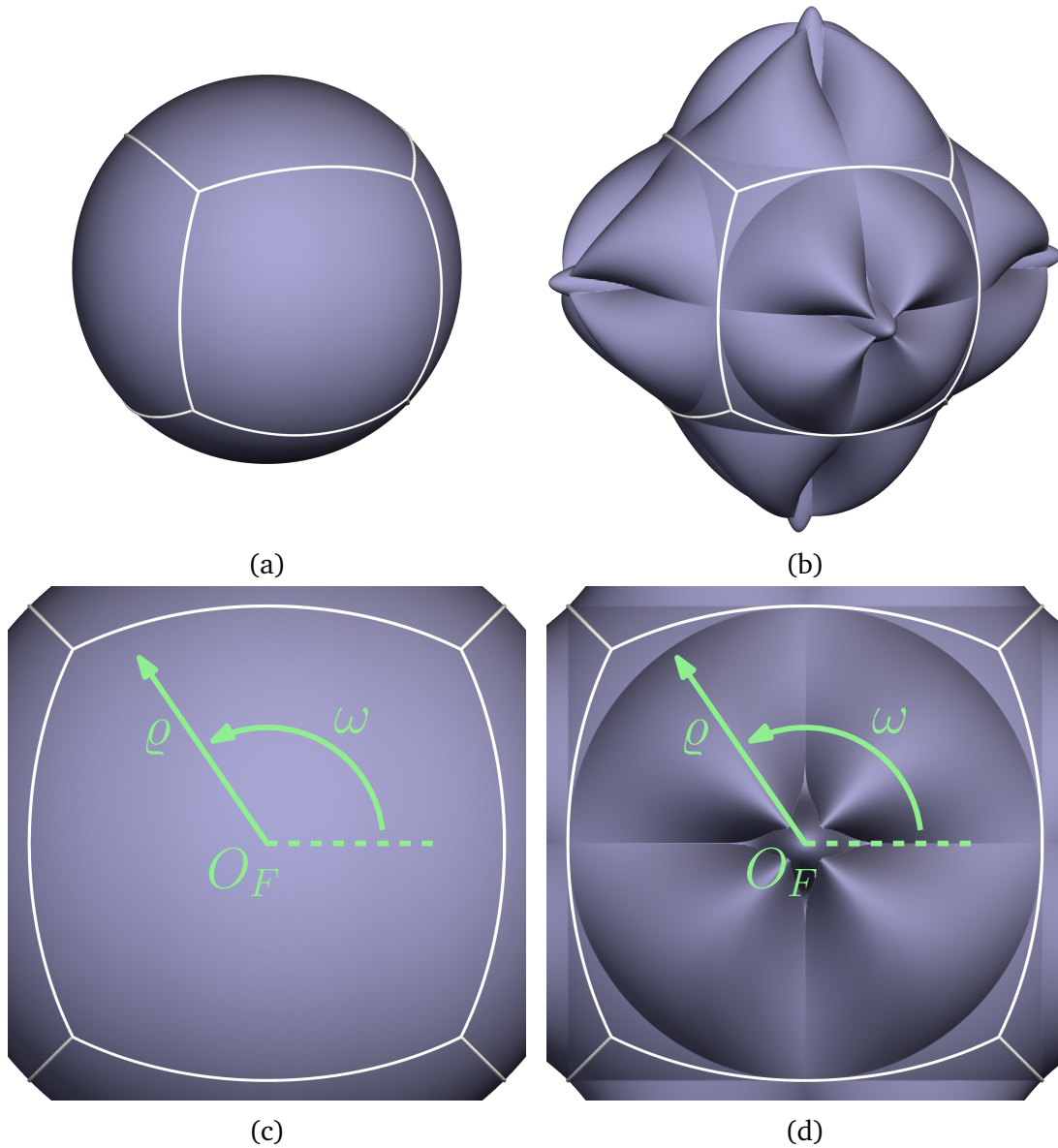


Figure 3.11: An example of the implicit parametrization. A parametrized star-shaped set (3.11b) is obtained from a corresponding spherical polyhedron: for a given point on the spherical hexahedron (3.11a) a closest face center \vec{O}_F is found, then the coordinates of the point are calculated in the local coordinate system (ρ, ω) centered at \vec{O}_F (3.11c). Finally, the face's profile (3.11d) is calculated in the local coordinates using a chosen parametrization (here four-fold rotation symmetry is imposed).

direction of the local coordinate system. Hence, the coordinates of \vec{x} can be defined as (ρ_x, ω_x) . As for regular polyhedra all the faces are identical, one needs just a single-valued function $f(\rho, \omega_x)$ which defines a profile of the faces and, thus, a shape of the parametrized set. There are only two requirements for the function $f(\rho, \omega)$: continuity and periodicity ($f(\rho, 0) = f(\rho, 2\pi)$). In case of semi-regular polyhedra, there are two different types of faces and,

thus, two profile functions $f_1(\varrho, \omega)$ and $f_2(\varrho, \omega)$ are required. In this work the following expression for the face's profile function was used:

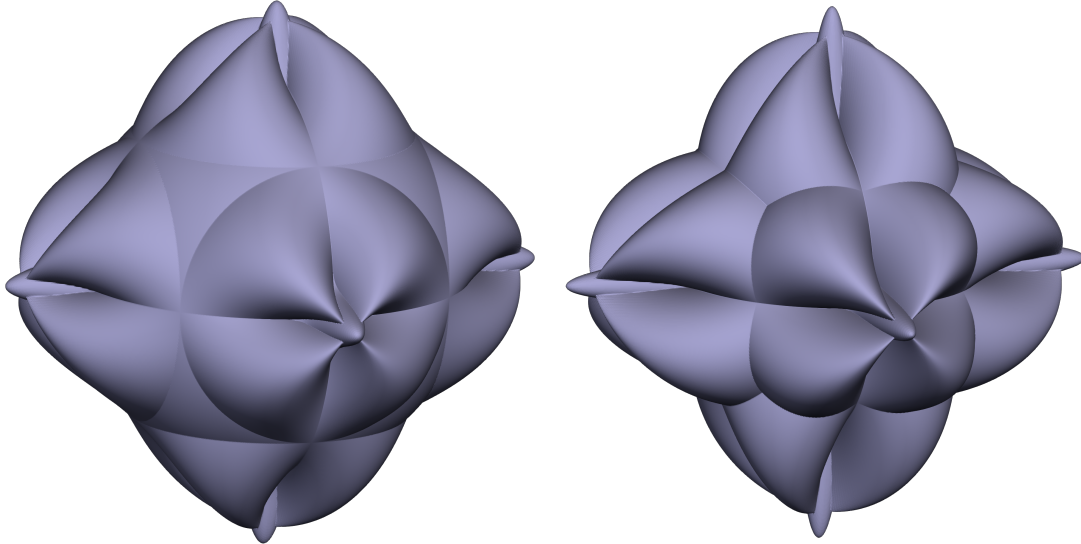
$$f(\vec{x}) = \begin{cases} 1 + C_m \max \left\{ 1.3e^{-\frac{\omega^2}{d_m}}, \left| \cos\left(\frac{\pi\varrho}{2\varrho_m}\right) \cos(\gamma_m\omega) \right| \right\} & \text{if } \varrho \leq \varrho_m, \\ 1 & \text{else.} \end{cases}$$

$$\varrho(\vec{x}_*) = \arctan \frac{\sqrt{x_*^2 + y_*^2}}{z_*}, \quad \omega(\vec{x}_*) = \arctan \frac{y_*}{x_*}, \quad \vec{x}_* = (x_*, y_*, z_*)$$

$$\vec{x}_*(\vec{x}, \vec{O}_F) = M_z(-\varphi_d) M_y(\theta_F) M_z(\varphi_F) \vec{x}, \quad \vec{O}_F = (1, \varphi_F, \theta_F).$$

Here $M_y(\alpha)$, $M_z(\alpha)$ denote rotation matrices by an angle α around y and z axes respectively. The final rotation angle φ_d is defined for each polyhedron face separately in order to choose orientation of the faces and, thus, to achieve desired symmetry of an obtained star-shaped set. A space position of the center of a face center $\vec{O}_F = (1, \varphi_F, \theta_F)$ is written in spherical coordinates.

Note. In order to avoid shape distortions connected to a change of the azimuth angle, the rotated point $\vec{x}_*(\vec{x}, \vec{O}_F)$ is obtained in Euclidean coordinate system.



(a) $C_m = 0.3$, $d_m = 0.01$, $\varrho_m = \frac{\pi}{4}$, $\gamma_m = 2$ (b) $C_m = 0.6$, $d_m = 0.01$, $\varrho_m = \arctan \sqrt{2}$, $\gamma_m = 2$

Figure 3.12: Two star-shaped sets obtained with the same implicit parametrization but different scaling parameters.

3.7 Materials with prescribed elastic tensor

In this work, a periodic homogenization of the cellular geometry is performed, theoretically assuming that the cellular structure's size is infinite and that all identical periodic cells deform in the same way (see Figure 4.1). This is a commonly made assumption to homogenize the elastic behavior of cellular structures. Here only linear elasticity (infinitesimal strains) is considered to give a numerical understanding of the elastic symmetries. In that case, the stress tensor σ is linearly proportional to the strain ϵ with respect to the elasticity tensor C (fourth-order symmetric tensor)

$$\sigma(\bar{\mathbf{x}}) = C(\bar{\mathbf{x}}) : \epsilon(\bar{\mathbf{x}}). \quad (3.14)$$

Periodic homogenization seeks to determine the homogenized elasticity tensor C of a periodic structure. All the homogenized elasticity tensors shown in this article follow the *Voigt* notation [221]

$$\begin{pmatrix} \sigma_{11} \\ \sigma_{22} \\ \sigma_{33} \\ \sigma_{23} \\ \sigma_{13} \\ \sigma_{12} \end{pmatrix} = \begin{pmatrix} C_{11} & C_{12} & C_{13} & C_{14} & C_{15} & C_{16} \\ & C_{22} & C_{23} & C_{24} & C_{25} & C_{26} \\ & & C_{33} & C_{34} & C_{35} & C_{36} \\ & & & C_{44} & C_{45} & C_{46} \\ & & & & C_{55} & C_{56} \\ & & & & & C_{66} \end{pmatrix} \begin{pmatrix} \epsilon_{11} \\ \epsilon_{22} \\ \epsilon_{33} \\ 2\epsilon_{23} \\ 2\epsilon_{13} \\ 2\epsilon_{12} \end{pmatrix}. \quad (3.15)$$

For more details on the homogenization methods used in this thesis, please, refer to Chapter 4.

The material's geometric symmetry constraints the symmetry of its elasticity tensor. In other words, it prescribes the type of (effective macroscopic) mechanical response of the structure. Thus, through imposing symmetry constraints on the designed material one can achieve a specific class of anisotropy or isotropy. This feature could be useful in various applications where there is need to obtain a range of materials with different microscopic behavior but within the same class of elasticity tensors. In particular, there are 8 material types based on the amount of invariant transformations allowed by the elasticity tensor:

- **Triclinic:** no particular symmetry (point group – $\mathbf{1}$ or $\bar{\mathbf{1}}$). These solids are completely anisotropic. The elasticity tensor has 21 independent components:

$$\begin{pmatrix} C_{11} & C_{12} & C_{13} & C_{14} & C_{15} & C_{16} \\ & C_{22} & C_{23} & C_{24} & C_{25} & C_{26} \\ & & C_{33} & C_{34} & C_{35} & C_{36} \\ & & & C_{44} & C_{45} & C_{46} \\ & & & & C_{55} & C_{56} \\ & & & & & C_{66} \end{pmatrix}$$

- **Monoclinic:** one plane of reflectional or one axis two-fold symmetry. The elasticity tensor has 13 independent components:

$$\begin{pmatrix} C_{11} & C_{12} & C_{13} & 0 & C_{15} & 0 \\ & C_{22} & C_{23} & 0 & C_{25} & 0 \\ & & C_{33} & 0 & C_{35} & 0 \\ & & & C_{44} & 0 & C_{46} \\ & & & & C_{55} & 0 \\ & & & & & C_{66} \end{pmatrix}$$

- **Orthorhombic** (or rhombic, orthotropic): three perpendicular planes of reflectional symmetry. The elasticity tensor has 9 independent components:

$$\begin{pmatrix} C_{11} & C_{12} & C_{13} & 0 & 0 & 0 \\ & C_{22} & C_{23} & 0 & 0 & 0 \\ & & C_{33} & 0 & 0 & 0 \\ & & & C_{44} & 0 & 0 \\ & & & & C_{55} & 0 \\ & & & & & C_{66} \end{pmatrix}$$

- **Trigonal**: one axis of three-fold symmetry with a perpendicular reflectional plane. The elasticity tensor has 6 independent components.

$$\begin{pmatrix} C_{11} & C_{12} & C_{13} & C_{14} & 0 & 0 \\ & C_{11} & C_{13} & -C_{14} & 0 & 0 \\ & & C_{33} & 0 & 0 & 0 \\ & & & C_{44} & 0 & 0 \\ & & & & C_{44} & C_{14} \\ & & & & & (C_{11} - C_{12})/2 \end{pmatrix}$$

- **tetragonal**: one axis of four-fold symmetry with three perpendicular reflectional planes. The elasticity tensor has 6 independent components:

$$\begin{pmatrix} C_{11} & C_{12} & C_{13} & 0 & 0 & 0 \\ & C_{11} & C_{13} & 0 & 0 & 0 \\ & & C_{33} & 0 & 0 & 0 \\ & & & C_{44} & 0 & 0 \\ & & & & C_{44} & 0 \\ & & & & & C_{66} \end{pmatrix}$$

- **Hexagonal** (or transversely isotropic): one axis of 6-fold rotational symmetry with three perpendicular reflectional planes. The elasticity tensor has 5 independent components:

$$\begin{pmatrix} C_{11} & C_{12} & C_{13} & 0 & 0 & 0 \\ & C_{11} & C_{13} & 0 & 0 & 0 \\ & & C_{33} & 0 & 0 & 0 \\ & & & C_{44} & 0 & 0 \\ & & & & C_{44} & 0 \\ & & & & & (C_{11} - C_{12})/2 \end{pmatrix}$$

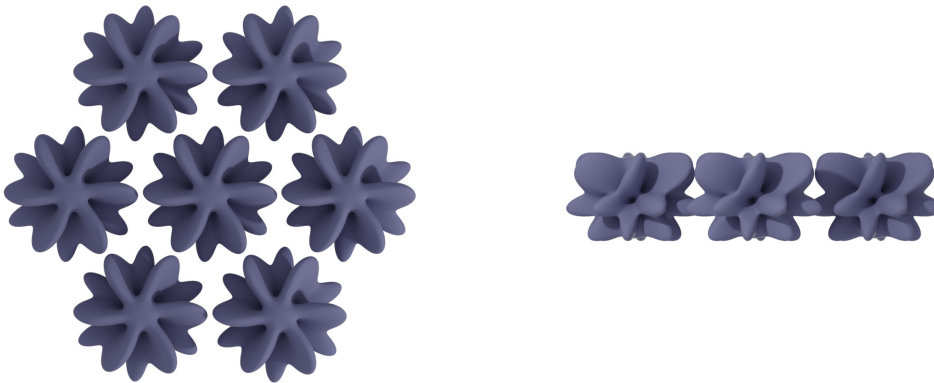
- **Cubic:** nine planes of elastic symmetry. Three of these nine planes are perpendicular to the coordinate axes, the other six have normals producing $\frac{\pi}{4}$ -angle with the latter. The elasticity tensor has 3 independent components:

$$\begin{pmatrix} C_{11} & C_{12} & C_{12} & 0 & 0 & 0 \\ & C_{11} & C_{12} & 0 & 0 & 0 \\ & & C_{11} & 0 & 0 & 0 \\ & & & C_{33} & 0 & 0 \\ & & & & C_{33} & 0 \\ & & & & & C_{33} \end{pmatrix}$$

- **Isotropic** structures have any plane as a plane of symmetry. The elasticity tensor has 2 independent components:

$$\begin{pmatrix} C_{11} & C_{12} & C_{12} & 0 & 0 & 0 \\ & C_{11} & C_{12} & 0 & 0 & 0 \\ & & C_{11} & 0 & 0 & 0 \\ & & & \frac{C_{11}-C_{12}}{2} & 0 & 0 \\ & & & & \frac{C_{11}-C_{12}}{2} & 0 \\ & & & & & \frac{C_{11}-C_{12}}{2} \end{pmatrix}$$

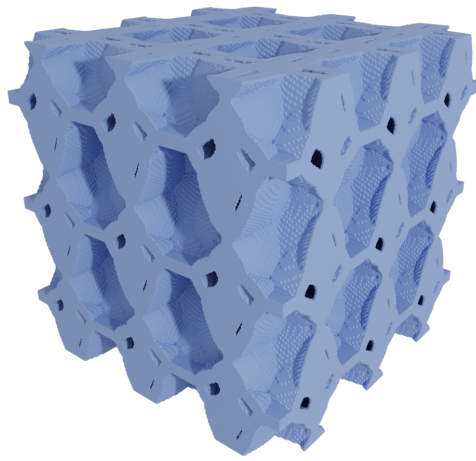
3.7.1 Symmetry: distance, lattice, and resulting structure



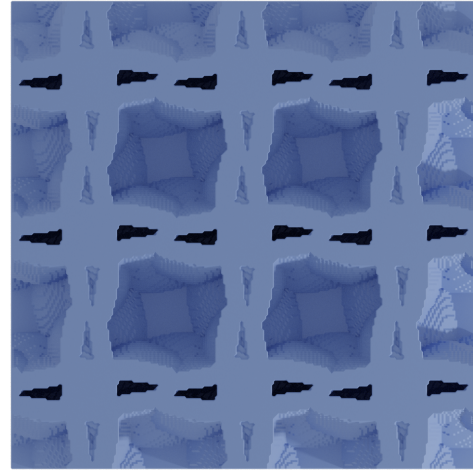
(a) Top view

(b) Lateral view

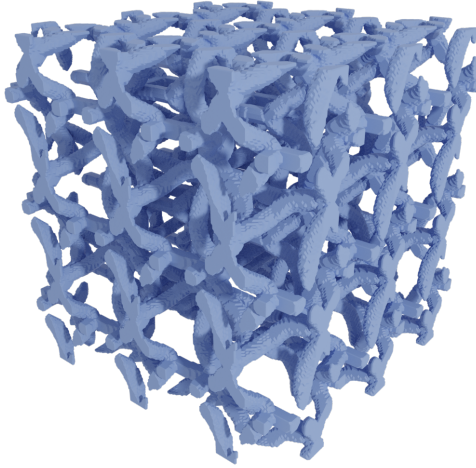
Figure 3.13: Some star-shaped sets are centered in a lattice, both sharing a hexagonal symmetry ($6/mmm$ (D_{6h}) for the lattice and 6 (C_6) for the distance). Here we can visually appreciate how a rotation of angle factor of $\frac{\pi}{6}$ around the origin of any star-shaped set keeps the periodic arrangement invariant (i.e., it leads to a 6 (C_6) point group).



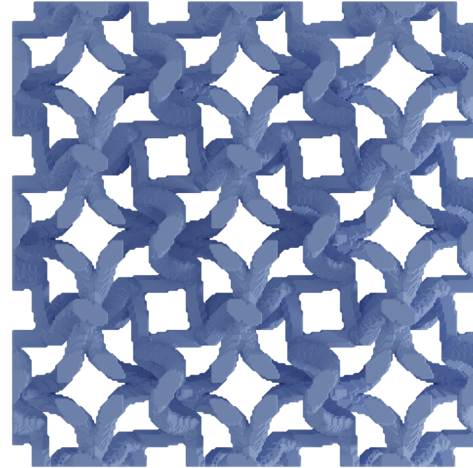
(a) Closed cell structure (general view).



(b) Closed cell structure (up view).



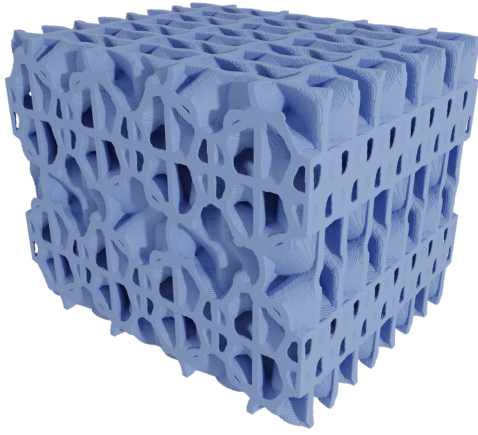
(c) Open cell structure (general view).



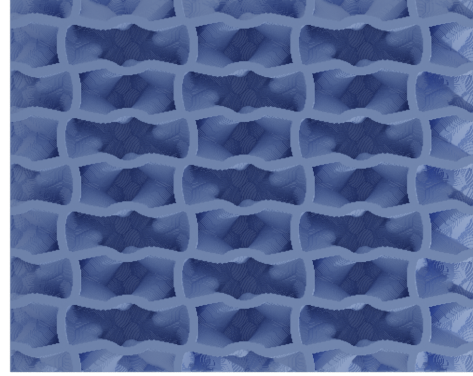
(d) Open cell structure (up view).

Figure 3.14: Example of closed and open cell structures corresponding to BCC crystal lattice in Figure 3.4b with a different type of a central nucleus with $\bar{4}$ symmetry.

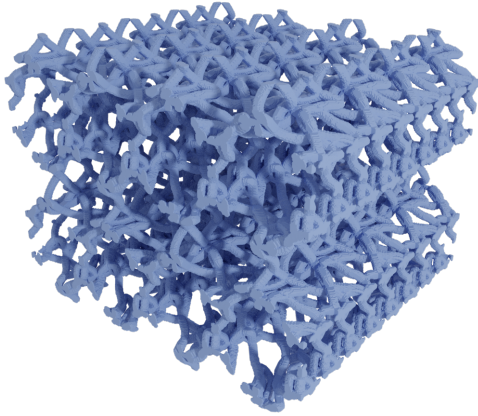
As we already defined the parametrized star-shaped distance, periodic crystal lattice, and the discrete growth method, it is possible to analyze the impact of combination star-shaped set S and lattice L on symmetry of the designed material in terms of point groups. Let us define point groups corresponding to the star-shaped set and the lattice as \mathcal{T}_S and \mathcal{T}_L respectively. It is important to point out that the point group of S is considered with respect to its central point O . The set is parametrized with respect to this point and the corresponding star-shaped distance is computed from this point. In addition, all point groups form a subgroup of an orthogonal group $O(n)$, therefore they contain only linear transformations. Let us define $\mathcal{T}_{L \cap S} = \mathcal{T}_L \cap \mathcal{T}_S$ – a subgroup of transformations (which is also a point group) shared by \mathcal{T}_S and \mathcal{T}_L .



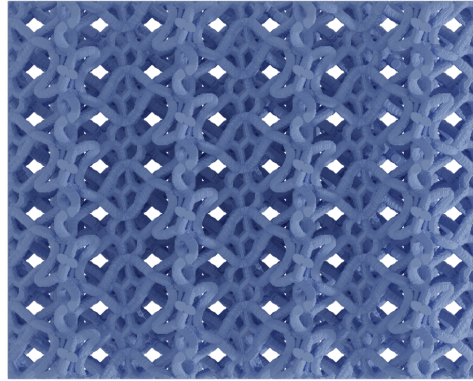
(a) Closed cell structure (general view).



(b) Closed cell structure (up view).



(c) Open cell structure (general view).



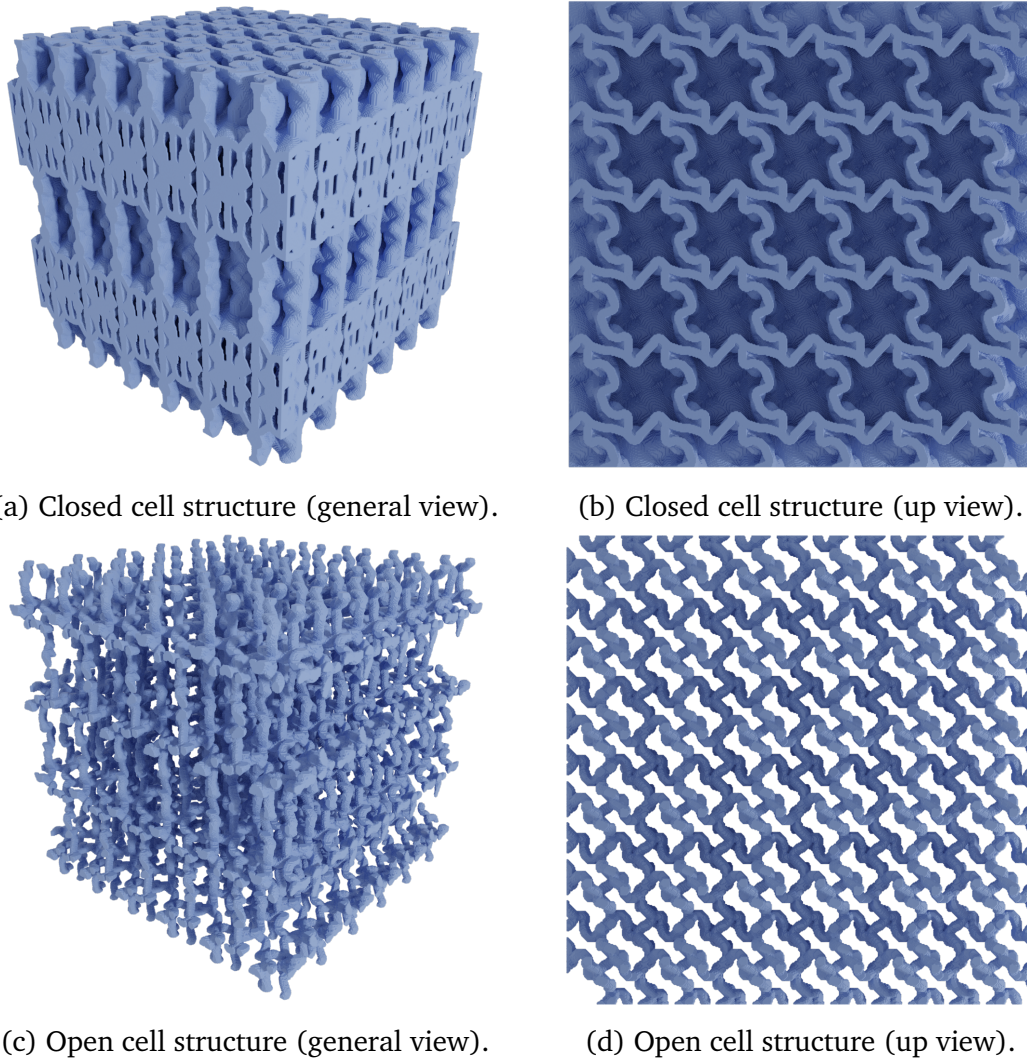
(d) Open cell structure (up view).

Figure 3.15: Example of closed and open cell structures corresponding to the complex crystal lattice in Figure 3.5 with 222 symmetry.

By the definition of \mathcal{T}_L and \mathcal{T}_S , it is true that $\forall g \in \mathcal{T}_{L\cap S} : g(S) = S$ and $g(L) = L$. Therefore, for any lattice point $p \in L$ and transformation $g \in \mathcal{T}_{L\cap S}$ there is a point $n \in L$ such that:

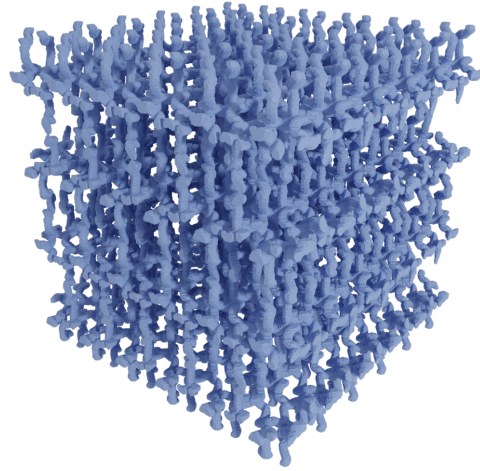
$$g(p + S) = g(p) + g(S) = n + S. \quad (3.16)$$

Equation 3.16 demonstrates that the discrete growth process presented in this work is invariant to any mapping from the point group $\mathcal{T}_{L\cap S}$ (see Figure 3.13) up to the voxelization of the computational domain G . This means that in order to compute an cellular structure which approximately prescribed symmetry \mathcal{T} it is sufficient to ensure that both the lattice L and the star-shaped set S share \mathcal{T} . As a visual demonstration of this result, closed and open cell structures obtained with the growth method are presented on Figures 3.14, 3.15, and 3.16: correct combination symmetries of star-shaped set(s) and a crystal lattice yields desired symmetry of a resulting structure.

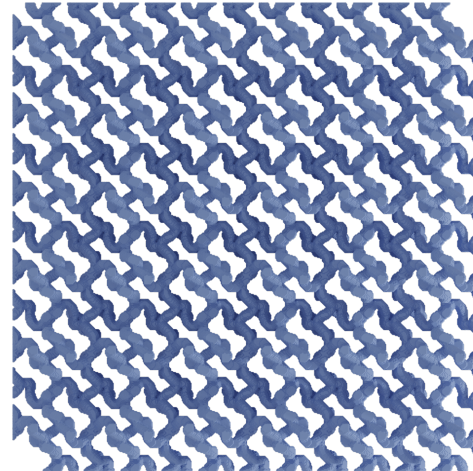


(a) Closed cell structure (general view).

(b) Closed cell structure (up view).



(c) Open cell structure (general view).



(d) Open cell structure (up view).

Figure 3.16: Example of closed and open cell structures corresponding to the complex crystal lattice in Figure 3.6 with $\frac{2}{m}$ symmetry.

3.7.2 Growth instabilities

The growth algorithm presented in this thesis is derived in discrete formulation as a process of cells growth through subsequent occupation of the closest neighboring voxels. Unfortunately, there is no continuous analog of the mathematical model for this problem yet. Nevertheless, the discrete growth method works very reliably with all the convex and most of star-shaped distances and lattices. However, in some particular cases growth instabilities may occur. These instabilities are reflected in degeneration of the microstructure's geometry. These undesired effects may appear at some specific areas of the boundaries between the cells where the star-shaped distance from both origins of neighboring cells is equal. Indeed, given two points $p, q \in L$ of the lattice (cells' origins) one can describe the bisector points $x_b \in \mathbb{R}^3$ as follows:

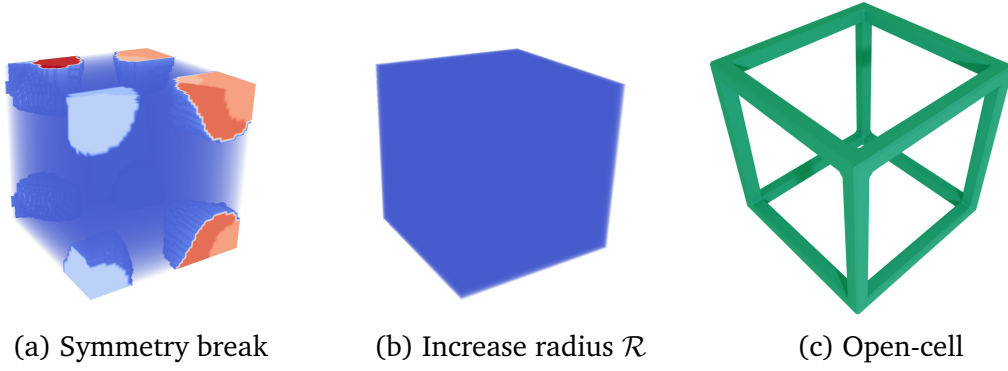


Figure 3.17: A simple example of growth instabilities. In this case, the periodic lattice L is a single point in the cube center. The star-shaped distance has orthorhombic-dipyramidal symmetries (3 orthogonal reflection planes). (a) Due to the discrete size of G , we obtain a result with symmetry-breaking artifacts (red regions). (b) Increasing the radius helps to overcome these events, obtaining the expected periodic open-cell (c).

$$\frac{\|\rho - x_b\|}{\|q - x_b\|} = \frac{f_S(\varphi_{\rho x_b}, \theta_{\rho x_b})}{f_S(\varphi_{q x_b}, \theta_{q x_b})}. \quad (3.17)$$

In addition, let us define a functional which for a point $x \in \mathbb{R}^3$ represents the balance between the distance from ρ to x and from q to x :

$$\mathfrak{B}(x, \rho, q) = \frac{\|\rho - x\|}{f_S(\varphi_{\rho x}, \theta_{\rho x})} - \frac{\|q - x\|}{f_S(\varphi_{q x}, \theta_{q x})}. \quad (3.18)$$

The bisector points x_b from Equation 3.17 may be significantly changed even by small perturbations on the points ρ and q , especially when the star-shaped function f_S varies rapidly. Moreover, the degenerative cases seem to appear when the bisectors' positions coincide with the centers of the voxels. In this case, during the growth process neighbor cells meet at some point and start expanding along the surface of x_b . Due to the fact that one deals not with convex but rather star-shaped function f_S , the balance function reaches zero value at the bisector points $\mathfrak{B}(x_b, \rho, q) = 0$ but does not necessarily change the sign when it crosses the surface x_b . In other words, once we cross the bisector the origin of one cell is still closer than another. In this occasion, the growth method is very sensitive to the numerical perturbations of the distance computation and it is not trivial to determine to which cell it is better to assign the "problematic" voxel in order to avoid the intrusion of a neighboring cell.

However, it was shown in [138], that increasing the resolution of the grid G or increasing the value of \mathcal{R} (see Figure 3.17b) lessens these occurrences and thus helps to resolve the problem of breaking the expected symmetry. In addition, a regular voxel grid also does not hold all sorts of rotational and reflectional symmetries which may result in slight distortion of the structure's symmetry. We have observed that in general increasing the grid resolution or

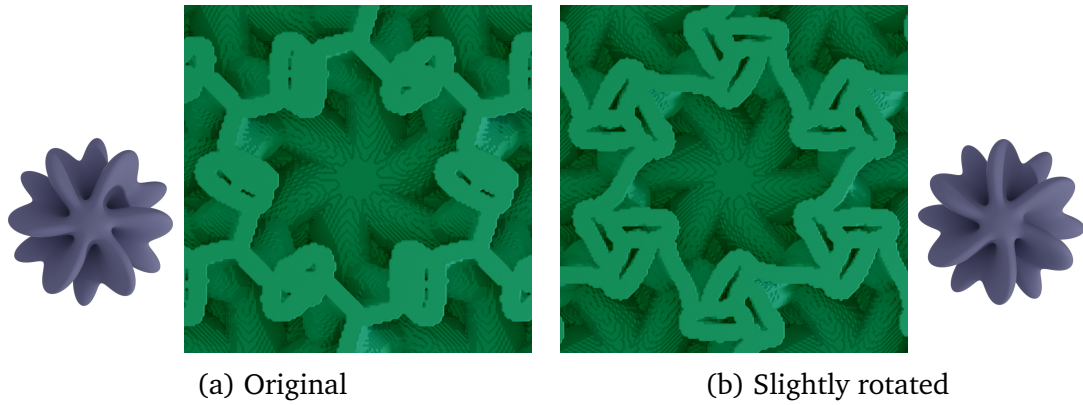


Figure 3.18: An example of slight rotational symmetry-breaking event. (a) A hexagonal distance leads to a closed-cell structure with a slight deviation from the expected 6-fold symmetry. (b) A slight rotation of the distance leads to a structure with better 6-fold symmetry.

slightly rotating the distance helps to diminish this problem (see Figure 3.18). The best recipe for dealing with the symmetry-breaking problems related to the voxelization would be to use a computational grid and domain with the same symmetry as the prescribed symmetry of the designed material.

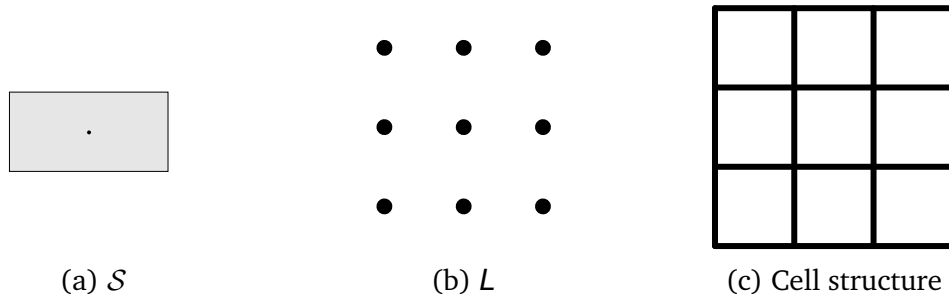


Figure 3.19: Illustrative coincident case in two-dimensions. The star-shaped set S has two reflectional planes. The lattice has four-fold symmetry. The resulting cellular structure has four-fold symmetry.

Thus, our method provides an opportunity to control the symmetry of the structure and thus the type of its effective elastic tensor. Unfortunately, it is currently impossible to strictly impose isotropic behavior as the necessary and sufficient criteria for isotropy in 3D case have not been found yet. In addition, the distance parametrization provides an enormous choice of different shapes which along with a wide range of crystal lattices spawn a great number of microstructures within a given elasticity class.

In Tables B.1 and B.2 galleries of some closed- and open-cell materials computed with the growth algorithm are presented. These examples show that the resulting structure’s symmetry coincides with the shared symmetry of the distance and the lattice and the effective elasticity tensor class corresponds to the symmetry of the material.

3.8 Materials with spatial grading

The main feature of the growth method presented in this thesis is an ability of effective generation of functionally graded materials. Indeed, the implicit parametrization offered here yields the implicit gradation between cells with different microstructure's geometry. Moreover, the growth method, unlike many others, does not require any additional technique to ensure proper transition from one type of cell to another while covering wide space of material's symmetries. We propose two approaches of spatial gradation: through varying a star-shaped set or through combining different periodic lattices.

3.8.1 Interpolation between star-shaped distances

First, let us define star-shaped sets $\{\mathcal{S}_i\}_{i=1}^N$ with points of origin which all coincide and are located at a point O and a set of corresponding functions $\{f_{\mathcal{S}_i}(\mathbf{x}, \mathbf{y})\}_{i=1}^N$ which define parametrised boundaries of these sets. In this thesis, the linear interpolation between the star-shaped boundaries was chosen to calculate star-shaped distance at a given point. Thus, the interpolated star-shaped boundary $f_{\mathcal{S}_\Sigma}(\mathbf{x}, \mathbf{y})$ and the corresponding spatially graded star-shaped distance $d_{\mathcal{S}_\Sigma}(\mathbf{x}, \mathbf{y})$ can be defined through the following expression:

$$f_{\mathcal{S}_\Sigma}(\mathbf{x}, \mathbf{y}) = \sum_{i=1}^N \alpha_i f_{\mathcal{S}_i}(\mathbf{x}, \mathbf{y}), \quad d_{\mathcal{S}_\Sigma}(\mathbf{x}, \mathbf{y}) = \frac{\|\mathbf{y} - \mathbf{x}\|}{f_{\mathcal{S}_\Sigma}(\mathbf{x}, \mathbf{y})}, \quad (3.19)$$

where the coefficients $\{\alpha_i\}_{i=1}^n$, depending on a type of a chosen parametrization, can be either discrete binary variables (for hard spatial grading) or continuous functions (for smooth structural transitions) and obey the following constraints:

$$0 \leq \alpha_i \leq 1, \quad \sum_{i=1}^N \alpha_i = 1. \quad (3.20)$$

Following the concept of this work, an important question to discuss here is if it is possible to preserve desired symmetry for functionally graded materials obtained with a distance function for an interpolated star-shaped set shown in Equation 3.19. Here we provide a formal proof that the symmetry of the resulting structure can be derived through the symmetries of the star-shaped sets involved in the considered interpolation.

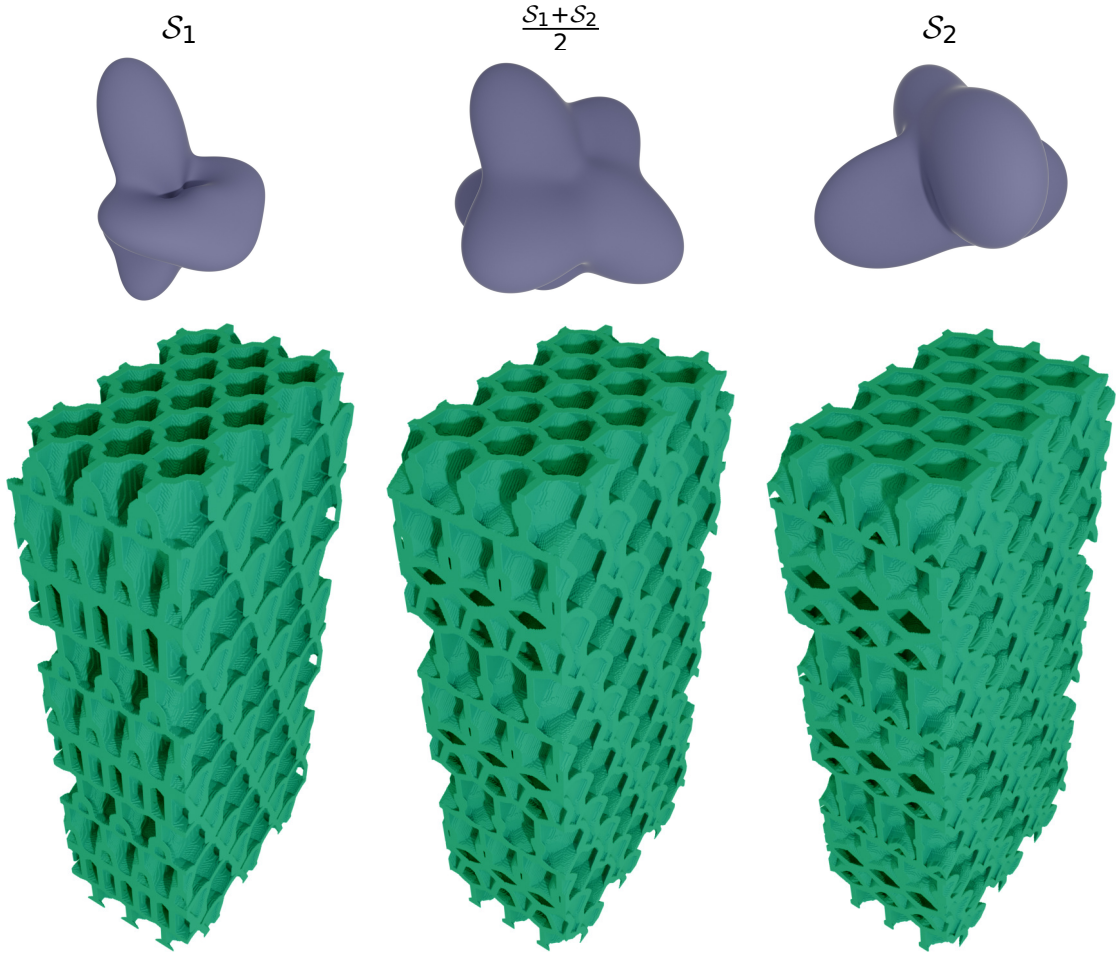


Figure 3.20: Linear interpolation between S_1 and S_2 . S_1 is a set with monoclinic domatic symmetry, while S_2 has hexagonal dipyramidal symmetry. Both sets share a monoclinic symmetry exhibited by the interpolating set $\frac{S_1+S_2}{2}$.

Statement. Let $\{S_i\}_{i=1}^N$ be a set of star-shaped sets with parametrized boundary functions $\{f_{S_i}(x, y)\}_{i=1}^N$ and the same point of origin O . Let all $\{S_i\}_{i=1}^N$ be invariant to any symmetry operator $g \in \mathcal{T}_S$ from a point group \mathcal{T}_S . Then the function $f_{S_\Sigma}(x, y)$ represents a boundary of a set S_Σ which is also star-shaped with respect to O and invariant to all $g \in \mathcal{T}_S$.

Formal proof. Due to their definition, boundary functions of each star-shaped set S_i are continuous, periodic, and single-valued. Therefore, their linear combination, which is $f_{S_\Sigma}(x, y)$, is also continuous, periodic, and single-valued. In addition, $f_{S_\Sigma}(x, y)$ is non-negative and bounded:

$$0 < r_{min} \leq f_{S_\Sigma}(x, y) \leq r_{max} < \infty. \quad (3.21)$$

Moreover, all mentioned properties make the considered function $f_{S_\Sigma}(x, y)$ a boundary function of a star-shaped set S_Σ with a point of origin O .

Now, let us consider a symmetry operator $g \in \mathcal{T}_S$. As all considered constituent star-shaped sets are invariant to this operator, their boundaries are also invariant to g :

$$\{g(S_i)\}_{i=1}^N = \{S_i\}_{i=1}^N \rightarrow \{f_{g(S_i)}(x, y)\}_{i=1}^N = \{f_{S_i}(x, y)\}_{i=1}^N \quad (3.22)$$

As it was already mentioned, all transformations from a point group \mathcal{T}_S are linear. Therefore, the resulting star-shaped set S_Σ has symmetry corresponding to \mathcal{T}_S :

$$f_{g(S_\Sigma)}(x, y) = \sum_{i=1}^N \alpha_i f_{g(S_i)}(x, y) = \sum_{i=1}^N \alpha_i f_{S_i}(x, y) = f_{S_\Sigma}(x, y) \quad (3.23)$$

End of proof.

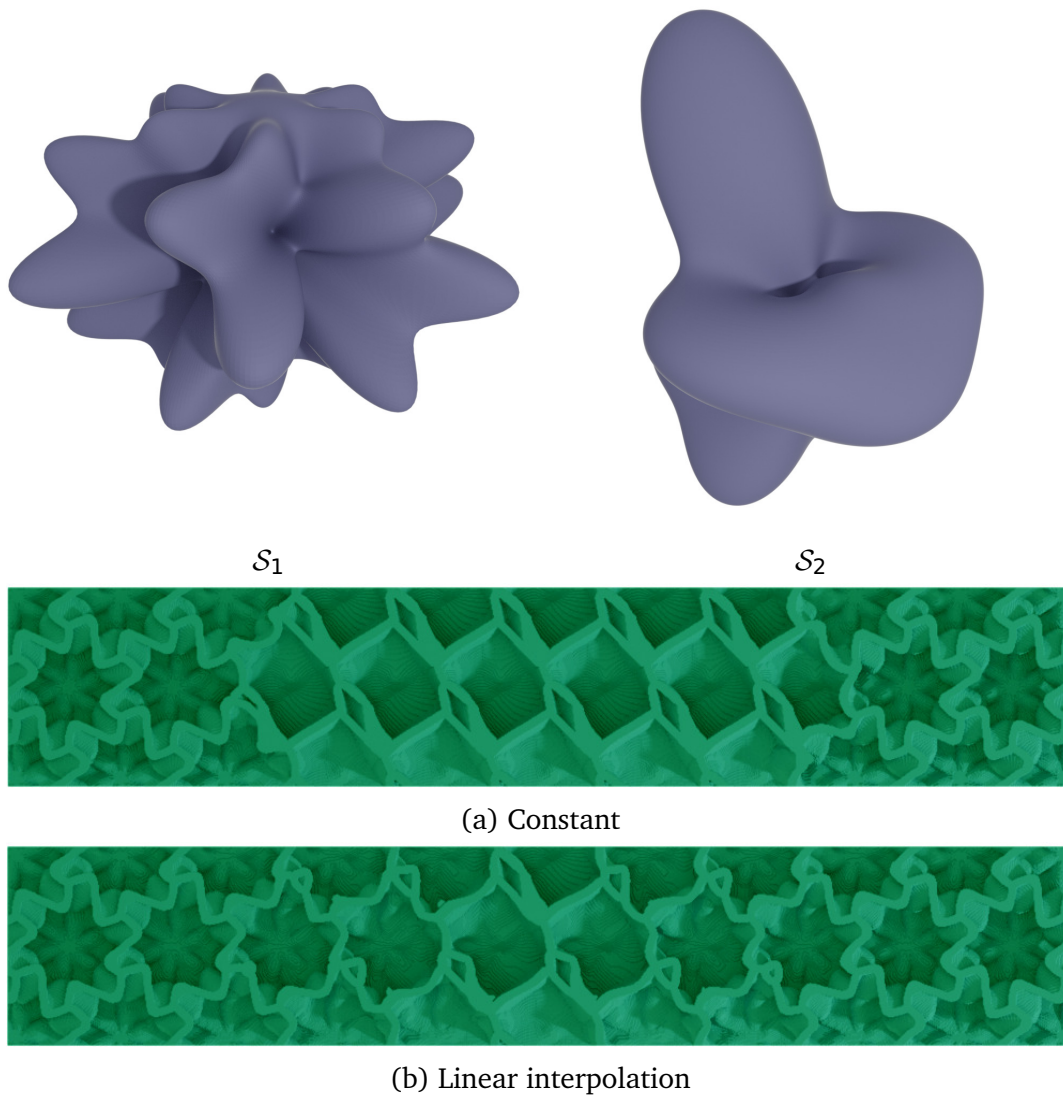


Figure 3.21: Closed-cell geometry gradation: central part with S_2 and the rest with S_1 .

Thus, a linear interpolation between an arbitrary number of parametrized star-shaped sets yields a parametrized star-shaped set with the symmetry shared between these sets and, by the properties of the growth method, imposes that symmetry to the resulting structure. This feature can be useful to explore the space of interpolated star-shaped sets given by $\{\mathcal{S}_i\}_{i=1}^N$ with user-defined symmetries. Moreover, the star-shaped distance $d_{\mathcal{S}_\Sigma}(\mathbf{x}, \mathbf{y})$ satisfies the axioms from Equations 3.4 - 3.6 and thus is (q_1, q_2) -quasimetric.

On Figure 3.20 we show an example of the linear interpolation between two given star-shaped sets \mathcal{S}_1 and \mathcal{S}_2 (see Figure 3.21b): for $\alpha \in [0, 1]$ we have $\alpha\mathcal{S}_1 + (1 - \alpha)\mathcal{S}_2$.

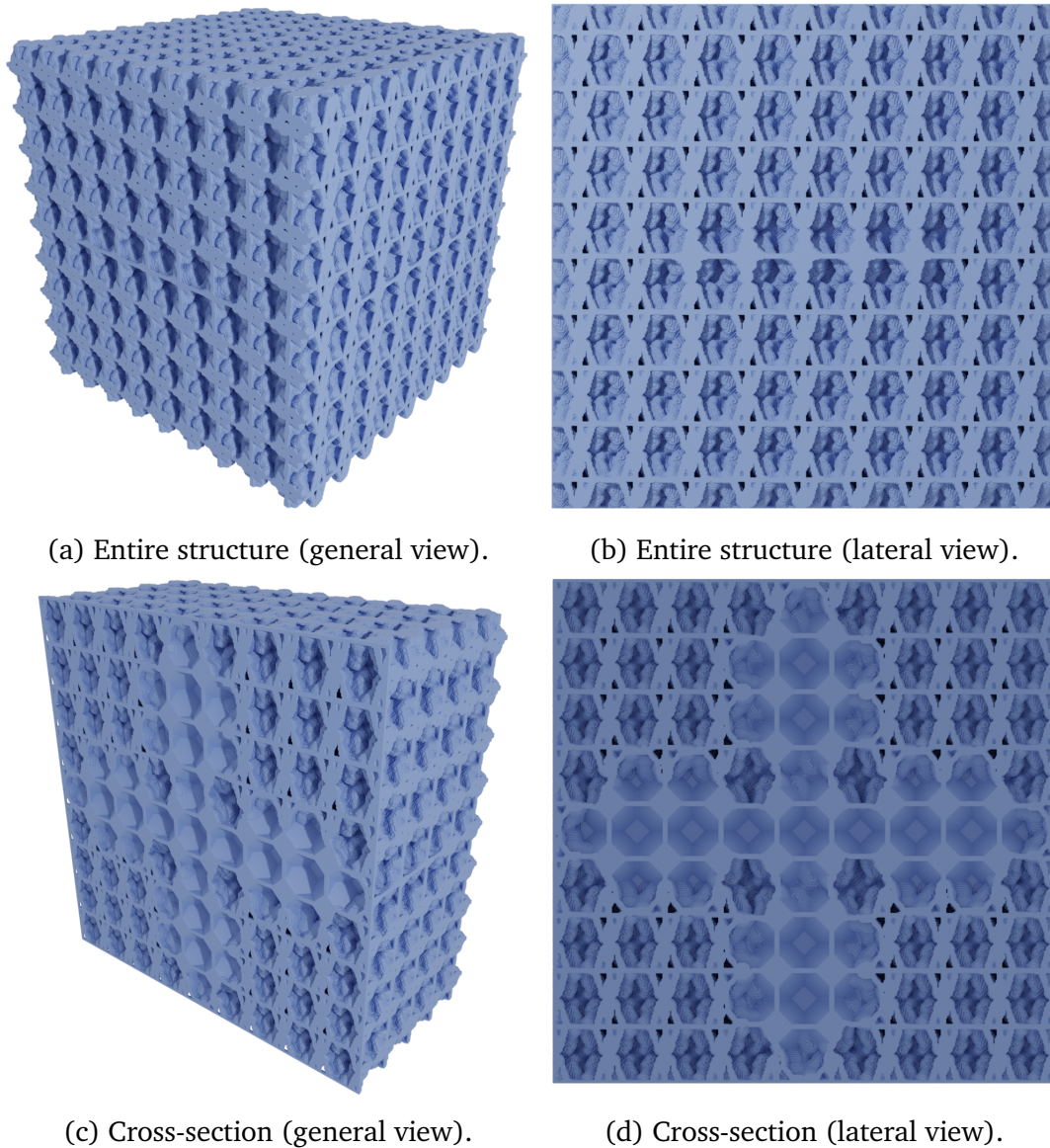


Figure 3.22: Example of a closed cell FDM with internal radial inclusion of Kelvin cells.

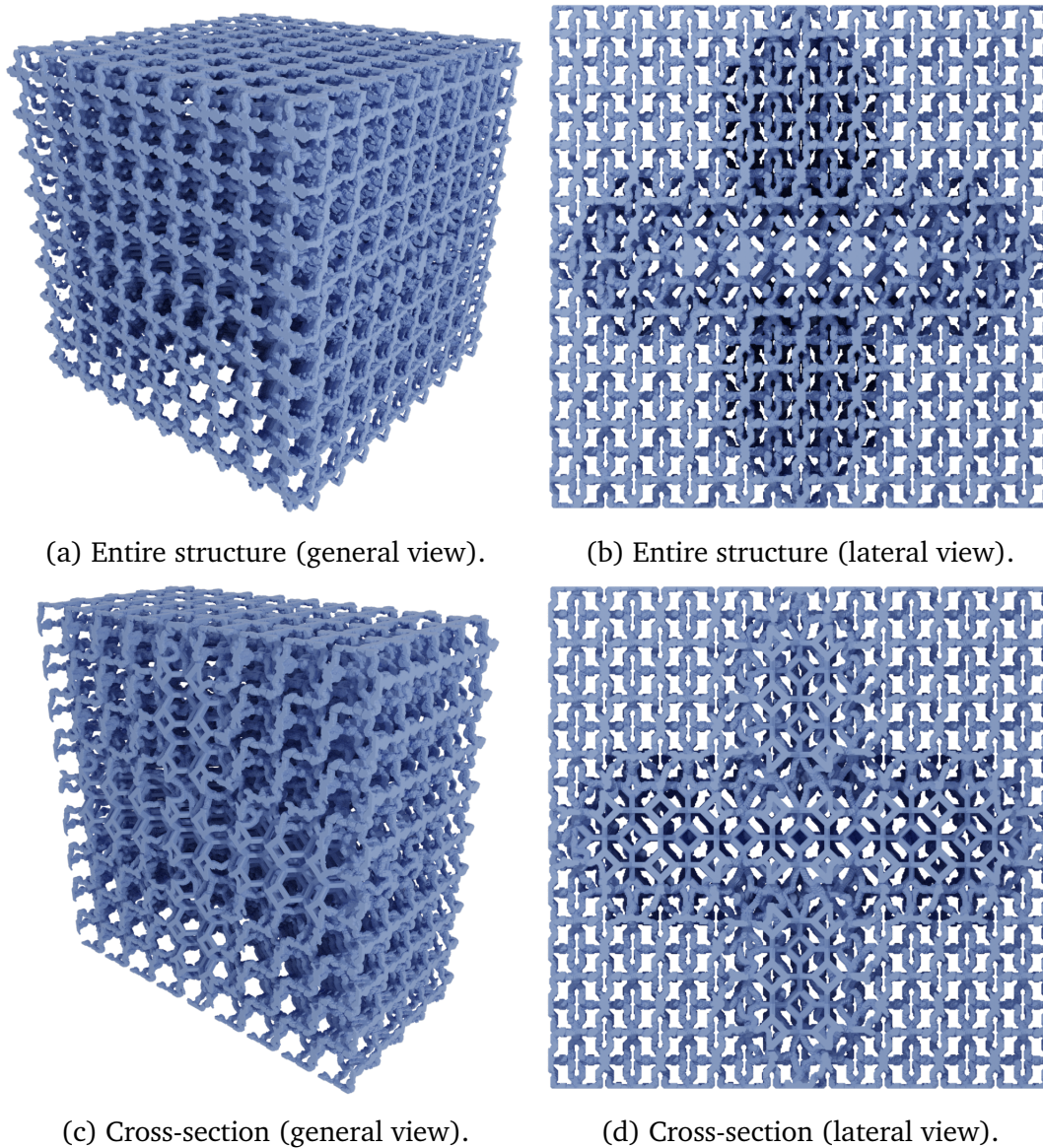


Figure 3.23: Example of an open cell FDM with internal radial inclusion of Kelvin cells.

3.8.2 Interpolation between lattices

As it was said in the beginning of this section, the growth method from this work allows one to obtain FGMs by combining different types of crystal lattices L . A simple example of this approach is demonstrated on Figure 3.24 where a combination of two lattices, orthorhombic and hexagonal, is used. Nevertheless, the problem of merging different lattice types correctly to preserve periodicity in the transition regions is not trivial and requires additional study.

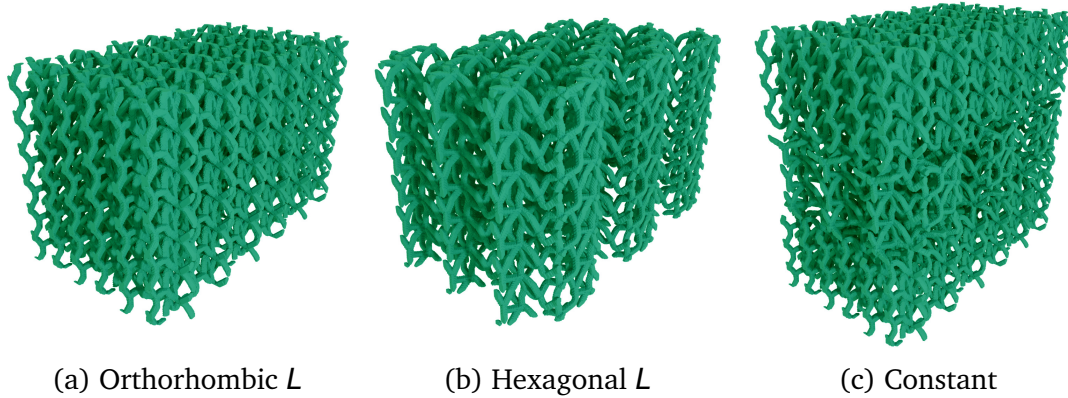


Figure 3.24: Cellular geometry gradation between two lattices (a) and (b). The top and bottom parts of (c) correspond to the orthorhombic lattice, while the middle one corresponds to the hexagonal.

3.9 Results

We now explore the variety of structures and elastic behaviors spanned by our method, focusing on symmetries. Please keep in mind that the approach presented in this chapter can seamlessly transition between all the shown structures of the same class (open or closed-cell) throughout the result sections.

3.9.1 Numerical results

Our method gives a tight control of the resulting periodic cellular material's symmetries. It produces all the elastic symmetries apart from strictly isotropic, a particular case in 3D (contrary to the 2D setting) that requires further optimization [179]. The mentioned above Figure B.1 and Figure B.2 showcase galleries of close and open-cell structures pertaining to different elastic symmetry.

Structure	Resolution	Algorithm 1	Homogenization
Triclinic	$106 \times 85 \times 80$	585s	3240s
Monoclinic	$50 \times 50 \times 150$	313s	1792s
Orthorhombic	$125 \times 50 \times 200$	1077s	5509s
Trigonal	$100 \times 173 \times 50$	715s	4345s
Tetragonal	$50 \times 50 \times 150$	340s	1626s
Hexagonal	$100 \times 173 \times 50$	721s	4244s
Cubic	$50 \times 50 \times 50$	112s	543s

Table 3.4: Computational timings for the closed-cell structures in Figure B.1.

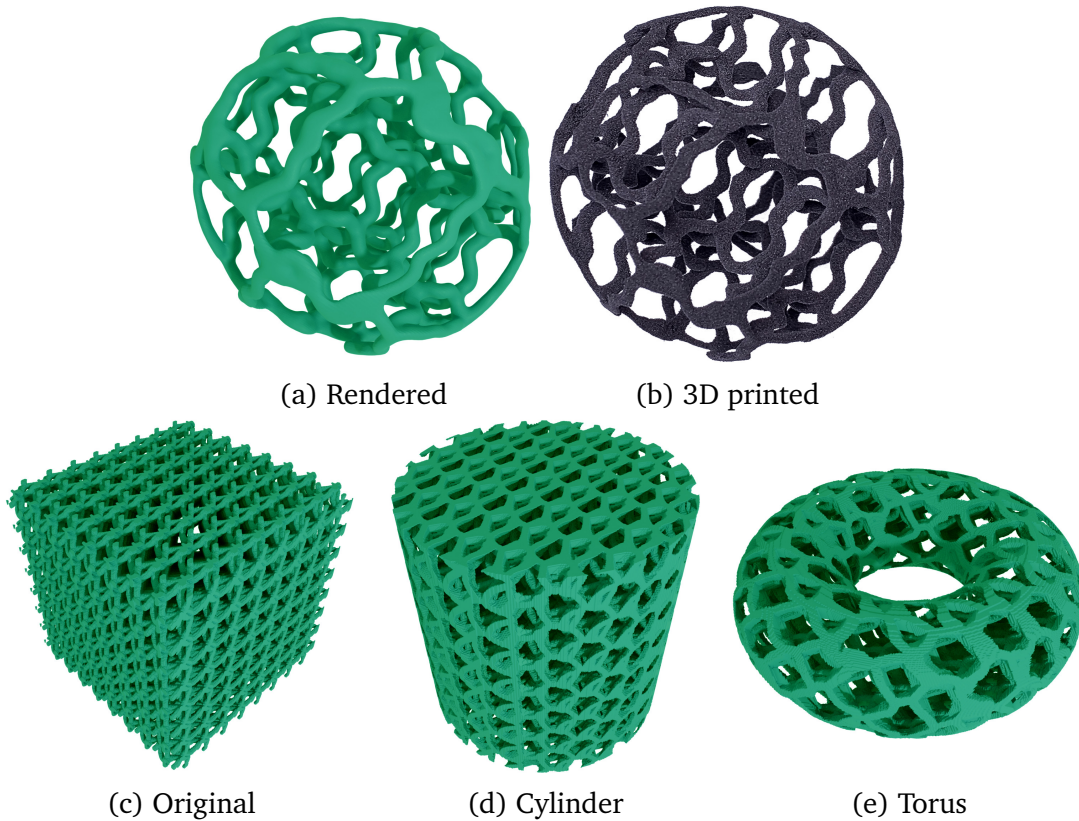


Figure 3.25: Different surface frame structures, geometrically smoothed. A rendered structure bounded by a sphere (a) and a printed one (b). A $8 \times 8 \times 8$ structure (c), which is fitted in a cylinder (d) and a torus (e).

The galleries reveal the wide variety of symmetries, geometries, and topologies that can be produced with our method. Nevertheless, the symmetries are precisely controlled and predicted while increasingly complex elasticity tensors are obtained. This can be seen by looking at the homogenized tensors in the last column. We recall the form of symmetric elasticity tensors in Table A.1 – note how some coefficients appear multiple times or are zero in these. Comparing the tensors with numerical results in Figure B.1 and Figure B.2 reveals a consistent agreement between the shared symmetries of L , S , and the elastic behavior. Occasional slight deviations are due to the voxel grid discretization. Ultimately, all the results of this article would benefit from a higher resolution of G .

It is worth noting the interplay of the distance and lattice symmetries. In some cases, the lattice has a low symmetry and the distance a high symmetry (e.g., open cell monoclinic structure in Figure B.2, rhombic-dipyramidal distance, and prismatic lattice), while conversely others use a lattice with high symmetry and a distance with low symmetry (e.g., closed-cell triclinic structure in Figure B.1, hexagonal-pyramidal distance, ditrigonal scalenohedral lattice). Only the shared symmetries exist in the result (see Section 3.7).

Also it is important to mention that changing the walls and beams' thickness would impact the overall structure's stiffness (but leave the symmetries

Structure	Resolution	Algorithm 1	Homogenization
Triclinic	$80 \times 80 \times 80$	430s	4776s
Monoclinic	$62 \times 50 \times 75$	192s	1642s
Orthorhombic	$100 \times 173 \times 50$	714s	7821s
Trigonal	$50 \times 86 \times 200$	708s	7830s
Tetragonal	$50 \times 50 \times 150$	308s	948s
Hexagonal	$100 \times 173 \times 50$	718s	8774s
Cubic	$50 \times 50 \times 50$	123s	699s

Table 3.5: Computational timings for the open-cell structures in Figure B.2.

unchanged).

We also report the timing results of Figures B.1 and B.2 in Tables 3.4 and 3.5, done with a Intel Xeon E-2186G (3.80Ghz) equipped with an NVidia GTX 1080. We consistently observe that the most time-consuming part is homogenization, and in particular, for open-cell structures.

3.9.2 Experimental results

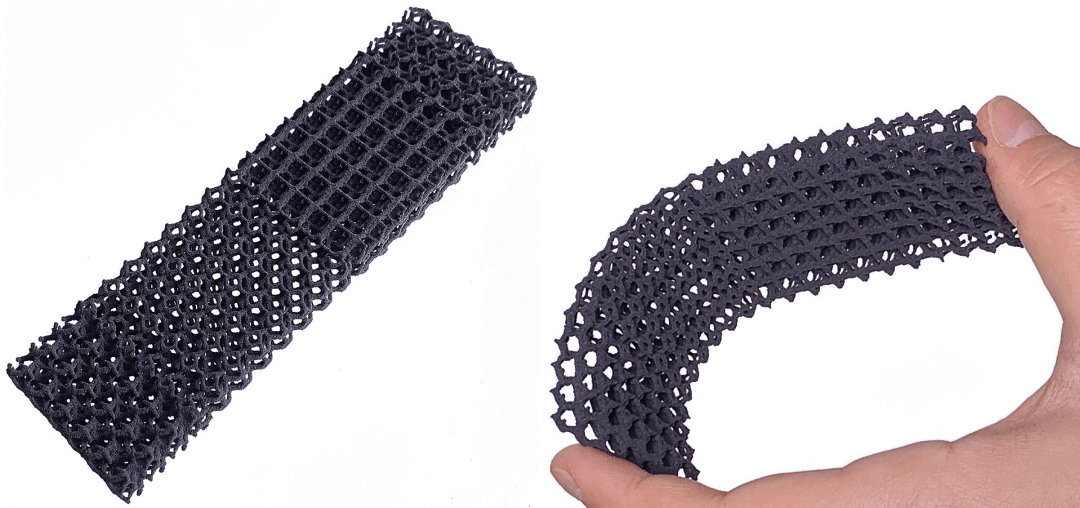


Figure 3.26: 3D printed elongated with spatially varying structures.

Figure 3.6 shows experimental results of compression tests. We obtain a good agreement between the predicted and measured values in terms of the relative Young's moduli of different directions.

We 3D printed different cellular structures obtained by our method. We use an SLS printer Lisa Sinterit and a TPU Flexa Black powder. Figure 3.27 shows some 3D printed samples of open-cell materials generated by our method.

3.9. RESULTS

Structure	Numerical			Experimental			Experimental/Numerical		
	E_x	E_y	E_z	E_x	E_y	E_z	x	y	z
Triclinic	0.258	0.493	0.250	0.247	0.484	0.269	0.959	0.982	1.078
Monoclinic	0.399	0.327	0.275	0.363	0.302	0.335	0.912	0.924	1.218
Cubic	0.325	0.337	0.339	0.296	0.313	0.391	0.913	0.930	1.153

Table 3.6: Comparison of the experimental and numerical relative Young’s moduli of three different specimens. The experimental Young’s modulus in each orthogonal direction x , y , and z was measured with an Instron 3345 machine. The direction z is the printing the direction. First and second column: for each specimen (triclinic, monoclinic, cubic), we divide the three values of Young’s moduli (experimental, numerical) with its average to obtain the relative value. The third column shows the division between the corresponding values of the first and second columns ; values close to one indicate that the relative moduli correspond.

These are highly flexible and exhibit the expected symmetries in their directional behaviors.

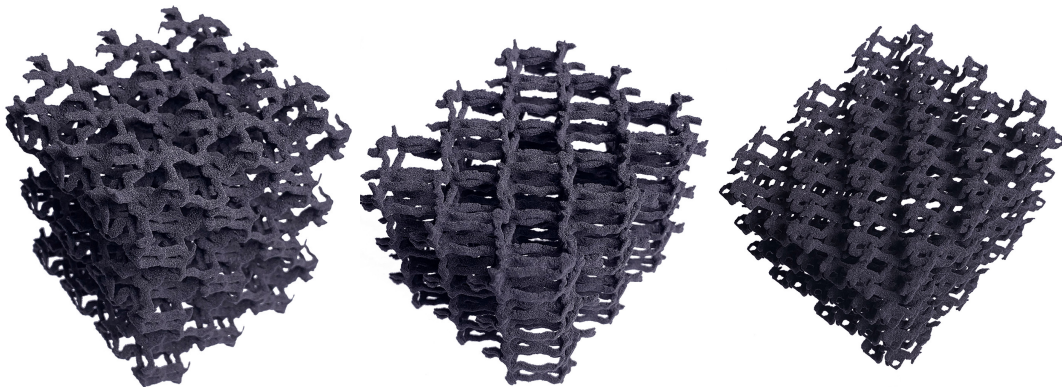


Figure 3.27: 3D printed periodic cellular materials.

Figure 3.25b shows a 3D printed sphere filled with an open-cell material that joins gracefully with the outer frame.

Figure 3.28 shows a progressive, linear interpolation between two closed-cell structures. Note how our method smoothly interpolates between these complex geometries.

Figure 3.29 shows a concentric gradation, where a different cellular geometry is used in the center. Our method correctly interpolates through this constant implicit gradation, which is usually challenging since the change of geometry is not aligned with the underlying lattice of periodic tiles.

Figure 3.26 shows an elongated box with different open-cell materials and constant change in the control field. The different elastic properties give rise to interesting non-uniform deformations. As long as the structures use a same lattice, progressive transitions are achievable (see Figure 3.28).

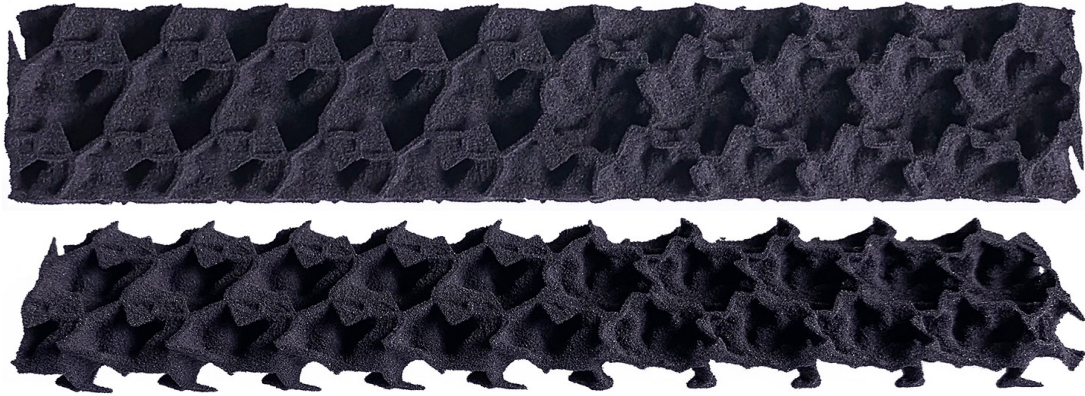


Figure 3.28: 3D printed, progressive gradation between two closed-cell materials.

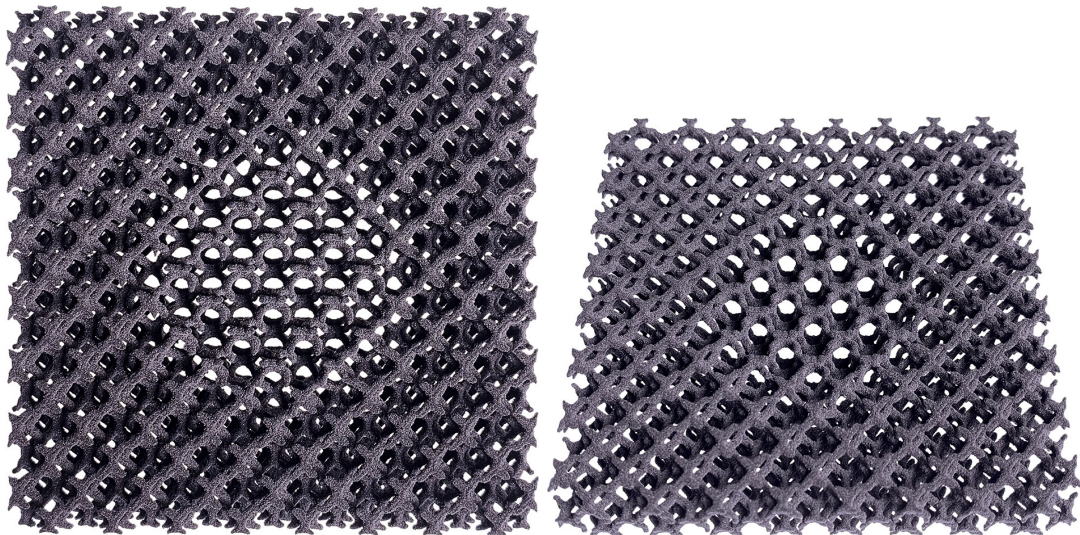


Figure 3.29: 3D printed concentric grading, with a sharp transition.

3.10 Conclusion

In this work, a novel method for the design of periodic cellular materials and FGMs with complex microstructure geometry was presented. The discrete growth method shows its effectiveness in achieving desired macroscopic properties. It is computationally efficient as it involves only the generation of a periodic tile. The method does not need an additional optimization technique to enforce the structural connectivity of the designed materials. Moreover, the growth method is flexible in that it allows to employ different models of distance or lattice without any significant change in the algorithm. It is also compatible with different shapes of the computational domain and types of the computational grid. The method exhibits good stability with the imposed radius of the neighborhood check for alleviating the cases of cell geometry degeneration. However, there is still a need for further investigations, especially dedicated to the numerical instabilities discussed in Section 3.7. It is important to understand how replacing metric with quasimetric affects the growth

process. Using a neighborhood check algorithm results in the corresponding thickness of the resulting structural elements. Thus, in order to perform the thickness gradation in space or to be able to change the thickness of the structure without reinitializing the growth method, an additional algorithm for skeleton extraction should be employed.

The main advantage of parametrized star-shaped distances is that they span a wide range of structures compared to convex distance functions. Indeed, a more complex shape of the set associated with the distance brings more complexity to the geometry of the resulting microstructure. On the other hand, as it was shown in this work, a star-shaped set spawns a (q_1, q_2) -quasimetric, which needs to be studied more through the perspective of the growth process. The different properties of this metric type provide, along with the benefits, some challenges: from the analytical derivation of the cellular material to its computational parallelization.

The main tool for controlling the resulting material's properties presented in this work is symmetry. Indeed, there is a strong connection between the mechanical properties of the material and its geometry, and this thesis shows again that symmetry plays a significant role in the design of metamaterials. The numerical results which were obtained in this work in the form of effective elasticity tensors confirm our initial assumption that it is possible to control the effective mechanical properties of a structure by only imposing symmetry to a distance function and a lattice. Hence, this control opens an ability to categorize the materials and operate only within one class, which seems to be a good technique to navigate in a vast 3D material space. Nevertheless, our approach is not aimed at achieving or optimizing specific values of mechanical parameters. Therefore, to design optimized mechanical materials, an additional optimization method should be investigated.

3.11 Future work

Growth process. To the best of our knowledge, there is no formulation of a continuous growth process guided by star-shaped sets, which would possibly allow employing existing classical and well-studied numerical techniques for solving this problem. Moreover, the problem of defining a tessellation yielded by star-shaped distance still remains open. Indeed, it is not trivial to find a formal mathematical definition of the growth process.

Although we use parallel algorithms in our computations of cellular structures (in the neighborhood check algorithm), the core growth algorithm is carried out subsequently as it is represented by step-wise insertion/extraction in/from an ordered queue. Finding an independent condition for each voxel to identify its attachment to a cell would allow one to build a parallel implementation of the growth method.

Symmetry and lattice. To solve the problem of the symmetry deviations connected with the use of the regular voxel grid, one can employ other types of

computational grid matching the corresponding symmetry. Here, the model of Bravais crystal lattices allows parametrizing the computational domain (and the computational grid) according to the corresponding parametrization of a chosen Bravais lattice. In addition, implementing complex lattices composed of different nuclei types (analogously some existing crystals where there are several molecules types in the crystal lattice) seems to be promising for creating even more complex microstructures with local anisotropy. One just needs to define different star-shaped functions for nuclei within a unit cell to do that.

In addition, the problem of the design of a structure with prescribed elastic symmetry can be expanded to the one of periodic cellular FGMs. Some results presented in this thesis show that it is possible to model periodic tiles with internal spatial gradation, which possesses prescribed symmetry. However, in this case, there are additional requirements for the gradation to yield desired symmetry.

Although we can reach seven different symmetries of the effective elastic tensor, there is no way to characterize the isotropy or auxeticity through symmetry. There are some secondary criteria such as chirality (for auxetic materials) or cubic symmetry (for isotropy), but they do not ensure the strict presence of these properties. Hence, once these criteria are found, it could decrease our dependence on optimization methods in material design.

Relation to the standard tiled approaches. Finally, in the context of the design of FGMs with different lattice types, there is still the problem of boundary compatibility between the interfaces in order to preserve periodicity. Moreover, there are possible ways to optimize the computation process of materials with spatial transitions that deserve further studies. For example, in the case of spatial transition between two different tiles, it may be necessary to use the growth method for computing the structure only locally in the transition area. On the other hand, one could use precomputed tiles of the given materials to compose the resulting structure for the rest of the domain.

Chapter 4

Computation of the elastic behavior of 3D periodic materials

4.1 Notations

Notation	Definition	First introduced
σ	stress field	Equation 4.1
ϵ	strain field	Equation 4.1
C	elasticity tensor	Equation 4.1
Σ	mean value of stress	Equation 4.3
Ξ	mean value of strain	Equation 4.3
$\langle \cdot \rangle$	integral average	Equation 4.4
E	Young's modulus	Equation 4.5
ν	Poisson's ratio	Equation 4.6
λ, μ	Lame parameters	Equation 4.6
$\Gamma^0(\vec{x})$	Green's operator	Equation 4.7
\mathcal{F}	Fourier transform	Equation 4.8
$G^0(\vec{x})$	Green's function	Equation 4.9

Table 4.1: Notations for Chapter 4.

4.2 Introduction

In multiple problems dedicated to study of physical properties of periodic media it appears that going down to a certain scale, which is small enough, reveals local heterogeneities in the structure of the considered object [143]. Moreover, these microscopic heterogeneities are often reflected in the properties arising on larger scales. To study this phenomenon there is a wide class of mathematical techniques called *multiscale methods* ([82], [248]). Homogenization methods represent a big part of the field of multiscale modelling. This approach is based on averaging theorems which state that effective macroscopic properties of a material are governed by the average of intrinsic microscopic

fields representing the same or related physical processes but with lower characteristic lengths. In the design of mechanical metamaterials homogenization problem is one of the main methods investigating various types of mechanical behavior including linear and nonlinear elasticity.

One of the most popular techniques for homogenization of elastic properties of periodic materials is based on the FEM approach. These methods perform high precision on a coarse mesh and are well-suited to sharp geometries [59]. Moreover, FEM-based algorithms are more universal in the sense of direct applicability to various physical settings without significant adjustments. The drawback of these methods is high computational complexity.

Another approach for solving the linear homogenization problem is represented by fixed-point algorithms for a corresponding integral equation [90]. These methods are often implemented through conjugate gradients algorithm or FFT-based iterative schemes [142] and have proved themselves to be efficient high-performance and low-memory alternative to FEM-based techniques with acceptable precision, particularly well-suited for grids.

In this work we have chosen the FFT-based approach as the most suitable technique to investigate the elastic properties. Although these methods can provide slower convergence rate for higher contrasts and some microstructure geometry, the parallelization ability and algorithmic simplicity result in lower computation time compared to FEM-based approach. Hence, high computational speed and implementation simplicity are significant advantages of the FFT-based approach, which were crucial in this work due to a large number of studied materials.

In this thesis two popular iterative schemes were implemented to study elastic behavior of 3D cellular materials: the method by *Moulinec et al* [154] (alternatively implemented based on a representation and a convergence criterion taken from [151]) and the algorithm presented by *Willot et al* [232]. The main difference between these two schemes lies in a type of the associated Green operator used for solving the integral equation. The contribution presented in this chapter is purely implementational. However, the author of this manuscript hopes that the results presented here will be useful for the other researchers in their projects as a final solution or a basis for building more improved algorithms. Three versions of these methods were implemented on Python: CPU based, GPU based with precomputed operators, and GPU based implementations with reduced memory consumption. The source code is available on the following GitHub repository (https://github.com/SemyonEfremov/iterative_FFT_homogenization_scheme).

4.3 Investigation and validation of mechanical properties of periodic materials

In this work, we used homogenization problem for investigation of mechanical properties of periodic materials. This approach allows to obtain both the effective parameters characterizing macroscopic properties of an periodic material

and its periodic deformation fields (stress, strain and displacements) which describe the microscopic behavior of the structure. Here we first consider the case of linear deformations (infinitesimal strains) to give a numerical understanding of the elastic symmetries.

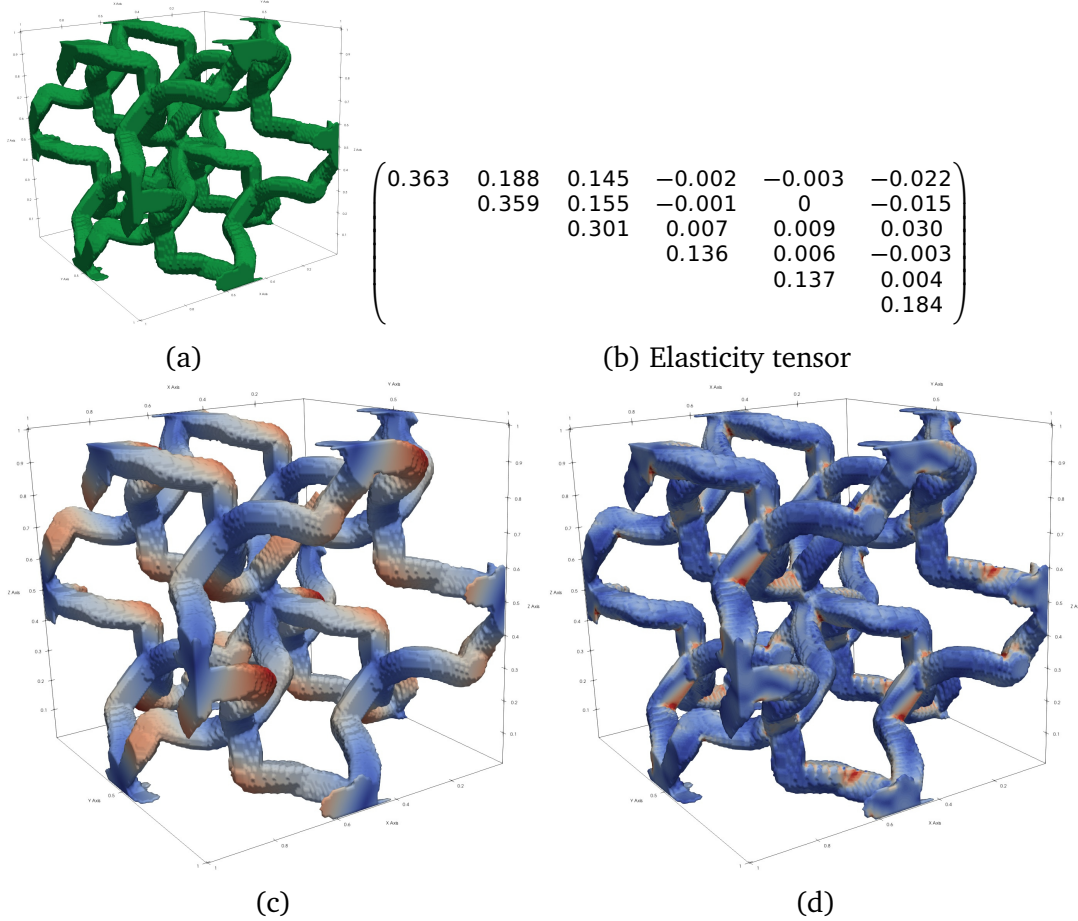


Figure 4.1: Given a periodic structure (a) we compute its homogenized elasticity tensor (b) from the prescribed strain and stress fields over G . From these, fields we can also visualize, for instance, the overall magnitude of displacement fields (c), or the Von mises stress the analyze the yielding of the structure (d).

Elastic deformations provide linear relations between stress $\sigma(\vec{x})$ and strain $\epsilon(\vec{x})$ through an elasticity tensor $C(\vec{x})$ governed by the Hooke's law

$$\sigma(\vec{x}) = C(\vec{x}) : \epsilon(\vec{x}). \quad (4.1)$$

The equivalent matrix form can be written as follows:

$$\begin{pmatrix} \sigma_{11} \\ \sigma_{22} \\ \sigma_{33} \\ \sigma_{23} \\ \sigma_{13} \\ \sigma_{12} \end{pmatrix} = \begin{pmatrix} C_{11} & C_{12} & C_{13} & C_{14} & C_{15} & C_{16} \\ & C_{22} & C_{23} & C_{24} & C_{25} & C_{26} \\ & & C_{33} & C_{34} & C_{35} & C_{36} \\ & & & C_{44} & C_{45} & C_{46} \\ & & & & C_{55} & C_{56} \\ & & & & & C_{66} \end{pmatrix} \begin{pmatrix} \epsilon_{11} \\ \epsilon_{22} \\ \epsilon_{33} \\ 2\epsilon_{23} \\ 2\epsilon_{13} \\ 2\epsilon_{12} \end{pmatrix}. \quad (4.2)$$

4.3.1 Homogenization of periodic material

Homogenization problem for computation of elastic deformations for a periodic structure is formed by three equations: the Hooke's law, equilibrium equation, and strain-displacement relation:

$$\begin{aligned} \sigma(\vec{x}) &= C(\vec{x}) : \epsilon(\vec{x}), \\ \operatorname{div} \sigma(\vec{x}) &= 0, \\ \epsilon(\vec{x}) &= \frac{1}{2} (\nabla u(\vec{x}) + \nabla^T u(\vec{x})). \end{aligned}$$

In this work, constituent materials of the considered periodic structures are assumed to be isotropic, therefore, the elasticity tensor $C(\vec{x})$ has only two independent components. In order to find the effective elasticity tensor C^* the stress and strain fields for several load cases were computed. C^* is defined with the average stress $\Sigma = \langle \sigma(\vec{x}) \rangle$ and strain $\Xi = \langle \epsilon(\vec{x}) \rangle$ through the Hooke's law:

$$\Sigma = C^* : \Xi. \quad (4.3)$$

Here, the integral averaging operator $\langle f(\vec{x}) \rangle$ of a function $f(\vec{x})$ is defined as follows:

$$\langle f(\vec{x}) \rangle = \int f(\vec{x}) d\vec{x}. \quad (4.4)$$

To compute the homogenized elasticity tensor C^* an FFT-based method has been chosen because it is well-suited for 3D grids and computationally efficient [145]. In this work two methods were implemented: the method of Monchiet et al. [151] and the algorithm of Willot et al. [232]. The principal difference between them is that [151] considers a continuous Green operator that is less dependent on the grid step while [232] considers a discrete one and contains the discrete approximation of differential operators. Both implementations were compared with each other, FEM homogenization method, and CraFT software on several test structures (see Subsection 4.3.3). Most of the results presented in this work were obtained with the method [151], but in cases when convergence was hard to reach [232] was used.

For all the numerical results provided in this thesis (except Figures 4.3 and 4.4), a solid phase with Young's modulus $E_s = 100$, a very soft phase (void) with $E_v = 0.1$, a homogeneous Poisson's ratio of 0.3, and a convergence threshold of $\psi = 10^{-4}$ were considered. Therefore for each point of computational domain the Young's modulus can be defined as follows:

$$E(\vec{x}) = \begin{cases} E_s & \text{if } \vec{x} \text{ is solid,} \\ E_v & \text{if } \vec{x} \text{ is void.} \end{cases} \quad (4.5)$$

The constituents materials were assumed to be isotropic, thus:

$$C(\vec{x}) = \begin{pmatrix} 2\mu(\vec{x}) + \lambda(\vec{x}) & \lambda(\vec{x}) & \lambda(\vec{x}) & 0 & 0 & 0 \\ & 2\mu(\vec{x}) + \lambda(\vec{x}) & \lambda(\vec{x}) & 0 & 0 & 0 \\ & & 2\mu(\vec{x}) + \lambda(\vec{x}) & 0 & 0 & 0 \\ & & & \mu(\vec{x}) & 0 & 0 \\ & & & & \mu(\vec{x}) & 0 \\ & & & & & \mu(\vec{x}) \end{pmatrix}.$$

The lame parameters $\lambda(\vec{x})$, $\mu(\vec{x})$ are computed based on the Poisson's ratio ν and the Young's modulus distribution $E(\vec{x})$:

$$\lambda(\vec{x}) = \frac{E\nu}{(1+\nu)(1-2\nu)}, \quad \mu(\vec{x}) = \frac{E}{2(1+\nu)}. \quad (4.6)$$

4.3.2 Numerical methods

Method with continuous Green's operator. Presented in [151], the iterative scheme for solving the homogenization problem is based on calculation of stress and strain fields using the Lippman-Schwinger equation:

$$\epsilon(\vec{x}) + \Gamma^0(\vec{x}) \star (\delta C(\vec{x}) : \epsilon(\vec{x})) = 0. \quad (4.7)$$

Here, $\delta C(\vec{x}) = C(\vec{x}) - C^0$, C^0 is a reference isotropic elasticity tensor computed with reference Lamé parameters λ_0 , μ_0 , and the Green's tensor $\Gamma^0(\vec{x})$ is computed using a spectral decomposition in Fourier space in a tensor basis:

$$\begin{aligned} \mathbb{E}_1(\vec{\xi}) &= \frac{1}{2} \vec{k}^\perp \otimes \vec{k}^\perp, & \mathbb{E}_4(\vec{\xi}) &= \vec{k}^\perp \underline{\otimes} \vec{k} + \vec{k} \underline{\otimes} \vec{k}^\perp, \\ \mathbb{E}_2(\vec{\xi}) &= \vec{k} \otimes \vec{k}, & \mathbb{E}_5(\vec{\xi}) &= \vec{k} \otimes \vec{k}^\perp, \\ \mathbb{E}_3(\vec{\xi}) &= \vec{k}^\perp \underline{\otimes} \vec{k}^\perp - \mathbb{E}_1(\vec{\xi}), & \mathbb{E}_6(\vec{\xi}) &= \vec{k}^\perp \otimes \vec{k}. \end{aligned}$$

Here $\vec{k}(\vec{\xi}) = \frac{1}{|\vec{\xi}|^2} \xi_i \otimes \xi_j$, $\vec{k}^\perp(\vec{\xi}) = \vec{l} - \vec{k}(\vec{\xi})$, \vec{l} is the identity tensor of the second order and $\vec{\xi} = (\xi_1, \xi_2, \xi_3)$ is a frequency vector. Then the tensor projectors can be define by following expressions:

$$\begin{aligned} \mathbb{Q}(\bar{\xi}) &= \mathbb{E}_1(\bar{\xi}) + \mathbb{E}_3(\bar{\xi}), & \mathbb{P}(\bar{\xi}) &= \mathbb{E}_2(\bar{\xi}) + \mathbb{E}_4(\bar{\xi}), \\ \mathbb{Q}(\bar{\xi}) : \epsilon(\bar{\xi}) &= 0, & \mathbb{P}(\bar{\xi}) : \sigma(\xi) &= 0. \end{aligned}$$

Thanks to the last properties of the projector tensors, they can be used for evaluation of the approximation error during the computations:

$$\frac{\langle \mathbb{P}(\bar{\xi}) : \sigma(\xi) \rangle^2}{\langle (\sigma(\bar{\xi}))^2 \rangle} < \psi.$$

Then, the Green's tensor in the presented basis can be computed using a following expression:

$$\Gamma^0(\bar{\xi}) = \frac{1}{\lambda_0 + 2\mu_0} \mathbb{E}_2(\bar{\xi}) + \frac{1}{2\mu_0} \mathbb{E}_4(\bar{\xi}),$$

where the reference Lamé parameters λ_0 and μ_0 produce significant impact on the method's convergence rate. In this work, following general advices from [151] these parameters were computed as:

$$\lambda_0 = \frac{1}{2}(\lambda_s + \lambda_v), \quad \mu_0 = \frac{1}{2}(\mu_s + \mu_v).$$

In this expression, pairs λ_s, μ_s and λ_v, μ_v denote Lamé parameters of two constituent phases (solid and very soft). Finally, the iterative algorithm can be represented by a following scheme:

$$\begin{aligned} \epsilon^i(\bar{x}) &= \mathcal{F}^{-1}[\epsilon^i(\bar{\xi})], \\ \sigma^i(\bar{x}) &= \mathbb{C}(\bar{x}) : \epsilon^i(\bar{x}), \\ \sigma^i(\bar{\xi}) &= \mathcal{F}[\sigma^i(\bar{x})], \\ &\text{convergence test,} \\ \epsilon^{i+1}(\bar{\xi}) &= \epsilon^i(\bar{\xi}) - \Gamma^0(\bar{\xi}) : \sigma^i(\bar{\xi}), \end{aligned} \tag{4.8}$$

The initial conditions are defined through the avrage strain value:

$$\epsilon^0(\bar{x}) = \begin{cases} 0 & \forall \bar{\xi} \neq 0, \\ \Xi & \bar{\xi} = 0. \end{cases}$$

Method for discrete Green's function. The method from [232] is also based on solving the homogenization problem through the Lippman-Schwinger equation but the method is formulated in terms of the displacement field $\bar{u}(\bar{x})$ and a corresponding deiscrete Green's function:

$$G^0(\xi) = -\frac{1}{\mu_0 |k^+|^2} I + \frac{\mu_0 + \lambda_0}{\mu_0 (2\mu_0 + \lambda_0)} \frac{1}{|k^+|^4} k^+ \otimes k^+,$$

with discrete multiplier arising from the discrete approximation of the spatial derivative in Fourier space:

$$k_j^\pm = \pm \frac{e^{\pm i\xi_j} - 1}{h_j}.$$

The reference Lamé parameter are computed in the same way as for the method with the continuous Green's tensor:

$$\lambda_0 = \frac{1}{2} (\lambda_s + \lambda_v), \quad \mu_0 = \frac{1}{2} (\mu_s + \mu_v).$$

However, a different type of convergence criteria is used here. The relative error is computed based on the equilibrium equation:

$$\frac{\langle \text{div} \sigma(\vec{x}) \rangle^2}{\langle (\sigma(\vec{x}))^2 \rangle} < \psi.$$

In fact, this approach of measuring the approximation error is more restricting than the one used in the previously discussed approach. Thus, it should be taken into account that convergence rate of the iterative FFT-based schemes crucially depends on a convergence test chosen. Please, refer to [90] for more details according this topic.

The algorithm is represented by the following scheme:

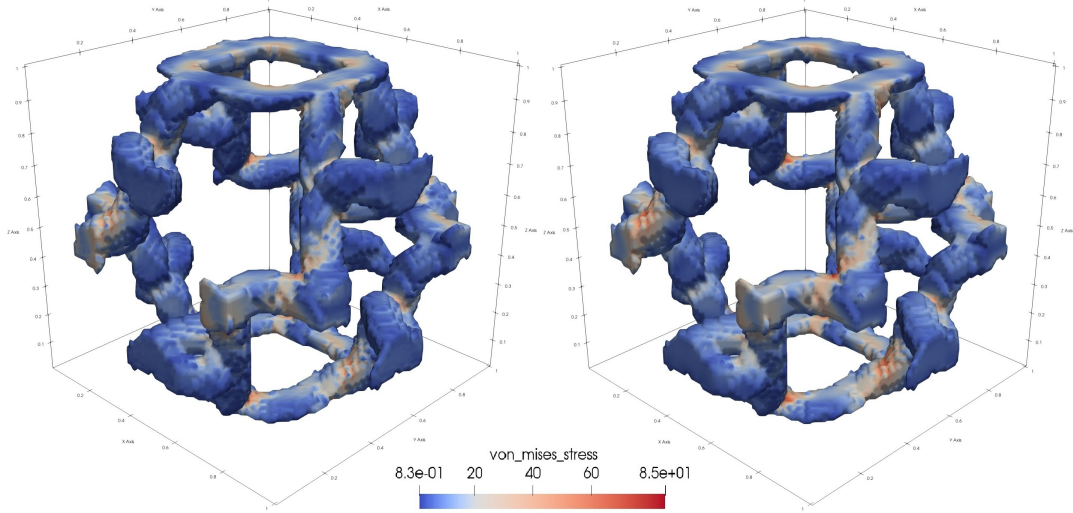
$$\begin{aligned} u^i(\vec{x}) &= -\text{div} [\delta C(\vec{x}) : \epsilon^i(\vec{x})], \\ u^i(\vec{\xi}) &= \mathcal{F}[u^i(\vec{x})], \\ u^i(\vec{\xi}) &= G^0(\vec{\xi}) u^i(\vec{\xi}), \quad u^i(0) = 0, \\ u^i(\vec{x}) &= \mathcal{F}^{-1}[u^i(\vec{\xi})], \\ \epsilon^{i+1}(\vec{x}) &= \frac{1}{2} (\nabla u^i(\vec{x}) + \nabla^T u^i(\vec{x})), \\ &\text{convergence test.} \end{aligned} \tag{4.9}$$

The initial condition is also defined by a prescribed mean strain value:

$$\epsilon^0(\vec{x}) = \begin{cases} 0 & \forall \vec{\xi} \neq 0, \\ \Xi & \vec{\xi} = 0. \end{cases}$$

4.3.3 Methods validation and comparison

To validate our implementations of previously discussed methods we carried out numerical tests and compared both methods presented here and two other approaches (FEM and CraFT software). As the test materials for the numerical experiments we chose three structures of $20 \times 60 \times 30$, $60 \times 60 \times 60$, and $80 \times 80 \times 80$ resolutions.



(a) Von Mises stress distribution: *Monchiet et Bonnet* (left) and *Willot et al.* (right).

$$\begin{pmatrix} 3.096261161 & 1.203359230 & 1.203358924 & -4.85200e-06 & -1.21449e-05 & -1.29547e-05 \\ & 2.313283742 & 1.060327236 & -2.45634e-03 & -4.78249e-06 & -1.20741e-05 \\ & & 2.313284983 & 2.44118e-03 & -1.25613e-05 & -5.04912e-06 \\ & & & 8.00233e-01 & -5.17435e-08 & -2.32465e-07 \\ & & & & 7.50595e-01 & -2.27524e-06 \\ & & & & & 7.50595e-01 \end{pmatrix}$$

(b) Elasticity tensor (*Monchiet et Bonnet*)

$$\begin{pmatrix} 3.119194922 & 1.210175728 & 1.211346337 & 1.71862e-03 & 1.33371e-02 & 1.36999e-02 \\ & 2.321558122 & 1.064116353 & 6.02278e-03 & 4.44239e-03 & 1.13548e-02 \\ & & 2.322006973 & 9.83796e-03 & 1.10724e-02 & 2.98371e-03 \\ & & & 8.03322e-01 & -2.44238e-03 & 3.59801e-03 \\ & & & & 7.54421e-01 & -3.19142e-04 \\ & & & & & 7.53707e-01 \end{pmatrix}$$

(c) Elasticity tensor (*Willot et al.*).

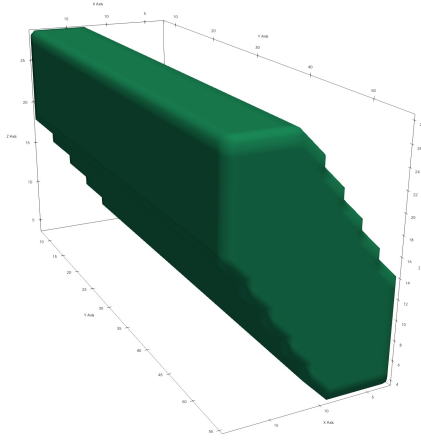
Figure 4.2: Von Mises stress distribution (4.2a) computed with both implementations (*Monchiet et Bonnet* on the left and *Willot et al.* on the right) and corresponding elastic tensors (4.2b and 4.2c). The material used for these computations has tetragonal symmetry and has been obtained with the growth method. The following parameters were used: $E_S = 100$, $E_V = 1$, $\nu = 0.3$, $\psi = 10^{-4}$. In average for the methods of *Monchiet et Bonnet* and *Willot et al.* it took 1590 and 340 iterations respectively to reach the given error value.

First, we applied our implementations to homogenization of a periodic tetrahedral material which has been computed with our growth method. We compared obtained Von Mises stress distributions and effective elastic tensors

(Figure 4.2). To set this test up, we have chosen the values of Young's modulus for two base materials as $E_S = 100$, $E_V = 1$, Poisson's ratio as $\nu = 0.3$ and the relative error $\psi = 10^{-4}$. The results revealed a good agreement between both methods. The method of *Willot et al.* generally performed higher convergence rate (1590 against 340 iterations in average), especially for the case of a high contrast between the base materials. However, we observed that the method of *Monchiet et Bonnet* approximates better the elements of a tensor that are equal to zero. Therefore, in this work, except the cases of a very high contrast, we gave preference to the method with continuous Green operator as it helps to better identify an elastic symmetry class of a designed material.

In addition, we chose two periodic composites and compared homogenized elastic tensor obtained with our implementations of iterative FFT-based schemes, homogenization method provided by CraFT software and in-house 3D FEM homogenization algorithm, done by directly extending the 2D approach of [9] to 3D.

In the first test (Figure 4.3), a low contrast between the values of Young's modulus was chosen ($E_S = 1$, $E_V = 0.1$), and $\nu = 0.3$. The error value for our implementations is $\psi = 10^{-4}$ and for the other methods it is equal to 10^{-10} . In the second experiment (Figure 4.4) the Young's modulus values were $E_S = 1$ and $E_V = 0.1$, Poisson's ratio was $\nu = 0.3$, and $\psi = 10^{-4}$. The resulting effective elastic tensors showed a good agreement for the FFT methods. We can notice that in Figure 4.4 the FEM diverges slightly, while in Figure 4.3 it does not. Please refer to the study of [59] for a more in-depth analysis of both methods (FFT and FEM).



(a) The first test structure.

$$\begin{pmatrix} 0.2140443 & 0.0810351 & 0.0902232 & 0 & 0.0054918 & 0 \\ & 29943 & 0.0854024 & 0 & 0.0032248 & 0 \\ & & 0.2387037 & 0 & 0.0143512 & 0 \\ & & & 0.0705032 & 0 & 0.0067662 \\ & & & & 0.0668151 & 0 \\ & & & & & 0.0637061 \end{pmatrix}$$

(b) Elasticity tensor (FEM)

$$\begin{pmatrix} 0.2109394 & 0.0808757 & 0.0909389 & 0 & 0.0054058 & 0 \\ & 0.2974678 & 0.0849823 & 0 & 0.0031834 & 0 \\ & & 0.2348937 & 0 & 0.0144266 & 0 \\ & & & 0.0699253 & 0 & 0.0068548 \\ & & & & 0.066431 & 0 \\ & & & & & 0.0632451 \end{pmatrix}$$

(c) Elasticity tensor (CraFT)

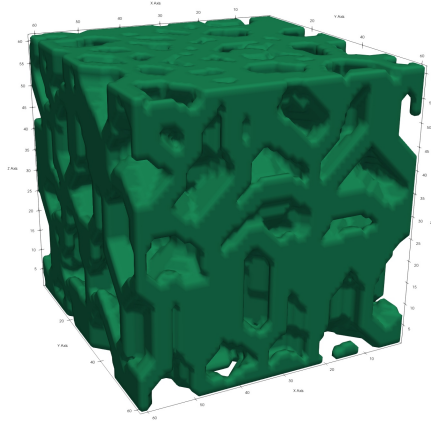
$$\begin{pmatrix} 0.210954 & 0.0808571 & 0.0909521 & -4.71958e-08 & 0.00540335 & -1.95478e-07 \\ & 0.297789 & 0.0849561 & -1.65161e-07 & 0.00317697 & -2.3381e-07 \\ & & 0.234914 & -1.18185e-07 & 0.0144239 & -3.81301e-08 \\ & & & 0.0699328 & -6.96891e-08 & 0.00685197 \\ & & & & 0.0664332 & -3.09071e-08 \\ & & & & & 0.0632506 \end{pmatrix}$$

 (d) Elasticity tensor (*Monchiet et Bonnet*)

$$\begin{pmatrix} 0.224916 & 0.082005 & 0.0942742 & 1.19242e-05 & 0.0114434 & 0.000116209 \\ & 0.274483 & 0.0816083 & 6.08227e-05 & 0.00267186 & 6.89727e-05 \\ & & 0.22288 & 8.66121e-05 & 0.0107664 & 1.29514e-05 \\ & & & 0.0657724 & -2.86392e-05 & 0.00566637 \\ & & & & 0.0692554 & -2.78781e-05 \\ & & & & & 0.0662082 \end{pmatrix}$$

 (e) Elasticity tensor (*Willot et al.*)

Figure 4.3: The first test tile of periodic material (4.3a) and corresponding effective elastic tensors computed with FEM (4.3b), iterative scheme in CraFT (4.3c) and our implementations of *Monchiet et Bonnet* (4.3d) and *Willot et al.* (4.3e). The following parameters were used: $E_S = 1$, $E_V = 0.1$, $\nu = 0.3$, $\psi = 10^{-4}$ for (4.4d), (4.4e), and 10^{-10} for (4.4b) and (4.4c).



(a) The second test structure.

$$\begin{pmatrix} 0.3122692 & 0.1115543 & 0.1092009 & 0.0004197 & -0.0047056 & -0.0014392 \\ & 0.3127 & 0.108973 & 0.0003312 & -0.0008623 & 0.0006772 \\ & & 0.3318756 & 0.001262 & -0.0035393 & 0.0002244 \\ & & & 0.1109744 & -0.0004005 & -0.0014638 \\ & & & & 0.1104297 & 0.0007235 \\ & & & & & 0.0988354 \end{pmatrix}$$

(b) Elasticity tensor (FEM)

$$\begin{pmatrix} 0.2562565 & 0.0937203 & 0.0888706 & 0.0005475 & -0.004602 & -0.0010722 \\ & 0.2569533 & 0.0885799 & 0.0005097 & -0.0007317 & 0.0006007 \\ & & 0.275949 & 0.0014189 & -0.0035513 & 0.0004676 \\ & & & 0.0928574 & -0.0001685 & -0.0014994 \\ & & & & 0.0925586 & 0.0008171 \\ & & & & & 0.0793466 \end{pmatrix}$$

(c) Elasticity tensor (CraFT)

$$\begin{pmatrix} 0.258746 & 0.094619 & 0.0896059 & 0.000531165 & -0.00462407 & -0.00109589 \\ & 0.259371 & 0.0893127 & 0.000478555 & -0.000734051 & 0.000594678 \\ & & 0.278557 & 0.00140304 & -0.00357823 & 0.00046972 \\ & & & 0.0934554 & -0.000180878 & -0.00150657 \\ & & & & 0.093142 & 0.000803539 \\ & & & & & 0.0800707 \end{pmatrix}$$

 (d) Elasticity tensor (*Monchiet et Bonnet*)

$$\begin{pmatrix} 0.268586 & 0.0976564 & 0.0923757 & 0.00122764 & 0.000488133 & 0.00550308 \\ & 0.270013 & 0.0923708 & 0.00550793 & 2.01807e-05 & 0.00723428 \\ & & 0.287934 & 0.00696213 & 0.00241702 & 0.00167797 \\ & & & 0.0977368 & -0.00292154 & -0.00261065 \\ & & & & 0.0971247 & -0.000528594 \\ & & & & & 0.0833768 \end{pmatrix}$$

 (e) Elasticity tensor (*Willot et al.*)

Figure 4.4: The second test tile of periodic material (4.4a) and corresponding effective elastic tensors computed with FEM (4.4b), iterative scheme in CraFT (4.4c) and our implementations of *Monchiet et Bonnet* (4.4d) and *Willot et al.* (4.4e). The following parameters were used: $E_S = 1$, $E_V = 0.001$, $\nu = 0.3$, $\psi = 10^{-4}$.

4.4 Implementation

We have only considered two FFT-based iterative schemes for the 3D homogenization problem of periodic materials, with continuous and discrete Green's operators, were implemented on Python. The methods were employed in the context of periodic cellular materials with both closed and open cells. In this thesis, only linear elastic deformations were considered. As the number of structures to analyze was significantly large, there was the need for an efficient implementation. Thus, in addition to the initial CPU-based instance, two versions of the accelerated GPU-based algorithms were built with CuPy: with precomputation of the Green's operator and the projector tensors and with the repetitive calculation of all the tensors at each iteration when needed.

The first implementation involves the computation of the tensor parameters of the method in the preliminary step. Hence, all this data is stored in RAM during the computational process. When the data is needed for calculations, it is copied from RAM to the buffer of GPU memory. This approach is the fastest of all three used in this work but consumes a significant amount of memory as the tensors are functionals defined on 3D space, and each of them contains 36 independent elements.

The second approach is based on writing explicit expressions on the Green's operator and the convergence criterion and calling these expressions as functions at each iteration when needed. Additional repetitive computations in every step of the iterative algorithms slow down the computational process but allow a reduction of memory usage.

The implementations of the methods were used to compute effective elasticity tensors of the structures computed with the growth method. Although the FFT-based approach with Green's operator is less precise, it proved to suit well for the purposes of this work thanks to its high computational performance and relative implementation simplicity.

4.5 Conclusion and future work

There are multiple possible improvements of the implementations presented here. For example, the algorithm can be better optimized not only for accelerating the computational process but also for structures with large resolutions. In particular, this is an important topic when a GPU with relatively low memory is used (the minimal VRAM consumption for my implementations for a periodic tile of $80 \times 80 \times 80$ - element resolution is around 300 MB which becomes 2.4 GB if one doubles the resolution). In this case, the data can be manipulated in blocks being subsequently transferred between the RAM and the VRAM.

Moreover, when the growth method is implemented with nonregular computational grids associated with Bravais lattices, the homogenization methods should also be adapted to the corresponding grid. In this case, the main difficulty is to implement the Fourier transform in the given non-orthogonal basis.

Finally, the topic of convergence of the iterative schemes is not trivial and depends on multiple factors, including the parameters of the model and different convergence tests, which were well studied in the literature. Moreover, my numerical results show a significant effect of the volume fraction between the constituent materials on the convergence of the iterative process. This topic is more complicated to investigate and, in my opinion, requires further studies. Indeed, it occurs that the proportion in the occupied volume between two different constituents, especially for high contrast in Young's modulus, may affect how fast the method converges. In [90] it was pointed out and demonstrated theoretically, that although the material microgeometry does not define the fact of convergence it affects the convergence rate of the iterative process. I assume, that the material proportion changes the microgeometry and, thus, can be considered as a parameter associated with it. Therefore, I believe that the convergence speed variations observed in the results presented here are strongly connected to the discussion about the microgeometry of materials from [90].

Chapter 5

Procedural phasor noise

5.1 Notations

Notation	Definition	First introduced
\mathcal{G}	Gabor noise	Equation 5.1
g	Gabor kernel	Equation 5.2
\vec{F}	Frequency and directional field of a noise	Equation 5.2
γ	Phase of a Gabor kernel	Equation 5.2
K	Amplitude of a Gabor kernel	Equation 5.2
b	Bandwidth of a Gabor kernel	Equation 5.2
\vec{x}_0	Position of a Gabor kernel in space	Equation 5.2
Ψ	phasor noise	Equation 5.4
\mathcal{I}	Inesity function of a Gabor noise	Equation 5.4
\sin	Phasor sinewave	Equation 5.5
\mathcal{G}	Complex Gabor noise	Equation 5.7
\mathcal{V}	Variance of a noise	Equation 5.9
\mathcal{E}	Mahtematical expectation	Equation 5.9
\mathcal{V}_G	Variance of a Gabor noise	Equation 5.10
\mathcal{V}_Ψ	Variance of a Phasor sinewave	Equation 5.11
\mathcal{F}	Fourier transform	Equation 5.12
ξ	Frequency vector	Equation 5.12
\mathcal{F}_D	Discrete Fourier transform	Equation 5.14
θ	Direction angle of a Gabor kernel	Equation 5.17

Table 5.1: Notations for Chapter 5.

5.2 Introduction

Methods originated in the field of computer graphics (namely texture synthesis) can be successfully used for architecturing solid composites ([127], [58], [137]). The methods for texture synthesis can be divided into two categories: data-driven [230] and procedural [107] approaches. Data-driven methods are usually based on reproducing with some precision an input data pattern (example) which usually requires an optimization process. These peculiarities result in relatively high computational time and significant memory requirements. On the other hand, procedural approaches are based on generation of a structure with a single procedure represented by a function. These methods usually provide high computational efficiency and low memory costs. The main challenge for employing procedural methods is that usually these models have a number of parameters and finding the values of these parameters to conform to a targeted result is not trivial (especially when specific physical properties are under consideration). Nevertheless, some works ([83], [75], [116], [218]) proved that one can benefit from the features of the procedural approach not only in direct generation of a family of materials but also in inverse material design. From now on, let us discuss the topic of the texture synthesis.

Most methods dedicated to procedural generation of patterns are based on procedural noise functions [107]. The procedural noise function generates a field with spatial structure corresponding to a given frequency distribution. Different types of procedural noises are often combined in order to reproduce complex patterns [62]. The main limitation of a standart procedural noise is no control over local characteristics of the generated patterns. The texture's sharpness, contrast and its local values' range and histogram simply cannot be set directly except partial control through thresholding a base noise, or through employing lookup tables (color maps) for reshaping the global histogram of the noise. Moreover, noise patterns generally suffer from some negative effects such as local loss of contrast or undesired variations of scales and orientations. The presence of these defects make it difficult to obtain a cosistent result through lookup tables or other methods for controlling the noise profile. In addition, lookup tables cannot distinguish between different 'sides' of an oscillation and thus does not allow synthesis of assymetric wave patterns.

In this chapter we discuss a procedural noise – phasor noise – which provides an ability to generate patterns exhibiting precisely controllable oscillations, in terms of their profile shape, minimum /maximum values, orientation and frequencies (scale). Moreover, the obtained patterns' parameters can be graded within planes (2D) and volumes (3D). Phasor noise also can be defined on surfaces (for surface noise see [108]) which can be used for patterns synthesis along an object changing its appearance and a surface roughness profile. In addition, our approach can be extended to 3D case and applied for generating heterogeneous microstructures within macroscopic objects. Contrary to most of existing techniques, phasor noise is represented not by a scalar field of values but rather a phase field which is ment to be subsequently modulated through a periodic function. The result of applying a periodic function to phasor noise is

a pattern with prescribed parameters: frequency and orientation. This feature provides full control over the oscillations profile allowing reproducing any sort of shapes (even assymmetric).

Feeding phasor noise to a sinewave produces a signal which resembles Gabor noise. It has similar spectrum but exhibits corrected uniform local contrast. Therefore, in this chapter we will perform theoretical analysis of spectrum of phasor noise and its variance and compare it to Gabor noise.

The work dedicated to study of phasor noise was carried out jointly with Thibault Tricard. My contribution was focused on the analysis and understanding on the noise behavior in terms of its spectral properties.

5.3 Notations and formulation of the problem

5.3.1 Gabor noise

We first define the main terms used in this chapter. In our work we use the model of Gabor noise and some of the results obtained in prior research. Gabor noise is a random field with zero average defined as a sum of n Gabor kernels [76]:

$$\mathcal{G}(\vec{x}) = \sum_{i=1}^n g(\vec{x} - (\vec{x}_0)_i, \vec{F}_i, \gamma_i, K_i, b_i), \quad (5.1)$$

where each kernel $g(\vec{x} - \vec{x}_0, \vec{F}, \gamma, K, b)$ is defined by a random point $\vec{x}_0 \in \mathbb{R}^3$ of the kernel's center, its frequency vector $\vec{F} \in \mathbb{R}^3$, a random phase $\gamma \in \mathbb{R}$, an amplitude $K \in \mathbb{R}$ and a bandwidth $b \in \mathbb{R}$ parameters:

$$g(\vec{x} - \vec{x}_0, \vec{F}, \gamma, a) = K \exp^{-b\|\vec{x} - \vec{x}_0\|^2} \sin(2\pi\vec{F} \cdot (\vec{x} - \vec{x}_0) + \gamma). \quad (5.2)$$

For further convenience, the Equation 5.1 can be rewritten as:

$$\mathcal{G}(\vec{x}) = \sum_{i=1}^n a_i(\vec{x} - (\vec{x}_0)_i) \sin \psi_i(\vec{x} - (\vec{x}_0)_i), \quad (5.3)$$

In this work, the 2D case is considered. Therefore $\vec{x} = (x^1, x^2)$, $\vec{x}_0 = (x_0^1, x_0^2)$, and $\vec{F} = (F^1, F^2)$. Nevertheless, all the definitions can be extended to the 3D case without loss of generality.

5.3.2 Phasor noise

The underlying idea of our work is that under a sequence of analytical transformations the Gabor noise can be represented by the intensity function $\mathcal{I}(\vec{x})$ and phasor noise $\Psi(\vec{x})$:

$$\mathcal{G}(\vec{x}) = \mathcal{I}(\vec{x}) \sin \Psi(\vec{x}). \quad (5.4)$$

This representation provides two major benefits. First, the noise is explicitly divided into two terms that have different functions: the intensity which defines the local amplitude (and is "responsible" for the local loss of contrast) and the oscillatory part represented by perfect sinusoidal fluctuations. As a result, it is possible to eliminate the intensity part and thus reach high contrast of the noise. The second advantage is the ability to control the profile of the fluctuations. Following the Equation 5.4, the *sin* function governed by phasor field $\Psi(\vec{x})$ can be replaced by any bounded spatially periodic function f . From now on, we will denote the function:

$$\sin(\vec{x}) = \sin \Psi(\vec{x}) \quad (5.5)$$

phasor sinwave and an instantaneous phase field Ψ – phasor noise.

5.3.3 Complex Gabor noise

Here we denote $Re\{z\}$ and $Im\{z\}$ as the imaginary and real parts of a complex number z , respectively. The argument of z is defined as $Arg\{z\} = \arctan \frac{Im\{z\}}{Re\{z\}}$. Since Gabor noise is represented in Equation 5.4 by multiplication of the intensity and sinewave fluctuative term it is possible to define it through complex exponent function:

$$\mathcal{G}(\vec{x}) = Im\{\mathcal{G}(\vec{x})\}. \quad (5.6)$$

The function $\mathcal{G}(\vec{x})$ is called complex Gabor noise and is defined as follows:

$$\mathcal{G}(\vec{x}) = \mathcal{I}(\vec{x}) e^{i\Psi(\vec{x})}. \quad (5.7)$$

Finally, the phasor noise is given by the argument of 5.7:

$$\Psi(\vec{x}) = Arg\{\mathcal{G}(\vec{x})\}. \quad (5.8)$$

5.3.4 Noise variance

In addition, an important tool widely used for analysis of noise properties is its variance. The non-averaged squared deviation of a noise from the mean (for further simplicity it is called variance, please, do not confuse it with the classical definition of variance) contains important information about spatial structure of a generated pattern such as local loss of amplitude and some filtering techniques can be employed to improve the noise contrast [158]. Let us define the variance $\mathcal{V}(\vec{x})$ of a noise $Y(\vec{x})$ as follows:

$$\mathcal{V}(\vec{x}) = \left(Y(\vec{x}) - \mathcal{E}[Y(\vec{x})] \right)^2. \quad (5.9)$$

Therefore, since the the average $\mathcal{E}[\cdot]$ of Gabor noise and phasor sinewave are equal to zero their variance $\mathcal{V}_{\mathcal{G}}(\vec{x})$ and $\mathcal{V}_{\Psi}(\vec{x})$ can be calculated as follows:

$$\mathcal{V}_G(\vec{x}) = (\mathcal{G}(\vec{x}))^2. \quad (5.10)$$

$$\mathcal{V}_\Psi(\vec{x}) = (\sin(\vec{x}))^2. \quad (5.11)$$

5.3.5 Fourier transform

In this work the Gabor and phasor sinewave characteristics were analyzed in Fourier space. To map a function $f(\vec{x})$ into Fourier space, we consider 2D Fourier transform:

$$\mathcal{F}[f](\vec{\xi}) = \hat{f}(\vec{\xi}) = \frac{1}{2\pi} \int_{\mathbb{R}^2} f(\vec{x}) e^{i\vec{\xi} \cdot \vec{x}} d\vec{x}, \quad (5.12)$$

where $\vec{\xi} = (\xi^1, \xi^2)$ is a frequency vector. The inverse transform is defined then as follows:

$$\mathcal{F}^{-1}[\hat{f}](\vec{x}) = \frac{1}{2\pi} \int_{\mathbb{R}^2} \hat{f}(\vec{\xi}) e^{-i\vec{\xi} \cdot \vec{x}} d\vec{\xi}, \quad (5.13)$$

For numerical computation of the spectrum the discrete analog of Fourier transform in Equations 5.12, 5.13 was used:

$$\mathcal{F}_D[f]_{k,l} = \hat{f}_{k,l} = \frac{1}{2\pi} \sum_{i,j=1}^M f_{i,j} e^{i(ki+lj)}, \quad (5.14)$$

$$\mathcal{F}_D^{-1}[f]_{i,j} = \frac{1}{2\pi N} \sum_{k,l=1}^M \hat{f}_{k,l} e^{-i(ki+lj)}. \quad (5.15)$$

For a more complete presentation of the model of phasor noise we will develop it in progressive steps. First, we will consider the most simple case of a bi-lobe noise where all the kernels are oriented in the same direction. Then we will move to a case with two different directions. Finally, we will extend the model to a case of an arbitrary composition of multiple kernels' orientations.

5.4 Bi-lobe case

We start with the simplest case of Gabor noise: all the kernels oriented in the same direction. Hence, all Gabor kernels have the same frequency vector \vec{F} . Then, the Gabor noise can be derived as:

$$\mathcal{G}(\vec{x}) = \sum_{i=1}^n a_i(\vec{r}_i) \sin(2\pi\vec{F} \cdot \vec{r}_i + \psi_i) = \sum_{i=1}^n a_i(\vec{r}_i) \sin(2\pi\vec{F} \cdot \vec{x} + u_i) \quad (5.16)$$

where $\vec{r}_i = \vec{x} - (\vec{x}_0)_i$ and $u_i = 2\pi\vec{F} \cdot (\vec{x}_0)_i + \psi_i$. An angle θ of bi-lobe Gabor noise with respect to the x -axis is defined as follows:

$$\vec{F} = \|\vec{F}\| (\cos \theta, \sin \theta). \quad (5.17)$$

By applying a sequence of transformations using simple trigonometric formulas we obtain an expression for the intensity:

$$\mathcal{I}(\vec{x}) = \sqrt{\left(\sum_{i=1}^n a_i(\vec{r}_i) \sin u_i\right)^2 + \left(\sum_{i=1}^n a_i(\vec{r}_i) \cos u_i\right)^2} \quad (5.18)$$

and the phasor field:

$$\Psi(\vec{x}) = 2\pi\vec{F} \cdot \vec{x} + u(\vec{x}) = 2\pi\vec{F} \cdot \vec{x} + \arctan \frac{\sum_{i=1}^n a_i(\vec{r}_i) \sin u_i}{\sum_{i=1}^n a_i(\vec{r}_i) \cos u_i}. \quad (5.19)$$

5.4.1 Spectrum of the intensity

Before the analysis of Gabor noise and phasor sinewave it is important to consider the intensity field (Equation 5.18). The square intensity will appear in the variance of Gabor noise and will help to obtain variance of phasor sinewave. Therefore, it will be useful to calculate its spectrum. Taking the square of the Equation 5.18 and applying the Fourier transform, it is possible to obtain an analytical expression for the spectrum of the intensity $\mathcal{F}[\mathcal{I}^2]$:

$$\mathcal{F}[\mathcal{I}^2](\vec{\xi}) = \sum_{i=1}^n e^{-\frac{\xi^2}{4b_i}} e^{i\vec{\xi} \cdot \vec{x}_i} C_{1,i} + \sum_{i=1}^n e^{-\frac{\xi^2}{4(b_i+b_j)}} e^{i\vec{\xi} \cdot \frac{(b_i\vec{x}_i+b_j\vec{x}_j)}{4(b_i+b_j)}} C_{2,ij}, \quad (5.20)$$

with constant values $(C_{1,i})$, $(C_{2,ij})$ which do not depend on $\vec{\xi}$:

$$C_{1,i} = K_i^2 \frac{(\sin^2 \psi_i + \cos^2 \psi_i)}{2\pi\sqrt{2b_i}}, \quad (5.21)$$

$$C_{2,ij} = K_i K_j e^{-\frac{b_i b_j (\vec{x}_i^2 + \vec{x}_j^2 - \vec{x}_i \cdot \vec{x}_j)}{(b_i + b_j)}} \frac{(\sin^2 \psi_i + \cos^2 \psi_i)}{2\pi\sqrt{2(b_i + b_j)}}. \quad (5.22)$$

We observe that the squared intensity spectrum is represented by a combination of Gaussian functions of frequency centered at $\vec{\xi} = 0$ multiplied by complex exponents. Therefore, the bandwidth of this spectrum is governed by the width $(4b_i$ and $4(b_i + b_j))$ of the Gaussian functions which is defined by the bandwidth parameters of the Gabor kernels. Finally, we conclude that the intensity spectrum contains only low frequencies with the width strictly bounded by the bandwidth of the considered set of Gabor kernels.

5.4.2 Spectrum of Gabor noise

As Gabor noise is defined as a sum of kernels with their frequency and amplitude characteristics (see Equation 5.3) its spectrum is formed by a sum of the Fourier transforms of these kernels. Due to the fact that a Gabor kernel is a multiplication of a Gaussian function and a sinewave in Fourier space, it becomes a convolution of a corresponding gaussian function and two delta-functions originated by the sinewave and centered at corresponding frequencies. Therefore, a Gabor kernel in Fourier space is represented by two equivalent Gaussians centered at frequencies corresponding to the constituent sinewave (see figure 5.1).

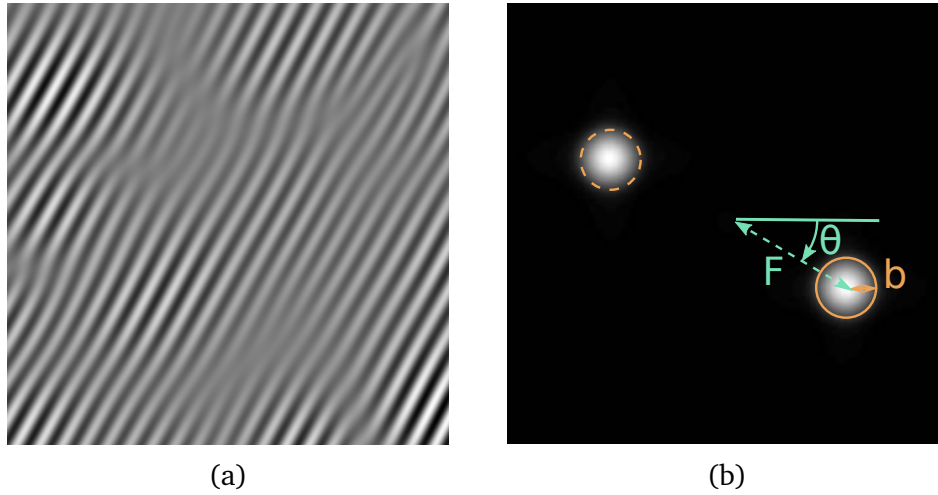


Figure 5.1: Bi-lobe Gabor noise (a) and its spectrum (b).

In the bi-lobe case, all the kernels share the same frequency \vec{F} . Thus, the resulting spectral image of the noise is represented by two lobes symmetrically opposed to the point $\vec{\xi} = 0$. Each of these lobes is centered at points (F^1, F^2) and $(-F^1, -F^2)$ respectively.

The spectrum of Gabor noise can be obtained directly following Equation 5.3:

$$\mathcal{F}[\mathcal{G}](\vec{\xi}) = \sum_{i=1}^n \frac{K_i}{\sqrt{8b_i}} \left(e^{-ib_i} e^{\frac{(\xi_i - F_i)^2}{4b_i}} e^{i\vec{x}_i(\vec{\xi} - \vec{F})} - e^{ib_i} e^{\frac{(\xi_i + F_i)^2}{4b_i}} e^{i\vec{x}_i(\vec{\xi} + \vec{F})} \right). \quad (5.23)$$

5.4.3 Variance spectrum of Gabor noise

As it was mentioned above a common drawback of procedural noises (and Gabor noise in particular) is the local loss of contrast. Moreover, it is known that information about the contrast contained in the variance spectrum of the noise. For Gabor noise in bi-lobe case the variance can be simplified as follows:

$$\begin{aligned}
 \mathcal{V}_G(\vec{x}) &= \left(\sin(2\pi\vec{F}\cdot\vec{x}) \sum_{i=1}^n a_i(\vec{r}_i) \cos(u_i) + \right. \\
 &\quad \left. + \cos(2\pi\vec{F}\cdot\vec{x}) \sum_{i=1}^n a_i(\vec{r}_i) \sin(u_i) \right)^2 = \\
 &= \frac{1}{2}\mathcal{I}(\vec{x}) + \sin(4\pi\vec{F}\cdot\vec{x}) \sum_{i,j=1}^n a_i(\vec{r}_i) a_j(\vec{r}_j) \sin(u_i) \cos(u_j) - \\
 &\quad - \frac{1}{2} \cos(4\pi\vec{F}\cdot\vec{x}) \sum_{i,j=1}^n a_i(\vec{r}_i) a_j(\vec{r}_j) (\cos(u_i) \cos(u_j) - \\
 &\quad - \sin(u_i) \sin(u_j)). \quad (5.24)
 \end{aligned}$$

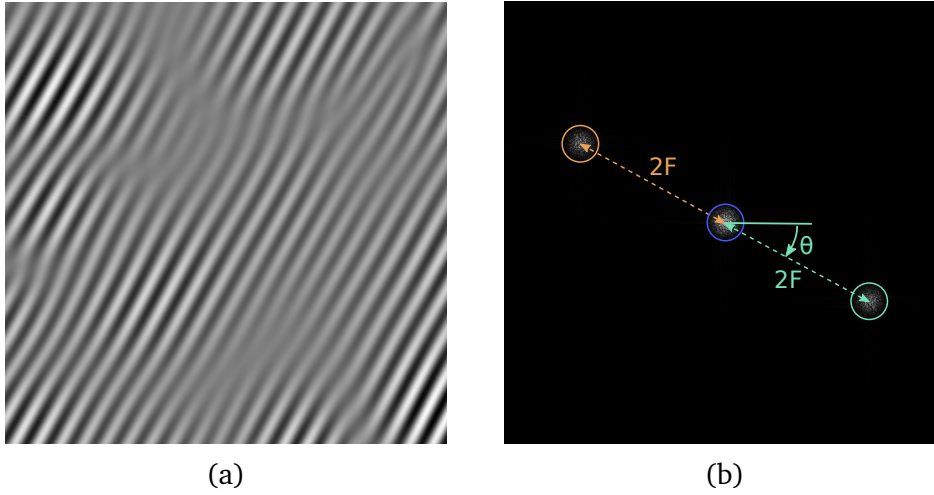


Figure 5.2: Bi-lobe Gabor noise (a) and its variance spectrum (b). Two lobes located at doubled frequencies are marked with orange and green circles and the low-frequency component (blue circle) is centered at $\vec{\xi} = 0$.

Furthermore, applying to the resulting expression in Equation 5.24 the Fourier transform and convolution theorem we can calculate the variance spectrum:

$$\begin{aligned}
 \mathcal{F}[\mathcal{V}_G](\vec{\xi}) &= \frac{1}{2}\mathcal{F}[\mathcal{I}](\vec{\xi}) + i \sum_{i,j=1}^n \left(\mathfrak{E}_{i,j}(\vec{\xi} - 4\pi\vec{F}) - \mathfrak{E}_{i,j}(\vec{\xi} + 4\pi\vec{F}) \right) \sin(u_i) \cos(u_j) \\
 &+ \sum_{i,j=1}^n \left(\mathfrak{E}_{i,j}(\vec{\xi} - 4\pi\vec{F}) + \mathfrak{E}_{i,j}(\vec{\xi} + 4\pi\vec{F}) \right) \left(\cos(u_i) \cos(u_j) - \sin(u_i) \sin(u_j) \right), \\
 \mathfrak{E}_{i,j}(\vec{\xi}) &= \frac{\pi}{2(b_i + b_j)} e^{-\frac{\vec{\xi}^2}{4(b_i + b_j)}} e^{i\frac{\vec{\xi} \cdot (b_i \vec{x}_i + b_j \vec{x}_j)}{b_i + b_j}} e^{-\frac{(\vec{x}_i - \vec{x}_j)^2}{b_i + b_j}}. \quad (5.25)
 \end{aligned}$$

The spectrum expression in Equation 5.25 consists of one low-frequency component (the intensity spectrum) that is a lobe centered at $\bar{\xi} = 0$ and four high-frequency components which form two lobes at doubled frequencies $\bar{\xi} \pm 4\pi\bar{F}$ the ones observed in the Gabor noise spectrum (Figure 5.2). Thus, we have shown analytically that the low frequency component $\frac{1}{2}\mathcal{F}[\mathcal{I}](\bar{\xi})$ of Gabor noise variance spectrum is formed only by its intensity which reflects the local loss of contrast.

5.4.4 Spectrum of phasor sinewave

To analyze the spectrum of phasor sinewave we refer to the Equation 5.19. In this case, the sinewave of phasor noise can be transformed into the following form which is convenient for applying Fourier transform:

$$\begin{aligned} \sin(\bar{x}) &= \sin \left\{ 2\pi\bar{F} \cdot \bar{x} + \arctan \frac{\sum_{i=1}^n a_i(\bar{r}_i) \sin u_i}{\sum_{i=1}^n a_i(\bar{r}_i) \cos u_i} \right\} = \\ &= \sin(2\pi\bar{F} \cdot \bar{x}) \mathfrak{T}_1(\bar{x}) + \cos(2\pi\bar{F} \cdot \bar{x}) \mathfrak{T}_2(\bar{x}), \quad (5.26) \\ \mathfrak{T}_1(\bar{x}) &= \left(1 + \frac{\left(\sum_{i=1}^n a_i(\bar{r}_i) \sin u_i \right)^2}{\left(\sum_{i=1}^n a_i(\bar{r}_i) \cos u_i \right)^2} \right)^{-\frac{1}{2}}, \\ \mathfrak{T}_2(\bar{x}) &= \left(1 + \frac{\left(\sum_{i=1}^n a_i(\bar{r}_i) \cos u_i \right)^2}{\left(\sum_{i=1}^n a_i(\bar{r}_i) \sin u_i \right)^2} \right)^{-\frac{1}{2}}. \end{aligned}$$

Here the functions $\mathfrak{T}_1(\bar{x})$ and $\mathfrak{T}_2(\bar{x})$ are bounded and continuous in all domain. Nevertheless, difficulty with definition occurs at the points where the intensity $\mathcal{I}(\bar{x})$ goes to zero. Indeed, the ratio $\frac{\left(\sum_{i=1}^n a_i(\bar{r}_i) \sin u_i \right)^2}{\left(\sum_{i=1}^n a_i(\bar{r}_i) \cos u_i \right)^2}$, $\frac{\left(\sum_{i=1}^n a_i(\bar{r}_i) \cos u_i \right)^2}{\left(\sum_{i=1}^n a_i(\bar{r}_i) \sin u_i \right)^2}$ produce singularities of $\frac{0}{0}$ -type when both components in 5.18 are equal to zero. At these singular points, one can visually observe in the phasor sinewave some "spiky" effects (see Figure 5.3). The problem of finding the limit of these functions at the indeterminate points is discussed in Section 5.7.

Nevertheless, taking Fourier transform of 5.27 and employing the convolution theorem one can obtain simplified spectrum decomposition:

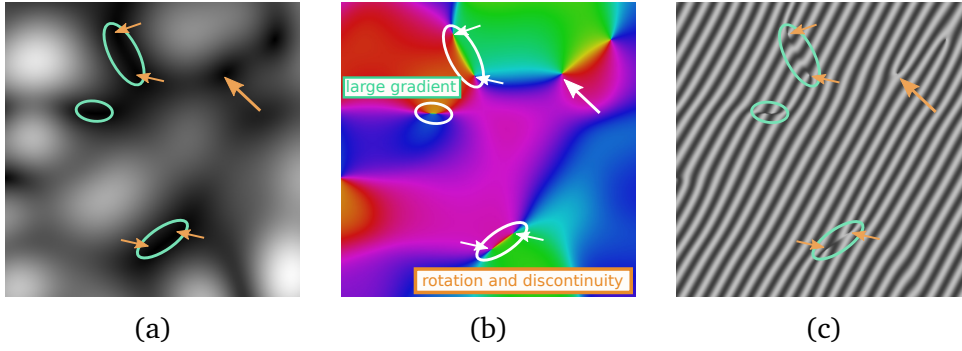


Figure 5.3: When the intensity field (a) of Gabor noise fades its reflects in discontinuities and large gradient points in the corresponding phasor field (b) which in turn results in discontinuities of the phasor sinewave (c).

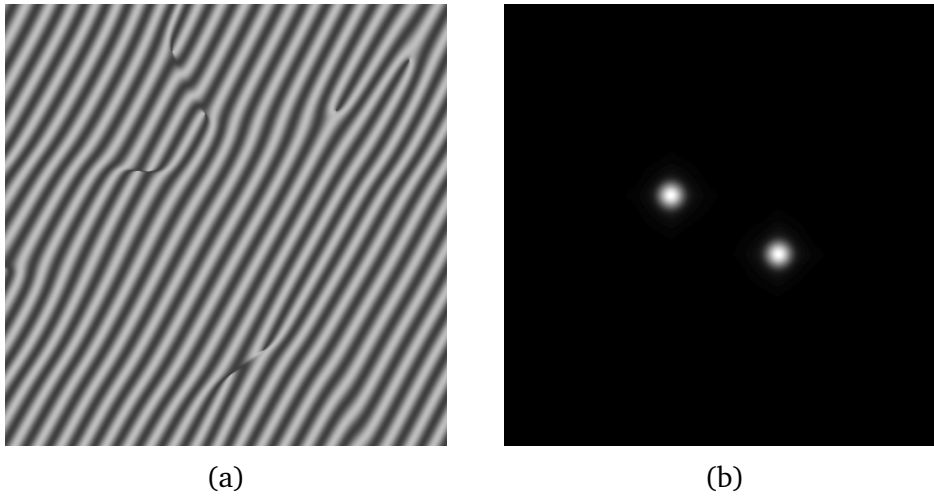


Figure 5.4: Bi-lobe phasor sinewave (a) and its spectrum (b).

$$\mathcal{F}[\sin](\vec{\xi}) = \left(\mathcal{F}[\sin(2\pi\vec{F}\cdot\vec{x})] \otimes \mathcal{F}[\mathfrak{T}_1] \right)(\vec{\xi}) + \left(\mathcal{F}[\cos(2\pi\vec{F}\cdot\vec{x})] \otimes \mathcal{F}[\mathfrak{T}_2] \right)(\vec{\xi}) = \quad (5.27)$$

$$= \delta(\vec{\xi} - 2\pi\vec{F}) \otimes (\mathcal{F}[\mathfrak{T}_2] + i\mathcal{F}[\mathfrak{T}_1])(\vec{\xi}) + \delta(\vec{\xi} + 2\pi\vec{F}) \otimes (\mathcal{F}[\mathfrak{T}_2] - i\mathcal{F}[\mathfrak{T}_1])(\vec{\xi}) = \quad (5.28)$$

$$= (\mathcal{F}[\mathfrak{T}_2] + i\mathcal{F}[\mathfrak{T}_1])(\vec{\xi} - 2\pi\vec{F}) + (\mathcal{F}[\mathfrak{T}_2] - i\mathcal{F}[\mathfrak{T}_1])(\vec{\xi} + 2\pi\vec{F}).$$

Thus, following the Equation 5.28 and numerically computed spectrum (figure 5.4) convolution (by its definition) of the delta-functions centered at $\vec{\xi} = \pm 2\pi\vec{F}$ brings the low-frequency lobes $\mathcal{F}[\mathfrak{T}_1](\vec{\xi})$, $\mathcal{F}[\mathfrak{T}_2](\vec{\xi})$ to the frequencies $\vec{\xi} = -2\pi\vec{F}$ and $\vec{\xi} = 2\pi\vec{F}$ of a corresponding instance of Gabor noise with comparable bandwidth (Figure 5.4).

5.4.5 Variance spectrum of phasor sinewave

The variance of phasor sinewave is obtained by applying the same technique as in Equation 5.27:

$$\begin{aligned} \nu_\psi(\vec{x}) &= \left(\sin(2\pi\vec{F}\cdot\vec{x})\mathfrak{T}_1(\vec{x}) + \cos(2\pi\vec{F}\cdot\vec{x})\mathfrak{T}_2(\vec{x}) \right)^2 = \frac{1}{2} + \\ &+ \sin(4\pi\vec{F}\cdot\vec{x})\mathfrak{T}_1(\vec{x})\mathfrak{T}_2(\vec{x}) - \frac{1}{2}\cos(4\pi\vec{F}\cdot\vec{x})\left(\mathfrak{T}_2^2(\vec{x}) - \mathfrak{T}_1^2(\vec{x})\right). \end{aligned} \quad (5.29)$$

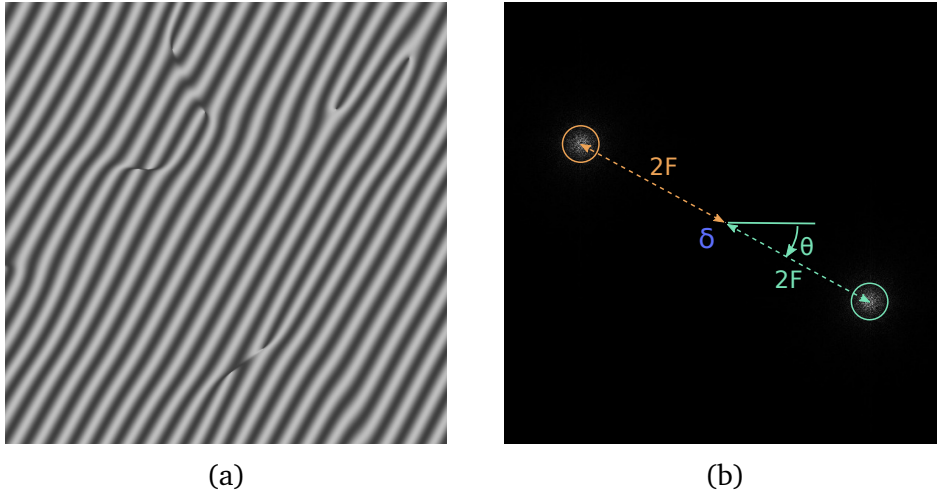


Figure 5.5: Bi-lobe phasor sinewave (a) and its variance spectrum (b). Two lobes located at doubled frequencies are marked with orange and green circles and delta-function is centered at $\vec{\xi} = 0$.

Finally, the Equation 5.30 shows that the phasor sinewave spectrum of variance (see Figure 5.5) in the bi-lobe case does not contain any low-frequency components except the delta-function at $\vec{\xi} = 0$ which results in perfect contrast of the noise in all domain. The other four terms form two lobes centered at frequencies $\vec{\xi} = \pm 4\pi\vec{F}$.

Employing Fourier transform with the convolution theorem allows one to obtain an expression for the variance spectrum:

$$\begin{aligned} \mathcal{F}[\nu_\psi](\vec{\xi}) &= \frac{1}{4\pi}\delta(\vec{\xi}) - \frac{1}{2}\left(\frac{1}{2}\mathcal{F}[\mathfrak{T}_2^2] - \frac{1}{2}\mathcal{F}[\mathfrak{T}_1^2] + i\mathcal{F}[\mathfrak{T}_1\mathfrak{T}_2]\right)(\vec{\xi} - 4\pi\vec{F}) + \\ &+ \frac{1}{2}\left(\frac{1}{2}\mathcal{F}[\mathfrak{T}_2^2] - \frac{1}{2}\mathcal{F}[\mathfrak{T}_1^2] - i\mathcal{F}[\mathfrak{T}_1\mathfrak{T}_2]\right)(\vec{\xi} + 4\pi\vec{F}). \end{aligned} \quad (5.30)$$

Here the functions $\mathfrak{T}_1(\vec{x})$, $\mathfrak{T}_2(\vec{x})$ are the same as defined in Subsection 5.4.4 and are bounded in all domain and continuous except the points where the intensity function $\mathcal{I}(\vec{x})$ goes to zero. Therefore, the functions $\mathfrak{T}_1^2(\vec{x})$, $\mathfrak{T}_2^2(\vec{x})$, and $\mathfrak{T}_1(\vec{x})\mathfrak{T}_2(\vec{x})$ are also bounded in all domain and continuous except the points where $\mathcal{I}(\vec{x}) = 0$.

5.5 Two-directional case

The next case to be considered is when Gabor noise contain n_1 and $n - n_1$ kernels with two different directions \vec{F}_1 and \vec{F}_2 respectively. In this case it is possible to define the noise as sum of two bi-lobe Gabor noises:

$$\mathcal{G}(\vec{x}) = \mathcal{G}_1(\vec{x}) + \mathcal{G}_2(\vec{x}) = \sum_{i=1}^{n_1} a_i(\vec{r}_i) \sin(2\pi\vec{F}_1 \cdot \vec{x} + u_{1,i}) + \sum_{j=n_1+1}^n a_j(\vec{r}_j) \sin(2\pi\vec{F}_2 \cdot \vec{x} + u_{2,j}). \quad (5.31)$$

However, it becomes complicated to obtain the single sinewave representation as in Equation 5.4. To do so we introduce a difference term $\vec{F}_{\Delta^-} = \vec{F}_2 - \vec{F}_1$ and a sum $\vec{F}_{\Delta^+} = \vec{F}_2 + \vec{F}_1$ of two directions. The angle between these two directions is $|\theta_2 - \theta_1|$. Note that $\vec{F}_{\Delta^-} < \vec{F}_{\Delta^+}$ in this work, but assuming the opposite does not impose any limitations on the results obtained further, except a switch on the notations. Now the other problem occurs: there are two different ways to define the intensity function: through the difference between the directions ($\mathcal{I}_{\Delta^-}(\vec{x})$) and their sum ($\mathcal{I}_{\Delta^+}(\vec{x})$) and it may not be clear what is the difference between these two functions and which one to use in the phasor noise. Both intensities are defined through auxiliary functions:

$$\mathcal{I}_{\Delta^\pm}(\vec{x}) = \left((\mathcal{I}_1(\vec{x}))^2 + (\mathcal{I}_2(\vec{x}))^2 \mp 2 \cos(2\pi\vec{F}_{\Delta^\pm} \cdot \vec{x}) \mathcal{I}_{c,\Delta^\pm}(\vec{x}) \pm \pm 2 \sin(2\pi\vec{F}_{\Delta^\pm} \cdot \vec{x}) \mathcal{I}_{s,\Delta^\pm}(\vec{x}) \right)^{\frac{1}{2}}, \quad (5.32)$$

$$\mathcal{I}_{c,\Delta^\pm}(\vec{x}) = \sum_{i=1}^{n_1} \sum_{j=n_1+1}^n a_i(\vec{r}_i) a_j(\vec{r}_j) \cos(u_{2,j} \pm u_{1,i}),$$

$$\mathcal{I}_{s,\Delta^\pm}(\vec{x}) = \sum_{i=1}^{n_1} \sum_{j=n_1+1}^n a_i(\vec{r}_i) a_j(\vec{r}_j) \sin(u_{2,j} \pm u_{1,i}),$$

where the functions $\mathcal{I}_1(\vec{x})$ and $\mathcal{I}_2(\vec{x})$ denote the intensities of $\mathcal{G}_1(\vec{x})$ and $\mathcal{G}_2(\vec{x})$. Then, the phasor noise can be defined as follows:

$$\Psi_{\Delta^\pm}(\vec{x}) = 2\pi\vec{F}_1 \cdot \vec{x} + u_{\Delta^\pm}(\vec{x}), \quad (5.33)$$

$$u_{\Delta^\pm}(\vec{x}) = \arctan \frac{\mathcal{I}_{1,\Delta^\pm}(\vec{x})}{\mathcal{I}_{2,\Delta^\pm}(\vec{x})}. \quad (5.34)$$

Here the functions $\mathcal{I}_{1,\Delta^\pm}(\vec{x})$, $\mathcal{I}_{2,\Delta^\pm}(\vec{x})$ can be calculated from the following expression:

$$\begin{aligned} \mathcal{I}_{1,\Delta^\pm}(\vec{x}) &= \sum_{i=1}^n \alpha_i(\vec{r}_i) \sin u_{1,i} + \sin(2\pi\vec{F}_{\Delta^\pm} \cdot \vec{x}) \sum_{j=n_1+1}^n \alpha_j(\vec{r}_j) \cos u_{2,j} + \\ &+ \cos(2\pi\vec{F}_{\Delta^\pm} \cdot \vec{x}) \sum_{j=n_1+1}^n \alpha_j(\vec{r}_j) \sin u_{2,j}, \end{aligned} \quad (5.35)$$

$$\begin{aligned} \mathcal{I}_{2,\Delta^\pm}(\vec{x}) &= \sum_{i=1}^n \alpha_i(\vec{r}_i) \cos u_{1,i} \mp \cos(2\pi\vec{F}_{\Delta^\pm} \cdot \vec{x}) \sum_{j=n_1+1}^n \alpha_j(\vec{r}_j) \cos u_{2,j} \pm \\ &\pm \sin(2\pi\vec{F}_{\Delta^\pm} \cdot \vec{x}) \sum_{j=n_1+1}^n \alpha_j(\vec{r}_j) \sin u_{2,j}. \end{aligned} \quad (5.36)$$

5.5.1 Spectrum of the intensity

As it can be seen from Equation 5.32 both intensity functions, besides low-frequency components corresponding to each of bi-lobe noises, contain also an additional term which is not located at $\vec{\xi} = \mathbf{0}$. Indeed, going to Fourier space allows to obtain the spectrum of the intensities:

$$\begin{aligned} \mathcal{F}[\mathcal{I}_{\Delta^\pm}^2](\vec{\xi}) &= \mathcal{F}[\mathcal{I}_1^2](\vec{\xi}) + \mathcal{F}[\mathcal{I}_2^2](\vec{\xi}) \mp (\mathcal{F}[\mathcal{I}_{c,\Delta^\pm}] - i\mathcal{F}[\mathcal{I}_{s,\Delta^\pm}])(\vec{\xi} - 2\pi\vec{F}_{\Delta^\pm}) \mp \\ &\mp (\mathcal{F}[\mathcal{I}_{c,\Delta^\pm}] + i\mathcal{F}[\mathcal{I}_{s,\Delta^\pm}])(\vec{\xi} + 2\pi\vec{F}_{\Delta^\pm}). \end{aligned} \quad (5.37)$$

Additional exponential functions are defined through the equations:

$$\mathcal{F}[\mathcal{I}_{c,\Delta^\pm}](\vec{\xi}) = \sum_{i=1}^{n_1} \sum_{j=n_1+1}^n \mathfrak{E}_{i,j}(\vec{\xi}) \cos(u_{2,j} \pm u_{1,i}) \quad (5.38)$$

$$\mathcal{F}[\mathcal{I}_{s,\Delta^\pm}](\vec{\xi}) = \sum_{i=1}^{n_1} \sum_{j=n_1+1}^n \mathfrak{E}_{i,j}(\vec{\xi}) \sin(u_{2,j} \pm u_{1,i}). \quad (5.39)$$

Here the exponential terms $\mathfrak{E}_{i,j}(\vec{\xi})$ are defined in the Equation 5.25. Thus, the spectrum of the intensity functions contains a low-frequency component equal to the sum of the intensities of the corresponding bi-lobe noises and two lobes centered at $\vec{\xi} = \pm 2\pi\vec{F}_{\Delta^-}$ for $\mathcal{I}_{\Delta^-}(\vec{x})$ or at $\vec{\xi} = \pm 2\pi\vec{F}_{\Delta^+}$ in case of $\mathcal{I}_{\Delta^+}(\vec{x})$.

5.5.2 Spectrum of Gabor noise

The spectrum of Gabor noise in the case of two directions thanks to additivity of Fourier transform can be calculated as a sum of spectrums of the corresponding bi-lobe Gabors in the Equation 5.31:

$$\begin{aligned}
 \mathcal{F}[\mathcal{G}](\vec{\xi}) &= \mathcal{F}[\mathcal{G}_1](\vec{\xi}) + \mathcal{F}[\mathcal{G}_2](\vec{\xi}) = \\
 &= \sum_{i=1}^{n_1} \frac{K_i}{\sqrt{8b_i}} \left(e^{-ib_i} e^{\frac{(\xi-\bar{F}_1)^2}{4b_i}} e^{i\bar{x}_i(\xi-\bar{F}_1)^2} - e^{ib_i} e^{\frac{(\xi+\bar{F}_1)^2}{4b_i}} e^{i\bar{x}_i(\xi+\bar{F}_1)^2} \right) + \\
 &+ \sum_{j=n_1+1}^n \frac{K_j}{\sqrt{8b_j}} \left(e^{-ib_j} e^{\frac{(\xi-\bar{F}_2)^2}{4b_j}} e^{i\bar{x}_j(\xi-\bar{F}_2)^2} - e^{ib_j} e^{\frac{(\xi+\bar{F}_2)^2}{4b_j}} e^{i\bar{x}_j(\xi+\bar{F}_2)^2} \right).
 \end{aligned} \tag{5.40}$$

Therefore, the spectrum of two-directional Gabor noise consists of two lobes centered at frequencies $\vec{\xi} = \pm 2\pi\bar{F}_1$ and the other two located at $\vec{\xi} = \pm 2\pi\bar{F}_2$.

5.5.3 Variance spectrum of Gabor noise

Taking Equation 5.31 and applying the variance definition in Equation 5.10 one can obtain an expression for the variance of Gabor noise:

$$\mathcal{V}_{\mathcal{G}}(\vec{x}) = \mathcal{V}_{\mathcal{G}_1}(\vec{x}) + \mathcal{V}_{\mathcal{G}_2}(\vec{x}) + 2\mathcal{G}_1(\vec{x})\mathcal{G}_2(\vec{x}). \tag{5.41}$$

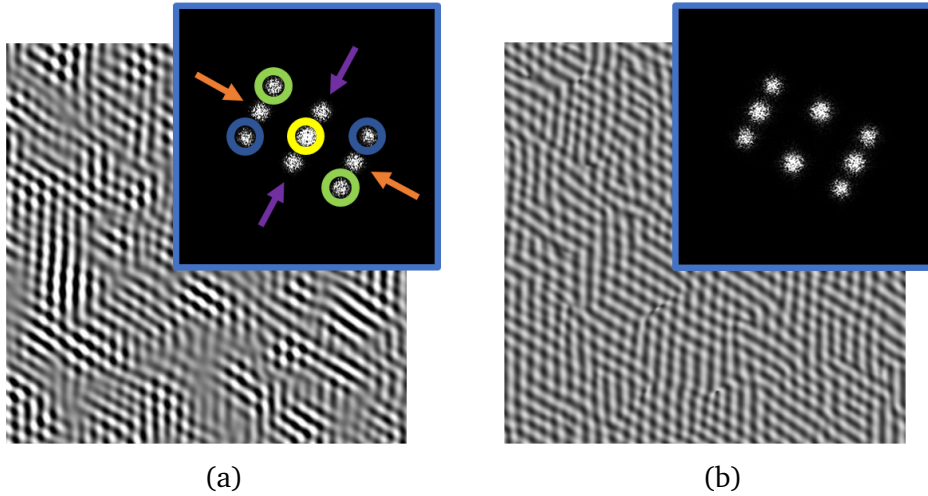


Figure 5.6: Two-directional Gabor noise (a) and its normalized version without low-frequency components in its variance spectrum. On each picture there is the noise (background) and its variance spectrum (top right). A yellow circle denotes the low-frequency component, blue and green circles show the high-frequency lobes of two bi-lobe noises' variance spectrum, and orange and purple arrows correspond to the $\bar{F}_{\Delta+}$ and $\bar{F}_{\Delta-}$ components respectively.

Here, the first two components $\mathcal{V}_{\mathcal{G}_1}(\vec{x})$ and $\mathcal{V}_{\mathcal{G}_2}(\vec{x})$ denote the variance of two constituent bi-lobe Gabor noises. The spectrum of these two terms was given in Subsection 5.4.3. On the other hand, the multiplication of bi-lobe

noises $2\mathcal{G}_1(\vec{x})\mathcal{G}_2(\vec{x})$ has not been analyzed yet. It is possible to obtain an equation expressing this term:

$$\begin{aligned} \mathcal{G}_1(\vec{x})\mathcal{G}_2(\vec{x}) &= 2 \cos(2\pi\vec{F}_{\Delta^-} \cdot \vec{x}) \mathcal{I}_{c,\Delta^-}(\vec{x}) - 2 \sin(2\pi\vec{F}_{\Delta^-} \cdot \vec{x}) \mathcal{I}_{s,\Delta^-}(\vec{x}) - \\ &- 2 \cos(2\pi\vec{F}_{\Delta^+} \cdot \vec{x}) \mathcal{I}_{c,\Delta^+}(\vec{x}) + 2 \sin(2\pi\vec{F}_{\Delta^+} \cdot \vec{x}) \mathcal{I}_{s,\Delta^+}(\vec{x}). \end{aligned} \quad (5.42)$$

Therefore, the spectrum of the variance (Figure 5.6 (a)) is formed by the spectrum of variance of two bi-lobe Gabors and spectrum of their multiplication:

$$\mathcal{F}[\mathcal{V}_{\mathcal{G}}](\vec{\xi}) = \mathcal{F}[\mathcal{V}_{\mathcal{G}_1}](\vec{\xi}) + \mathcal{F}[\mathcal{V}_{\mathcal{G}_2}](\vec{\xi}) + \mathcal{F}[\mathcal{G}_1\mathcal{G}_2](\vec{\xi}), \quad (5.43)$$

Thus, from Equation 5.43 it follows that the spectrum of variance contains two low-frequency components centered at $\vec{\xi} = 0$ and four pairs of lobes located at $\vec{\xi} = \pm 4\pi\vec{F}_1$, $\vec{\xi} = \pm 4\pi\vec{F}_2$, $\vec{\xi} = \pm 2\pi\vec{F}_{\Delta^-}$, and $\vec{\xi} = \pm 2\pi\vec{F}_{\Delta^+}$ respectively.

5.5.4 Spectrum of phasor sinewave

Analogously to the case of bi-lobe noise (Subsection 5.4.4), one can represent phasor sinewave as in the Equation 5.27. Two types of phasor sinewave function can be defined depending on the type of intensity function: $\sin_{\Delta^-}(\vec{x}) = \sin \Psi_{\Delta^-}(\vec{x})$ in case of $\mathcal{I}_{\Delta^-}(\vec{x})$ and $\sin_{\Delta^+}(\vec{x}) = \sin \Psi_{\Delta^+}(\vec{x})$ for $\mathcal{I}_{\Delta^+}(\vec{x})$:

$$\sin_{\Delta^\pm}(\vec{x}) = \sin(2\pi\vec{F}_1 \cdot \vec{x}) \mathfrak{T}_{1,\Delta^\pm}(\vec{x}) + \cos(2\pi\vec{F}_1 \cdot \vec{x}) \mathfrak{T}_{2,\Delta^\pm}(\vec{x}), \quad (5.44)$$

$$\mathfrak{T}_{1,\Delta^\pm}(\vec{x}) = \left(1 + \frac{(\mathcal{I}_{1,\Delta^\pm}(\vec{x}))^2}{(\mathcal{I}_{2,\Delta^\pm}(\vec{x}))^2} \right)^{-\frac{1}{2}}, \quad (5.45)$$

$$\mathfrak{T}_{2,\Delta^\pm}(\vec{x}) = \left(1 + \frac{(\mathcal{I}_{2,\Delta^\pm}(\vec{x}))^2}{(\mathcal{I}_{1,\Delta^\pm}(\vec{x}))^2} \right)^{-\frac{1}{2}}. \quad (5.46)$$

Here, the functions $\mathfrak{T}_{1,\Delta^\pm}(\vec{x})$ and $\mathfrak{T}_{2,\Delta^\pm}(\vec{x})$ are bounded in all the domain and continuous except the points where the intensity is equal to zero. For more details, please, refer to Section 4.7. Moreover, these functions carry in their spectrum both: low-frequency components and lobes located at $\vec{\xi} = \pm 2\pi\vec{F}_{\Delta^-}$ or $\vec{\xi} = \pm 2\pi\vec{F}_{\Delta^+}$.

By applying Fourier transform and the convolution theorem one can obtain an expression for the spectrum of phasor sinewave:

$$\begin{aligned}
 \mathcal{F}[\sin_{\Delta^{\pm}}](\vec{\xi}) &= \left(\mathcal{F}[\sin(2\pi\vec{F}_1 \cdot \vec{x})] \otimes \mathcal{F}[\mathfrak{I}_{1,\Delta^{\pm}}] \right)(\vec{\xi}) + \\
 &\quad + \left(\mathcal{F}[\cos(2\pi\vec{F}_1 \cdot \vec{x})] \otimes \mathcal{F}[\mathfrak{I}_{2,\Delta^{\pm}}] \right)(\vec{\xi}) = \\
 &= \left(\mathcal{F}[\mathfrak{I}_{2,\Delta^{\pm}}] + i\mathcal{F}[\mathfrak{I}_{1,\Delta^{\pm}}] \right)(\vec{\xi} - 2\pi\vec{F}_1) + \\
 &\quad + \left(\mathcal{F}[\mathfrak{I}_{2,\Delta^{\pm}}] - i\mathcal{F}[\mathfrak{I}_{1,\Delta^{\pm}}] \right)(\vec{\xi} + 2\pi\vec{F}_1). \quad (5.47)
 \end{aligned}$$

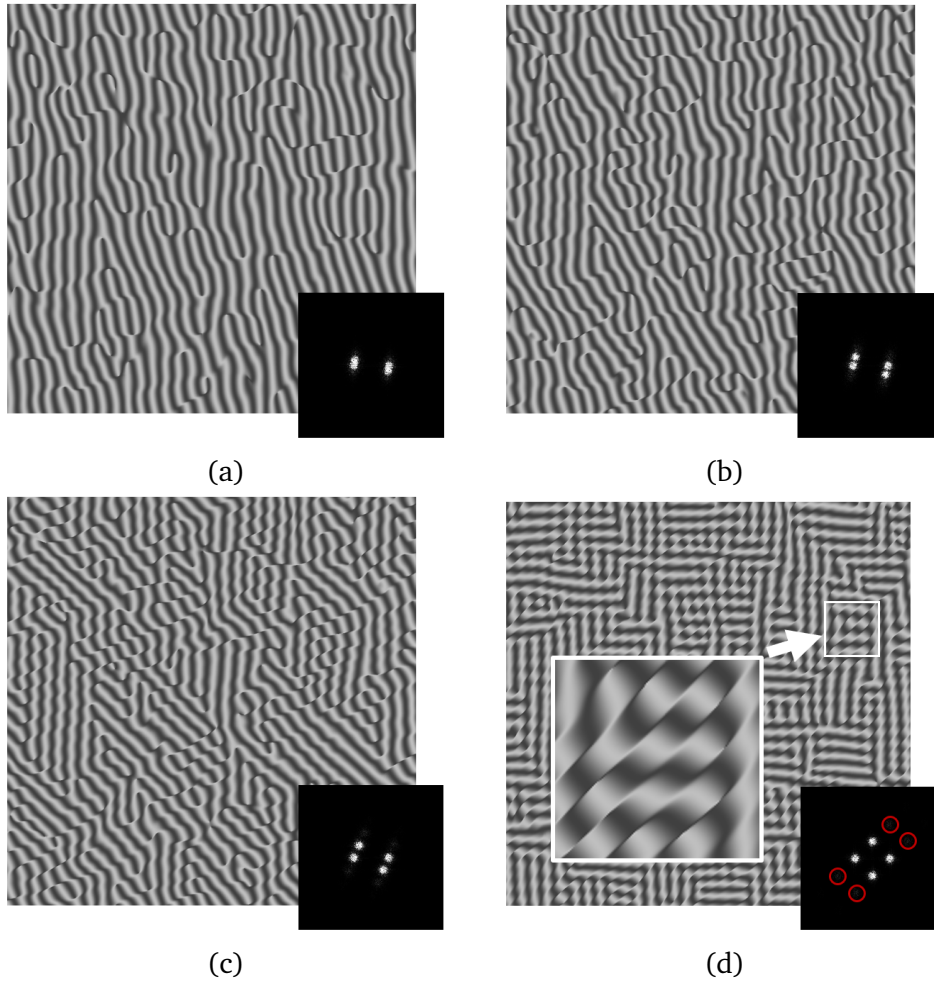


Figure 5.7: Phasor sinewave instances for different angles between the directions \vec{F}_1 and \vec{F}_2 of constituent bi-lobes. On each picture the noise (background) and its spectrum (bottom right) are shown. It can be seen that as the angle $|\theta_2 - \theta_1|$ between \vec{F}_1 and \vec{F}_2 increases the interference between two bi-lobes appears which results in additional high-frequency and low-amplitude components (d) in the spectrum of phasor sinewave.

The convolution of $\mathcal{F}[\mathfrak{I}_{1,\Delta^{\pm}}](\vec{\xi})$ and $\mathcal{F}[\mathfrak{I}_{2,\Delta^{\pm}}](\vec{\xi})$ component with the sine and cosine functions relocates the low-frequency components to $\vec{\xi} = \pm 2\pi\vec{F}_1$ and the other high-frequency components are translated to $\vec{\xi} =$

$\pm 2\pi\vec{F}_2$. Thus, the spectrum of phasor sinewave consists of four lobes centered at $\vec{\xi} = \pm 2\pi\vec{F}_1$ and $\vec{\xi} = \pm 2\pi\vec{F}_2$ which comply with the frequencies of the corresponding Gabor noise. In addition, when the angle $|\theta_2 - \theta_1|$ between the directions F_1, F_2 of the kernels gets closer to $\frac{\pi}{2}$ the interference appears (5.7). As a result, in the spectrum of phasor sinewave undesired low-frequency components appear. These lobes are centered at the frequencies corresponding to the frequencies of the main components translated to the direction \vec{F}_{Δ^-} for $\Psi_{\Delta^-}(\vec{x})$ and \vec{F}_{Δ^+} for $\Psi_{\Delta^+}(\vec{x})$.

5.5.5 Variance spectrum of phasor sinewave

Finally, the variance spectrum of both phasor sinewave variants can be obtained combining Equations 5.46 and 5.10 and applying the Fourier transform:

$$\begin{aligned} \mathcal{F}[\nu_{\Psi_{\Delta^\pm}}](\vec{\xi}) &= \frac{1}{4\pi} \delta(\vec{\xi}) - \\ &- \frac{1}{2} \left(\frac{1}{2} \mathcal{F}[\mathfrak{T}_{2,\Delta^\pm}^2] - \frac{1}{2} \mathcal{F}[\mathfrak{T}_{1,\Delta^\pm}^2] + i \mathcal{F}[\mathfrak{T}_{1,\Delta^\pm} \mathfrak{T}_{2,\Delta^\pm}] \right) (\vec{\xi} - 4\pi\vec{F}) + \\ &+ \frac{1}{2} \left(\frac{1}{2} \mathcal{F}[\mathfrak{T}_{2,\Delta^\pm}^2] - \frac{1}{2} \mathcal{F}[\mathfrak{T}_{1,\Delta^\pm}^2] - i \mathcal{F}[\mathfrak{T}_{1,\Delta^\pm} \mathfrak{T}_{2,\Delta^\pm}] \right) (\vec{\xi} + 4\pi\vec{F}). \end{aligned} \quad (5.48)$$

The function $\mathfrak{T}_{1,\Delta^\pm}(\vec{x}) \mathfrak{T}_{2,\Delta^\pm}(\vec{x})$ is bounded and well defined in all the domain as the functions $\mathfrak{T}_{1,\Delta^\pm}(\vec{x})$ and $\mathfrak{T}_{2,\Delta^\pm}(\vec{x})$ are defined everywhere. Convolution with the sinewave of the doubled frequency $4\pi\vec{F}_1$ yields relocation of the spectrum components to the frequencies $\vec{\xi} = \pm 4\pi\vec{F}_1$, $\vec{\xi} = \pm 4\pi\vec{F}_1$ and $\vec{\xi} = \pm 2\pi\vec{F}_{\Delta^\pm}$ (in the case of Ψ_{Δ^-}) or $\vec{\xi} = \pm 2\pi\vec{F}_{\Delta^\pm}$ (for Ψ_{Δ^+}). Hence, the variance spectrum of phasor sinewave contains two pairs of high-frequency components formed by two bi-lobe spectrums of variance and one pair of "interference" components (at either $\vec{\xi} = \pm 2\pi\vec{F}_{\Delta^-}$ or $\vec{\xi} = \pm 2\pi\vec{F}_{\Delta^+}$).

Therefore, it is very important to point out that the fact whether one excludes only lower frequencies from the noise crucially depend on the difference between the directions \vec{F}_1 and \vec{F}_2 (figure 5.8). Indeed, the lobes located at $\vec{\xi} = \pm 2\pi\vec{F}_{\Delta^-}$ represent low frequencies only when the angle between \vec{F}_1 and \vec{F}_2 is between $-\frac{\pi}{2}$ and $\frac{\pi}{2}$. If it goes beyond this range, the "interference" components switch their roles and the lobes at $\vec{\xi} = \pm 2\pi\vec{F}_{\Delta^+}$ become low-frequency. Here we will call \vec{F}_1 the principal direction as the decomposition if the noise (Equation 5.33) was carried out based on this direction. It also can be seen on Figure 5.8 that additional low-amplitude components appear in the variance spectrum of phasor sinewave due to interference of between two different bi-lobes. It is remarkable that these components are centered at the frequencies corresponding to the frequencies of the main components translated by the cancelled direction (either \vec{F}_{Δ^-} or \vec{F}_{Δ^+}).

In addition, it is possible to extract only low-frequency components centered at $\vec{\xi} = 0$ from the variance of Gabor noise (see Figure 5.6(b)). In this case its intensity $\mathcal{I}(\vec{x})$ should be divided by $\mathcal{I}_0(\vec{x})$ defined as:

$$\mathcal{I}_0(\vec{x}) = \sqrt{(\mathcal{I}_1(\vec{x}))^2 + (\mathcal{I}_2(\vec{x}))^2}. \quad (5.49)$$

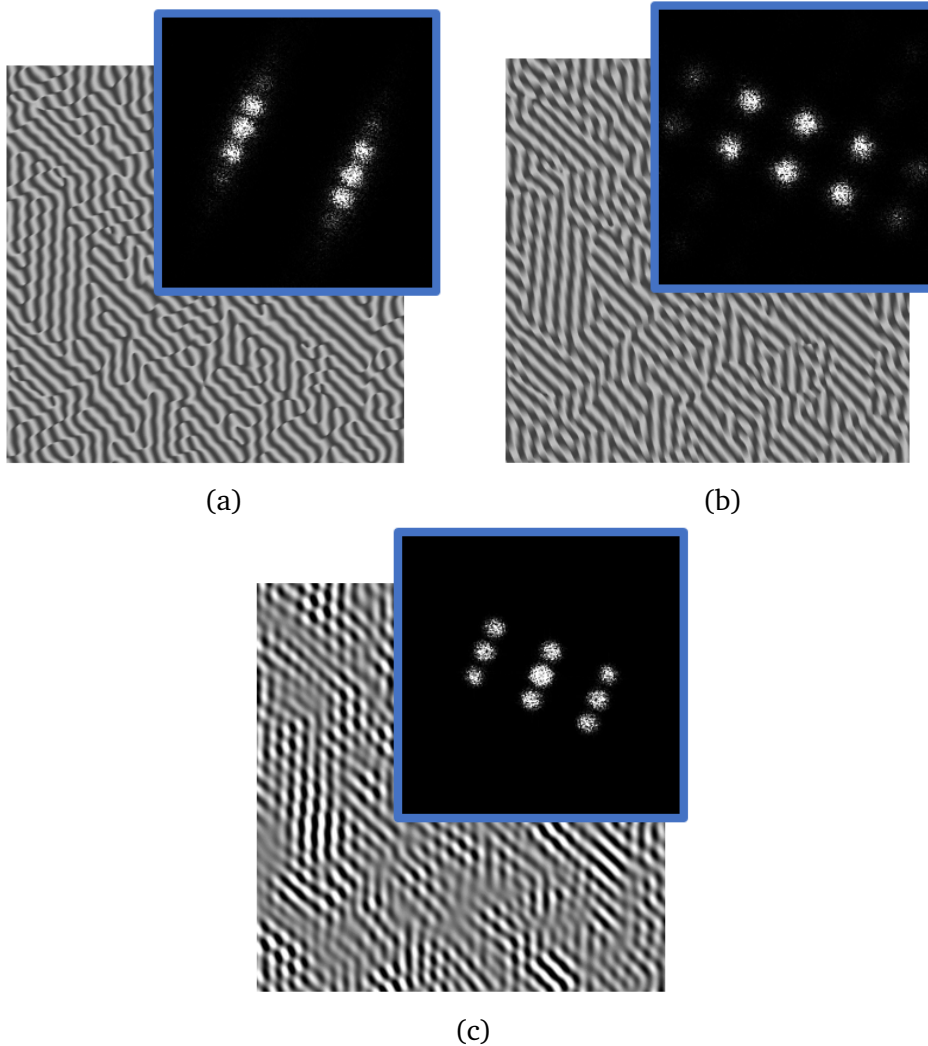


Figure 5.8: Phasor sinewaves $\Psi_{\Delta-}$ (a) and $\Psi_{\Delta+}$ (b) and corresponding Gabor noise $\mathcal{G}(\vec{x})$ (c). On each picture there is the noise (background) and its variance spectrum (top right). One can see that for each phasor sinewave some additional high-frequency components appear in its variance spectrum due to the interference. Moreover, these additional components have significantly lower amplitude.

5.6 General case

The representation of the intensity $\mathcal{I}_{\Delta-}(\vec{x})$ and corresponding phasor sinewave $\sin_{\Delta-}(\vec{x})$ showed in Equations 5.32 and 5.33 respectively can be simplified and

written in terms of bi-lobe phasor noises $\Psi_1(\vec{x})$ and $\Psi_2(\vec{x})$:

$$\mathcal{I}(\vec{x}) = \left((\mathcal{I}_1(\vec{x}) \sin \Psi_1(\vec{x}) + \mathcal{I}_2(\vec{x}) \sin \Psi_2(\vec{x}))^2 + (\mathcal{I}_1(\vec{x}) \cos \Psi_1(\vec{x}) + \mathcal{I}_2(\vec{x}) \cos \Psi_2(\vec{x}))^2 \right)^{\frac{1}{2}}. \quad (5.50)$$

In this case the phasor sinewave function can be calculated as follows:

$$\Psi(\vec{x}) = \arctan \frac{\mathcal{I}_1(\vec{x}) \sin \Psi_1(\vec{x}) + \mathcal{I}_2(\vec{x}) \sin \Psi_2(\vec{x})}{\mathcal{I}_1(\vec{x}) \cos \Psi_1(\vec{x}) + \mathcal{I}_2(\vec{x}) \cos \Psi_2(\vec{x})}. \quad (5.51)$$

This representation corresponds to the decomposition presented in the previous section.

Thus, all results obtained above allow one to define phasor noise and its sinewave in general case when each Gabor kernel can have an arbitrary direction F_k . Assuming that there are $n_k \geq 1$ kernels for each F_k one can generalize Equation 5.31:

$$\mathcal{G}(\vec{x}) = \sum_{k=1}^m \mathcal{G}_k(\vec{x}) = \sum_{k=1}^m \sum_{i=1}^{n_k} a_i(\vec{r}_i) \sin(2\pi \vec{F}_k \cdot \vec{x} + u_{k,i}) \quad (5.52)$$

Then, following Equation 5.50 one can obtain an expression for the Gabor noise intensity function through corresponding bi-lobe phasors:

$$\mathcal{I}(\vec{x}) = \sqrt{\left(\sum_{k=1}^m \mathcal{I}_k(\vec{x}) \sin \Psi_k(\vec{x}) \right)^2 + \left(\sum_{k=1}^m \mathcal{I}_k(\vec{x}) \cos \Psi_k(\vec{x}) \right)^2} \quad (5.53)$$

Finally, phasor noise in general case can be obtained through combination of bi-lobe intensity functions and phasor noises:

$$\Psi(\vec{x}) = \arctan \frac{\sum_{k=1}^m \mathcal{I}_k(\vec{x}) \sin \Psi_k(\vec{x})}{\sum_{k=1}^m \mathcal{I}_k(\vec{x}) \cos \Psi_k(\vec{x})}. \quad (5.54)$$

5.6.1 Spectrum of the intensity

In general case the intensity shown in Equation 5.53 can be rewritten in two terms: one corresponds to a sum of intensities of the corresponding bi-lobe Gabor noises and the second describes their low-frequency ($\vec{F}_k - \vec{F}_l$) pair-wise interaction:

$$\begin{aligned}
\mathcal{I}^2(\vec{x}) &= \sum_{k,l=1}^m \mathcal{I}_k(\vec{x}) \mathcal{I}_l(\vec{x}) \cos(\psi_k(\vec{x}) - \psi_l(\vec{x})) = \\
&= \sum_{k=1}^m \mathcal{I}_k^2(\vec{x}) + \sum_{k \neq l} \mathcal{I}_k(\vec{x}) \mathcal{I}_l(\vec{x}) \cos(\psi_k(\vec{x}) - \psi_l(\vec{x})). \quad (5.55)
\end{aligned}$$

Indeed, following the definition of phasor noise in bi-lobe case it possible to bring the previous expression to the following form through the bi-lobe direction vectors \vec{F}_k :

$$\begin{aligned}
\sum_{k \neq l} \mathcal{I}_k(\vec{x}) \mathcal{I}_l(\vec{x}) \cos(\psi_k(\vec{x}) - \psi_l(\vec{x})) &= \\
&= \sum_{k \neq l} \mathcal{I}_k(\vec{x}) \mathcal{I}_l(\vec{x}) \cos\left(2\pi(\vec{F}_k - \vec{F}_l) \cdot \vec{x} + u_k - u_l\right). \quad (5.56)
\end{aligned}$$

Moreover, one can note that the last term in Equation 5.55 corresponds do the one in $\mathcal{I}_{\Delta^-}(\vec{x})$ (Equation 5.32). Therefore, the spectrum of the intensity function is derived as follows:

$$\begin{aligned}
\mathcal{F}[\mathcal{I}^2](\vec{\xi}) &= \sum_{k=1}^m \mathcal{F}[\mathcal{I}_k^2](\vec{\xi}) + \\
&+ \mathcal{F}\left[\cos\left(2\pi(\vec{F}_k - \vec{F}_l) \cdot \vec{x}\right)\right](\vec{\xi}) \otimes \left(\cos(u_k - u_l) \sum_{k \neq l} \mathcal{F}[\mathcal{I}_k \mathcal{I}_l](\vec{\xi})\right) - \\
&- \mathcal{F}\left[\sin\left(2\pi(\vec{F}_k - \vec{F}_l) \cdot \vec{x}\right)\right](\vec{\xi}) \otimes \left(\sin(u_k - u_l) \sum_{k \neq l} \mathcal{F}[\mathcal{I}_k \mathcal{I}_l](\vec{\xi})\right) \quad (5.57)
\end{aligned}$$

Finally, the spectrum of the intensity function in the general case is formed by low frequency intensities of each bi-lobe centered at $\vec{\xi} = \mathbf{0}$ and pair-wise interaction components (described in the previous section for the case of two-directional noise) with frequencies at $\vec{\xi} = 2\pi(\vec{F}_k - \vec{F}_l)$.

5.6.2 Spectrum of Gabor noise

Gabor noise in the case of kernels with multiple directions can be represented as a sum of multiple bi-lobe Gabor noises. Therefore, following Equation 5.23 one can obtain analytical spectrum of multidirectional Gabor:

$$\mathcal{F}[G](\vec{\xi}) = \sum_{k=1}^m \mathcal{F}[G_k](\vec{\xi}) = \sum_{k=1}^m \sum_{i=1}^{n_k} \frac{K_i}{\sqrt{8b_i}} \left(e^{-ib_i} e^{\frac{(\vec{\xi}-\vec{F}_k)^2}{4b_i}} e^{i\vec{x}_i(\vec{\xi}-\vec{F}_k)^2} - e^{ib_i} e^{\frac{(\vec{\xi}+\vec{F}_k)^2}{4b_i}} e^{i\vec{x}_i(\vec{\xi}+\vec{F}_k)^2} \right). \quad (5.58)$$

Thus, the spectrum of Gabor noise (Figure 5.9) consists of m pairs of lobes centered at frequencies $\vec{\xi} = \pm 2\pi\vec{F}_k$ each formed by spectrum of a corresponding constituent bi-lobe noise $G_k(\vec{x})$.

5.6.3 Variance spectrum of Gabor noise

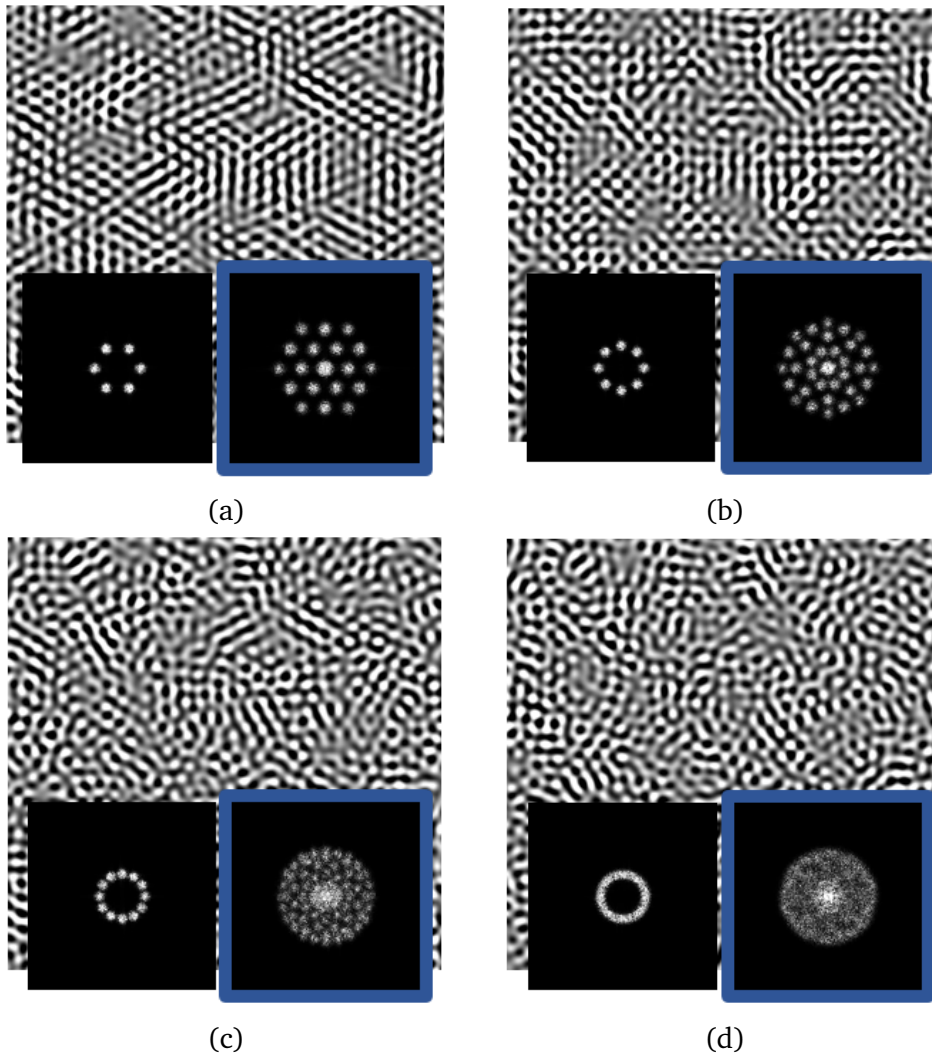


Figure 5.9: Four instances of Gabor noise (background), its spectrum (left bottom) and its variance spectrum (right bottom) for combinations of three (a), four (b), six (c), and multiple (d) directions \vec{F}_k within the range $-\frac{\pi}{2} \leq \theta_k \leq \frac{\pi}{2}$.

Analogously to the Subsection 5.5.3, one can take variance of the representation shown in Equation 5.52:

$$\mathcal{V}_{\mathcal{G}}(\vec{\mathbf{x}}) = \mathcal{V}\left(\sum_{k=1}^m \mathcal{G}_k(\vec{\mathbf{x}})\right) = \sum_{k=1}^m \mathcal{V}_{\mathcal{G}_k}(\vec{\mathbf{x}}) + \sum_{k,l=1}^m \mathcal{G}_k(\vec{\mathbf{x}})\mathcal{G}_l(\vec{\mathbf{x}}). \quad (5.59)$$

The variance here is defined by a sum of two terms. The first one represents a sum of each bi-lobe noise variance $\mathcal{V}_{\mathcal{G}_k}(\vec{\mathbf{x}})$ and the second is a sum of pair-wise interaction $\mathcal{G}_k(\vec{\mathbf{x}})\mathcal{G}_l(\vec{\mathbf{x}})$ between each two bi-lobes. Thanks to additivity of Fourier transform, the spectrum is represented by a sum of Fourier transform of each component:

$$\mathcal{F}[\mathcal{V}_{\mathcal{G}}(\vec{\mathbf{x}})](\vec{\xi}) = \sum_{k=1}^m \mathcal{F}[\mathcal{V}_{\mathcal{G}_k}(\vec{\mathbf{x}})](\vec{\xi}) + \sum_{k,l=1}^m \mathcal{F}[\mathcal{G}_k(\vec{\mathbf{x}})\mathcal{G}_l(\vec{\mathbf{x}})](\vec{\xi}). \quad (5.60)$$

Thus, the spectrum of Gabor noise (Figure 5.9) in the general case consists of one low-frequency component centered at $\vec{\xi} = 0$, m pairs of high-frequency lobes at doubled frequencies $\vec{\xi} = \pm 4\pi\vec{F}_k$, and $2m - 2$ components representing pair-wise interaction between bi-lobe noises which form $m - 1$ pairs located at frequencies $\vec{\xi} = \pm 2\pi(\vec{F}_k - \vec{F}_l)$ and $m - 1$ pairs at $\vec{\xi} = \pm 2\pi(\vec{F}_k + \vec{F}_l)$.

5.6.4 Spectrum of phasor sinewave

Following Equations 5.53 and 5.54 it is possible to derive phasor sinewave through a function $\mathfrak{T}(\vec{\mathbf{x}})$ similar to the ones defined in the previous sections (Equations 5.27 or 5.46):

$$\sin(\vec{\mathbf{x}}) = \mathfrak{T}(\vec{\mathbf{x}}), \quad (5.61)$$

$$\mathfrak{T}(\vec{\mathbf{x}}) = \left(1 + \frac{\left(\sum_{k=1}^m \mathcal{I}_k(\vec{\mathbf{x}}) \cos \Psi_k(\vec{\mathbf{x}})\right)^2}{\left(\sum_{k=1}^m \mathcal{I}_k(\vec{\mathbf{x}}) \sin \Psi_k(\vec{\mathbf{x}})\right)^2} \right)^{-\frac{1}{2}}.$$

Here the function $\mathfrak{T}(\vec{\mathbf{x}})$ is bounded and defined everywhere. To see the limit of the function at points where the intensity $\mathcal{I}(\vec{\mathbf{x}})$ is equal to zero the function, please, refer to Section 5.7. Moreover, the expression for $\mathfrak{T}(\vec{\mathbf{x}})$ in Equation 5.5 can be written in the following form:

$$\mathfrak{T}(\vec{\mathbf{x}}) = \frac{\sum_{k=1}^m \mathcal{I}_k(\vec{\mathbf{x}}) \sin \Psi_k(\vec{\mathbf{x}})}{\mathcal{I}(\vec{\mathbf{x}})}.$$

Here, one sees that the numerator in the previous equation is the sum of bi-lobe Gabor noises. Thus, the spectrum of phasor sinewave (Figure 5.10) has a similar structure in sense that it is formed by m pairs of lobes located at corresponding frequencies $\vec{\xi} = \pm 2\pi\vec{F}_k$.

5.6.5 Variance spectrum of phasor sinewave

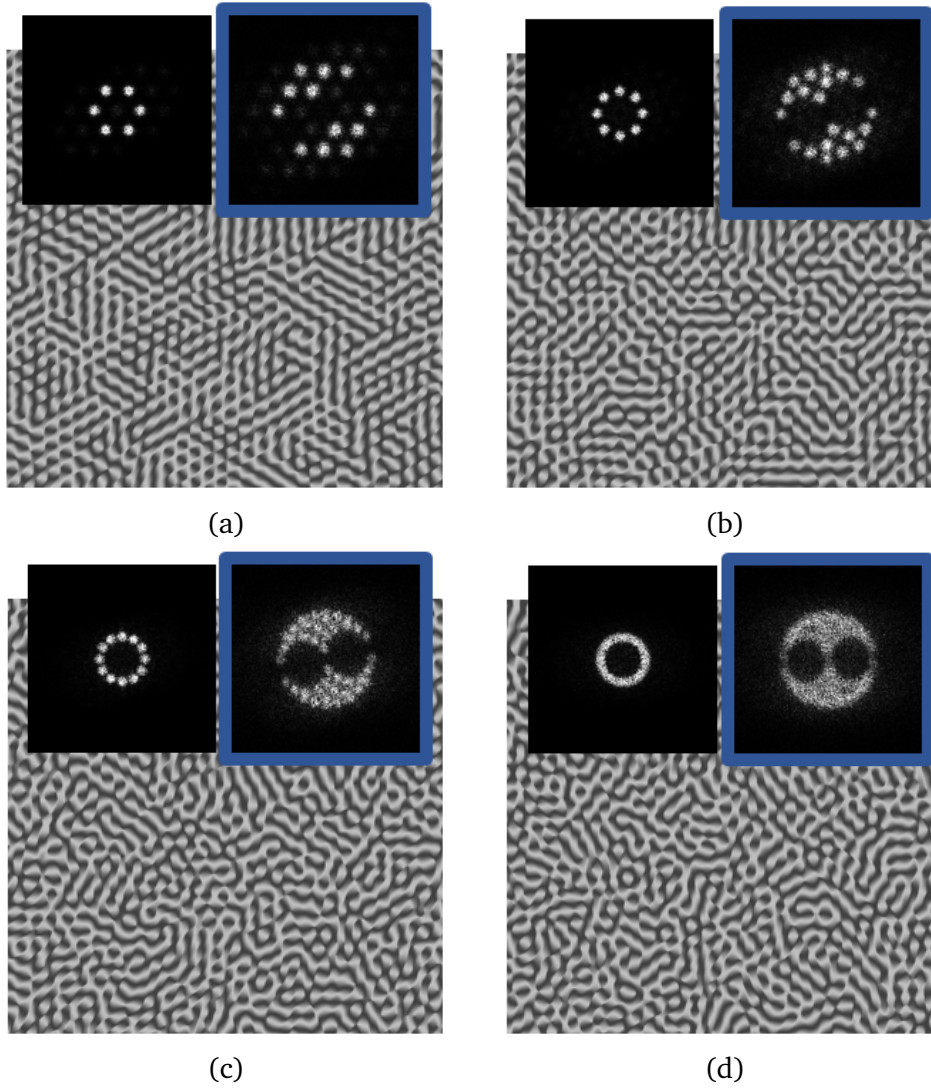


Figure 5.10: Four instances of phasor sinewave (background), its spectrum (left bottom) and its variance spectrum (right bottom) for combinations of three (a), four (b), six (c), and multiple (d) directions \vec{F}_k within the range $-\frac{\pi}{2} \leq \theta_k \leq \frac{\pi}{2}$. Two black circles occur as only one part of interference corresponding to $\vec{F}_k - \vec{F}_l$ is cancelled.

The variance of phasor sinewave can be written in the following form (from Equation 5.5):

$$\nu_{\psi}(\vec{x}) = \frac{1}{2} - \frac{\sum_{k=1}^m I_k^2(\vec{x}) \cos 2\psi_k(\vec{x})}{I^2(\vec{x})} - \frac{\sum_{k \neq l} I_k(\vec{x}) I_l(\vec{x}) \cos(\psi_k(\vec{x}) + \psi_l(\vec{x}))}{I^2(\vec{x})} \quad (5.62)$$

This expression reveals that the variance consists of a constant, cosines of doubled bi-lobe phasors, and cosines of different bi-lobe phasor sums which become in Fourier space a delta-function, high-frequency lobes centered mainly at doubled frequencies $\vec{\xi} = \pm 4\pi\vec{F}_k$, and lobes mainly located at $\vec{\xi} = \pm 2\pi(\vec{F}_k + \vec{F}_l)$:

$$\begin{aligned} \mathcal{F}[\mathcal{V}_{\Psi_{\Delta^\pm}}](\vec{\xi}) = & \frac{1}{4\pi}\delta(\vec{\xi}) - \frac{1}{2}\mathcal{F}\left[\frac{\sum_{k=1}^m \mathcal{I}_k^2(\vec{x}) \cos 2\Psi_k(\vec{x})}{\mathcal{I}^2(\vec{x})}\right](\vec{\xi}) - \\ & - \frac{1}{2}\mathcal{F}\left[\frac{\sum_{k \neq l} \mathcal{I}_k(\vec{x}) \mathcal{I}_l(\vec{x}) \cos(\Psi_k(\vec{x}) + \Psi_l(\vec{x}))}{\mathcal{I}^2(\vec{x})}\right](\vec{\xi}). \end{aligned} \quad (5.63)$$

It was said that the high-frequency components are "mainly" located at the corresponding frequencies, because the division by the intensity function produces some phantom spectral components which are the lobes with lower intensity and centered at higher frequencies than the former components. On Figure 5.10 one can see that not there are still low-frequency components in the variance spectrum. This happen due to that fact that only $\vec{F}_k - \vec{F}_l$ components are cancelled in phasor sinewave which indeed correspond to low frequencies when the angle $|\theta_k - \theta_l|$ between the directions of the corresponding constituent bi-lobes is not big enough. As this angle increases, the frequencies of the other component $\vec{F}_k + \vec{F}_l$ get lower and at the same time the lobes of $\vec{F}_k - \vec{F}_l$ become high-frequency.

5.7 A note on indeterminate points

In this section let us consider the following functions (which arise in Subsections 5.4.4, 5.5.4, 5.6.4) written in an alternative form:

$$\mathfrak{T}_1(\vec{x}) = \frac{\sum_{i=1}^n a_i(\vec{r}_i) \sin u_i}{\mathcal{I}(\vec{x})}, \quad (5.64)$$

$$\mathfrak{T}_2(\vec{x}) = \frac{\sum_{i=1}^n a_i(\vec{r}_i) \cos u_i}{\mathcal{I}(\vec{x})}, \quad (5.65)$$

$$\mathfrak{T}_{1,\Delta^-}(\vec{x}) = \frac{\mathcal{I}_1(\vec{x}) \sin \Psi_1(\vec{x}) + \mathcal{I}_2(\vec{x}) \sin \Psi_2(\vec{x})}{\mathcal{I}_{\Delta^-}(\vec{x})}, \quad (5.66)$$

$$\mathfrak{T}_{2,\Delta^-}(\vec{x}) = \frac{\mathcal{I}_1(\vec{x}) \sin \Psi_1(\vec{x}) + \mathcal{I}_2(\vec{x}) \sin \Psi_2(\vec{x})}{\mathcal{I}_{\Delta^-}(\vec{x})}, \quad (5.67)$$

$$\mathfrak{T}(\vec{x}) = \frac{\sum_{k=1}^m \mathcal{I}_k(\vec{x}) \sin \Psi_k(\vec{x})}{\mathcal{I}(\vec{x})} \quad (5.68)$$

Taking these expressions and using the complex Gabor noise formulation presented in Equation 5.7 one can obtain a complex function representation of the considered functions:

$$\begin{aligned} \mathfrak{G}_0(\vec{x}) &= e^{-i2\pi\vec{F}\cdot\vec{x}}\mathfrak{G}(\vec{x}), \\ \mathfrak{T}_1(\vec{x}) &= \frac{\text{Im}\{\mathfrak{G}_0(\vec{x})\}}{\mathfrak{G}_0(\vec{x})\overline{\mathfrak{G}_0(\vec{x})}}, \end{aligned} \quad (5.69)$$

$$\mathfrak{T}_2(\vec{x}) = \frac{\text{Re}\{\mathfrak{G}_0(\vec{x})\}}{\mathfrak{G}_0(\vec{x})\overline{\mathfrak{G}_0(\vec{x})}}, \quad (5.70)$$

$$\mathfrak{T}_{1,\Delta^-}(\vec{x}) = \frac{\text{Im}\{\mathfrak{G}(\vec{x})\}}{\mathfrak{G}(\vec{x})\overline{\mathfrak{G}(\vec{x})}}, \quad (5.71)$$

$$\mathfrak{T}_{2,\Delta^-}(\vec{x}) = \frac{\text{Re}\{\mathfrak{G}(\vec{x})\}}{\mathfrak{G}(\vec{x})\overline{\mathfrak{G}(\vec{x})}}, \quad (5.72)$$

$$\mathfrak{T}(\vec{x}) = \frac{\text{Im}\{\mathfrak{G}(\vec{x})\}}{\mathfrak{G}(\vec{x})\overline{\mathfrak{G}(\vec{x})}}, \quad (5.73)$$

where the upper bar \bar{f} denotes a complex conjugate of f . The singularities of $\frac{0}{0}$ type occur when both numerator and denominator are equal to zero. Moreover, as the denominator is the sum of the squared real and imaginary parts it is equal to zero only when both squares reach zero values. Thus, the problem of searching the value of the functions defined by Equations 5.64-5.68 can be reduced to finding the following limits of a complex-valued functional $f: \mathbb{R}^3 \rightarrow \mathbb{Z}$:

$$\lim_{\text{Re}\{f\}, \text{Im}\{f\} \rightarrow 0} \frac{\text{Im}\{f(\vec{x})\}}{\sqrt{f(\vec{x})\overline{f(\vec{x})}}}, \quad \lim_{\text{Re}\{f\}, \text{Im}\{f\} \rightarrow 0} \frac{\text{Re}\{f(\vec{x})\}}{\sqrt{f(\vec{x})\overline{f(\vec{x})}}}. \quad (5.74)$$

These limits can be transformed into equivalent limits with a complex variable $z \in \mathbb{Z}$:

$$\lim_{z \rightarrow 0} \frac{i(\bar{z} - z)}{2\sqrt{z\bar{z}}}, \quad \lim_{z \rightarrow 0} \frac{z + \bar{z}}{2\sqrt{z\bar{z}}}, \quad z = x + iy. \quad (5.75)$$

By the definition, a limit of a complex function $f(z)$ at a point z_0 exists if the following is true:

$$\forall \epsilon > 0 \exists \delta > 0 : \forall z \in |z - z_0| < \delta, |f(z) - f(z_0)| < \epsilon. \quad (5.76)$$

This means, that regardless of the chosen path $z(t) \rightarrow z_0$ the function should approach the same value. Let us rewrite these limits in terms of real x and imaginary y parts of z :

$$\lim_{(x,y) \rightarrow (0,0)} \frac{y}{\sqrt{x^2 + y^2}}, \quad \lim_{(x,y) \rightarrow (0,0)} \frac{x}{\sqrt{x^2 + y^2}}, \quad (5.77)$$

and consider the complex variable in Euler notation:

$$z = re^{i\theta} \rightarrow \begin{cases} x = r \cos \theta, \\ y = r \sin \theta. \end{cases}$$

Then, according to the definition in Equation 5.76 the limits of $(x, y) \rightarrow (0, 0)$ considered here are equivalent to the following limits of $r \rightarrow 0$:

$$\lim_{r \rightarrow 0} \frac{r \sin \theta}{\sqrt{r^2 \cos^2 \theta + r^2 \sin^2 \theta}} = \sin \theta, \quad (5.78)$$

$$\lim_{r \rightarrow 0} \frac{r \cos \theta}{\sqrt{r^2 \cos^2 \theta + r^2 \sin^2 \theta}} = \cos \theta. \quad (5.79)$$

Finally, the values of considered functions at $z = 0$ depend on θ which means that the limits are path-dependent and, thus, do not exist in the general definition.

Following the definition in Equation 5.7, one can notice that here $r = \mathcal{I}(\vec{x})$ and $\theta = \Psi(\vec{x})$. For a better definition and continuity of our noise in Equations 5.19, 5.34, and 5.54 we used $atan2(y, x)$ additionally augmented at a point $(x, y) = (0, 0)$ instead of $\arctan\left(\frac{x}{y}\right)$:

$$atan2(x, y) = \begin{cases} 2 \arctan\left(\frac{y}{\sqrt{x^2 + y^2} + x}\right) & \text{if } x > 0, \\ 2 \arctan\left(\frac{y}{\sqrt{x^2 + y^2} - x}\right) & \text{if } x \leq 0 \text{ and } y \neq 0, \\ \pi & \text{if } x < 0 \text{ and } y = 0, \\ 0 & \text{if } x = 0 \text{ and } y = 0. \end{cases}$$

It is also important to point out, that when the intensity goes to zero ($\mathcal{I}(\vec{x}) = 0$) phasor noise goes to zero too ($\Psi(\vec{x}) = 0$). Therefore, the limits 5.78, 5.79 in the case of phasor noise can be represented as follows:

$$\lim_{\mathcal{I}(\vec{x}) \rightarrow 0} \frac{Im\{\mathfrak{G}(\vec{x})\}}{\mathfrak{G}(\vec{x})\mathfrak{G}(\vec{x})} = \sin \Psi(\vec{x}) = 0,$$

$$\lim_{\mathcal{I}(\vec{x}) \rightarrow 0} \frac{Re\{\mathfrak{G}(\vec{x})\}}{\mathfrak{G}(\vec{x})\mathfrak{G}(\vec{x})} = \cos \Psi(\vec{x}) = 1.$$

Hence, the functions from Equations 5.64-5.68 are defined and bounded in all considered domain.

5.8 Conclusion

In this work, a new type of procedural noise, phasor noise, was presented, and its properties were studied. Phasor noise was formulated in strong relation with Gabor noise to build a comparative study. This approach allowed us to understand better the influence of the model parameters on the resulting pattern and find if phasor noise can be an efficient solution for some drawbacks associated with Gabor noise.

The theoretical analysis of phasor noise was carried out from the simplest bi-lobe case to the case of two bi-lobes, and finally finished with the most general formulation with kernels with an arbitrary number of directions. For each case, the analytical expressions for the spectrum of phasor sinewave and its variance were obtained and then analyzed and compared with Gabor noise. This analysis revealed good control over the properties of phasor and great potential in the fields of both computer graphics and computer-aided design thanks to the high contrast of the generated patterns and the ability to change the profile of the oscillations.

In addition, some effects occurring in the case of two and more directions showed the presence of additional lower frequencies in phasor sinewave. These effects were studied theoretically in the spectrum variance of the noise. As a result, the constituent frequencies were obtained, and the analytical expression of the variance spectrum was separated into different terms corresponding to four main frequencies contained in it: the low-frequency intensity components, the mid-low and the mid-high frequency lobes corresponding to the interference between kernels, and the high-frequency part corresponding to the doubled main frequency of the noise. Moreover, two techniques that cancel out either mid-low or high-low frequencies were presented.

Finally, the general case analysis showed that modeling phasor sinewave with pure isotropic variance spectrum (without low frequencies) is not trivial and requires some additional techniques to avoid local interference between the neighboring kernels.

5.9 Future work

As a future work challenge, implementing a 3D version of phasor noise could be an interesting subject to study in the framework of the design of composites with heterogeneous microstructures. It is also important to understand better the connection between the noise parameters and mechanical properties of the designed structure. In addition, one can study the "spiky" effect which occurs in the wavefront due to the interference, how strongly it affects the macroscopic properties, and how to reduce these artifacts.

Moreover, due to the spatial characteristics of a gabor kernel (a fixed direction) it is possible to impose prescribed symmetry to a phasor noise pattern by assembling and rotating the kernels in space according to this symmetry ([133] is a good example of this approach). This could help to achieve specific

mechanical properties of the designed structure. Finally, phasor noise provides an ability of generating periodic structures simply by imposing periodicity to the spatial distribution of the kernels with constraints on their directions.

Chapter 6

Conclusion

6.1 General discussion

In this work the topic of mechanical metamaterials design was studied through two different lenses: modelling periodic structures through parametrized growth model and by means of noise functions. The results obtained in this thesis along with the literature studied during this work revealed that although there are numerous approaches to generate 3D materials with optimized properties or tailored behavior the space size of possible geometries spawned by these materials is beyond modern computational capabilities. Moreover, even for fixed values of targeted effective parameters the number of possible microgeometries can be large.

Nevertheless, there are several approaches widely utilized to reduce complexity of the problem and ease the exploration process. Symmetry is one of them. It was observed already in the past that geometrical symmetry of an object affects its mechanical properties. Moreover, for periodic materials their symmetry defines the symmetry class of the elastic tensor which directly represents their macroscopic elastic properties. This relation was used in this thesis in Chapter 3 as it allows to reduce the considered range of materials. In addition, some specific extremal or hardly achievable mechanical properties, such as auxeticity or isotropy, are associated with symmetry (chirality is known to yield negative values of Poisson ratio [42] and isotropy is usually searched within materials with cubic symmetry [179]). Some recent papers dedicated to the design of periodic cellular microgeometries with topology optimization methods have employed symmetry restrictions into a computational process for performance boost and increased quality of an optimal design. The author of this work believes that symmetry is a promising tool in the material design and, more important, is one of the main ingredients for building theoretical criteria and models for design of structures with extremal properties.

Other important problems are material reproduction and design objects with non-trivial macroscopic geometry and heterogeneous microstructure that conforms to it. Methods from texture synthesis showed high efficiency in solving these challenges. Indeed, the methods originated from this field are usually dedicated to the reproduction of different natural or even artificial patterns

in the sense of replicating the properties of the original sample. Data-driven methods have shown remarkable results in generating an infinite number of patterns, all closely conforming to targeted average properties. The other class of methods, including Phasor noise presented in Chapter 5, is based on the definition through a procedural function which allows imposing a given spatial variation of the noise pattern through a prescribed spatial field directly. These noise types provide an ability of low-memory and high-performance calculations, which makes it even more suitable for employing in an optimization process for targeting specific physical properties. A recent work showed high potential the use procedural noise functions for the design of optimal materials using a machine learning approach [106]. In particular, generative adversarial networks are a good solution for this purpose. It can be seen that with the increase of computational capability the development of CAD methods, the fields of computer graphics and material design are getting more connected. And the author of this thesis believes that in the future, the link between these two domains will become even stronger.

In conclusion, all the examples presented here underline the importance of interdisciplinary research as it is effective for the solution of current problems and helps evolve the methodology, bringing new ideas and perspectives which will possibly help for solution of future problems as well.

Bibliography

- [1] Jacob Aboudi. Micromechanical analysis of composites by the method of cells. 1989.
- [2] Diab W Abueidda, Mohamed Elhebeary, Cheng-Shen Andrew Shiang, Siyuan Pang, Rashid K Abu Al-Rub, and Iwona M Jasiuk. Mechanical properties of 3d printed polymeric gyroid cellular structures: Experimental and finite element study. *Materials & Design*, 165:107597, 2019.
- [3] Lukmon Owolabi Afolabi, Zulkifli Mohamad Ariff, Syed Fuad Saiyid Hashim, Thamer Alomayri, Shahrudin Mahzan, Kamarul-Azhar Kamarudin, and Ibrahim Dauda Muhammad. Syntactic foams formulations, production techniques, and industry applications: A review. *Journal of Materials Research and Technology*, 9(5):10698–10718, 2020.
- [4] Oraib Al-Ketan, Ahmad Soliman, Ayesha M AlQubaisi, and Rashid K Abu Al-Rub. Nature-inspired lightweight cellular co-continuous composites with architected periodic gyroidal structures. *Advanced Engineering Materials*, 20(2):1700549, 2018.
- [5] Giacomo Aletti, Enea G Bongiorno, and Vincenzo Capasso. Integration in a dynamical stochastic geometric framework. *ESAIM: Probability and Statistics*, 15:402–416, 2011.
- [6] G Allaire and GA Francfort. A numerical algorithm for topology and shape optimization. In *Topology design of structures*, pages 239–248. Springer, 1993.
- [7] Grégoire Allaire, François Jouve, and Anca-Maria Toader. A level-set method for shape optimization. *Comptes Rendus Mathématique*, 334(12):1125–1130, 2002.
- [8] Grégoire Allaire, François Jouve, and Anca-Maria Toader. Structural optimization using sensitivity analysis and a level-set method. *Journal of computational physics*, 194(1):363–393, 2004.
- [9] Erik Andreassen and Casper Schousboe Andreasen. How to determine composite material properties using numerical homogenization. *Computational Materials Science*, 83:488–495, 2014.
- [10] Michael F Ashby and RF Mehl Medalist. The mechanical properties of cellular solids. *Metallurgical Transactions A*, 14(9):1755–1769, 1983.

- [11] Gilles Aubert, Pierre Kornprobst, and Giles Aubert. *Mathematical problems in image processing: partial differential equations and the calculus of variations*, volume 147. Springer, 2006.
- [12] Sahab Babae, Jongmin Shim, James C Weaver, Elizabeth R Chen, Nikita Patel, and Katia Bertoldi. Metamaterials: 3d soft metamaterials with negative poisson's ratio (adv. mater. 36/2013). *Advanced Materials*, 25(36):5116–5116, 2013.
- [13] J Baumeister et al. Verfahren zur herstellung poröser metallkörper. *German Patent*, 40(18):360, 1991.
- [14] J Baumeister and H Schrader. Verfahren zur herstellung aufschäumbarer metallkörper und verwendung derselben. *German Patent*, 41(01):630, 1992.
- [15] Frank Baumgärtner, Isabel Duarte, and John Banhart. Industrialization of powder compact toaming process. *Advanced Engineering Materials*, 2(4):168–174, 2000.
- [16] Martin P Bendsøe and Ole Sigmund. Material interpolation schemes in topology optimization. *Archive of applied mechanics*, 69(9):635–654, 1999.
- [17] Martin Philip Bendsøe and Noboru Kikuchi. Generating optimal topologies in structural design using a homogenization method. *Computer methods in applied mechanics and engineering*, 71(2):197–224, 1988.
- [18] Martin Philip Bendsoe and Ole Sigmund. *Topology optimization: theory, methods, and applications*. Springer Science & Business Media, 2003.
- [19] Alain Bensoussan, Jacques-Louis Lions, and George Papanicolaou. *Asymptotic analysis for periodic structures*, volume 374. American Mathematical Soc., 2011.
- [20] David J Bergman and Yakov M Strel'niker. Calculation of strong-field magnetoresistance in some periodic composites. *Physical Review B*, 49(23):16256, 1994.
- [21] Katia Bertoldi. Harnessing instabilities to design tunable architected cellular materials. *Annual Review of Materials Research*, 47:51–61, 2017.
- [22] Katia Bertoldi, Vincenzo Vitelli, Johan Christensen, and Martin Van Hecke. Flexible mechanical metamaterials. *Nature Reviews Materials*, 2(11):1–11, 2017.
- [23] Dhruv Bhate, Clint A Penick, Lara A Ferry, and Christine Lee. Classification and selection of cellular materials in mechanical design: Engineering and biomimetic approaches. *Designs*, 3(1):19, 2019.

- [24] Bernd Bickel, Moritz Bächer, Miguel A Otaduy, Hyunho Richard Lee, Hanspeter Pfister, Markus Gross, and Wojciech Matusik. Design and fabrication of materials with desired deformation behavior. *ACM Transactions on Graphics (TOG)*, 29(4):1–10, 2010.
- [25] Bernd Bickel, Moritz Bächer, Miguel A Otaduy, Wojciech Matusik, Hanspeter Pfister, and Markus Gross. Capture and modeling of non-linear heterogeneous soft tissue. *ACM transactions on graphics (TOG)*, 28(3):1–9, 2009.
- [26] FSL Bobbert, K Lietaert, Ali Akbar Eftekhari, Behdad Pourn, SM Ahmadi, Harrie Weinans, and AA Zadpoor. Additively manufactured metallic porous biomaterials based on minimal surfaces: A unique combination of topological, mechanical, and mass transport properties. *Acta biomaterialia*, 53:572–584, 2017.
- [27] Helmut J Böhm. Continuum micromechanics of materials. *Institut für Leichtbau und Biomechanik, TU Wien*, 2011.
- [28] Soheila Bazzaz Bonabi, Jalal Kahani Khabushan, Rahman Kahani, and Abbas Honarbakhsh Raouf. Fabrication of metallic composite foam using ceramic porous spheres “light expanded clay aggregate” via casting process. *Materials & Design*, 64:310–315, 2014.
- [29] Colin Bonatti and Dirk Mohr. Mechanical performance of additively-manufactured anisotropic and isotropic smooth shell-lattice materials: Simulations & experiments. *Journal of the Mechanics and Physics of Solids*, 122:1–26, 2019.
- [30] Thomas Borrvall. Topology optimization of elastic continua using restriction. *Archives of Computational Methods in Engineering*, 8(4):351–385, 2001.
- [31] Blaise Bourdin. Filters in topology optimization. *International journal for numerical methods in engineering*, 50(9):2143–2158, 2001.
- [32] Kenneth A Brakke. The surface evolver. *Experimental mathematics*, 1(2):141–165, 1992.
- [33] Marc Briane and Graeme W Milton. An antisymmetric effective hall matrix. *SIAM Journal on Applied Mathematics*, 70(6):1810–1820, 2010.
- [34] Marc Briane, Graeme W Milton, and Vincenzo Nesi. Change of sign of the corrector’s determinant for homogenization in three-dimensional conductivity. *Archive for rational mechanics and analysis*, 173(1):133–150, 2004.
- [35] S Broxtermann, M Taherishargh, IV Belova, GE Murch, and T Fiedler. On the compressive behaviour of high porosity expanded perlite-metal syntactic foam (p-msf). *Journal of Alloys and Compounds*, 691:690–697, 2017.

- [36] Tyler E Bruns and Daniel A Tortorelli. Topology optimization of non-linear elastic structures and compliant mechanisms. *Computer methods in applied mechanics and engineering*, 190(26-27):3443–3459, 2001.
- [37] Tiemo Bückmann, Michael Thiel, Muamer Kadic, Robert Schittny, and Martin Wegener. An elasto-mechanical unfeelability cloak made of pentamode metamaterials. *Nature communications*, 5(1):1–6, 2014.
- [38] Joseph Cappello, John Crissman, Mary Dorman, Marcia Mikolajczak, Garret Textor, Magda Marquet, and Franco Ferrari. Genetic engineering of structural protein polymers. *Biotechnology progress*, 6(3):198–202, 1990.
- [39] Josephine V Carstensen, Reza Lotfi, James K Guest, Wen Chen, and Jan Schroers. Topology optimization of cellular materials with maximized energy absorption. In *International Design Engineering Technical Conferences and Computers and Information in Engineering Conference*, volume 57083, page V02BT03A014. American Society of Mechanical Engineers, 2015.
- [40] Peter Chadwick, Maurizio Vianello, and Stephen C Cowin. A new proof that the number of linear elastic symmetries is eight. *Journal of the Mechanics and Physics of Solids*, 49(11):2471–2492, 2001.
- [41] Vivien J Challis and James K Guest. Level set topology optimization of fluids in stokes flow. *International journal for numerical methods in engineering*, 79(10):1284–1308, 2009.
- [42] YJ Chen, Fabrizio Scarpa, YJ Liu, and JS Leng. Elasticity of anti-tetrachiral anisotropic lattices. *International Journal of Solids and Structures*, 50(6):996–1004, 2013.
- [43] Peng Cheng, Ganesan Yogeewaranm, Lu Yang, and Lou Jun. Size dependent mechanical properties of single crystalline nickel nanowires. *Journal of Applied Physics*, 2012.
- [44] Xavier Chermain, Basile Sauvage, J-M Dischler, and Carsten Dachsbacher. Procedural physically based brdf for real-time rendering of glints. In *Computer Graphics Forum*, volume 39, pages 243–253. Wiley Online Library, 2020.
- [45] Jasgurpreet Singh Chohan, Rupinder Singh, Kamaljit Singh Boparai, Rosa Penna, and Fernando Fraternali. Dimensional accuracy analysis of coupled fused deposition modeling and vapour smoothing operations for biomedical applications. *Composites Part B: Engineering*, 117:138–149, 2017.
- [46] Peter W Chung, Kumar K Tamma, and Raju R Namburu. Asymptotic expansion homogenization for heterogeneous media: computational issues and applications. *Composites Part A: Applied Science and Manufacturing*, 32(9):1291–1301, 2001.

- [47] Francisco Conde-Rodríguez, Á-L García-Fernández, and Juan Carlos Torres. Modelling material microstructure using the perlin noise function. In *Computer Graphics Forum*, volume 40, pages 195–208. Wiley Online Library, 2021.
- [48] Tie Jun Cui, David R Smith, and Ruopeng Liu. *Metamaterials*. Springer, 2010.
- [49] Steven A Cummer, Johan Christensen, and Andrea Alù. Controlling sound with acoustic metamaterials. *Nature Reviews Materials*, 1(3):1–13, 2016.
- [50] Ahmed S Dalaq, Diab W Abueidda, Rashid K Abu Al-Rub, and Iwona M Jasiuk. Finite element prediction of effective elastic properties of interpenetrating phase composites with architected 3d sheet reinforcements. *International Journal of Solids and Structures*, 83:169–182, 2016.
- [51] Kostas Danas. Effective response of classical, auxetic and chiral magnetoelastic materials by use of a new variational principle. *Journal of the Mechanics and Physics of Solids*, 105:25–53, 2017.
- [52] Kostas Danas, SV Kankanala, and Nicolas Triantafyllidis. Experiments and modeling of iron-particle-filled magnetorheological elastomers. *Journal of the Mechanics and Physics of Solids*, 60(1):120–138, 2012.
- [53] MA De Meller. Produit métallique pour l’obtention d’objets laminés, moulés ou autres, et procédés pour sa fabrication. *French Patent*, 615(147):1926, 1925.
- [54] J.D. Debord and L.A. Lyon. Thermoresponsive photonic crystals. *The Journal of Physical Chemistry B*, 104(27):6327–6331, 2000.
- [55] Vikram S Deshpande, Norman A Fleck, and Michael F Ashby. Effective properties of the octet-truss lattice material. *Journal of the Mechanics and Physics of Solids*, 49(8):1747–1769, 2001.
- [56] Riccardo Di Sipio, Michele Faucci Giannelli, Sana Ketabchi Haghighat, and Serena Palazzo. Dijetgan: a generative-adversarial network approach for the simulation of qcd dijet events at the lhc. *Journal of High Energy Physics*, 2019(8):1–17, 2019.
- [57] Rui Dou, Tianming Wang, Yunshan Guo, and Brian Derby. Ink-jet printing of zirconia: Coffee staining and line stability. *Journal of the American Ceramic Society*, 94(11):3787–3792, 2011.
- [58] Jérémie Dumas, An Lu, Sylvain Lefebvre, Jun Wu, and Christian Dick. By-example synthesis of structurally sound patterns. *ACM Transactions on Graphics (TOG)*, 34(4):1–12, 2015.

- [59] Cyrille F Dunant, Benoît Bary, Alain B Giorla, Christophe Péniguel, Julien Sanahuja, Charles Toulemonde, Anh-Binh Tran, François Willot, and Julien Yvonnet. A critical comparison of several numerical methods for computing effective properties of highly heterogeneous materials. *Advances in Engineering Software*, 58:1–12, 2013.
- [60] George Dvorak. *Micromechanics of Composite Materials*. Springer, 2013.
- [61] George J Dvorak. Transformation field analysis of inelastic composite materials. *Proceedings of the Royal Society of London. Series A: Mathematical and Physical Sciences*, 437(1900):311–327, 1992.
- [62] David S Ebert, F Kenton Musgrave, Darwyn Peachey, Ken Perlin, and Steven Worley. *Texturing & modeling: a procedural approach*. Morgan Kaufmann, 2003.
- [63] Zak C Eckel, Chaoyin Zhou, John H Martin, Alan J Jacobsen, William B Carter, and Tobias A Schaedler. Additive manufacturing of polymer-derived ceramics. *Science*, 351(6268):58–62, 2016.
- [64] Semyon Efremov, Jonàs Martínez, and Sylvain Lefebvre. 3d periodic cellular materials with tailored symmetry and implicit grading. *Computer-Aided Design*, 140:103086, 2021.
- [65] John C Elliott. Method of producing metal foam, June 19 1956. US Patent 2,751,289.
- [66] John C Elliott. Metal foam and method for making, May 9 1961. US Patent 2,983,597.
- [67] John C Elliott. Metal foaming process, October 24 1961. US Patent 3,005,700.
- [68] Hongbin Fang, Shih-Cheng A Chu, Yutong Xia, and Kon-Well Wang. Programmable self-locking origami mechanical metamaterials. *Advanced Materials*, 30(15):1706311, 2018.
- [69] Fedor I Fedorov. General equations of the theory of elasticity. In *Theory of Elastic Waves in Crystals*, pages 1–33. Springer, 1968.
- [70] Lorenzo Ferrari, Chihhui Wu, Dominic Lepage, Xiang Zhang, and Zhaowei Liu. Hyperbolic metamaterials and their applications. *Progress in Quantum Electronics*, 40:1–40, 2015.
- [71] Thomas Fiedler, Andreas Öchsner, and José Grácio. Numerical investigations on the mechanical properties of adhesively bonded hollow sphere structures. *Journal of composite materials*, 44(10):1165–1178, 2010.
- [72] N. A. Fleck, V. S. Deshpande, and M. F. Ashby. Micro-architected materials: past, present and future. *Proc. R. Soc.*, 2010.

- [73] Tobias Frenzel, Jan David Brehm, Tiemo Bückmann, Robert Schittny, Muamer Kadic, and Martin Wegener. Three-dimensional labyrinthine acoustic metamaterials. *Applied Physics Letters*, 103(6):061907, 2013.
- [74] Tobias Frenzel, Muamer Kadic, and Martin Wegener. Three-dimensional mechanical metamaterials with a twist. *Science*, 358(6366):1072–1074, 2017.
- [75] Oleg Fryazinov, Turlif Vilbrandt, and Alexander Pasko. Multi-scale space-variant frep cellular structures. *Computer-Aided Design*, 45(1):26–34, 2013.
- [76] Bruno Galerne, Ares Lagae, Sylvain Lefebvre, and George Drettakis. Gabor noise by example. *ACM Transactions on Graphics (TOG)*, 31(4):1–9, 2012.
- [77] Paul JF Gandy, Sonny Bardhan, Alan L Mackay, and Jacek Klinowski. Nodal surface approximations to the p, g, d and i-wp triply periodic minimal surfaces. *Chemical physics letters*, 336(3-4):187–195, 2001.
- [78] Justyna K Gansel, Michael Latzel, Andreas Frölich, Johannes Kaschke, Michael Thiel, and Martin Wegener. Tapered gold-helix metamaterials as improved circular polarizers. *Applied Physics Letters*, 100(10):101109, 2012.
- [79] Justyna K Gansel, Michael Thiel, Michael S Rill, Manuel Decker, Klaus Bade, Volker Saile, Georg von Freymann, Stefan Linden, and Martin Wegener. Gold helix photonic metamaterial as broadband circular polarizer. *Science*, 325(5947):1513–1515, 2009.
- [80] Victor M García-Chocano, Johan Christensen, and José Sánchez-Dehesa. Negative refraction and energy funneling by hyperbolic materials: An experimental demonstration in acoustics. *Physical review letters*, 112(14):144301, 2014.
- [81] Tomasz Grzegorz Gawel. Review of additive manufacturing methods. In *Solid State Phenomena*, volume 308, pages 1–20. Trans Tech Publ, 2020.
- [82] Marc GD Geers, Varvara G Kouznetsova, Karel Matouš, and Julien Yvonnet. Homogenization methods and multiscale modeling: nonlinear problems. *Encyclopedia of Computational Mechanics Second Edition*, pages 1–34, 2017.
- [83] Djamchid Ghazanfarpour and Jean-Michel Dischler. Spectral analysis for automatic 3-d texture generation. *Computers & Graphics*, 19(3):413–422, 1995.
- [84] Lorna J Gibson and Michael F Ashby. *Cellular solids: structure and properties*. Cambridge university press, 1999.

- [85] James K Guest, Jean H Prévost, and Ted Belytschko. Achieving minimum length scale in topology optimization using nodal design variables and projection functions. *International journal for numerical methods in engineering*, 61(2):238–254, 2004.
- [86] Ryan Hahnen and Marcelo J Dapino. Niti–al interface strength in ultrasonic additive manufacturing composites. *Composites Part B: Engineering*, 59:101–108, 2014.
- [87] Behrooz Hassani and Ernest Hinton. A review of homogenization and topology optimization i—homogenization theory for media with periodic structure. *Computers & Structures*, 69(6):707–717, 1998.
- [88] Roy Frederick Stanley Hearmon and Alexei A Maradudin. An introduction to applied anisotropic elasticity. *Physics Today*, 14(10):48, 1961.
- [89] Adam Hehr and Marcelo J Dapino. Interfacial shear strength estimates of niti–al matrix composites fabricated via ultrasonic additive manufacturing. *Composites Part B: Engineering*, 77:199–208, 2015.
- [90] Moulinec Herve, Suquet Pierre, and Milton Graeme. Convergence of iterative methods based on neumann series for composite materials: Theory and practice. *International Journal for Numerical Methods in Engineering*, 114(10):1103–1130, 2018.
- [91] Xiaodong Huang and Yi-Min Xie. A further review of eso type methods for topology optimization. *Structural and Multidisciplinary Optimization*, 41(5):671–683, 2010.
- [92] Xiaodong Huang and YM Xie. Convergent and mesh-independent solutions for the bi-directional evolutionary structural optimization method. *Finite elements in analysis and design*, 43(14):1039–1049, 2007.
- [93] Ian Gibson Ian Gibson. Additive manufacturing technologies 3d printing, rapid prototyping, and direct digital manufacturing, 2015.
- [94] Alexandra Ion, Johannes Frohnhofen, Ludwig Wall, Robert Kovacs, Mirela Alistar, Jack Lindsay, Pedro Lopes, Hsiang-Ting Chen, and Patrick Baudisch. Metamaterial mechanisms. In *Proceedings of the 29th annual symposium on user interface software and technology*, pages 529–539, 2016.
- [95] Alexandra Ion, Robert Kovacs, Oliver S Schneider, Pedro Lopes, and Patrick Baudisch. Metamaterial textures. In *Proceedings of the 2018 CHI Conference on Human Factors in Computing Systems*, pages 1–12, 2018.
- [96] Alexandra Ion, David Lindlbauer, Philipp Herholz, Marc Alexa, and Patrick Baudisch. Understanding metamaterial mechanisms. In *Proceedings of the 2019 CHI Conference on Human Factors in Computing Systems*, pages 1–14, 2019.

- [97] Ying Jiang, Zhiyuan Liu, Naoji Matsuhisa, Dianpeng Qi, Wan Ru Leow, Hui Yang, Jiancan Yu, Geng Chen, Yaqing Liu, Changjin Wan, et al. Auxetic mechanical metamaterials to enhance sensitivity of stretchable strain sensors. *Advanced Materials*, 30(12):1706589, 2018.
- [98] Muamer Kadic, Tiemo Bückmann, Nicolas Stenger, Michael Thiel, and Martin Wegener. On the practicability of pentamode mechanical metamaterials. *Applied Physics Letters*, 100(19):191901, 2012.
- [99] Muamer Kadic, Graeme W. Milton, Martin van Hecke, and Martin Wegener. 3D metamaterials. *Nature Reviews Physics*, 1(3):198–210, 2019.
- [100] Muamer Kadic, Robert Schittny, Tiemo Bückmann, Christian Kern, and Martin Wegener. Hall-effect sign inversion in a realizable 3d metamaterial. *Physical Review X*, 5(2):021030, 2015.
- [101] Harshini D KanagaMadhuraN, J Sneha, G Gnanavel, and N Prabhu. Review on manufacturing of cellular polymers and its applications.
- [102] Johannes Kaschke, Leonard Blume, Lin Wu, Michael Thiel, Klaus Bade, Zhenyu Yang, and Martin Wegener. A helical metamaterial for broadband circular polarization conversion. *Advanced Optical Materials*, 3(10):1411–1417, 2015.
- [103] Johannes Kaschke and Martin Wegener. Gold triple-helix mid-infrared metamaterial by sted-inspired laser lithography. *Optics letters*, 40(17):3986–3989, 2015.
- [104] Behrokh Khoshnevis. Automated construction by contour crafting—related robotics and information technologies. *Automation in construction*, 13(1):5–19, 2004.
- [105] Harish NS Krishnamoorthy, Zubin Jacob, Evgenii Narimanov, Ilona Kretzschmar, and Vinod M Menon. Topological transitions in metamaterials. *Science*, 336(6078):205–209, 2012.
- [106] Siddhant Kumar, Stephanie Tan, Li Zheng, and Dennis M Kochmann. Inverse-designed spinodoid metamaterials. *npj Computational Materials*, 6(1):1–10, 2020.
- [107] Ares Lagae, Sylvain Lefebvre, Robert L Cook, Tony Derosé, George Drettakis, David S Ebert, John P Lewis, Ken Perlin, and Matthias Zwicker. State of the art in procedural noise functions. In *Eurographics (State of the Art Reports)*, pages 1–19, 2010.
- [108] Ares Lagae, Sylvain Lefebvre, George Drettakis, and Philip Dutré. Procedural noise using sparse gabor convolution. *ACM Transactions on Graphics (TOG)*, 28(3):1–10, 2009.

- [109] N I Landy, S Sajuyigbe, Jack J Mock, David R Smith, and Willie J Padilla. Perfect metamaterial absorber. *Physical review letters*, 100(20):207402, 2008.
- [110] Hyub Lee, Chin Huat Joel Lim, Mun Ji Low, Nicholas Tham, Vadakke Matham Murukeshan, and Young-Jin Kim. Lasers in additive manufacturing: A review. *International Journal of Precision Engineering and Manufacturing-Green Technology*, 4(3):307–322, 2017.
- [111] Min-Geun Lee and Ki-Ju Kang. Mechanical behaviors of wire-woven metals composed of two different thickness of wires. *Procedia Materials Science*, 4:21–25, 2014.
- [112] Min-Geun Lee, Gyeong-Deuk Ko, Junye Song, and Ki-Ju Kang. Compressive characteristics of a wire-woven cellular metal. *Materials Science and Engineering: A*, 539:185–193, 2012.
- [113] Young Pak Lee, Joo Yull Rhee, Young Joon Yoo, and Ki Won Kim. *Metamaterials for perfect absorption*, volume 236. Springer, 2016.
- [114] Dirk Lehmhus, Matej Vesenjok, Sven De Schampheleire, and Thomas Fiedler. From stochastic foam to designed structure: Balancing cost and performance of cellular metals, 2017.
- [115] Dirk Lehmhus, Axel von Hehl, Kambiz Kayvantash, Rudolf Gradinger, Thomas Becker, Kai Schimanski, and Massimiliano Avalle. Taking a downward turn on the weight spiral—lightweight materials in transport applications. *Materials and Design*, (66):385–389, 2015.
- [116] Dawei Li, Ning Dai, Xiaotong Jiang, and Xiaosheng Chen. Interior structural optimization based on the density-variable shape modeling of 3d printed objects. *The International Journal of Advanced Manufacturing Technology*, 83(9):1627–1635, 2016.
- [117] J Li, T Monaghan, TT Nguyen, RW Kay, RJ Friel, and RA Harris. Multifunctional metal matrix composites with embedded printed electrical materials fabricated by ultrasonic additive manufacturing. *Composites Part B: Engineering*, 113:342–354, 2017.
- [118] Ming Li, Liangchao Zhu, Jingzhi Li, and Kai Zhang. Design optimization of interconnected porous structures using extended triply periodic minimal surfaces. *Journal of Computational Physics*, 425:109909, 2021.
- [119] Ming-Zhen Li, Günter Stephani, and Ki-Ju Kang. New cellular metals with enhanced energy absorption: Wire-woven bulk kagome (wbk)-metal hollow sphere (mhs) hybrids. *Advanced Engineering Materials*, 13(1-2):33–37, 2011.

- [120] Yan Li, Zuying Feng, Liang Hao, Lijing Huang, Chenxing Xin, Yushen Wang, Emiliano Bilotti, Khamis Essa, Han Zhang, Zheng Li, et al. A review on functionally graded materials and structures via additive manufacturing: from multi-scale design to versatile functional properties. *Advanced Materials Technologies*, 5(6):1900981, 2020.
- [121] Zixian Liang and Jensen Li. Extreme acoustic metamaterial by coiling up space. *Physical review letters*, 108(11):114301, 2012.
- [122] WB Liao, S Lan, LB Gao, HT Zhang, S Xu, J Song, XL Wang, and Y Lu. Nanocrystalline high-entropy alloy (CoCrFeNiAl_{0.3}) thin-film coating by magnetron sputtering. 638:383–388, 2017.
- [123] Ismo Lindell, Ari Sihvola, Sergei Tretyakov, and Ari J Viitanen. *Electromagnetic waves in chiral and bi-isotropic media*. Artech House, 1994.
- [124] R Bruce Lindsay. *Nonhomogeneous media and vibration theory*, by Enrique Sanchez-Palencia, 1981.
- [125] Na Liu, Lutz Langguth, Thomas Weiss, Jürgen Kästel, Michael Fleischhauer, Tilman Pfau, and Harald Giessen. Plasmonic analogue of electromagnetically induced transparency at the drude damping limit. *Nature materials*, 8(9):758–762, 2009.
- [126] Sheng Liu, Michael B Sinclair, Thomas S Mahony, Young Chul Jun, Salvatore Campione, James Ginn, Daniel A Bender, Joel R Wendt, Jon F Ihlefeld, Paul G Clem, et al. Optical magnetic mirrors without metals. *Optica*, 1(4):250–256, 2014.
- [127] Xingchen Liu and Vadim Shapiro. Random heterogeneous materials via texture synthesis. *Computational Materials Science*, 99:177–189, 2015.
- [128] Giselle Hsiang Loh, Eujin Pei, David Harrison, and Mario D Monzón. An overview of functionally graded additive manufacturing. *Additive Manufacturing*, 23:34–44, 2018.
- [129] William Longley and Thomas J McIntosh. A bicontinuous tetrahedral structure in a liquid-crystalline lipid. *Nature*, 303(5918):612–614, 1983.
- [130] Eric A Lord and Alan L Mackay. Periodic minimal surfaces of cubic symmetry. *Current Science*, pages 346–362, 2003.
- [131] Thomas S Lumpe and Tino Stankovic. Unit cell catalog: Exploring the property space of periodic cellular structures based on crystal networks. 2021.
- [132] Zhen Luo, Michael Yu Wang, Shengyin Wang, and Peng Wei. A level set-based parameterization method for structural shape and topology optimization. *International Journal for Numerical Methods in Engineering*, 76(1):1–26, 2008.

- [133] Nicolas Lutz, Basile Sauvage, and Jean-Michel Dischler. Cyclostationary gaussian noise: theory and synthesis. In *Computer Graphics Forum*, volume 40, pages 239–250. Wiley Online Library, 2021.
- [134] Dalia Mahmoud and Mohamed A Elbestawi. Lattice structures and functionally graded materials applications in additive manufacturing of orthopedic implants: a review. *Journal of Manufacturing and Materials Processing*, 1(2):13, 2017.
- [135] Jill Z Manapat, Qiyi Chen, Piaoran Ye, and Rigoberto C Advincula. 3d printing of polymer nanocomposites via stereolithography. *Macromolecular Materials and Engineering*, 302(9):1600553, 2017.
- [136] D Martella, D Antonioli, S Nocentini, DS Wiersma, Giancarlo Galli, M Laus, and C Parmeggiani. Light activated non-reciprocal motion in liquid crystalline networks by designed microactuator architecture. *RSC advances*, 7(32):19940–19947, 2017.
- [137] Jonàs Martínez, Jérémie Dumas, Sylvain Lefebvre, and Li-Yi Wei. Structure and appearance optimization for controllable shape design. *ACM Transactions on Graphics (TOG)*, 34(6):1–11, 2015.
- [138] Jonàs Martínez, Mélina Skouras, Christian Schumacher, Samuel Hornus, Sylvain Lefebvre, and Bernhard Thomaszewski. Star-shaped metrics for mechanical metamaterial design. *ACM Transactions on Graphics*, 38(4), 2019.
- [139] Ian Maskery, AO Aremu, Luke Parry, RD Wildman, CJ Tuck, and IA Ashcroft. Effective design and simulation of surface-based lattice structures featuring volume fraction and cell type grading. *Materials & Design*, 155:220–232, 2018.
- [140] Ian Maskery, L Sturm, AO Aremu, Ajit Panesar, CB Williams, CJ Tuck, Ricky D Wildman, IA Ashcroft, and Richard JM Hague. Insights into the mechanical properties of several triply periodic minimal surface lattice structures made by polymer additive manufacturing. *Polymer*, 152:62–71, 2018.
- [141] Mark W Matsen and Frank S Bates. Unifying weak-and strong-segregation block copolymer theories. *Macromolecules*, 29(4):1091–1098, 1996.
- [142] Matthias Kabel Matti Schneider, Felix Ospald. Computational homogenization of elasticity on a staggered grid. *International Journal for Numerical Methods in Engineering*, 105(9):693–720, 2016.
- [143] Chiang C Mei and Bogdan Vernescu. *Homogenization methods for multi-scale mechanics*. World scientific, 2010.

- [144] Ferry PW Melchels, Jan Feijen, and Dirk W Grijpma. A review on stereolithography and its applications in biomedical engineering. *Biomaterials*, 31(24):6121–6130, 2010.
- [145] Jean-Claude Michel, Hervé Moulinec, and Pierre Suquet. Effective properties of composite materials with periodic microstructure: a computational approach. *Computer methods in applied mechanics and engineering*, 172(1-4):109–143, 1999.
- [146] Graeme W Milton and Andrej V Cherkaev. Which elasticity tensors are realizable? 1995.
- [147] Tetsuji Miyoshi, Shigeta Hara, Toshiji Mukai, and Kenji Higashi. Development of a closed cell aluminum alloy foam with enhancement of the compressive strength. *Materials Transactions*, 42(10):2118–2123, 2001.
- [148] Tetsuji Miyoshi, Masao Itoh, Shigeru Akiyama, and Akira Kitahara. Al-porras aluminum foam: production process, properties, and applications. *Advanced engineering materials*, 2(4):179–183, 2000.
- [149] Omar A Mohamed, Syed H Masood, and Jahar L Bhowmik. Optimization of fused deposition modeling process parameters: a review of current research and future prospects. *Advances in Manufacturing*, 3(1):42–53, 2015.
- [150] Farhang Momeni, Xun Liu, Jun Ni, et al. A review of 4d printing. *Materials & design*, 122:42–79, 2017.
- [151] Vincent Monchiet and Guy Bonnet. A polarization-based FFT iterative scheme for computing the effective properties of elastic composites with arbitrary contrast. *International Journal for Numerical Methods in Engineering*, 89(11):1419–1436, 2012.
- [152] H Moulinec and P Suquet. A fft-based numerical method for computing the mechanical properties of composites from images of their microstructures. In *IUTAM symposium on microstructure-property interactions in composite materials*, pages 235–246. Springer, 1995.
- [153] Herve Moulinec and Pierre Suquet. A fast numerical method for computing the linear and nonlinear mechanical properties of composites. *Comptes rendus de l'Académie des sciences. Série II. Mécanique, physique, chimie, astronomie.*, 1994.
- [154] Hervé Moulinec and Pierre Suquet. A numerical method for computing the overall response of nonlinear composites with complex microstructure. *Computer methods in applied mechanics and engineering*, 157(1-2):69–94, 1998.
- [155] Jochen Mueller and Kristina Shea. Stepwise graded struts for maximizing energy absorption in lattices. *Extreme Mechanics Letters*, 25:7–15, 2018.

- [156] H Nakajima, T Ikeda, and SK Hyun. Fabrication of lotus-type porous metals and their physical properties. *Advanced Engineering Materials*, 6(6):377–384, 2004.
- [157] Hideo Nakajima. Fabrication of lotus-type porous metals through hydride decomposition. *Advanced engineering materials*, 10(9):816–819, 2008.
- [158] Fabrice Neyret and Eric Heitz. *Understanding and controlling contrast oscillations in stochastic texture algorithms using Spectrum of Variance*. PhD thesis, LJK/Grenoble University-INRIA, 2016.
- [159] Tuan D Ngo, Alireza Kashani, Gabriele Imbalzano, Kate TQ Nguyen, and David Hui. Additive manufacturing (3D printing): A review of materials, methods, applications and challenges. *Composites Part B: Engineering*, 143:172–196, 2018.
- [160] Akihiro Nishiguchi, Ahmed Mourran, Hang Zhang, and Martin Möller. In-gel direct laser writing for 3d-designed hydrogel composites that undergo complex self-shaping. *Advanced Science*, 5(1):1700038, 2018.
- [161] John F Nye, RD Spence, and MT Sprackling. Photoelastic study of dislocation arrangements in crystals. *Philosophical Magazine*, 2(18):772–776, 1957.
- [162] Atsuyuki Okabe, Barry Boots, Kokichi Sugihara, and Sung Nok Chiu. *Spatial tessellations: concepts and applications of Voronoi diagrams*, volume 501. John Wiley & Sons, 2009.
- [163] Michael O’Keeffe, Maxim A Peskov, Stuart J Ramsden, and Omar M Yaghi. The reticular chemistry structure resource (rcsr) database of, and symbols for, crystal nets. *Accounts of chemical research*, 41(12):1782–1789, 2008.
- [164] Al-Ketan Oraib, Rezgui Rachid, Rowshan Reza, Du Huifeng, Nicholas X. Fang, and Rashid K. Abu Al-Rub. Microarchitected stretching-dominated mechanical metamaterials with minimal surface topologies. *Advanced Engineering Materials*, 20, 2018.
- [165] José María Ortolano González, Joaquín Alberto Hernández Ortega, and Xavier Oliver Olivella. *A comparative study on homogenization strategies for multi-scale analysis of materials*. Centre Internacional de Mètodes Numèrics en Enginyeria (CIMNE), 2013.
- [166] Stanley Osher and Ronald P Fedkiw. *Level set methods and dynamic implicit surfaces*, volume 153. Springer, 2003.
- [167] Stanley Osher and James A Sethian. Fronts propagating with curvature-dependent speed: Algorithms based on hamilton-jacobi formulations. *Journal of computational physics*, 79(1):12–49, 1988.

- [168] M Paley and J Aboudi. Micromechanical analysis of composites by the generalized cells model. *Mechanics of materials*, 14(2):127–139, 1992.
- [169] Ajit Panesar, Meisam Abdi, Duncan Hickman, and Ian Ashcroft. Strategies for functionally graded lattice structures derived using topology optimisation for additive manufacturing. *Additive Manufacturing*, 19:81–94, 2018.
- [170] Haedong Park, Hyungho Kwon, Yongsan An, Woong-Ryeol Yu, Myoung-Woon Moon, and Kahyun Hur. Mechanical metamaterials with thermoresponsive switching between positive and negative poisson’s ratios. *physica status solidi (RRL)–Rapid Research Letters*, 12(5):1800040, 2018.
- [171] John B Pendry, Anthony J Holden, David J Robbins, and WJ Stewart. Magnetism from conductors and enhanced nonlinear phenomena. *IEEE transactions on microwave theory and techniques*, 47(11):2075–2084, 1999.
- [172] Joakim Petersson. A finite element analysis of optimal variable thickness sheets. *SIAM journal on numerical analysis*, 36(6):1759–1778, 1999.
- [173] Carl Pfeiffer and Anthony Grbic. Metamaterial Huygens’ surfaces: tailoring wave fronts with reflectionless sheets. *Physical review letters*, 110(19):197401, 2013.
- [174] Radivoje S Popovic. *Hall effect devices*. CRC Press, 2003.
- [175] Caroline Pouya, Johannes TB Overvelde, Mathias Kolle, Joanna Aizenberg, Katia Bertoldi, James C Weaver, and Pete Vukusic. Characterization of a mechanically tunable gyroid photonic crystal inspired by the butterfly *parides sesostris*. *Advanced Optical Materials*, 4(1):99–105, 2016.
- [176] A. Radman, X. Huang, and Y.M. Xie. Topology optimization of functionally graded cellular materials. *Journal of Materials Science*, 48(4):1503–1510, 2013.
- [177] Ahmad Rafsanjani, Abdolhamid Akbarzadeh, and Damiano Pasini. Metamaterials: Snapping mechanical metamaterials under tension (adv. mater. 39/2015). *Advanced Materials*, 27(39):5930–5930, 2015.
- [178] Vanessa Robins, Stuart Ramsden, and Stephen Hyde. Epinet: euclidean patterns in non-euclidean tilings. In *ACM SIGGRAPH 2006 Research posters*, pages 95–es. 2006.
- [179] N Rossi, Rolando Yera, CG Méndez, Sebastian Toro, and Alfredo Edmundo Huespe. Numerical technique for the 3D microarchitecture design of elastic composites inspired by crystal symmetries. *Computer Methods in Applied Mechanics and Engineering*, 359:112760, 2020.

- [180] Donald E Sands. *Introduction to crystallography*. Courier Corporation, 1993.
- [181] M Sautter, Ch Dietrich, MH Poech, S Schmauder, and HF Fischmeister. Finite element modelling of a transverse-loaded fibre composite effects of section size and net density. *Computational materials science*, 1(3):225–233, 1993.
- [182] Krishna Kumar Saxena, Raj Das, and Emilio P Calius. Three decades of auxetics research- materials with negative poisson’s ratio: a review. *Advanced Engineering Materials*, 18(11):1847–1870, 2016.
- [183] S A Schelkunoff. *Advanced Antenna Theory*. Wiley, 1952.
- [184] Alan Hugh Schoen. *Infinite periodic minimal surfaces without self-intersections*. National Aeronautics and Space Administration, 1970.
- [185] Arthur Schoenflies. *Krystallsysteme und Krystallstruktur*. Teubner, 1891.
- [186] Rick C Schrodin, Mohammed Al-Daous, Christopher F Blanford, and Andreas Stein. Optical properties of inverse opal photonic crystals. *Chemistry of materials*, 14(8):3305–3315, 2002.
- [187] Hermann Amandus Schwarz. *Gesammelte mathematische abhandlungen*, volume 260. American Mathematical Soc., 1972.
- [188] James Albert Sethian. *Level set methods and fast marching methods: evolving interfaces in computational geometry, fluid mechanics, computer vision, and materials science*, volume 3. Cambridge university press, 1999.
- [189] V Shapovalov and L Boyko. Gasar—a new class of porous materials. *Advanced engineering materials*, 6(6):407–410, 2004.
- [190] Vladimir I Shapovalov. Method for manufacturing porous articles, January 26 1993. US Patent 5,181,549.
- [191] Li Shen, Hany Farid, and Mark A McPeck. Modeling three-dimensional morphological structures using spherical harmonics. *Evolution: international journal of organic evolution*, 63(4):1003–1016, 2009.
- [192] Ole Sigmund. On the design of compliant mechanisms using topology optimization. *Journal of Structural Mechanics*, 25(4):493–524, 1997.
- [193] Ole Sigmund. Morphology-based black and white filters for topology optimization. *Structural and Multidisciplinary Optimization*, 33(4-5):401–424, 2007.
- [194] Ole Sigmund and Kurt Maute. Topology optimization approaches. *Structural and Multidisciplinary Optimization*, 48(6):1031–1055, 2013.

- [195] Ole Sigmund and Joakim Petersson. Numerical instabilities in topology optimization: a survey on procedures dealing with checkerboards, mesh-dependencies and local minima. *Structural optimization*, 16(1):68–75, 1998.
- [196] Peter-Pike Sloan, Jan Kautz, and John Snyder. Precomputed radiance transfer for real-time rendering in dynamic, low-frequency lighting environments. In *Proceedings of the 29th annual conference on Computer graphics and interactive techniques*, pages 527–536, 2002.
- [197] GF Smith, MMu Smith, and RS Rivlin. Integrity bases for a symmetric tensor and a vector—the crystal classes. *Archive for rational mechanics and analysis*, 12(1):93–133, 1963.
- [198] Jian Song, Wenzhao Zhou, Yuejiao Wang, Rong Fan, Yinchu Wang, Junying Chen, Yang Lu, and Lixiao Li. Octet-truss cellular materials for improved mechanical properties and specific energy absorption. *Materials & Design*, 173:107773, 2019.
- [199] Yakov M Strelniker and David J Bergman. Thermoelectric response of a periodic composite medium in the presence of a magnetic field: Angular anisotropy. *Physical Review B*, 96(23):235308, 2017.
- [200] Martien A Cohen Stuart, Wilhelm TS Huck, Jan Genzer, Marcus Müller, Christopher Ober, Manfred Stamm, Gleb B Sukhorukov, Igal Szleifer, Vladimir V Tsukruk, Marek Urban, et al. Emerging applications of stimuli-responsive polymer materials. *Nature materials*, 9(2):101–113, 2010.
- [201] James Utama Surjadi, Libo Gao, Huifeng Du, Xiang Li, Xiang Xiong, Nicholas Xuanlai Fang, and Yang Lu. Mechanical metamaterials and their engineering applications. *Advanced Engineering Materials*, 2019.
- [202] M Taherishargh, IV Belova, GE Murch, and T Fiedler. Pumice/aluminium syntactic foam. *Materials Science and Engineering: A*, 635:102–108, 2015.
- [203] M Taherishargh, IV Belova, GE Murch, and T Fiedler. The effect of particle shape on mechanical properties of perlite/metal syntactic foam. *Journal of Alloys and Compounds*, 693:55–60, 2017.
- [204] M Taherishargh, MA Sulong, IV Belova, GE Murch, and T Fiedler. On the particle size effect in expanded perlite aluminium syntactic foam. *Materials & Design (1980-2015)*, 66:294–303, 2015.
- [205] Naoki Takano, Masaru Zako, and Toru Okazaki. Efficient modeling of microscopic heterogeneity and local crack in composite materials by finite element mesh superposition method. *JSME International Journal Series A Solid Mechanics and Material Engineering*, 44(4):602–609, 2001.

- [206] Maria-Gabriella Tarantino and Kostas Danas. Programmable higher-order euler buckling modes in hierarchical beams. *International Journal of Solids and Structures*, 167:170–183, 2019.
- [207] Patrick Theato, Brent S Sumerlin, Rachel K O'Reilly, and Thomas H Epps III. Stimuli responsive materials. *Chemical Society Reviews*, 42(17):7055–7056, 2013.
- [208] Skylar Tibbits. 4d printing: multi-material shape change. *Architectural Design*, 84(1):116–121, 2014.
- [209] Kristina Shea Tino Stankovic. Investigation of a Voronoi diagram representation for the computational design of additively manufactured discrete lattice structures. *Journal of Mechanical Design*, 142, 11 2020.
- [210] A. Schaedler Tobias and B. Carter William. Architected cellular materials. *Annual Review of Materials Research*, 46:187–210, 2016.
- [211] M Tornow, Dieter Weiss, K v Klitzing, K Eberl, David J Bergman, and Yakov M Strelniker. Anisotropic magnetoresistance of a classical antidot array. *Physical review letters*, 77(1):147, 1996.
- [212] Nahum Travitzky, Alexander Bonet, Benjamin Dermeik, Tobias Fey, Ina Filbert-Demut, Lorenz Schlier, Tobias Schlordt, and Peter Greil. Additive manufacturing of ceramic-based materials. *Advanced engineering materials*, 16(6):729–754, 2014.
- [213] SA Tretyakov, AH Sihvola, AA Sochava, and CR Simovski. Magneto-electric interactions in bi-anisotropic media. *Journal of electromagnetic waves and applications*, 12(4):481–497, 1998.
- [214] Thibault Tricard, Semyon Efremov, Cédric Zanni, Fabrice Neyret, Jonàs Martínez, and Sylvain Lefebvre. Procedural phasor noise. *ACM Transactions on Graphics (TOG)*, 38(4):1–13, 2019.
- [215] Thibault Tricard, Vincent Tavernier, Cédric Zanni, Jonàs Martínez, Pierre-Alexandre Hugron, Fabrice Neyret, and Sylvain Lefebvre. Freely orientable microstructures for designing deformable 3d prints. *ACM Transactions on Graphics (TOG)*, 39(6):1–16, 2020.
- [216] I Ullah, J Elambasseril, M Brandt, and S Feih. Performance of bio-inspired kagome truss core structures under compression and shear loading. *Composite Structures*, 118:294–302, 2014.
- [217] Ben Utela, Duane Storti, Rhonda Anderson, and Mark Ganter. A review of process development steps for new material systems in three dimensional printing (3dp). *Journal of Manufacturing Processes*, 10(2):96–104, 2008.

- [218] Kiril Vidimčec, Szu-Po Wang, Jonathan Ragan-Kelley, and Wojciech Matusik. Openfab: A programmable pipeline for multi-material fabrication. *ACM Transactions on Graphics (TOG)*, 32(4):1–12, 2013.
- [219] Davide Viterbo. Crystal lattices and crystal symmetry. In *Quantum-Mechanical Ab-initio Calculation of the Properties of Crystalline Materials*, pages 1–29. Springer, 1996.
- [220] Woldemar Voigt. *Lehrbuch der kristallphysik:(mit ausschluss der kristaloptik)*, volume 34. BG Teubner, 1910.
- [221] Woldemar Voigt. *Lehrbuch der kristallphysik*, volume 962. Teubner Leipzig, 1928.
- [222] Mathias Wallin, Matti Ristinmaa, and Henrik Askfelt. Optimal topologies derived from a phase-field method. *Structural and Multidisciplinary Optimization*, 45(2):171–183, 2012.
- [223] Rodger M. Walser. Electromagnetic metamaterials. In *SPIE Optics + Photonics*, 2001.
- [224] Chun Feng Wang, Fei Zhou, Hua Zhi Gu, Hong Xi Zhu, and Ya Wei Li. Preparation and microstructure of al-intercalated vermiculite. In *Advanced Materials Research*, volume 399, pages 683–687. Trans Tech Publ, 2012.
- [225] Michael Yu Wang, Xiaoming Wang, and Dongming Guo. A level set method for structural topology optimization. *Computer methods in applied mechanics and engineering*, 192(1-2):227–246, 2003.
- [226] Michael Yu Wang, Shiwei Zhou, and Han Ding. Nonlinear diffusions in topology optimization. *Structural and Multidisciplinary Optimization*, 28(4):262–276, 2004.
- [227] Xin Wang, Man Jiang, Zuowan Zhou, Jihua Gou, and David Hui. 3d printing of polymer matrix composites: A review and prospective. *Composites Part B: Engineering*, 110:442–458, 2017.
- [228] Claire M Watts, Xianliang Liu, and Willie J Padilla. Metamaterial electromagnetic wave absorbers. *Advanced materials*, 24(23):OP98–OP120, 2012.
- [229] Martin Wegener, Gunnar Dolling, and Stefan Linden. Backward waves moving forward. *Nature materials*, 6(7):475–476, 2007.
- [230] Li-Yi Wei, Sylvain Lefebvre, Vivek Kwatra, and Greg Turk. State of the art in example-based texture synthesis. In *Eurographics 2009, State of the Art Report, EG-STAR*, pages 93–117. Eurographics Association, 2009.

- [231] Stewart W Williams, Filomeno Martina, Adrian C Addison, Jialuo Ding, Goncalo Pardal, and P Colegrove. Wire+ arc additive manufacturing. *Materials science and technology*, 32(7):641–647, 2016.
- [232] François Willot. Fourier-based schemes for computing the mechanical response of composites with accurate local fields. *Comptes Rendus Mécanique*, 343(3):232–245, 2015.
- [233] Maximilian Wormser, Franziska Warmuth, and Carolin Körner. Evolution of full phononic band gaps in periodic cellular structures. *Applied Physics A*, 123(10):1–8, 2017.
- [234] Andrew Wright and Andrew Kennedy. The processing and properties of syntactic al foams containing low cost expanded glass particles. *Advanced Engineering Materials*, 19(11):1600467, 2017.
- [235] Zheng Xiaoyu, Lee Howon, Weisgraber Todd H., Shusteff Maxim, DeOtte Joshua, Duoss Eric B., Kuntz Joshua D., Biener Monika M., Ge Qi, Jackson Julie A., Kucheyev Sergei O., Fang Nicholas X., and Spadaccini Christopher M. Ultralight, ultrastiff mechanical metamaterials. *Science*, 344(6190):1373–1377, 2014.
- [236] Shengli Xu, Yuanwu Cai, and Gengdong Cheng. Volume preserving non-linear density filter based on heaviside functions. *Structural and Multidisciplinary Optimization*, 41(4):495–505, 2010.
- [237] Takayuki Yamada, Kazuhiro Izui, Shinji Nishiwaki, and Akihiro Takezawa. A topology optimization method based on the level set method incorporating a fictitious interface energy. *Computer Methods in Applied Mechanics and Engineering*, 199(45-48):2876–2891, 2010.
- [238] Min Yang, Shuyu Chen, Caixing Fu, and Ping Sheng. Optimal sound-absorbing structures. *Materials Horizons*, 4(4):673–680, 2017.
- [239] Nan Yang, Zhi Quan, Dawei Zhang, and Yanling Tian. Multi-morphology transition hybridization cad design of minimal surface porous structures for use in tissue engineering. *Computer-Aided Design*, 56:11–21, 2014.
- [240] Nuo Yang, Shiqian Hu, Dengke Ma, Tingyu Lu, and Baowen Li. Nanoscale graphene disk: a natural functionally graded material—how is fourier’s law violated along radius direction of 2d disk. *Scientific reports*, 5(1):1–8, 2015.
- [241] Jie Yao, Zhaowei Liu, Yongmin Liu, Yuan Wang, Cheng Sun, Guy Bartal, Angelica M Stacy, and Xiang Zhang. Optical negative refraction in bulk metamaterials of nanowires. *Science*, 321(5891):930–930, 2008.
- [242] Chor Yen Yap, Chee Kai Chua, Zhi Li Dong, Zhong Hong Liu, Dan Qing Zhang, Loong Ee Loh, and Swee Leong Sing. Review of selective laser melting: Materials and applications. *Applied physics reviews*, 2(4):041101, 2015.

- [243] Rolando Yera, N Rossi, CG Méndez, and Alfredo Edmundo Huespe. Topology design of 2d and 3d elastic material microarchitectures with crystal symmetries displaying isotropic properties close to their theoretical limits. *Applied Materials Today*, 18:100456, 2020.
- [244] Athanasios D Zacharopoulos, Simon R Arridge, Oliver Dorn, Ville Kolehmainen, and Jan Sikora. Three-dimensional reconstruction of shape and piecewise constant region values for optical tomography using spherical harmonic parametrization and a boundary element method. *Inverse Problems*, 22(5):1509, 2006.
- [245] Hao Zeng, Piotr Wasylczyk, Camilla Parmeggiani, Daniele Martella, Matteo Burrelli, and Diederik Sybolt Wiersma. Light-fueled microscopic walkers. *Advanced Materials*, 27(26):3883–3887, 2015.
- [246] O Zerhouni, MG Tarantino, and K Danas. Numerically-aided 3d printed random isotropic porous materials approaching the hashin-shtrikman bounds. *Composites Part B: Engineering*, 156:344–354, 2019.
- [247] Ning Zhang, Tahir Khan, Haomin Guo, Shaoshuai Shi, Wei Zhong, and Weiwei Zhang. Functionally graded materials: an overview of stability, buckling, and free vibration analysis. *Advances in Materials Science and Engineering*, 2019, 2019.
- [248] Tarek I Zohdi. Homogenization methods and multiscale modeling. *Encyclopedia of Computational Mechanics Second Edition*, pages 1–24, 2017.
- [249] Frank W Zok, Ryan M Latture, and Matthew R Begley. Periodic truss structures. *Journal of the Mechanics and Physics of Solids*, 96:184–203, 2016.
- [250] Hongming Zong, Hongying Zhang, Yiqiang Wang, Michael Yu Wang, and Jerry YH Fuh. On two-step design of microstructure with desired poisson’s ratio for am. *Materials & Design*, 159:90–102, 2018.

Appendices

Appendix A

Symmetry notation and definitions

We describe the notation used for the different symmetries and the corresponding definition in Table A.1.

Crystal system	Point group			Example of $f_S(\varphi, \theta)$
	Crystal class name	Hermann-Mauguin	Schoenflies	
Triclinic	Pedial	1	C_1	$1 + 0.8(Y_2^1(\varphi + 0.5\pi, \theta) + Y_3^1(\varphi, \theta) + Y_2^2(\varphi + 0.35\pi, \theta))$
Monoclinic	Sphenoidal	2	C_2	$1 + Y_5^4(\varphi, \theta) + Y_6^4(\varphi, \theta) + Y_3^1(\varphi, \theta)$
	Domatic	m	C_{1h}	$1 + Y_2^1(\varphi, \theta) + Y_3^2(\varphi - 0.25\pi, \theta) + Y_3^4(\varphi, \theta)$
	Prismatic	$2/m$	C_{2h}	$1 + Y_4^1(\varphi, \theta) + Y_6^4(\varphi, \theta)$
Orthorhombic	Rhombic-disphenoidal	222	D_2	$1 + Y_3^2(\varphi - 0.25\pi, \theta) + Y_5^4(\varphi - 0.375\pi, \theta)$
	Rhombic-pyramidal	$mm2$	C_{2v}	$1 + Y_3^2(\varphi, \theta) + Y_4^4(\varphi, \theta)$
	Rhombic-dipyramidal	mmm	D_{2h}	$1 + Y_4^2(\varphi, \theta) + Y_6^4(\varphi, \theta)$
Trigonal	Trigonal-pyramidal	3	C_3	$1.3 + Y_4^3(\varphi, \theta) + Y_5^3(\varphi, \theta) + Y_6^3(\varphi - 0.08\pi, \theta)$
	Rhombohedral	$\bar{3}$	S_6	$1 + Y_4^3(\varphi, \theta) + Y_6^6(\varphi, \theta) + Y_6^6(\varphi - 0.08\pi, \theta)$
	Trigonal-trapezohedral	32	D_3	$1 + Y_4^3(\varphi - \frac{\pi}{6}, \theta) + Y_5^3(\varphi, \theta) + Y_6^3(\varphi - \frac{\pi}{6}, \theta)$
	Ditrigonal-pyramidal	$3m$	C_{3v}	$1.3 + Y_5^3(\varphi, \theta) + Y_6^3(\varphi, \theta) + Y_7^6(\varphi, \theta)$
	Ditrigonal-scalenohedral	$\bar{3}m$	D_{3d}	$1 + Y_4^3(\varphi, \theta) + Y_6^6(\varphi, \theta)$
Tetragonal	Tetragonal-pyramidal	4	C_4	$1 + Y_4^4(\varphi - 0.12\pi, \theta) + Y_5^4(\varphi, \theta) + Y_6^4(\varphi, \theta)$
	Tetragonal-disphenoidal	$\bar{4}$	S_4	$1 + Y_3^2(\varphi, \theta) + Y_4^4(\varphi, \theta) + Y_6^4(\varphi - 0.08\pi, \theta)$
	Tetragonal-dipyramidal	$4/m$	C_{4h}	$1 + Y_4^4(\varphi - 0.12\pi, \theta) + Y_6^4(\varphi, \theta) + Y_8^4(\varphi, \theta)$
	Tetragonal-trapezohedral	422	D_4	$1 + Y_4^4(\varphi - 0.125\pi, \theta) + Y_6^4(\varphi - 0.250\pi, \theta)$
	Ditetragonal-pyramidal	$4mm$	C_{4v}	$1 + Y_5^4(\varphi, \theta) + Y_6^4(\varphi, \theta)$
	Tetragonal-scalenohedral	$\bar{4}2m$	D_{2d}	$1 + Y_3^2(\varphi, \theta) + Y_4^4(\varphi, \theta)$
	Ditetragonal-dipyramidal	$4/mmm$	D_{4h}	$1 + Y_4^4(\varphi, \theta) + Y_8^8(\varphi, \theta)$
Hexagonal	Hexagonal-pyramidal	6	C_6	$1 + Y_7^6(\varphi, \theta) + Y_8^6(\varphi, \theta) + Y_9^6(\varphi - 0.1\pi, \theta)$
	Trigonal-dipyramidal	$\bar{6}$	C_{3h}	$1 + Y_5^3(\varphi, \theta) + Y_7^4(\varphi, \theta) + Y_8^6(\varphi - 0.1\pi, \theta)$
	Hexagonal-dipyramidal	$6/m$	C_{6h}	$1.1 + Y_6^6(\varphi - 0.08\pi, \theta) + Y_8^6(\varphi, \theta) + Y_{10}^6(\varphi - 0.15\pi, \theta)$
	Hexagonal-trapezohedral	622	D_6	$1.2 + Y_6^6(\varphi, \theta) + Y_7^6(\varphi - \frac{\pi}{12}, \theta) + Y_8^6(\varphi, \theta) + Y_{11}^6(\varphi - \frac{\pi}{12}, \theta)$
	Dihexagonal-pyramidal	$6mm$	C_{6v}	$1.3 + Y_6^6(\varphi, \theta) + Y_7^6(\varphi, \theta) + Y_8^6(\varphi, \theta) + Y_{10}^6(\varphi, \theta)$
	Ditrigonal-dipyramidal	$\bar{6}m2$	D_{3h}	$1 + Y_5^3(\varphi, \theta) + Y_6^6(\varphi, \theta)$
	Dihexagonal-dipyramidal	$6/mmm$	D_{6h}	$1 + Y_6^6(\varphi, \theta) + Y_8^6(\varphi, \theta) + Y_{10}^6(\varphi, \theta)$
Cubic	Tetartoidal	23	T	Spherical snub tetrahedral
	Diploidal	$m\bar{3}$	T_h	Spherical cube
	Gyroidal	432	O	Spherical snub cube
	Hextetrahedral	$\bar{4}3m$	T_d	Spherical tetrahedron / truncated tetrahedron
	Hexoctahedral	$m\bar{3}m$	O_h	Spherical hexahedron / octahedron / cuboctahedron

Table A.1: Crystal systems, associated point groups, and its the corresponding definition of the star-shaped set \mathcal{S} (either using spherical harmonics or spherical polyhedra). In this table we consider two standard nomenclatures for crystal point groups (Hermann-Mauguin [180] and Schoenflies [185]). For a comprehensive introduction to 3D elasticity tensor symmetries see [60]. Please note that for monoclinic, tetragonal, trigonal, and hexagonal crystal systems the elasticity tensor may vary depending on the axis of symmetry (in the table we only show one of such possibilities). Let m be the number of independent constants of the elasticity tensor. Let Y_l^k be the spherical harmonic function of degree l and order k .

Appendix B

Structures gallery

We present a gallery of closed and open cell structures corresponding to different point groups computed with our method in Tables B.1 and B.2.

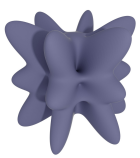
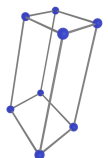
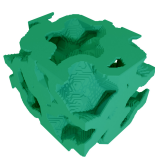
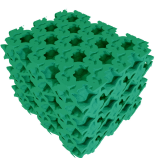
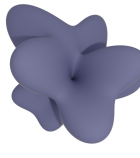
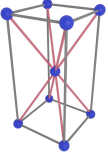


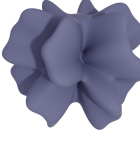
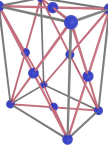
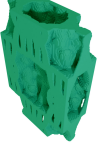
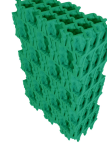

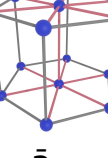
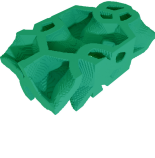
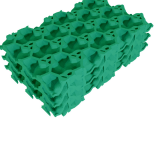
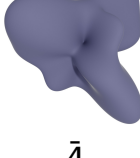
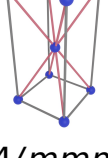

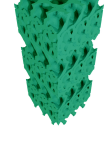

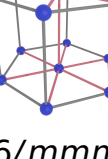
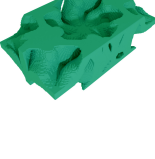
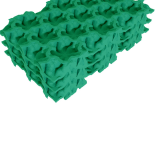

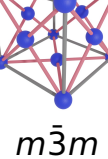

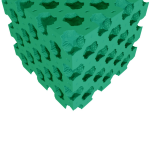
S	L	\mathcal{T}_{LNS}	Unit cell	3×3	Tensor
		1			$\begin{pmatrix} 21.159 & 7.115 & 7.052 & -0.067 & 1.7572 & -1.371 \\ 21.911 & 6.730 & 19.245 & 1.070 & 0.477 & -1.579 \\ & & & 0.110 & 0.762 & 1.262 \\ & & & & 7.361 & 0.535 & 0.726 \\ & & & & & & 7.382 & 0.052 \\ & & & & & & & & 8.275 \end{pmatrix}$
$6/mmm$	1	1			Triclinic
		m			$\begin{pmatrix} 21.742 & 6.144 & 6.525 & -0.001 & -2.000 & -0.001 \\ & 17.346 & 6.020 & -0.002 & -0.312 & -0.001 \\ & & 23.814 & -0.003 & -3.912 & 0.000 \\ & & & & 5.066 & 0.000 & -1.421 \\ & & & & & & 6.838 & 0.000 \\ & & & & & & & & 6.012 \end{pmatrix}$
m	$4/mmm$	m			Monoclinic
		222			$\begin{pmatrix} 16.737 & 5.131 & 4.270 & 0.001 & 0.00 & 0.011 \\ & 14.456 & 4.028 & 0.000 & 0.000 & 0.009 \\ & & 27.632 & 0.002 & 0.000 & 0.008 \\ & & & & 4.954 & 0.000 & 0.003 \\ & & & & & & 5.798 & 0.001 \\ & & & & & & & & 5.079 \end{pmatrix}$
622	mmm	222			Orthorhombic
		3			$\begin{pmatrix} 13.839 & 5.276 & 3.386 & -0.186 & 0.075 & -0.007 \\ & 13.958 & 3.362 & 0.214 & -0.030 & 0.010 \\ & & 15.391 & -0.006 & 0.036 & 0.006 \\ & & & & 4.434 & 0.000 & -0.043 \\ & & & & & & 4.441 & -0.188 \\ & & & & & & & & 4.302 \end{pmatrix}$
6	$\bar{3}m$	3			Trigonal
		$\bar{4}$			$\begin{pmatrix} 26.683 & 7.063 & 8.039 & 0.000 & -0.001 & -0.112 \\ & 26.684 & 8.039 & 0.000 & 0.00 & 0.109 \\ & & 31.751 & 0.000 & 0.000 & 0.000 \\ & & & & 7.716 & 0.000 & 0.000 \\ & & & & & & 7.716 & 0.000 \\ & & & & & & & & 8.009 \end{pmatrix}$
$\bar{4}$	$4/mmm$	$\bar{4}$			Tetragonal
		6			$\begin{pmatrix} 15.115 & 3.776 & 3.149 & 0.000 & 0.000 & -0.061 \\ & 15.149 & 3.180 & 0.003 & -0.001 & -0.066 \\ & & 17.607 & 0.010 & -0.001 & -0.017 \\ & & & & 4.507 & -0.012 & 0.000 \\ & & & & & & 4.470 & 0.000 \\ & & & & & & & & 5.709 \end{pmatrix}$
6	$6/mmm$	6			Hexagonal
		23			$\begin{pmatrix} 37.339 & 14.344 & 14.334 & 0.016 & 0.027 & 0.018 \\ & 37.619 & 14.437 & -0.009 & 0.011 & 0.014 \\ & & 37.531 & 0.021 & 0.011 & 0.003 \\ & & & & 12.541 & -0.003 & 0.006 \\ & & & & & & 12.404 & 0.014 \\ & & & & & & & & 12.354 \end{pmatrix}$
23	$m\bar{3}m$	23			Cubic

Table B.1: Gallery closed-cell


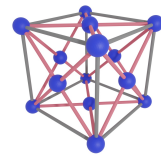

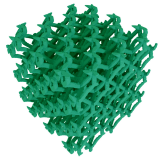
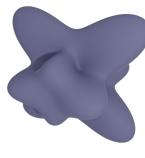
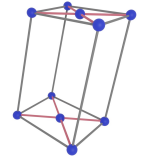

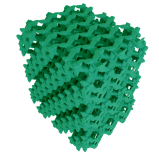
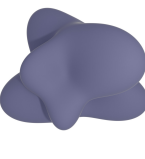
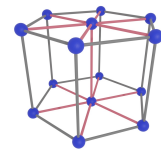

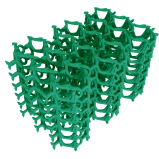
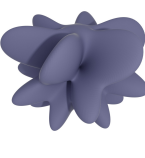
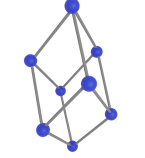

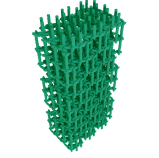
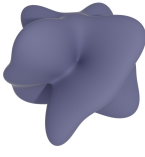
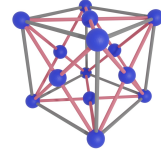

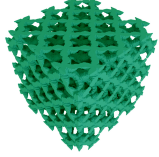
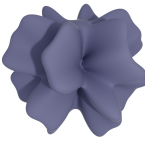
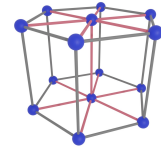

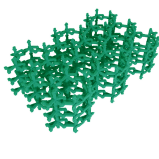

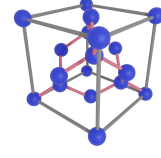
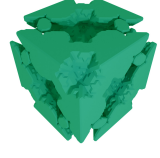

S	L	\mathcal{T}_{Lns}	Unit cell	3×3	Tensor
		1			$\begin{pmatrix} 1.264 & 1.002 & 0.610 & 0.026 & -0.117 & -0.422 \\ & 2.500 & 1.107 & 0.618 & -0.017 & -0.492 \\ & & 1.265 & 0.485 & -0.101 & -0.076 \\ & & & 0.788 & -0.006 & -0.004 \\ & & & & 0.436 & -0.011 \\ & & & & & 0.591 \end{pmatrix}$
1	$m\bar{3}m$	1			Triclinic
		2/m			$\begin{pmatrix} 3.393 & 2.276 & 1.318 & 0.000 & -0.821 & 0.000 \\ & 6.828 & 2.913 & 0.000 & -1.388 & 0.000 \\ & & 4.128 & 0.000 & -1.181 & 0.000 \\ & & & 3.041 & 0.000 & -1.385 \\ & & & & 1.277 & 0.000 \\ & & & & & 1.569 \end{pmatrix}$
mmm	2/m	2/m			Monoclinic
		222			$\begin{pmatrix} 0.447 & 0.291 & 0.050 & 0.000 & 0.000 & 0.000 \\ & 0.450 & 0.107 & 0.000 & 0.000 & 0.000 \\ & & 1.758 & 0.000 & 0.000 & 0.000 \\ & & & 0.127 & 0.000 & 0.000 \\ & & & & 0.115 & 0.000 \\ & & & & & 0.101 \end{pmatrix}$
222	6/mmm	222			Orthorhombic
		3			$\begin{pmatrix} 1.362 & 0.500 & 0.680 & 0.040 & 0.002 & -0.004 \\ & 1.367 & 0.656 & -0.038 & 0.004 & -0.015 \\ & & 3.079 & -0.003 & 0.001 & -0.003 \\ & & & 0.136 & 0.000 & 0.003 \\ & & & & 0.134 & 0.039 \\ & & & & & 0.453 \end{pmatrix}$
6	$\bar{3}m$	3			Trigonal
		422			$\begin{pmatrix} 6.710 & 4.235 & 2.925 & 0.000 & 0.000 & -0.003 \\ & 6.710 & 2.925 & -0.001 & 0.000 & -0.003 \\ & & 4.115 & 0.000 & 0.000 & 0.000 \\ & & & 1.913 & 0.123 & 0.000 \\ & & & & 1.913 & 0.000 \\ & & & & & 3.0314 \end{pmatrix}$
422	4/mmm	422			Tetragonal
		622			$\begin{pmatrix} 0.859 & 0.612 & 0.105 & 0.000 & 0.000 & 0.000 \\ & 0.858 & 0.100 & 0.000 & 0.000 & 0.000 \\ & & 1.474 & 0.000 & 0.000 & 0.000 \\ & & & 0.070 & 0.000 & 0.000 \\ & & & & 0.068 & 0.000 \\ & & & & & 0.119 \end{pmatrix}$
622	6/mmm	622			Hexagonal
		I_h			$\begin{pmatrix} 14.559 & 5.893 & 5.922 & -0.010 & -0.014 & 0.027 \\ & 14.392 & 5.873 & 0.077 & 0.004 & 0.075 \\ & & 14.411 & 0.081 & -0.059 & -0.005 \\ & & & 6.844 & -0.017 & 0.010 \\ & & & & 6.894 & -0.028 \\ & & & & & 6.865 \end{pmatrix}$
I_h	23	23			Cubic

Table B.2: Gallery open-cell